Atom Probe Tomography Insights into Stacking Faults in Zincblende InGaN/GaN Quantum Well Devices

Ruiying Shu

St Catherine's College

University of Oxford

A thesis submitted for the degree of *Doctor of Philosophy*

Michaelmas Term 2025

To study matter is to listen for the echo of consciousness

To my mother

Abstract

InGaN-based III-nitride light-emitting diodes (LEDs) have revolutionised optoelectronics, offering tunable bandgaps across the visible spectrum for applications ranging from solid-state lighting and displays to optical communication, sensing, and emerging quantum technologies. However, their emission efficiency in the green spectral region remains significantly lower than that of blue counterparts, which is a long-standing limitation known as the 'green gap'. A promising strategy to overcome this challenge is to apply the zincblende (cubic) phase, which combines a reduced bandgap with the absence of internal polarisation fields and therefore providing a pathway toward more efficient green emission. However, these cubic structures are inherently prone to extended planar defects, such as stacking faults (SFs), whose influence on local chemical environment and on device performance remain to be investigated.

This project employs atom probe tomography (APT) to reveal atomic-scale compositional inhomogeneities associated with SFs in zincblende InGaN/GaN quantum well (QW) structures. The first part of the thesis establishes an experimental framework for obtaining reproducible and reliable APT data from GaN-based layered materials. It addresses challenges such as APT sample preparation, focused ion beam (FIB)-induced artefacts, and stoichiometric drift, and introduces optimised acquisition parameters and site-fraction quantification methods.

The second part demonstrates and presents the 3D visualisation of SFs and their associated chemical variations in group III-nitride semiconductors through correlative APT and scanning transmission electron microscopy (STEM) studies. Rod-like indium enrichment and aluminium segregation along SFs within the multi-quantum well (MQW) samples are observed. It reveals SFs as preferential sites for localised compositional inhomogeneity.

The final part employs a single quantum well (SQW) sample to isolate the effects of individual SFs. Correlated APT-STEM analyses reveal that both indium and magnesium preferentially segregate along SFs, although they exhibited distinct behaviours. Magnesium segregation also indicates the polarity of the SF. In addition, intersecting SFs promote impurity accumulation due to combined strain and internal electrostatic effects. These structural and chemical variations correlate with cathodoluminescence (CL) results, where SF-rich regions show reduced near-band-edge emission and enhanced defect-related luminescence.

In summary, this work demonstrates the capability of APT to reveal nanoscale defect chemistry in III-nitrides. It provides new insights into how SFs influence the optical and electronic properties of zincblende InGaN/GaN QW devices. These findings advance the understanding of relationships between defect and property in cubic III-nitrides and have important implications for improving the performance of future III-nitride-based optoelectronic and quantum devices.

Preface

The work presented in this DPhil thesis has been carried out at the Department of Materials, University of Oxford from April 2021 to October 2025, under the supervision of Prof. Michael P. Moody, Dr. Paul A. J. Bagot, and Dr. Christina Hofer, in collaboration with Prof. Rachel A. Oliver. The work in this thesis is original, and the work of others included within is acknowledged and clearly referenced and acknowledged. No part of this thesis has been submitted for a degree at this or any other university. Some of the work in this thesis has been published in peer-reviewed journals and presented at conferences as detailed below:

List of publications:

R. Shu, R. A. Oliver, M. Frentrup, M. J. Kappers, H. Xiu, G. Kusch, D. J. Wallis, C. Hofer, P. A. J. Bagot, and M. P. Moody, "Atom Probe Tomography Investigation of the Impact of Stacking Faults on InGaN/GaN Quantum Well LED Systems," *Microscopy and Microanalysis*, vol. 30, no. Supplement_1, 2024.

R. Shu, R. A. Oliver, M. Frentrup, M. J. Kappers, H. Xiu, G. Kusch, D. J. Wallis, C. Hofer, P. A. Bagot, and M. P. Moody, "Beyond transmission electron microscopy imaging: Atom probe tomography reveals chemical inhomogeneity at stacking fault interfaces in InGaN/GaN light-emitting diodes," *Materialia*, pp. 102417, 2025.

A. Gundimeda, G. Kusch, M. Frentrup, H. Xiu, **R. Shu**, C. Hofer, P. A. J. Bagot, M. P. Moody, M. J. Kappers, D. J. Wallis, and R. A. Oliver, "Impact of stacking faults on the luminescence of a zincblende InGaN/GaN single quantum well," *Journal of Physics D: Applied Physics*, vol. 58, no. 2, pp. 025112, 2024/10/24, 2025.

X. Xu, M. Frentrup, G. Kusch, **R. Shu**, C. Hofer, P. A. J. Bagot, M. P. Moody, M. J. Kappers, D. J. Wallis, and R. A. Oliver, "Point defect luminescence associated with stacking faults in magnesium doped zincblende GaN," *Journal of Applied Physics*, vol. 137, no. 23, 2025.

List of conference talks:

"APT investigation on the role of Indium in InGaN quantum wells", V-APT&M, Nanjing China (virtual), October 2022

"APT investigation on the role of Indium in InGaN quantum wells" (poster), Microscopy of Semi-Conducting Materials, Cambridge UK, April 2023

“Exploring Stacking Faults in GaN-Based LEDs through APT Investigation”, APT&M, Leuven Belgium, Sep 2023

Student Scholar Award & Travel award: “APT Investigation of the Impact of Stacking Faults on InGaN/GaN Multi-Quantum Well LED Systems”, Microscopy and Microanalysis, Cleveland USA, July 2024

“From Sample to Data: Methodologies in APT for Enhanced Results”, UK-APT workshop, Oxford UK, Nov 2024

“3D Insights into Stacking Faults and Elemental Segregation in InGaN/GaN Quantum Wells via Atom Probe Tomography”, E-MRS 2025 FALL MEETING, Warsaw Poland, Sep 2025

Best Presentation Award: “Atom Probe Tomography Insights into Stacking Faults in Zincblende InGaN/GaN Quantum Well Devices”, CEMS 2025, Wuhan China, Sep 2025

In addition, I have contributed to further publications during my DPhil, which are not directly focus of my work and where I am not the main author. These works are:

- Yang *et al.*, “Development of the high-strength ductile ferritic alloys via regulating the intragranular and grain boundary precipitation of G-phase,” *Journal of Materials Science & Technology*, 2023. 136: p. 180-199.

- Liu *et al.*, “Hot-Isostatic Pressed Al Melt-Spun Ribbons with Tailored Microstructures and Mechanical Properties for Metallic Optics,” *Metallurgical and Materials Transactions A*, 2024. 55(9): p. 3147-3154.

Acknowledgements

I would like to begin by expressing my sincere gratitude to Professor Michael Moody and Dr Paul Bagot for giving me the opportunity to undertake this DPhil project. I am thankful to all three of my supervisors, Michael, Paul, and Dr Christina Hofer, for their supervision throughout my studies. I am especially indebted to Michael, who has been a true role model to me both as a scientist and as a person. His patience, generosity, and integrity will continue to influence me for the rest of my life, and I am profoundly grateful for his support. I would also like to thank Professor Mauro Pasta, whose thoughtful recommendation during my interview guided me to join this group, which has proven to be an excellent fit for my research interests and my development as a researcher.

I am also grateful to my examiners, Dr Tomas Martin and Professor Lorenzo Rigutti, for the engaging discussion during the viva and for their constructive feedback, which have helped to further improve this thesis.

I have been fortunate to work with collaborators from the University of Cambridge during my DPhil. I would like to thank Professor Rachel Oliver, Dr Martin Frentrup, Dr Menno Kappers, Dr Gunnar Kusch, and Professor David Wallis for their constructive discussions and valuable insights. I am especially grateful to Professor Rachel Oliver, whose generous support and guidance have been invaluable to me. Her dedication, patience, and encouragement have had a lasting impact on both my research and personal development.

I would like to thank all members of the Atom Probe group for creating a friendly and supportive environment and for maintaining the smooth operation of the laboratory. I am deeply grateful to Dr Jaspreet Singh for the generous amount of time he devoted to training and guiding me through the FIB specimen preparation process. My sincere thanks go to Dr Martin Meier and Dr Megan Jones for their expert assistance with MATLAB for APT data analysis, and to Dr Megan Carter for her expert help with the FIB experiments after my countless failed attempts at preparing layered GaN needles. I would also like to thank Dr Benjamin Jenkins for always being open to questions and for providing valuable insights on many topics. I am grateful to Dr Sophia Ungermann for her helpful suggestions on my writing and for the thoughtful painting cards. I am very thankful to my wonderful office colleagues, Laura Lain, Dr Megan Jones, Dr Laura Wheatley, Dr Minyi Zhang, and Wenyu Zhang, for the research discussions, mutual help, and shared experiences, and for the many conversations through which we supported each other in both work and life. Their warmth and positivity made my DPhil journey much brighter and more meaningful. Finally, I would like to thank Dr Przemyslaw Klups, Dr Yanru Ren, Dr Victoria Strutt, Dr Kieran Rivers, Holly, Hannah, Anthony, Andrew, Yuhan (Zhuge), Evie, and the Oxford Raptors for their insights and for the unforgettable memories.

I would also like to acknowledge my undergraduate mentors, Professor Gang Sha, Professor Shenbao Jin, and Professor Sen Yang, who guided and encouraged me to explore the fascinating world of scientific research. I am thankful to Professor Lorenzo Rigutti and Professor David Saxey, whose research and publications have long been a source of great intellectual inspiration. I am grateful to Professor Eason Chen for his recognition and encouragement, which have meant a great deal to me.

I am also grateful to the community of St Catherine's College (Catz) and the Catz Rowing Team for their camaraderie and spirit, which made my time at Oxford truly memorable. I owe my heartfelt gratitude to my counsellor, and to Ms Celine Mok, for their kindness and support during difficult times.

Thank you to my extraordinary friends in Oxford. I will always cherish the laughter, memories, and support I received from the wonderful community I was fortunate to become part of. My heartfelt thanks go to Kun, Ruining, Kai Ling, Houzhi, Yuhan (He), Yi, Kenny, Lina, Zhixin, Yige, Yumeng, Nuolin, Celeste, and the countless others who made Oxford a place I can truly call home and made my DPhil journey so much brighter. I would also like to thank Jiale Fu for his support and companionship during part of this journey.

From the bottom of my heart, I would like to thank my mother for her unconditional love and support, both emotional and financial, and for her steadfast confidence in me even when I doubted myself. Her regular calls and messages over the past four years have given me the strength to keep pushing forward from time to time in this beautiful yet distant country.

Completing this DPhil has been a challenging yet valuable journey, and I am proud of how much I have grown through it. To the quiet moments of clarity that reminded me I wasn't alone.

Most of all, I thank myself —
for walking through the fog with quiet feet,
for thinking gently when silence would have been simpler,
and for keeping a soft light on, even when no one was looking.

For tending to small hopes, for loving ideas that had no name yet,
and for believing, always, that something good would bloom —
somewhere, somehow, with time.

Acronyms

ABF	Annular Bright-Field
AFM	Atomic Force Microscopy
APT	Atom Probe Tomography
BSE	Backscattered Electron
CL	Cathodoluminescence
CSR	Charge State Ratio
DFT	Density-Functional Theory
DUV	Deep-Ultraviolet
EBL	Electron Blocking Layer
EDX	Energy-Dispersive X-Ray Spectroscopy
EQE	External Quantum Efficiency
e-SF	Extrinsic Stacking Fault
FIB	Focused Ion Beam
HAADF	High-Angle Annular Dark Field
HR	High-Resolution
HRXRD	High-Resolution X-Ray Diffraction
i-SF	Intrinsic Stacking Fault
IQE	Internal Quantum Efficiency
kNN	k-Nearest-Neighbour
LED	Light-Emitting Diodes
MBE	Molecular Beam Epitaxy
MQW	Multi-Quantum Well
MOVPE	Metalorganic Vapour Phase Epitaxy
MPPL	Multiphoton Photoluminescence
NIR	Near-Infrared
PAP	Photonic Atom Probe
PL	Photoluminescence
QCSE	Quantum-Confined Stark Effect
QW	Quantum Well
ROI	Regions of Interest
SE	Secondary Electron
SF	Stacking Fault

SIMS	Secondary Ion Mass Spectrometry
SQW	Single Quantum Well
SSL	Solid-State Lighting
STEM	Scanning Transmission Electron Microscopy
TD	Threading Dislocation
TEM	Transmission Electron Microscopy
ToF-MS	Time-of-Flight Mass Spectrometry
wz	wurtzite
XRD	X-Ray Diffraction
zb	zincblende

Table of Contents

Chapter I Introduction 1

1.1. Motivation 1

1.2. Thesis Structure 3

Chapter II Literature Review 6

2.1. Fundamentals of Zincblende InGaN/GaN Quantum Wells 7

2.1.1. Introduction 7

2.1.2. Crystal Structures of GaN: Wurtzite vs. Cubic 8

2.1.3. Polarisation and QCSE in III-Nitrides 10

2.1.4. Cubic InGaN/GaN Quantum Wells 13

2.2. Stacking Faults (SFs) in Cubic GaN 20

2.2.1. Origin of SFs in Cubic GaN 20

2.2.2. Impact of SFs on Optical and Electronic Properties 23

2.2.3. Brief Overview of MOVPE Growth 26

2.3. Developing Atom Probe Tomography (APT) for III-Nitride 28

2.3.1. Current Characterisation Approaches and Limitations 28

2.3.2. Applications of APT in III-Nitride Research 31

2.3.3. Challenges in APT Analysis of III-Nitride Systems 37

2.4. Summary 44

Chapter III Materials and Experimental Methods 45

3.1. Materials 46

3.2. Electron Microscopy 47

3.2.1. Scanning Electron Microscopy (SEM) 47

3.2.2. Focused Ion Beam (FIB) 49

3.2.3. Transmission Electron Microscopy (TEM) & Scanning Transmission Electron Microscopy (STEM) 50

3.3. Atom Probe Tomography (APT) 52

3.3.1. Basic Principles 53

3.3.2. Common Artefacts and Challenges 56

3.3.3. Atom Probe Sample Preparation 59

3.3.4. APT Data Collection and Reconstruction 62

3.3.5. APT Data Analysis Tool and Techniques 69

3.4. Summary 77
Chapter IV Best Practices for APT of Layered GaN 78
4.1. Challenges of GaN in Practical APT 79
4.2. FIB APT Specimen Preparation 80
4.2.1. Best-Practice Protocol for GaN 80
4.2.2. Layer-Targeted Positioning by Correlative SEM-EDX and FIB 85
4.2.3. Accurate Height and Diameter Control 87
4.3. Protocol for Reproducible GaN APT Acquisition 90
4.3.1. APT Parameter Effect on GaN 90
4.3.2. APT Results 93
4.3.3. Discussion 100
4.3.4. Optimised Parameters for Stable Running on layered InGaN/GaN 107
4.4. Conclusion 108
Chapter V Multi-quantum well LED Analysis 109
5.1. Experimental 110
5.1.1. Zincblende InGaN/GaN MQW Sample Growth 110
5.1.2. Experimental methods 111
5.2. Results 112
5.2.1. Visualisation of Atomic Structures with STEM 112
5.2.2. APT Results 113
5.2.3. Detection of SFs Using APT 116
5.2.4. Elemental Segregation at SFs 118
5.3. Discussion 120
5.3.1. STEM Structural Interpretation 120
5.3.2. Analysis of APT Results 122
5.3.3. Analysis of SFs 122
5.3.4. Impact of SFs on Elemental Segregation 127
5.4. Conclusion 132
Chapter VI Single quantum well LED Analysis 134
6.1. Experimental 136
6.1.1. Zincblende InGaN/GaN SQW Sample Growth 136
6.1.2. Experimental Methods 137
6.2. Results 139

6.2.1. Visualisation with STEM 139
6.2.2. APT Analysis of SF Configurations 141
6.2.3. Detection and Orientation-Dependent Indium Segregation at SFs 144
6.2.4. Mg Segregation and Local Field Variations at SFs 150
6.3. Discussion 156
6.3.1. Interaction between SFs 156
6.3.2. Orientation-Dependent Segregation Behaviour 158
6.3.3. Different Types of SFs and Their Field and Chemical Characteristics 161
6.3.4. Implications for Other Dopant Species 169
6.3.5. Related Optical Properties 171
6.4. Conclusion 175
Chapter VII Conclusions and Future Work 176
7.1. Conclusion 176
7.2. Outlook 178
7.2.1. Growth-Condition Dependence 178
7.2.2. Crystallographic Orientation and Polarity Correlation 178
7.2.3. Atomistic Modelling of Bonding and Segregation Energetics 179
References 180
Appendix A: Preliminary APT Study on Carbon-Doped Wurtzite GaN 200
Appendix B: Operating Conditions for GaN Analysis 202

Chapter I Introduction

1.1. Motivation

Gallium Nitride (GaN) is an important topic in materials science. It has a wide range of applications in a variety of disciplines, including, but not limited to, power electronics, optoelectronics, photonics and logic circuits. It is promising for its unique properties, including a wide direct bandgap, high breakdown voltage, and remarkable thermal stability, which have led to advancements in power converters [1], wireless communication [2], and solid-state lighting (SSL) [3, 4]. Among them all, its most significant impact has been in the field of optoelectronics, where it has led to a revolution in technologies such as light-emitting diodes (LEDs), lasers and photodetectors [5, 6]. It remains the near-perfect solution to several challenges, including achieving high energy efficiency in lighting [7], enabling high-power operation in compact laser systems [8], improving device longevity under extreme conditions [9], and advancing miniaturisation for next-generation photonic devices [10]. Notably, the development of blue LEDs revolutionised SSL [11-14]. While challenges such as the green gap are emerging [13, 15-20], research into GaN and its related alloys remains a key driver of innovation and a foundational element in modern materials science.

As technologies for micro-displays develop, there is increasing demand for red, green, and blue nitride micro-LEDs based on the expectation that they can be used to achieve long lifetimes,

low energy consumption, high resolution, and wide colour gamut with high purity [21, 22]. To address the issue of reduced radiative recombination rates caused by piezoelectric and spontaneous polarisation fields in wurtzite (wz) nitrides, zincblende (zb) InGaN/GaN-based devices have been introduced. This alternative structure helps enhance the efficiency and performance in optoelectronic applications by minimising the effects of fields. However, intrinsic {111} stacking faults (SFs) are commonly found in zincblende nitrides [23]. These extended planar defects may lead to local variations in indium content in the quantum wells (QWs), potentially reducing the spectral purity and negatively influencing device efficiency [24, 25]. The impact of SFs on devices fabricated using this alternative nitride crystal structure is still relatively unexplored, and further characterisation of their structure and composition can help us understand how they influence the performance of LEDs.

Therefore, the objective of this thesis is to understand the compositional and structural characteristics of SFs and their impact across different structural layers including QWs, via atomic resolution analytic techniques. In this thesis, atom probe tomography (APT) and scanning transmission electron microscopy (STEM) are the two primary tools employed for such characterisation, with APT being especially useful in accessing atomic-scale levels of chemical information and evidence of element segregation in three-dimensions. The preparation of samples for APT analysis is a major focus in this work, as it is a significant challenge to overcome for effective, targeted application of APT to semiconductor characterisation. Furthermore, the combination of APT with STEM and cathodoluminescence (CL) spectroscopy enables a comprehensive correlation between defect chemistry, structure, and optical response, providing new insights into the behaviour of SFs in cubic GaN.

Overall, this thesis contains three high-level aims:

1. Develop a reliable APT sample preparation and acquisition methodology that enables accurate and reproducible quantification of GaN-based materials, including layered InGaN/GaN heterostructures
2. Characterise the compositional and structural variations associated with SFs in zincblende GaN using APT, and establish reliable quantification approaches for extended defects
3. Correlate the structural, chemical, and optical characteristics of SFs by integrating APT with STEM and CL spectroscopy, to reveal how SF-related segregation influences luminescence and recombination behaviour in cubic GaN

1.2. Thesis Structure

This thesis is divided into 6 chapters.

Chapter II provides a brief introduction to GaN-based optoelectronic devices, their structure, defects and growing methods. Furthermore, current methods for characterising such devices are reviewed, with particular emphasis on APT. A critical overview of the state of the literature regarding the microscopic characterisation of defects within InGaN/GaN-based devices is also presented, with particular emphasis placed on atomic-scale resolution characterisation.

Chapter III briefly describes the growing methods of the materials analysed in further chapters along with a description of the analysis methods and data analysis tools used throughout the course of the study.

Chapter IV presents the development and validation of a reliable methodology for APT analysis of GaN and InGaN/GaN heterostructures. Specimen preparation and data acquisition protocols are optimised to address challenges such as specimen fracture, Ga implantation, and stoichiometric drift, thereby enabling accurate and reproducible quantification. This methodological framework provides the foundation for subsequent defect analyses and can be extended to other III-nitride material systems.

Chapter V focuses on SFs behaviour in multi-quantum well (MQW) GaN devices. It demonstrates that SFs in zincblende GaN can be visualised and quantitatively characterised using APT. Quantitative APT-STEM correlation shows that the apparent Ga-concentration variations arise from local field-evaporation effects, whereas the In enrichment at SFs intersecting QWs and the Al enrichment at SF/AlGaN intersections reflect genuine compositional segregation. The application of a site-fraction quantification method enables reliable chemical analysis of extended defects in GaN.

Chapter VI describes the results of APT analysis of SFs in single quantum well (SQW) GaN devices. This chapter integrates CL spectroscopy with correlative STEM and APT to link defect structure, chemistry, and optical properties. Both In and Mg are found to segregate preferentially along SFs, with the degree of segregation depending on local SF polarity. CL measurements show that SF-rich regions exhibit quenched near-band-edge emission and enhanced defect-related luminescence, providing insights into how SF-related segregation influences radiative recombination in cubic GaN.

Chapter VII provides a summary of the key findings presented throughout the thesis and closes with a discussion of potential future research to build on the findings in this thesis.

Chapter II Literature Review

This chapter provides a comprehensive literature review structured in three main parts, following the outline shown above. It first introduces the fundamental concepts relevant to zincblende InGaN/GaN quantum wells (QWs), including the crystal structures of GaN, polarisation and quantum-confined Stark effect (QCSE) effects, and the specific features of zincblende InGaN/GaN QWs.

It then summarises the current understanding of SFs in zincblende GaN, discussing their origins, their influence on the optical and electronic properties of III-nitride devices, and a brief overview of metalorganic vapour phase epitaxy (MOVPE) growth relevant to the formation of such defects.

Finally, it reviews the development of atom probe tomography (APT) for III-nitride semiconductors. This includes an overview of current characterisation approaches and their limitations, the applications of APT in III-nitride research, and the key challenges associated with APT analysis of these materials. Together, these sections provide the necessary background for interpreting the structural and compositional behaviour of III-nitride QW systems.

2.1. Fundamentals of Zincblende InGaN/GaN Quantum Wells

2.1.1. Introduction

In the modern world, artificial lighting plays an essential role in our life. We spend a significant amount of time, either indoors or outdoors, in environments illuminated by artificial light. The quality of light, including brightness, colour and colour temperature, has been shown to impact our physiological well-being and physical health directly [26]. Traditional illumination technologies, including incandescent, halogen, and compact fluorescent lamps, rely on thermal or phosphor-mediated emission mechanisms and therefore suffer from low energy efficiency, limited lifespans, and environmental concerns such as mercury content in fluorescent lamps. In contrast, light-emitting diodes (LEDs) have transformed solid-state lighting (SSL) due to their high luminous efficacy, long operational lifetimes, and capacity for spectrally tailored emission [27]. Recent demonstrations, such as Cree's 303 lm/W laboratory result [28], confirm that nitride-based LEDs already approach the theoretical limits projected for SSL [29], providing substantial reductions in energy consumption and carbon emissions [12, 30, 31].

The rapid progress in this field can be attributed to the development of efficient blue LEDs that are based on InGaN semiconductors [32]. Owing to their direct and composition-tunable bandgap, InGaN alloys support emission across the entire visible spectrum and have enabled the widespread use of phosphor-converted white LEDs in both residential and industrial settings [33-37]. Despite this success, achieving efficient direct green emission remains challenging. Green emitters exhibit significantly lower internal quantum efficiencies compared to their blue and red counterparts, a phenomenon known as the 'green gap' that persists to this day [13, 15, 16, 18-20]. However, as yellowish green is the colour to which our eyes are most sensitive [38], addressing the green gap is therefore vital in developing highly efficient artificial light sources to light up our living and working environments. Additionally, emerging

applications such as micro-displays and visible-light communication demand highly efficient red, green, and blue micro-LEDs, further emphasising the need to improve green nitride emitters [21, 22].

This chapter introduces the structural, electronic and optical foundations of III-nitride materials relevant to cubic InGaN/GaN QWs. It outlines the key differences between wurtzite and zincblende GaN, the role of polarisation and QCSE in InGaN-based emitters, and the significance of SFs in determining the performance of zincblende heterostructures, paving the way for the APT investigations presented later in this thesis.

2.1.2. Crystal Structures of GaN: Wurtzite vs. Cubic

Typically, GaN is found in the wurtzite phase, which has a hexagonal, non-centrosymmetric arrangement of Ga and N atoms, as shown in Figure 2-1 [39]. This lack of inversion symmetry leads to strong spontaneous and strain-induced piezoelectric polarisation fields along the c-axis [40]. These built-in fields strongly influence the behaviour of III-nitride optoelectronic devices and become a key factor limiting the efficiency of long-wavelength InGaN-based emitters. In contrast, zincblende GaN has a higher-symmetry cubic structure compared with wurtzite GaN, as illustrated in Figure 2-1, and therefore does not exhibit spontaneous and piezoelectric polarisation [41]. Along the ⟨111⟩ direction, zincblende GaN exhibits an -ABCABC- stacking sequence, while wurtzite GaN follows an -ABAB- sequence. This distinction in stacking sequence and symmetry leads to differences in band structure, lattice constants, and electronic properties between the two phases.

Although wurtzite (wz) GaN is the thermodynamically favoured structure under ambient conditions, the zincblende phase presents several attractive advantages for long-wavelength emitters. Firstly, zincblende GaN exhibits a slightly narrower bandgap than its wurtzite counterpart [40], offering more flexibility and efficiency in producing light at longer wavelengths, such as green light. In addition, the absence of internal polarisation fields means that InGaN/GaN QWs grown along the (001) direction exhibit a flat band profile, enabling stronger electron-hole wavefunction overlap and potentially higher radiative recombination efficiencies [41, 42]. Together, these properties make zincblende InGaN/GaN structures an attractive route for overcoming the limitations of conventional wurtzite-based green LEDs [43, 44].

Table 2-1 provides a concise comparison of the physical and electronic parameters of wurtzite and zincblende GaN, highlighting the differences that influence strain, polarisation fields, and carrier recombination.

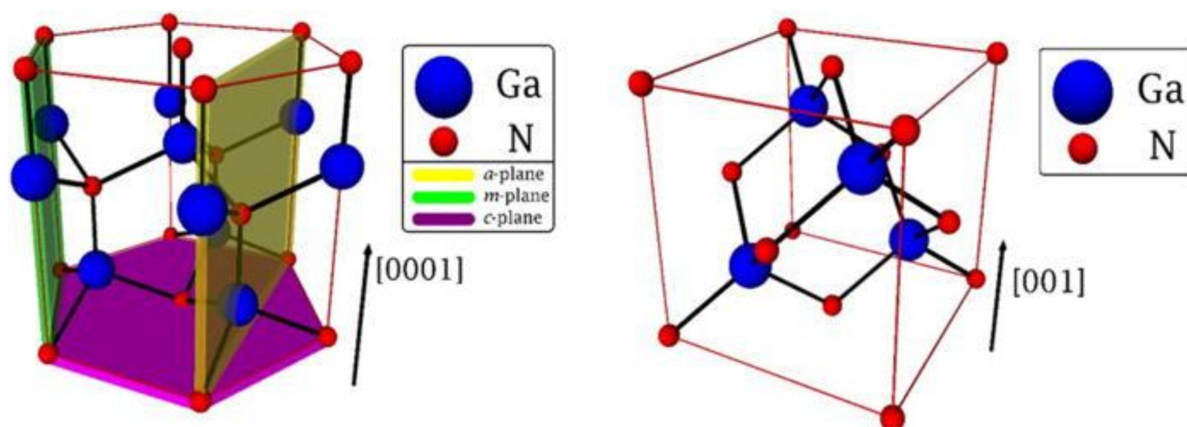

Figure 2-1 Crystal structures of wurtzite GaN (left) and zincblende GaN (right), illustrating the positions of cations (Ga, blue) and anions (N, red). Adapted from [39], with permission from AIP Publishing.

Table 2-1 Key physical and electronic properties of wurtzite (wz) and zincblende (zb) GaN relevant to InGaN/GaN quantum well optoelectronics

Property	Wurtzite GaN	Zincblende GaN	Impact on QW physics
Energy band gap (eV)	3.39 [45]	3.2 [46]	Smaller bandgap enables longer-wavelength (green) emission (zb)
Lattice constant (Å)	*a*=3.189, *c*=5.185 [47]	*a*=4.50 [47]	Larger mismatch increases strain and promotes SF formation (zb)
Polarisation fields	Strong (spontaneous + piezo)	None	Strong polarisation enhances QCSE (wz); QCSE suppressed in zb
Electron mobility ($cm^2/V\cdot s$)	~1000 [48-50]	≤1000 [51]	Higher mobility improves carrier transport into QWs (wz)
Hole mobility ($cm^2/V\cdot s$)	≤200 [52]	≤350 [53, 54]	Higher mobility improves hole injection and recombination (zb)
Electron effective mass (m_0)	0.2 [55]	0.13 [55]	Lower mass enhances electron wavefunction overlap (zb)
Hole effective mass (m_0)	~1.4 [56]	~1.3 [56]	Lower mass reduces hole localisation (zb)

2.1.3. Polarisation and QCSE in III-Nitrides

Polarisation effects play a vital role in determining the electronic and optical behaviour of III-nitride QWs. In wurtzite InGaN/GaN heterostructures, the absence of inversion symmetry enhances strong spontaneous polarisation, while lattice-mismatch-induced strain generates substantial piezoelectric polarisation. Together, these polarisation components produce a large built-in electric field across the QW. This internal field tilts the conduction and valence band edges, driving electrons and holes toward opposite sides of the well and reducing their wavefunction overlap. The effect is known as the QCSE (quantum-confined Stark effect), which is widely recognised as a major contributor to reduced radiative recombination efficiency in high-indium-content InGaN/GaN emitters [17, 57].

Although the indium composition can be adjusted to tune the emission wavelength, higher indium incorporation significantly increases the lattice mismatch between the InGaN QW and

both the GaN barrier and the underlying GaN buffer layer, thereby promoting the formation of structural defects [58]. In the meantime, QCSE becomes increasingly severe at higher indium compositions, since the larger strain enhances the piezoelectric polarisation, and the increased polarisation charge at the interfaces strengthens the internal electric field across the QW [59, 60]. This intensified field further separates electron and hole wavefunctions and deepens the reduction in radiative recombination efficiency [60]. As a result, wurtzite-based green LEDs often suffer from red-shifted emission, reduced oscillator strength, and efficiency droop at high current densities. This inefficiency thereby limits the colour purity and overall performance of LED applications [61].

Figure 2-2 illustrates the contrast between non-polar (zincblende) and polar (wurtzite) InGaN/GaN QWs. In the zincblende structure, the absence of spontaneous and piezoelectric polarisation fields results in flat band edges and strong electron-hole wavefunction overlap, enabling efficient radiative recombination. However, in wurtzite QWs, large internal polarisation fields tilt the conduction and valence band edges. This built-in field spatially separates electrons and holes, reduces their overlap, and lowers the transition energy ($h\nu_2 < h\nu_1$), which is a phenomenon commonly associated with the QCSE.

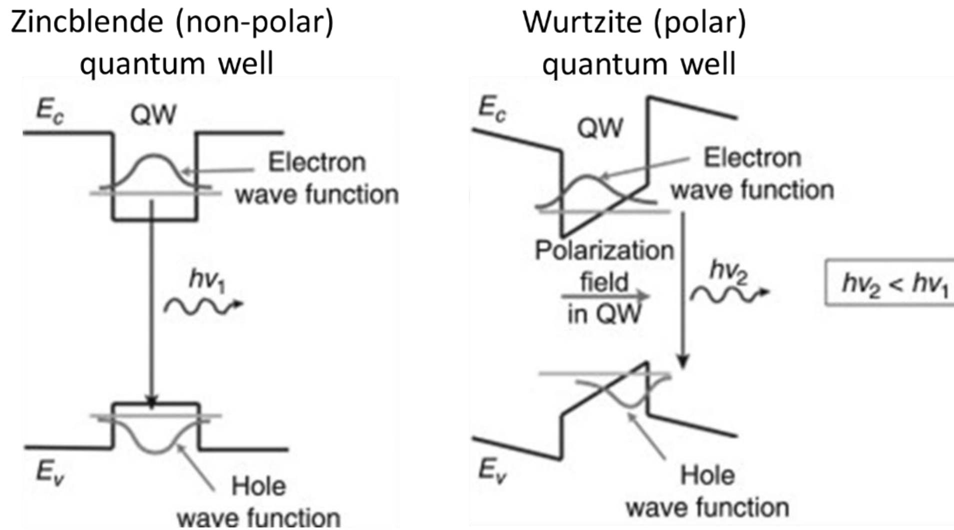

Figure 2-2 Comparison of non-polar (zincblende) and polar (wurtzite) InGaN/GaN QWs. Internal polarisation fields in the wurtzite structure tilt the band edges and reduce electron-hole overlap, characteristic of the QCSE. Adapted from [62]

Recent studies have provided deeper insight into how the QCSE affects the performance of wurtzite III-nitride emitters. Daami *et al.* [63] demonstrated that QCSE-induced red shifts are particularly pronounced in wurtzite green LEDs due to high indium content and the resulting interface charge density. They further showed that increased injection voltage partially screens the internal field, producing a corresponding blue shift. Singh *et al.* [64] proposed an optimised electron-blocking-layer (EBL) design that mitigates polarisation-induced energy spikes at the last barrier/EBL interface, enhancing self-screening and increasing the internal quantum efficiency by ~45%, while halving the voltage required to reach 1 A/cm². Agata *et al.* [65] reported non-uniform carrier distribution in InGaN/GaN multi-quantum wells (MQWs), finding that only the well closest to the p-layer dominates emission due to QCSE-affected carrier injection, emphasising the need for careful QW placement and design. It should be noted that all the studies discussed above examine the QCSE in wurtzite-phase InGaN/GaN structures.

In contrast to wurtzite, zincblende GaN is non-polar and exhibits negligible spontaneous and piezoelectric polarisation. As a result, InGaN/GaN QWs grown in the cubic phase exhibit negligible QCSE, allowing strong electron-hole overlap and potentially higher radiative recombination rates [44]. The suppression of QCSE makes zincblende III-nitrides an attractive option for creating high-efficiency, high-brightness LEDs with reduced efficiency droop [43].

2.1.4. Cubic InGaN/GaN Quantum Wells

2.1.4.1. Overview of InGaN/GaN Quantum Well LEDs

LEDs are p-n junction devices fabricated from direct-bandgap III–V semiconductors such as GaAs, InP, and InGaN [66]. Under forward bias, electrons from the n-type region and holes from the p-type region are injected into the junction, where they recombine radiatively. Because materials such as GaN and InGaN possess direct bandgaps, their conduction-band minimum and valence-band maximum align in momentum space, enabling efficient photon emission without phonon assistance [67, 68]. As a result, radiative recombination dominates over non-radiative processes, contributing to the high efficiency of LEDs based on these materials. The emission wavelength λ of a p-n junction is determined by the semiconductor bandgap E_g, following $\lambda = \frac{hc}{E_g}$. Therefore, achieving a specific emission wavelength requires selecting a semiconductor with an appropriate direct bandgap [67]. Figure 2-3 shows the basic principle of radiative recombination in a p-n junction LED, where electrons and holes recombine within the depletion region to produce light.

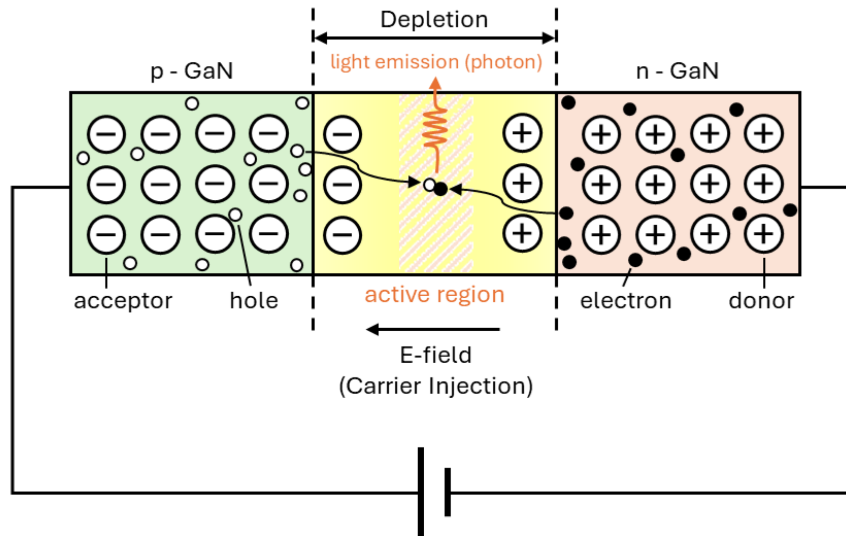

Figure 2-3 Structure of p-n junction of LED

InGaN/GaN QWs form the active region in modern III-nitride LEDs. A typical device structure is shown in Figure 2-4. The substrate provides mechanical support, while a GaN buffer layer reduces defect density. The n-type GaN layer supplies electrons, and the p-type GaN layer supplies holes. Between them, one or multiple thin InGaN QWs confine both carriers due to their smaller bandgap relative to the GaN barriers. An EBL, typically p-AlGaN, is often incorporated to suppress electron overflow into the p-side and ensure efficient radiative recombination within the QWs [69, 70].

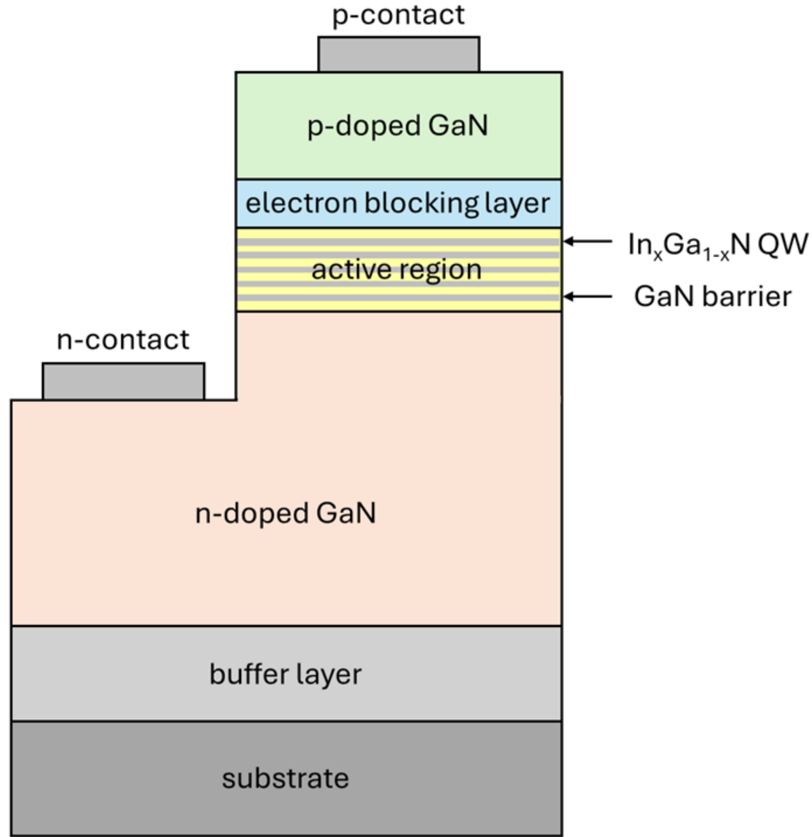

Figure 2-4 Schematic of a basic GaN LED structure.

In those optoelectronic devices, the efficiency is determined by the competition between radiative and non-radiative recombination processes. The internal quantum efficiency (IQE) is a critical parameter that quantifies the fraction of carriers contributing to radiative recombination relative to all recombination processes, which can be defined as:

$$IQE = \frac{I_{rad}}{I} = \frac{I_{rad}}{I_{rad} + I_{lost}}$$

where I_{rad} is the radiative recombination current and I_{lost} represents non-radiative losses. IQE is a basic measure of material quality and device performance and is unaffected by external optical losses [68]. Meanwhile, there is another related concept, external quantum efficiency (EQE), includes additional external factors. The EQE is the fraction of the incident photons

that are converted into a usable output, i.e. emitted light, and therefore is more straightforward to measure than IQE. The EQE can be expressed as:

$$EQE = \eta_{inj} \times IQE \times \eta_{ext}$$

where η_{inj} represents the efficiency of carriers into the active region, and η_{ext} is the photon extraction efficiency [68].

Following the early observation of electroluminescence in SiC [71-76], major advances in III–V semiconductors, including the development of visible GaAsP LEDs [77] and the realisation of p-type GaN [78, 79], which led to the first high-brightness GaN-based blue LEDs. The introduction of high-quality InGaN QWs and the optimisation of MOVPE growth processes enabled efficient blue emission, culminating in the commercialisation of GaN-based LEDs in the 1990s [11, 80, 81]. This progress ultimately resulted in the Nobel Prize in Physics in 2014, awarded to Akasaki, Amano and Nakamura for their pioneering contributions to GaN-based LEDs [82, 83].

Today, InGaN/GaN QW LEDs underpin a wide range of applications, from SSL to micro-displays and laser diodes, owing to their broad and composition-tunable emission range spanning the ultraviolet to the near-infrared (NIR) [6, 84-87]. However, conventional devices based on the wurtzite crystal phase experience strong polarisation fields that degrade radiative efficiency, particularly at high indium compositions. These limitations have stimulated growing interest in cubic (zincblende) III-nitrides, whose non-polar crystal symmetry offers a promising route for improved carrier confinement and enhanced QW luminescence efficiency.

As shown in Figure 2-5 (a), wurtzite GaN has a bandgap of approximately 3.4 eV, while binary III-nitride compounds such as wurtzite-InN and wurtzite-AlN possess bandgaps of 0.7 eV and 6 eV, respectively [88]. These materials exhibit band-to-band optical transitions spanning the deep-ultraviolet (DUV) to the NIR spectral regions. Therefore, by adjusting the In and/or Al mole fractions in ternary or quaternary InAlGaN alloys, the emission wavelength of III-nitride semiconductors can be effectively tuned across the DUV-visible-NIR spectrum through band engineering. Beyond their central role in the development of blue and white SSL, III-nitride light emitters have expanded into a wide range of emerging photonic applications, as illustrated in Figure 2-5(b) [88]. Those wide-ranging applications highlight the technological importance of InGaN/GaN QWs and motivate continued efforts to improve long-wavelength performance, particularly in the green spectral region where wurtzite devices suffer from strong polarisation effects and reduced efficiency.

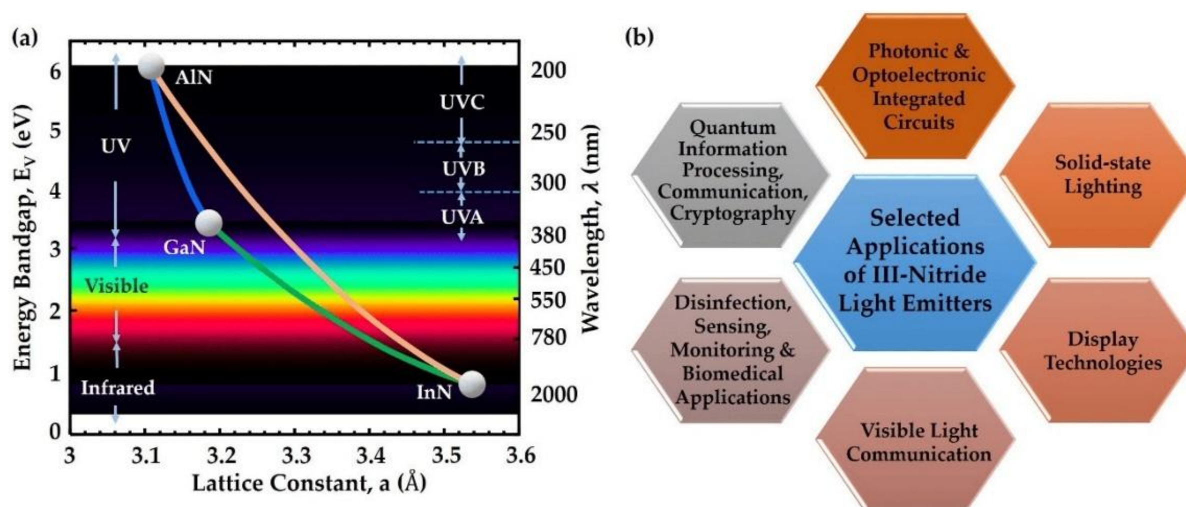

Figure 2-5 (a) Energy bandgaps and corresponding emission wavelengths of different III-nitride materials shown against their lattice constant; (b) selected applications of III-Nitride light-emitting devices. Reproduced from [88], under the terms of the Creative Commons Attribution (CC BY) license (https://creativecommons.org/licenses/by/4.0/).

2.1.4.2.Band Structure and Carrier Confinement in Cubic QWs

QWs are heterostructures in which a thin, narrow-bandgap semiconductor layer is confined between materials with wider bandgaps. When the well thickness approaches the de Broglie wavelength of charge carriers, quantum confinement occurs, leading to discrete electron and hole energy levels and enhanced carrier localisation within the well [89]. Such quantisation allows precise control over transition energies, strengthens carrier confinement, and improves radiative recombination efficiency. As a result, QWs are central to modern optoelectronic devices such as LEDs and laser diodes. In zincblende GaN LEDs, the InGaN QW is the key active region responsible for efficient light emission.

A key distinction between cubic (zincblende) and wurtzite InGaN/GaN QWs lies in their band structure and the influence of internal polarisation fields. In the wz phase, the lack of inversion symmetry generates strong spontaneous and piezoelectric polarisation fields along the c-axis. These fields tilt the conduction and valence band edges, spatially separating electrons and holes across the QW. This reduced wavefunction overlap slows radiative recombination and increases the relative contribution of non-radiative pathways, thereby lowering efficiency [43, 90, 91]. The magnitude of these fields is substantial, typically on the order of 1–3 MV/cm in wz InGaN/GaN structures [91], and becomes more severe at higher indium compositions.

In contrast, the zincblende III-nitrides grown along the [001] direction are non-polar, resulting in flat band edges of zincblende InGaN/GaN QWs and minimal internal electric fields (<0.1 MV/cm [43]). This enables strong electron-hole wavefunction overlap and more efficient radiative recombination than their wurtzite counterparts at comparable indium compositions [43, 90, 91]. This intrinsic advantage directly addresses one of the fundamental limitations of

wurtzite green emitters, where QCSE-induced carrier separation contributes to reduced oscillator strength and efficiency droop.

Recent optical studies have provided direct experimental verification of these advantages. Church *et al.* demonstrated that cubic InGaN/GaN QWs exhibit radiative lifetimes of approximately 600 ps, which is indicative of electric-field-free recombination and strong wavefunction overlap [92]. At cryogenic temperatures, these QWs show near-unity internal quantum efficiency due to the absence of competing non-radiative channels. Even at room temperature, appreciable emission is maintained, with relative photoluminescence intensities of 4–5% for 5–7.5 nm-thick QWs, significantly higher than the ~0.2% observed for single thin QWs [92]. Importantly, because band tilting is absent, increasing the QW thickness can enhance radiative efficiency by suppressing thermionic carrier escape. This behaviour contrasts with that of wurtzite QWs, where thicker wells amplify QCSE and reduce radiative recombination.

Together with the direct and composition-tunable bandgap of InGaN, which spans the near-UV to visible spectral region [39, 90], the field-free band structure of cubic InGaN/GaN QWs provides an electronically favourable environment for efficient long-wavelength emission. Its intrinsic suppression of QCSE, combined with enhanced carrier confinement and strong radiative recombination, makes cubic QWs a promising structure for next-generation III-nitride optoelectronic devices.

Despite these attractive electronic and optical properties, the practical implementation of zincblende GaN and related QW structures remains limited. This is mainly due to the metastability of the cubic phase relative to wurtzite GaN, which makes phase stabilisation during epitaxial growth challenging [25]. Growth on lattice-mismatched substrates further introduces high densities of extended defects, such as SFs, originating from local disruptions of the ideal ABC stacking sequence [93, 94]. In addition, the absence of native bulk cubic GaN substrates and the strong sensitivity of phase stability to growth conditions hinder the realisation of device-grade material quality [95]. These challenges have so far limited the widespread adoption of zincblende III-nitride optoelectronic devices.

2.2. Stacking Faults (SFs) in Cubic GaN

2.2.1. Origin of SFs in Cubic GaN

SFs are among the most common extended defects in both wurtzite and zincblende III-nitrides [96-98]. Their formation is closely related to the small free-energy difference between the zb and wz phases of GaN, with the wz structure being thermodynamically favoured under ambient conditions [39, 99]. As a result, local variations in growth conditions have been reported to correlate with wz–zb polytype transitions in III-nitrides [94]. In cubic GaN, most SFs lie on the {111} planes, corresponding to disruptions of the ideal -ABCABC- stacking sequence [23]. As shown in Figure 2-6, the SFs in cubic GaN epitaxial layers are clearly resolved at the atomic scale, corresponding to local disruptions of the ideal -ABCABC- stacking sequence, while the highlighted zb region on the left represents the ideal cubic stacking sequence for comparison. As reported in Ref. [94], such SFs in cubic GaN occur on close-packed {111} planes.

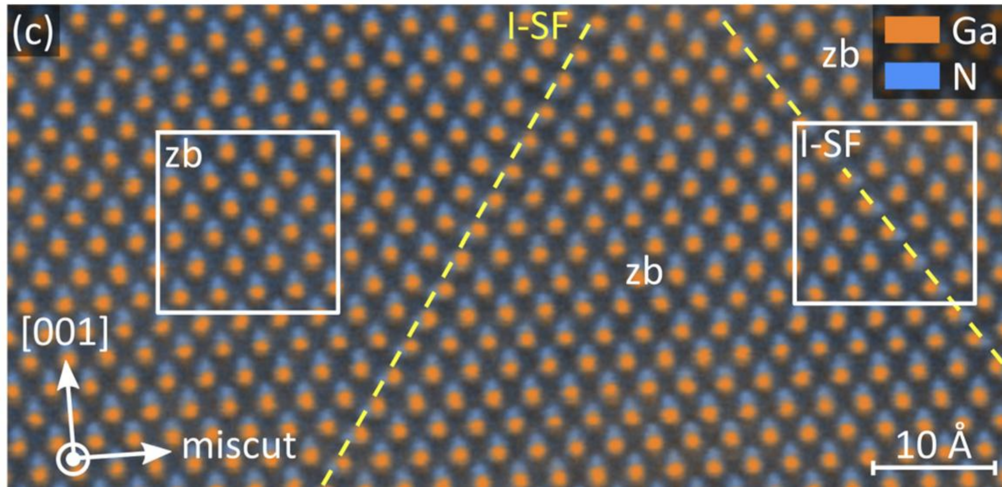

Figure 2-6 High-resolution STEM image (panel c) showing an intrinsic SF (I-SF) in cubic GaN, with the disrupted stacking sequence highlighted relative to the surrounding zincblende (zb) regions. Ga and N atomic columns are shown in orange and blue, respectively. Adapted from Ref. [94].

A major driving force for SF formation in zb-GaN heteroepitaxy is the significant lattice and thermal-expansion mismatch between cubic GaN and substrates such as Si, GaAs, and 3C-SiC. Table 2-2 summarises the lattice parameters and thermal expansion coefficients of commonly used substrates, together with their corresponding mismatches to zincblende GaN [39]. Such mismatches generate substantial interfacial strain during MOVPE growth and cooldown. Combined with the relatively low formation energies of SFs predicted by first-principles calculations for wz GaN and related nitrides [100, 101], this strain facilitates nucleation of SFs and twins at the heterointerface. These early defects often act as 'seeds' for polytype transformation.

The large lattice and thermal-expansion mismatch generate significant interfacial strain during MOVPE growth and cooldown. More importantly, cubic GaN is a metastable phase relative to wurtzite GaN, and epitaxial growth on (001) substrates requires maintaining a stable ABCABC stacking sequence along the {111} planes [39].

During epitaxy, local fluctuations in surface reconstruction, step-flow kinetics, and strain relaxation can locally disrupt the ideal stacking sequence, causing local insertion of ABAB stacking segments. These local stacking rearrangements correspond to intrinsic or extrinsic SFs, which can further propagate as twins or nucleate wurtzite inclusions within the cubic matrix.

As shown in Table 2-2, different substrates are employed to enable heteroepitaxial growth of cubic GaN, despite the absence of native bulk substrates. GaAs offers a cubic lattice symmetry compatible with zb-GaN but suffers from large lattice mismatch and thermal instability. Silicon is technologically attractive and scalable, but it introduces significant thermal-expansion mismatch and high defect densities. In contrast, 3C-SiC provides the closest lattice match and cubic symmetry, making it one of the most favourable substrates for stabilising the zincblende phase, although residual strain still promotes SF formation.

Table 2-2 Key substrate properties (lattice parameters, thermal expansion coefficients) and their mismatch with zincblende GaN. Data source: Ref. [39]

Substrate	Lattice parameter	Lattice parameter mismatch to zincblende GaN	Coefficient of thermal expansion	Coefficient of thermal expansion mismatch to zincblende GaN
Zincblende GaN	0.4520 nm	0%	$\approx 5.6 \times 10^{-6}$ K^{-1}	0%
GaAs	0.5653 nm	−20.0%	5.7×10^{-6} K^{-1}	−1.7%
Silicon	0.5431 nm	−16.8%	2.6×10^{-6} K^{-1}	+115%
3C-SiC	0.4360 nm	+3.7%	2.8×10^{-6} K^{-1}	+100%

In practice, cubic GaN layers are commonly grown on miscut (001) substrates. The intentional misorientation introduces surface steps that promote step-flow growth rather than island nucleation [39, 102]. This suppresses the formation of antiphase domains and helps stabilise a single cubic stacking sequence [103]. However, the presence of steps and local strain relaxation at step edges can also act as preferential nucleation sites for SFs, thereby linking growth kinetics to the observed SF density, as reported in cubic GaN and III–V epitaxy studies [104].

Recent multimicroscopy studies by Ding *et al.* [105] reveal how these structural irregularities evolve during growth. High densities of SF bundles form near the zb-GaN/3C-SiC interface, where interfacial strain and the metastability of cubic GaN favour local rearrangement of the stacking sequence. As the film gets thicker, many SFs terminate or react with other extended defects, reducing their density with increasing distance from the interface. This trend also consistent with prior reports and summarised in recent reviews on cubic GaN [39].

Importantly, SFs in zb-GaN do not merely represent planar defects but can locally introduce the wz stacking sequence. Ding *et al.* show that multiple consecutive SFs (SF bunches) may give rise to twins, which can in turn nucleate wz inclusions within the otherwise cubic matrix [105]. This behaviour is consistent with theoretical work showing that wz GaN has slightly lower energy than zb-GaN [39], making local zb-to-wz transitions energetically favourable. Consequently, the incorporation of even a small number of {111} SFs can initiate local wz-like regions that may propagate into active QW layers.

Since SF bunches and twins can trigger polytype transitions and locally modify strain and symmetry, understanding their origins is essential for evaluating the structural quality of cubic GaN heterostructures and interpreting their optical behaviour.

2.2.2. Impact of SFs on Optical and Electronic Properties

SFs in cubic GaN significantly influence optical and electronic properties through modifications of the local band structure, strain fields and carrier localisation. In zb-GaN

epilayers, SFs and associated wz inclusions produce characteristic signatures in photoluminescence (PL). In particular, a so-called high-energy band (or shoulder) appears between the cubic and wurtzite band edges due to the larger bandgap of wz-GaN relative to zb-GaN [39]. This trend is similar to the well-established luminescence associated with SFs in wz-GaN, where zb-like segments formed by basal SFs exhibit distinct transition energies and modified confinement behaviour [106, 107].

Conversely, thicker wz segments embedded within a cubic matrix can also generate low-energy emission due to QCSE and altered confinement potentials. Although most detailed QCSE analyses have been performed for wz/zb QWs in wurtzite GaN [106], the same physical principles apply to mixed-phase regions in cubic GaN. Figure 2-7 illustrates the general electronic structure expected at mixed-phase boundaries. The diagram highlights the band alignment between the two polytypes, as well as the polarisation-induced sheet charges and the resulting QCSE-related shift of the transition energy.

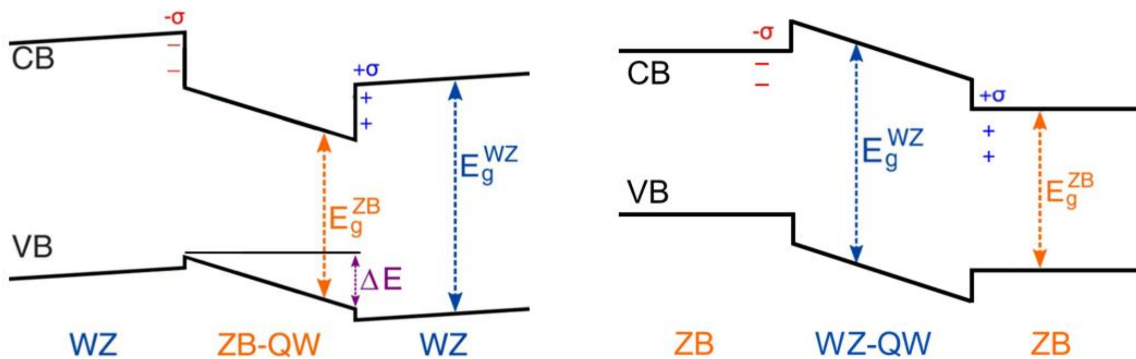

Figure 2-7 Schematic band diagrams of mixed-phase WZ/ZB interfaces illustrating band alignment, polarisation-induced sheet charges, and the resulting QCSE-related reduction of the optical transition energy. The left panel is adapted from Ref. [106], while the right panel is drawn by the author.

Within InGaN/GaN QWs, the influence of SFs becomes even more pronounced. Ding *et al.* [105] demonstrated that when SFs intersect QWs, they disrupt both QW thickness and indium distribution, creating spatially varying confinement energies. Regions that adopt wz stacking feature reduced bandgap and strong internal polarisation fields, in contrast to the non-polar zb matrix. These wz-derived segments therefore emit at lower energies than the surrounding cubic QW regions, consistent with QCSE in wurtzite InGaN [39, 105]. Such effects contribute to spectral broadening and may produce distinct low-energy peaks depending on the distribution and extent of the wz inclusions [105, 106]. In addition, SF-related quantum-wire-like emission and pronounced linear polarisation have been reported in zb-InGaN/GaN QWs, as the local indium redistribution around SFs forms one-dimensional nano-structures that strongly confine carriers [108].

SF-rich regions also exhibit strong exciton localisation and modified recombination dynamics, as shown by time-resolved and spatially-resolved luminescence studies in III-nitride heterostructures [106, 107]. While such localisation can enhance radiative efficiency by trapping carriers away from extended non-radiative defects, certain SF configurations or SF-impurity complexes may also act as non-radiative centres when they intersect active regions [109-111]. The overall impact therefore depends on the SF density, geometry and proximity to the QWs.

Overall, SFs can enhance radiative efficiency through exciton localisation, but they may also introduce non-radiative pathways and local QCSE-driven, red-shifted emission. These mechanisms are particularly relevant when interpreting the emission characteristics of cubic InGaN/GaN QWs, especially in devices designed for long-wavelength operation.

2.2.3. Brief Overview of MOVPE Growth

A brief overview of MOVPE is included here to provide context for SF formation in cubic GaN. In MOVPE, precursors such as trimethylgallium (TMGa) and ammonia (NH_3) react at the heated substrate surface to form GaN via surface-mediated reactions (Figure 2-8). Growth parameters strongly influence adatom mobility and surface reconstruction, and thus the stability of cubic GaN during growth.

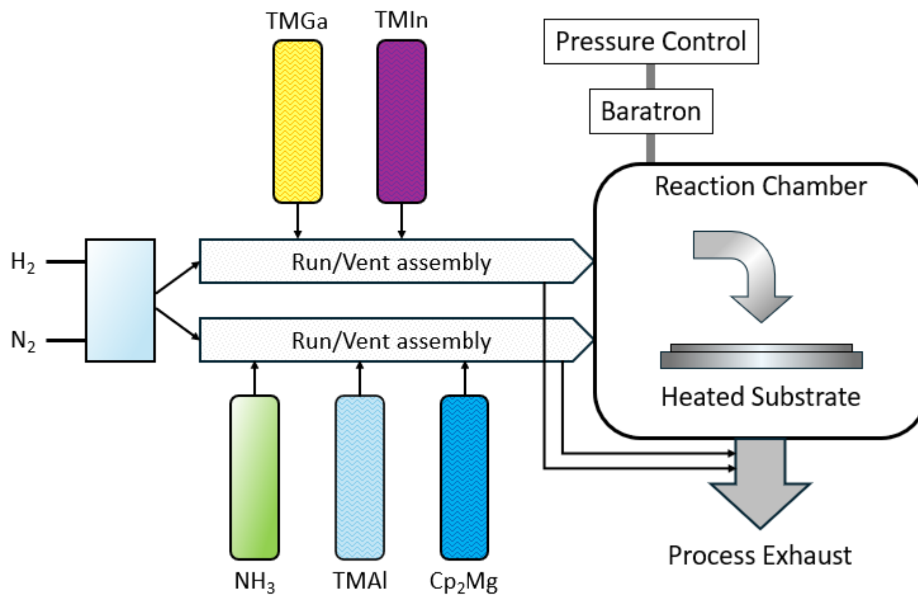

Figure 2-8 Structure and element of MOVPE

Because cubic GaN is metastable relative to the wz phase [39], MOVPE growth along the (001) direction requires conditions that suppress spontaneous transformation toward the energetically favoured wz stacking. Even small deviations in surface energy, temperature or impurity incorporation can lead to SF formation as the system locally reverts toward wz stacking. This is consistent with the low energetic cost of basal SF formation in wz GaN predicted by first-

principles calculations [100, 101]. Consequently, SFs and occasional wz inclusions are frequently observed in MOVPE-grown zb-GaN on mismatched substrates and remain a recurring theme in reviews of cubic III-nitride epitaxy [39].

Figure 2-9 shows a basic MOVPE reaction schematic of the III-nitride deposition process. Taking zincblende GaN for example, the reaction can be described as follows:

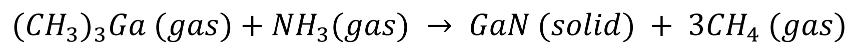

$$(CH_3)_3Ga\ (gas) + NH_3(gas)\ \rightarrow\ GaN\ (solid)\ +\ 3CH_4\ (gas)$$

Ga and N species incorporate layer-by-layer along the cubic facets. Under sub-optimal growth conditions, the ideal atomic stacking sequence could be disrupted, leading to the formation of SFs. Therefore, while MOVPE enables large-area cubic GaN films, SF formation is an inherent risk unless growth parameters are carefully controlled.

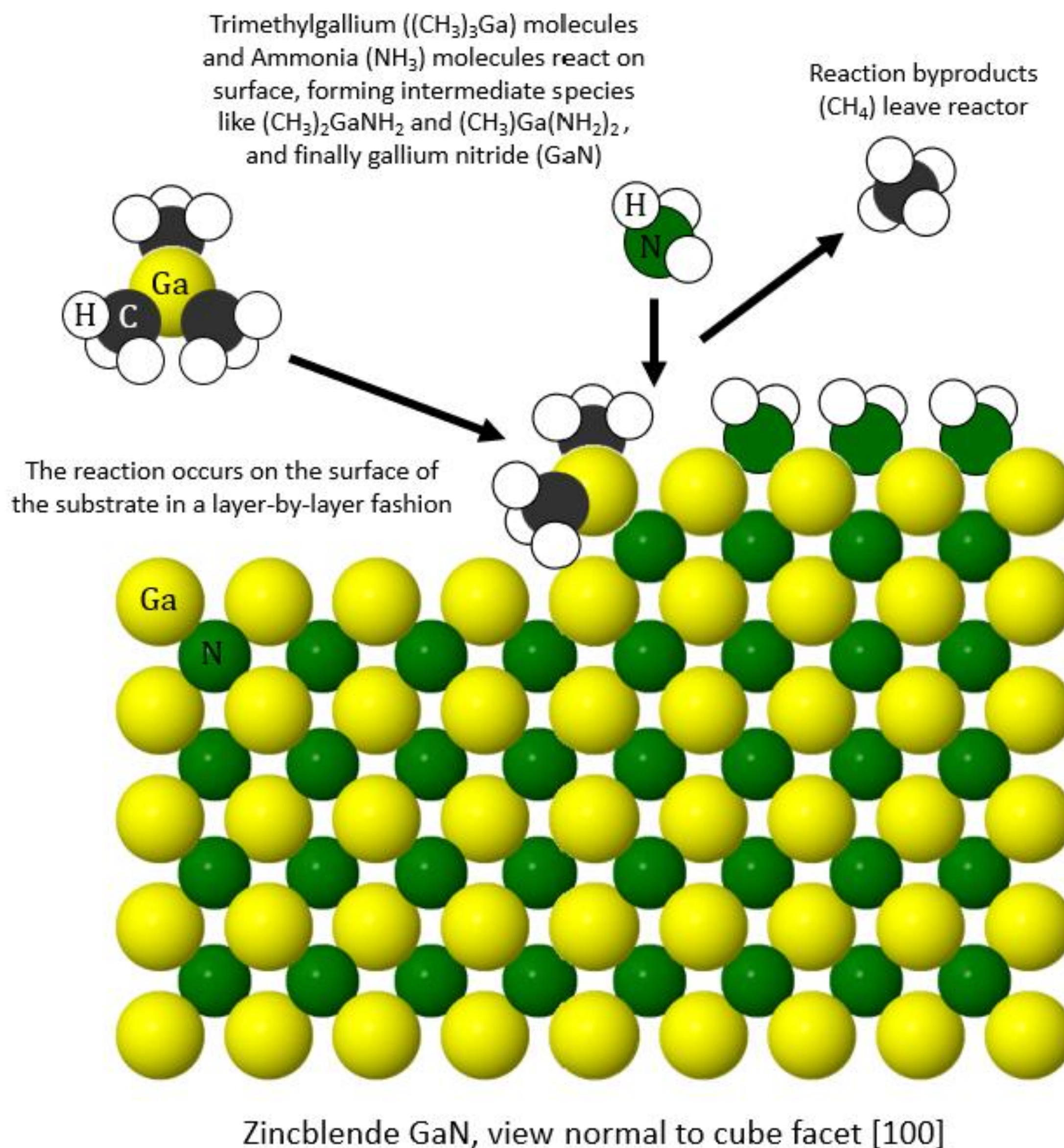

Figure 2-9 MOVPE process for zincblende GaN

2.3. Developing Atom Probe Tomography (APT) for III-Nitride

2.3.1. Current Characterisation Approaches and Limitations

III-Nitride semiconductors, like GaN and AlGaN, are promising for optoelectronic devices and high-power electronics due to their exceptional electronic and optical properties [112]. However, further development towards device applications demands an in-depth understanding of the atomic-scale relationships between microstructure, composition, and device performance [113]. Current approaches are mainly empirical regarding composition and

process optimisation. It is evident that significant gaps remain in the research, particularly concerning insights into the nature of defect dynamics, interfacial chemistry, and impurity distributions [114].

Before the implementation of APT, a wide range of characterisation techniques had been employed to study III-nitride materials. For example, high-resolution X-ray diffraction (HRXRD) [115-117] and electron microscopy techniques [105, 116, 118-120], including scanning electron microscopy (SEM), transmission electron microscopy (TEM), and scanning transmission electron microscopy (STEM), remain indispensable for analysing crystal quality, strain, dislocations, and interface structures in III-nitride materials. While HRXRD can resolve sub-nanometre layer thicknesses and TEM/STEM can image atomic-scale features in two dimensions, neither provides reliable 3D compositional characterisation at this scale like APT. In addition, since InGaN QWs are likely to have In segregation and clustering during growth, their microstructural analysis often aims to reveal the distribution of In-rich regions. However, these clusters are extremely sensitive to electron-beam exposure, and several studies have shown that apparent In clustering in TEM and STEM images can instead arise from beam-induced artefacts, rather than actual compositional fluctuations [121-123].

PL and cathodoluminescence (CL) spectroscopy provide complementary insights into the optical properties of III-nitride materials by probing bandgap energy, radiative efficiency, and defect-related emission [124, 125]. Unlike UV–Vis spectroscopy, which probes optical absorption in depth (one-dimensional), PL and CL are surface-sensitive two-dimensional techniques mapping luminescence across the sample plane. In particular, CL can map dislocation-related luminescence, revealing local variations in recombination behaviour [126].

Raman spectroscopy serves as a non-destructive probe for phonon modes, strain, and carrier concentration, allowing detailed assessment of lattice deformation and material quality in GaN-based heterostructures [127]. Despite their high sensitivity to optical and strain effects, PL and Raman are fundamentally constrained by the optical diffraction limit (about 200-500 nm), while CL offers tens-of-nanometre spatial resolution, none of them can directly correlate luminescence features to microstructural-chemical mapping [128, 129]. For example, recent CL investigations have demonstrated suppressed non-radiative recombination at V-pits in InGaN QWs [130]; however, such studies remain unable to quantify atomic-scale compositional segregation at pit edges, limiting further mechanistic understanding [131]. Secondary ion mass spectrometry (SIMS) provides an accurate elemental depth profile with high chemical sensitivity, with detection limits typically ranging from parts-per-billion to parts-per-million(10^{10} and 10^{16} atoms·cm^{-3}) [132]. Even for light elements such as C or O in Si, practical limits are ≈ 2×10^{15} atoms·cm^{-3} (≈2 ppm) [133]. While standard SIMS typically offers micrometre-scale lateral resolution, advanced variants such as NanoSIMS and ToF-SIMS can achieve tens-of-nanometre resolution under optimised conditions. However, their strong matrix-dependent ion yields and limited quantitative accuracy can still complicate nanoscale compositional analysis [134, 135]. Atomic Force Microscopy (AFM) complements SIMS by providing nanoscale surface imaging and topographical characterisation of III-nitride materials. It enables detailed mapping of surface roughness and defect-related features such as pits or leakage paths [136]. However, AFM is limited to surface analysis and lacks chemical sensitivity, restricting its ability to probe subsurface or compositional variations.

In summary, these techniques establish a multidimensional framework for understanding III-nitride materials, with each facing limitations in spatial resolution, depth quantification, or chemical sensitivity. APT introduces complementary capabilities, enabling true 3D, atomic-

scale compositional mapping with sub-nanometre resolution and near-atomic chemical accuracy. By correlating structure and composition at this scale, it helps bridge the gap between structural and chemical characterisation in III-nitride semiconductors [137].

2.3.2. Applications of APT in III-Nitride Research

With unique capabilities such as ppm-level detection limits, near-equal sensitivity to all elements, and 3D compositional mapping at sub-nanometre spatial resolution, APT is capable to address some of the challenges mentioned above [137]. As a powerful tool for nanoscale characterisation, it has been increasingly applied to III-nitride semiconductors, where its ability to correlate structural and compositional information at near-atomic resolution has yielded new insights into defect chemistry and dopant distribution.

The first systematic use of APT to study III-nitride epitaxy was carried out in a series of studies by Galtrey *et al.* As early as 2007, they reported the first 3D compositional mapping of bright-emitting InGaN/GaN MQWs, where they found no indication of indium clustering. This directly contradicted earlier TEM-based claims [138]. Building on this, their study in early 2008 examined a high-efficiency ultraviolet InGaN/$Al_yGa_{1-y}N$ MQW emitter using APT [139]. The analysis revealed morphological features that had not been resolved before, including 20-100 nm discontinuities in the QWs. Small amounts of indium were also detected in the barrier layers. These inhomogeneities were proposed to help isolate threading dislocations (TDs) from the radiative region and thereby contribute to the exceptionally high internal quantum efficiency [139]. Later that year, they applied APT with a wider field of view to green- and blue-emitting MQWs, where they confirmed that the indium distribution was still consistent with a random alloy and there is no indium clustering. In addition, the upper interface was

rougher and more diffuse than the lower interface. Monolayer QW width fluctuations were present, which would contribute to the localisation of carriers at room temperature [140]. Collectively, these studies established APT as a useful tool for resolving nanoscale composition and interface structure in III-nitride devices.

Subsequent progress further demonstrated the effectiveness of APT in resolving critical issues in the III-nitride systems. For instance, Bennett *et al.* validated that APT can reliably distinguish true compositional inhomogeneity from electron-beam-induced artefacts in InGaN QWs [141]. In addition, Müller *et al.* applied APT to thick, partially relaxed InGaN epilayers and identified indium-rich domains arising from spinodal decomposition, thereby showing that APT is also capable of quantitatively resolving phase separation phenomena in bulk-like InGaN [142]. In terms of GaN/AlGaN QWs, the APT analyses indicate that AlGaN forms a compositionally disordered alloy. Consistent with PL measurements, the continuum-based theoretical model, further indicates that random compositional fluctuations can lead to carrier localisation [143].

Figure 2-10 (a, b) shows the APT results of $In_{0.18}Al_{0.82}N$ grown by plasma assisted molecular beam epitaxy (MBE) [144], which is proven to be statistically non-random by an frequency distribution analysis (Figure 2-10(c)).

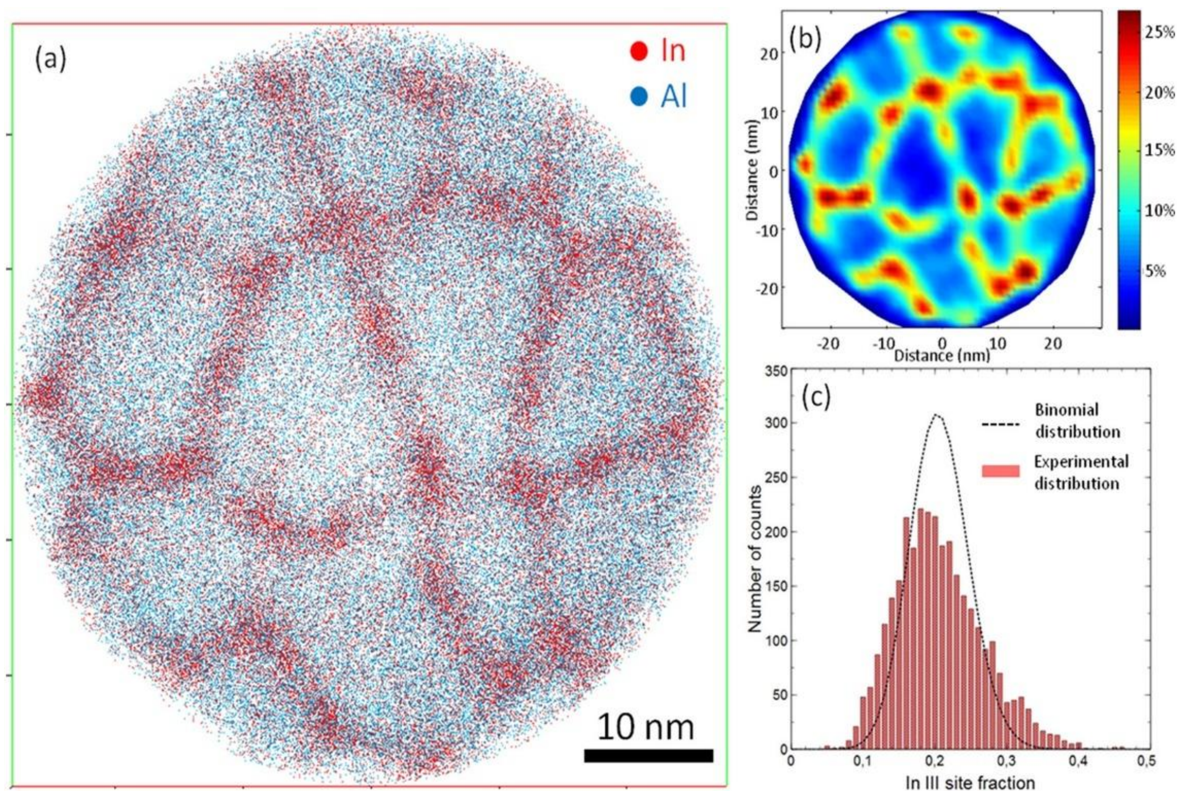

Figure 2-10 (a) 2D atom map showing the honeycomb microstructure in InAlN. (b) Associated In site fraction map showing the segregation of indium into concentrated regions at the boundaries of the cells. (c) Statistical distribution analysis performed with a sampling volume of 100 atoms highlighting the gap between the honeycomb microstructure and a random alloy. Adapted from [144]

By 2014, Rigutti *et al.* significantly expanded APT's application by combining it with micro-photoluminescence (μPL) and high-resolution (HR) STEM, using it in a correlative multi-scale analysis study of individual InGaN/GaN microwires containing MQWs [123]. Their study demonstrated for the first time a direct correlation between indium clustering and excitonic localisation, highlighting how compositional fluctuations influence optical emission properties. Through this work, APT emerged as a vital technique for investigating the optical mechanisms in functional materials. Figure 2-11 shows the 3D distribution of indium atoms in the sample analysed, highlighting the large number of QWs which can now be routinely examined.

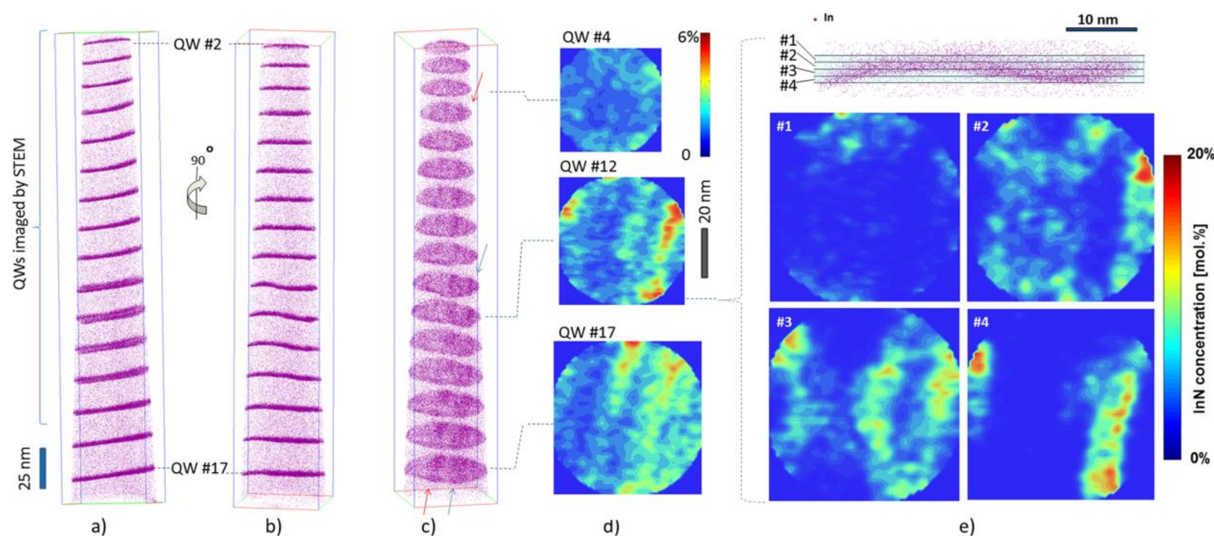

Figure 2-11 APT analysis of In distribution in GaN/InGaN QWs, revealing compositional nonuniformities and In-rich features within multiple QWs, along both the growth and in-plane directions. Adapted from [123]

Apart from resolving chemical composition gradients, APT also has an irreplaceable advantage in characterising atomic-scale structures, such as dislocations and other defects. For example, Yamaguchi's team utilised correlative TEM and APT to directly observe indium diffusion along TDs in InGaN/GaN MQWs [145]. As shown in Figure 2-12, the APT result visually represents indium diffusion along a TD in InGaN/GaN MQWs. Their work reveals a pipe diffusion mechanism driven by strain energy relaxation, which contributes to indium redistribution and potential efficiency losses in optoelectronic devices.

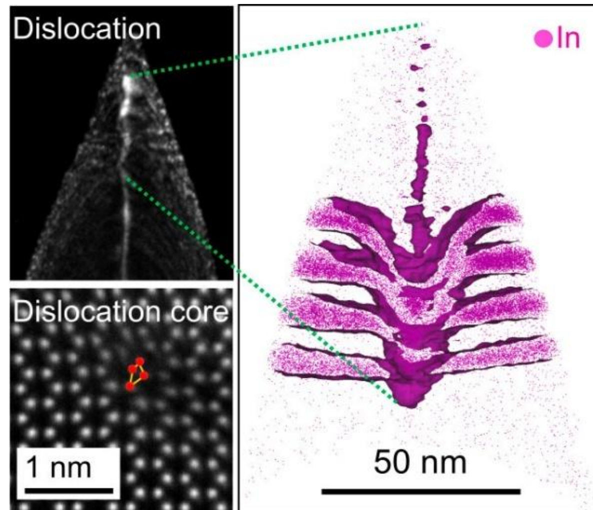

Figure 2-12 Left Top: WBDF-TEM image of the needle sample, where the TD is highlighted, and indium is seen to accumulate along the defect. Left Bottom: A STEM image of the dislocation core overlaid, with red markers indicating atomic positions within the defect structure. Right Panel: A 3D APT reconstruction map showing indium distribution (pink dots) around the TD, revealing a pipe diffusion mechanism where indium preferentially segregate along the dislocation line. [145]

Lately, a newly established photonic atom probe (PAP) has been introduced. It integrates the functionalities of APT and PL spectroscopy in an *in-situ*, online configuration, and has been employed successfully to differentiate between optical signals from distinct QWs separated by roughly 10 nm and characterised by emission wavelengths differing by several nanometres [146, 147]. Figure 2-13 presents PAP experimental results, including an APT reconstructed volume clearly showing distinct device layers, along with compositional profiles, PL spectra, and intensity evolution plots [148]. In a very recent work, the PAP has been used to investigate nanosecond-scale thermal effects during field evaporation in III-nitride materials, revealing correlations between local temperature changes and optical emission behaviour during APT analysis [149].

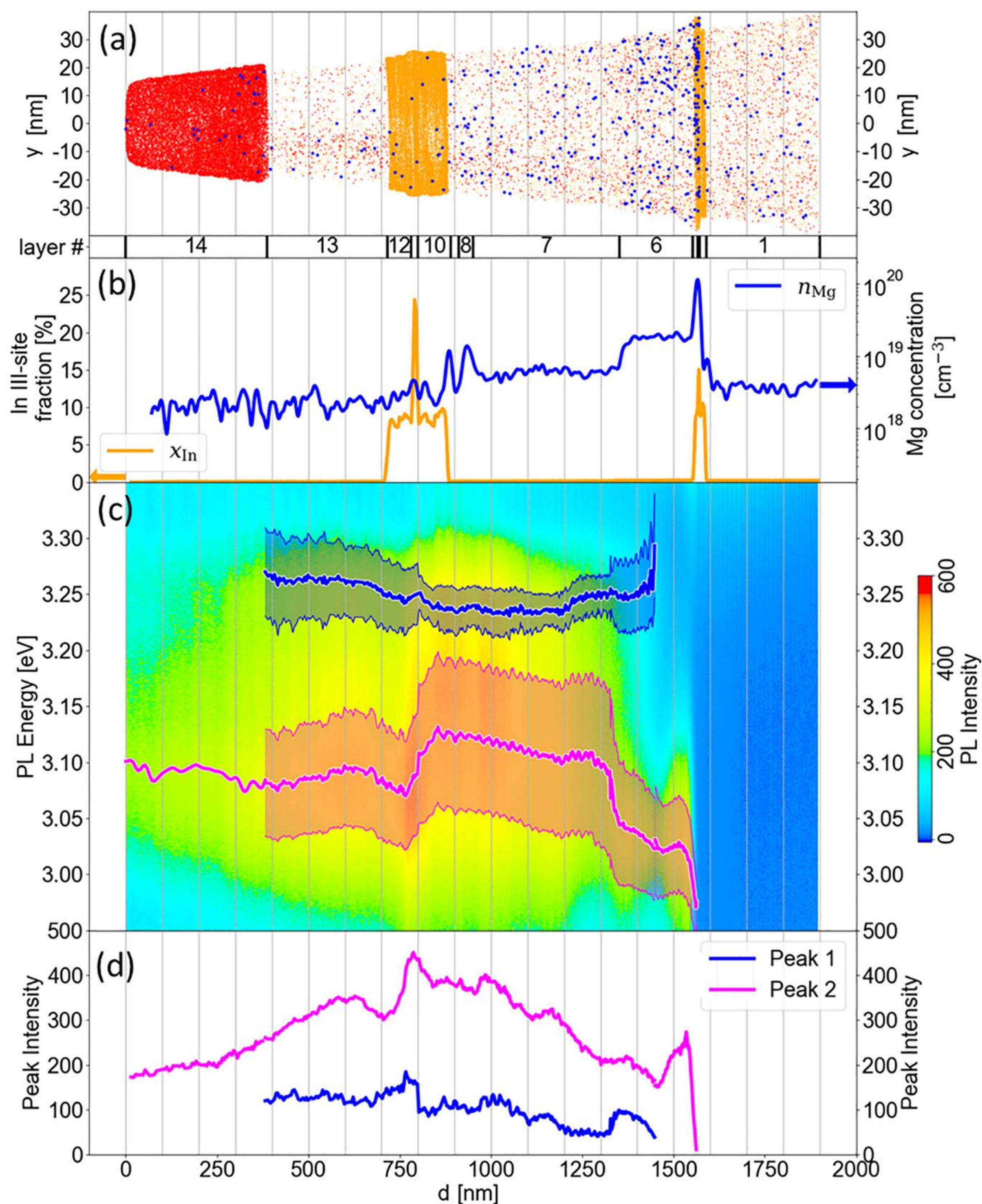

Figure 2-13 Correlative nanoscale analysis using PAP. Atomic-scale composition (a–b) and depth-resolved photoluminescence spectra (c–d) are simultaneously acquired during field evaporation, enabling direct correlation between dopant distribution and optical emission in III-nitride heterostructures. [148]

2.3.3. Challenges in APT Analysis of III-Nitride Systems

In theory, APT has the same chemical sensitivity to all elements, including the light ones. However, its accuracy is influenced by electric field effects, laser parameters, and evaporation mechanisms. For wurtzite GaN tips oriented along the [0001] direction, it was observed that at low laser pulse energy (0.7 nJ UV), corresponding to high effective fields (~26 V/nm), a higher-than-expected nitrogen signal (as shown in Figure 2-14(a)) and elevated background levels were observed. In contrast, at higher laser pulse energy (1.7 nJ UV) and lower effective fields (~23 V/nm), Ga enrichment and reduced background were observed [150]. Mancini's team investigated the measurement biases in III-N materials, showing that electric field variations caused by different laser pulse energy significantly affect compositional accuracy [151]. Preferential evaporation of Ga at high fields would lead to Ga/N ratio deviations. Further, varying evaporation fields between different material layers (e.g., GaN vs. AlGaN) can also affect interface characterisation accuracy. Figure 2-14 reports how the average measured fraction of the Ga and N changes under different conditions [150]. Such APT measurement artefacts were further investigated by Gault *et al.* [152], examining the field evaporation mechanisms and molecular ion behaviour in APT, especially in dissociation and neutral species behaviour in III-Nitride semiconductors. They used Kingham curves [153, 154], which describe the probability of multiple charge states (e.g., Ga^{+}, Ga^{2+}, N^{+}, N^{2+}) as a function of the applied electric field strength, to demonstrate that the ratio of different charge states in GaN in APT is highly field-dependent. Their analysis and calculation proved that, under typical APT field conditions (~20–27 V/nm), N and N_2 should predominantly ionise as N^{+} and N_2^{+}, respectively, contradicting earlier hypotheses that neutral N_2 might escape detection due to thermal desorption [155, 156]. This finding suggests that APT stoichiometry discrepancies in III-N semiconductors are more likely caused by molecular dissociation and post-ionisation effects rather than selective field evaporation of specific elements. To support this, Table 2-3

summarises the dissociation paths and dissociation energies of Ga_nN_m cations, calculated using density-functional theory (DFT) simulations. The negative ΔE values indicate that these ions are metastable and can spontaneously dissociate. One of the pathways leads to the formation of neutral N_2, which would escape detection in APT. This supports the view that undetected neutral fragments may significantly contribute to the observed nitrogen loss. This mechanism will be revisited in the context of my own experimental results in Chapter 4.

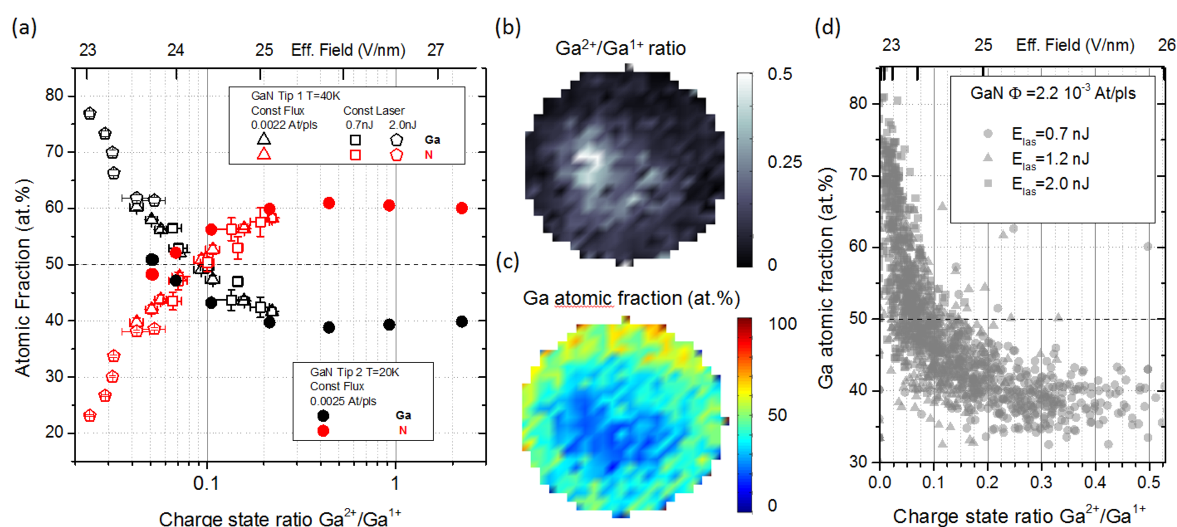

Figure 2-14 (a) Average Ga and N atomic fractions plotted in function of the Ga^{2+}/Ga^{1+} charge state ratio (corresponding effective surface field reported in top x-scale), computed for acquisitions from Tip1 analysed by Protocol A at T = 40K (empty symbols) and from Tip2 analysed only at constant detection rate (full symbols). (b) Ga^{2+}/Ga^{1+} charge state ratio and (c) Ga atomic fractions visualised through detector statistics. (d) Correlation plot of Ga atomic fraction and Ga^{2+}/Ga^{1+} charge state ratio as assessed by detector statistics for acquisitions at laser energy E_{laser} = 0:7, 1.2 and 2.0 nJ. [150]

Table 2-3 Dissociation energies for a selection of molecular ions observed experimentally. [152]

Parent				Fragments			Delta E (eV)
GaN^{2+}	–>	Ga+	+	N^+			−1.63
GaN^{3+}		Ga^{2+}	+	N^+			−9.94
$GaN_3{}^{2+}$	–>	Ga^+	+	$N_3{}^+$			−7.86
$GaN_3{}^{2+}$	–>	Ga^+	+	N^+	+	N_2	−3.98

Although improved compositional accuracy is needed for certain elements, APT remains highly effective for dopant mapping, interface characterisation, and defect segregation [157]. Di Russo *et al.* further demonstrated that measurement bias in GaN APT is primarily governed by electric field effects, where Ga tends to evaporate preferentially at high electric fields and N is underestimated at low electric fields [158]. This makes correction models necessary. In a more recent study, Diagne *et al.* extended APT's scope beyond compositional analysis by investigating hydride formation (NH^+, NH_2^+) in III-N semiconductors (Figure 2-15). They showed that hydrogen incorporation varies with electric field strength, implying that field conditions can influence surface reactions during analysis. This demonstrates that APT is sensitive not only to bulk composition but also to surface chemistry and potential environmental factors, such as residual gases or adsorbates, which may interact with the specimen surface under high electric fields [159].

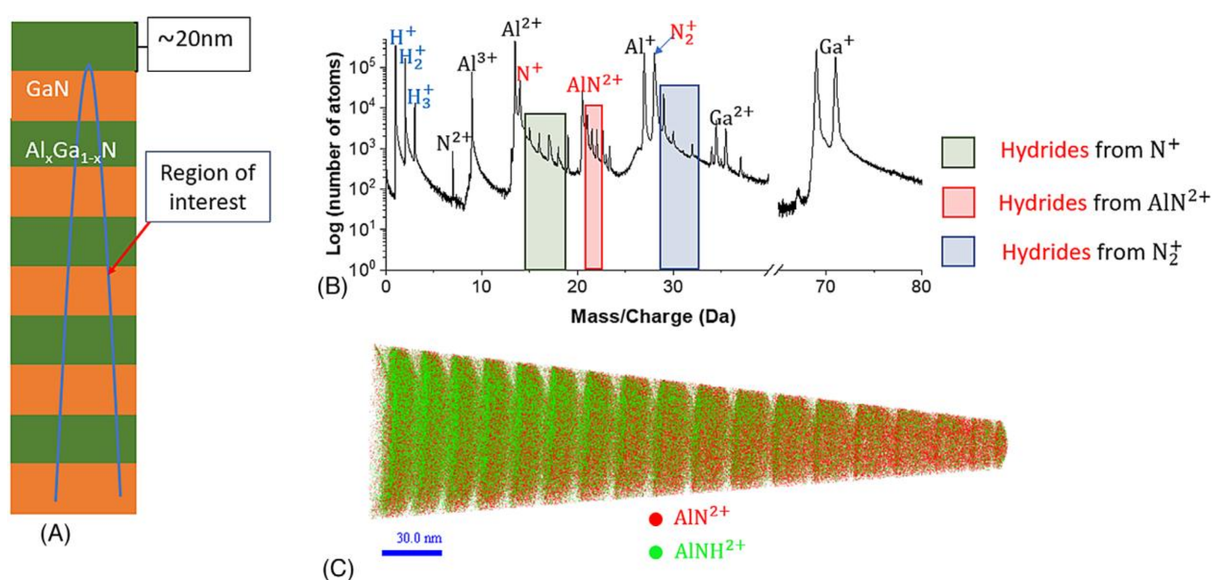

Figure 2-15 (A) Schematic structure of the analysed system (in blue, the approximate position of the APT specimen). (B) Mass spectrum from APT analysis of the AlGaN/GaN heterostructure. (C) 3D reconstructed volumes showing the spatial distribution of AlN^{2+} and $AlNH^{2+}$ molecular ion species. [159]

As a promising nanoscale characterisation tool which is still evolving, researchers are increasingly integrating advanced data processing techniques, such as machine learning [160],

to improve accuracy on compositional quantification and reconstruction model, and further expanding its capabilities in materials science.

In summary, conventional analytical techniques such as STEM have been applied to characterise the composition, structure and other properties of group III nitride semiconductors. A comparison of characterisation methods for GaN LEDs is shown in Table 2-4. While these approaches have provided important basis for understanding the morphology and a range of properties of III-nitrides, the atomic-scale composition and segregation behaviour at certain features, such as defects, remains less explored. Although significant progress has been made so far, further APT analysis of elemental distributions in the vicinity of features such as TDs and SFs is required to understand how these defects affect carrier recombination, internal quantum efficiency, and device reliability. It should be noted that in cases where there is little or no elemental segregation associated with these defects, APT may not provide sufficient contrast to directly image them. These atomic-level insights could inform strategies for optimising material growth conditions, reducing defect formation, designing new devices and ultimately improving device performance. By combining APT with other advanced techniques, it is possible to gain a multi-scale understanding of GaN-based device growth and defect engineering, thus paving the way for the development of more efficient and reliable III-nitride optoelectronic devices.

Table 2-4 Multial resolution and applications of characterisation techniques for GaN LEDs

Technique	Destructive	Dimension Probed*	Lateral Resolution (x-y)	Depth Resolution (z)	Characterised Properties	Key Applications in GaN LEDs	Strengths	Limitations
XRD [161]	No	Primarily 3D (bulk)	--	Few µm penetration; nm-scale thickness sensitivity	Crystal structure, strain, defects (e.g., dislocation density)	Epitaxial layer quality, strain, QW width and composition	Fast, quantitative structural analysis	No direct defect visualisation
PL [128]	No	2D (surface)	~500 nm (diffraction-limited)	Tens–hundreds nm (excitation-dependent)	Bandgap, radiative efficiency, defect-related emission (incl. dislocation-induced non-radiative centres)	QW efficiency; yellow luminescence	Non-destructive; high sensitivity; temperature-dependent analysis possible	Surface sensitivity; limited quantitative accuracy without calibration
CL [162-164]	No	2D (surface)	10-50 nm	20-100 nm	Bandgap, composition, and defect-related luminescence (including near-surface defects)	Local defect mapping (coupled with SEM)	Morphology and optical properties	Electron-beam damage
UV-Vis [165]	No	1D (z)	--	mm–cm (path-length dependent)	Bandgap, thickness	Film thickness estimation	Simple, fast	Model-dependent
SEM [166, 167]	No (possible e-beam damage)	2D (surface to sub-surface)	0.6-10 nm	Few nm (SEs) – hundreds nm (BSEs)	Surface morphology, defect distribution, composition (with EDS)	Surface defect, elemental mapping	High-resolution surface imaging, fast	May need conductive coating; limited bulk information unless cross-section imaged; possible beam damage
TEM [167-169]	Yes (sample preparation)	2D projection (atomic scale)	<0.2 nm	~50 nm (foil); nm-scale with tomography	Dislocations, interfaces, nanostructures, atomic defects	Dislocation types, QW interface roughness	Ultra-high resolution***	Challenging sample preparation, potential artefacts

Technique	Destructive	Dimension Probed*	Lateral Resolution (x-y)	Depth Resolution (z)	Characterised Properties	Key Applications in GaN LEDs	Strengths	Limitations
STEM [168, 170]	Yes (sample preparation)	2D/3D (with tomography)	<0.1 nm	~1 nm (tomography)	Elemental mapping (with EDS), atomic structure	Dopant distribution	Light-element sensitivity, high-resolution	Challenging sample preparation, potential artefacts
SIMS [171, 172]	Yes	1D (z) / 3D (with mapping)	50-500 nm**	1-2 nm	Dopant/impurity depth profiles	Impurity concentration	ppb-level sensitivity	Matrix-dependent quantification; limited chemical-state info; poor H detection
Raman Spectroscopy [129]	No	2D (surface)	200-300 nm	≤ 1 μm	Strain, phonon modes, carrier concentration	Stress analysis	Non-destructive, *in-situ*	Weak signal for buried layers, smooth surfaces required
AFM [173]	No	2D (surface topography)	1-5 nm	0.1 nm	Surface topography, roughness, electrical properties	Surface defect mapping, leakage paths	Nanoscale surface imaging	No chemical analysis; mainly surface-sensitive
APT [137]	Yes	3D	0.3-0.5 nm	0.1-0.3 nm	3D atomic-scale composition, interfacial atomic concentration	Dopant distribution, cluster analysis	3D reconstruction, high resolution	Challenging sample preparation, small analysis volume

* Note: Certain techniques can achieve higher-dimensional characterisation through specific operational modes.

XRD: Layer thicknesses and compositional variations in multilayer or QW structures can be determined using high-resolution XRD (HRXRD).

PL: The probe depth varies strongly with excitation wavelength and material absorption coefficient; in GaN, it typically ranges from tens to hundreds of nanometres. 3D optical property imaging can be achieved through Z-axis scanning of the laser focus combined with optical slice stacking (Z-Stacking), or by utilising the intrinsic tomographic capability of multiphoton PL (MPPL).

CL: 3D composition/optical property can be achieved via sample tilting combined with tomographic reconstruction.

TEM: 3D structural imaging can be achieved via sample tilting and tomographic reconstruction.

STEM: 3D structural/compositional imaging can be achieved via sample tilting and tomographic reconstruction; 4D-STEM mode can acquire full diffraction patterns at each scan point for quantitative phase imaging (e.g., strain, electric field, charge density distribution).

SIMS: 3D elemental distribution maps can be directly constructed through sequential sputtering and surface mapping (3D Imaging SIMS).

Raman Spectroscopy/AFM: 3D correlative imaging can be achieved via Z-axis scanning (3D Raman/AFM correlative imaging)

APT: Simultaneous 3D atomic-scale compositional mapping and nanoscale optical characterisation can be achieved via PAP

** Upper bound applies to dynamic SIMS; ToF-SIMS is at the lower end. [174]

*** Conventional TEM reaches ≈0.20 nm point resolution, comparable to conventional STEM (≈0.14 – 0.20 nm); with Cs-correction, both HR-TEM and STEM achieve sub-Å (<0.10 nm) resolution. [175-177]

2.4. Summary

This chapter reviewed the fundamental concepts and current literature relevant to zincblende InGaN/GaN QW optoelectronic devices, with particular focus on SFs and advanced nanoscale characterisation. The key differences between wurtzite and zincblende GaN were highlighted, particularly the absence of polarisation fields and suppression of the QCSE in the zincblende phase, which enhance electron–hole wavefunction overlap and radiative recombination efficiency.

The origin and impact of SFs in cubic GaN were then discussed, including their formation due to lattice mismatch and phase metastability, and their influence on local band structure, carrier localisation, and emission characteristics. Growth considerations, particularly MOVPE conditions influencing SF formation, were also briefly discussed.

Finally, the chapter reviewed characterisation approaches for III-nitride semiconductors, highlighting APT as a powerful technique for 3D atomic-scale compositional analysis, while also noting key measurement challenges. Overall, this chapter provides the necessary background for the APT studies of III-nitrides discussed in subsequent chapters.

Chapter III Materials and Experimental Methods

This chapter aims to introduce the details of materials analysed, techniques, and procedure of analyse in this project. The first section briefly covers the details of samples and electron microscopy methods, and the second part describes the atom probe principle, analysis methods and tools.

Three forms of samples were investigated in the thesis: pure GaN, multi-quantum well (MQW) GaN and single quantum well (SQW) GaN. The details of the process of preparing these materials will be introduced in each related chapter, while this chapter mainly discuss the stages of data collection and analysis. Essential electron microscopy techniques and atom probe tomography (APT) are introduced. The special emphasis is placed on APT sample preparation methods for layered semiconductor materials and its associated analytical techniques.

3.1.Materials

All the InGaN/GaN samples in this study were generously supplied by Dr. Menno Kappers from the Department of Materials Science and Metallurgy, University of Cambridge. Each of them was uniquely designed and grown under varying conditions by metalorganic vapour phase epitaxy (MOVPE) to meet with different research objectives. Figure 3-1 shows the open reaction chamber of the MOVPE system; additional details are provided in Chapter 2.

Figure 3-1 Open reaction chamber of a MOVPE reactor. The showerhead lid (top) delivers precursor gases, while the SiC-coated graphite susceptor (bottom) rotates to ensure uniform deposition on four mounted wafers and two square samples. Photograph taken on an Aixtron reactor at the Cambridge Centre for Gallium Nitride

In this study, pure GaN, MQW InGaN/GaN and SQW InGaN/GaN were produced through this method, and the details of each sample can be found in its related chapters.

3.2.Electron Microscopy

Most of this thesis focuses on the investigation of quantum wells (QWs) and stacking faults (SFs), which are features only a few nanometres in scale. To characterise these nanoscale phenomena, advanced microscopy techniques were employed throughout the research. Transmission electron microscopy (TEM) and scanning transmission electron microscopy (STEM) were used to obtain detailed microstructural information, while focused ion beam (FIB) milling and scanning electron microscopy (SEM) were used for APT specimen fabrication and supplementary imaging. The following sections present a brief overview of the electron microscopy techniques and FIB milling used in this study.

3.2.1. Scanning Electron Microscopy (SEM)

SEM is an essential tool for examining the surface morphology and structural characteristics of GaN-based materials, including defects, grain boundaries, and layer uniformity [166, 178]. In SEM, a focused electron beam is scanned across a sample within a vacuum, producing interactions that emit various signals, as shown in Figure 3-2(a). SEM imaging was performed using both secondary electron (SE) mode and backscattered electron (BSE) detection mode [178]. As can be found in Figure 3-2(b), SE signals are generated by inelastic scattering of the primary beam with the sample's outer-shell electrons. Low-energy electrons are ejected from the sample surface, and it provides high-resolution surface topography due to their low energy and shallow escape depth. On the contrary, BSE result from elastic scattering of the primary beam by atomic nuclei, retaining much of their initial energy and emerging from deeper sample regions. While BSE images exhibit lower spatial resolution, they generate atomic-number (Z)-

dependent contrast, allowing phase contrast between regions of differing mean atomic number, and can additionally reveal crystallographic information [166, 179]. In terms of GaN research, SE imaging is widely employed to assess film morphology (e.g., surface roughness, defect distribution, and growth uniformity), while BSE imaging provides atomic-number contrast that can qualitatively indicate compositional or dopant-related variations.

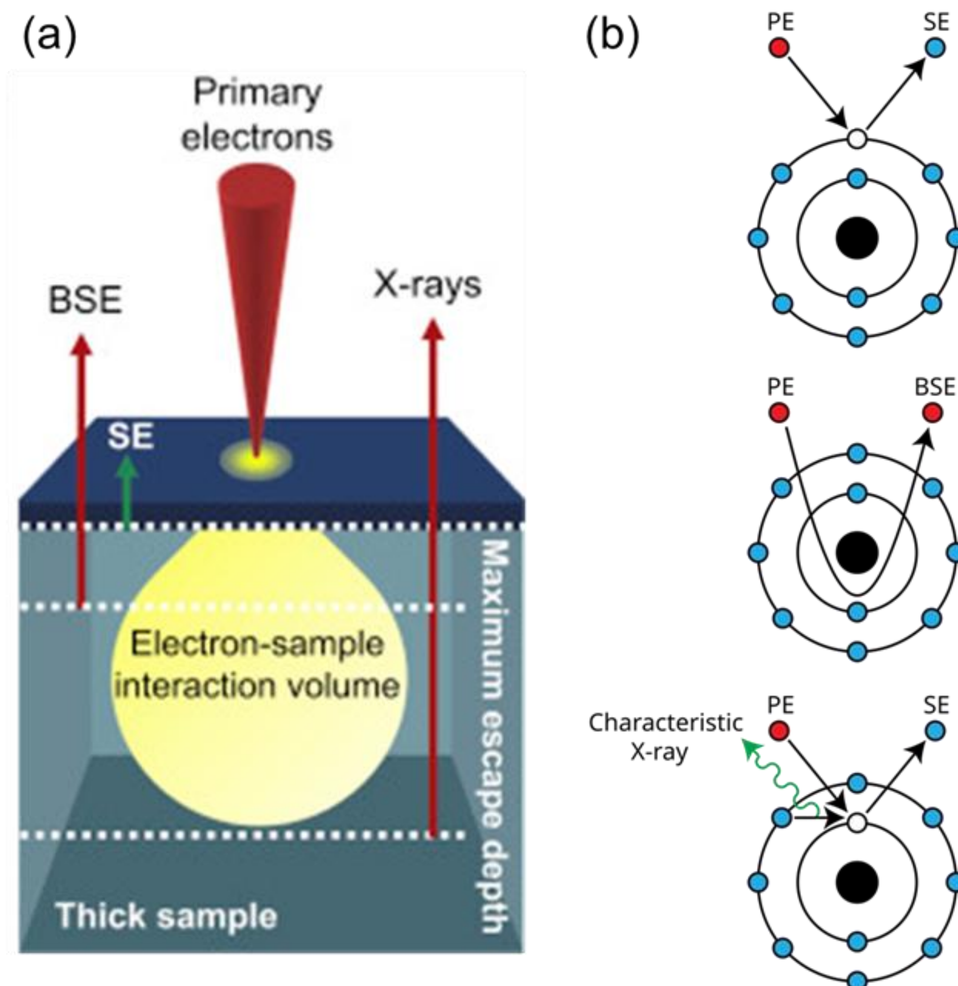

Figure 3-2 (a) Electron-sample interaction volume and types of signals generated in thick samples by SEM [180]. (b) Schematic of electron emission mechanisms, adapted from Rob Hurt (Wikimedia Commons, CC BY-SA 4.0).

Additionally, X-ray signals are generated by the electron-sample interaction. As can been seen from the Figure 3-2(b), an inner-shell electron is ejected and replaced by a higher-energy

electron. The energy is emitted in the form of a characteristic X-ray photon, whose energy depends on the specific electronic structure of the element. They can escape from greater depths and are typically used for elemental analysis via energy-dispersive X-ray spectroscopy (EDX), which is often coupled with SEM.

3.2.2. Focused Ion Beam (FIB)

FIB microscopy is an important technique widely used for site-specific specimen preparation and nanoscale material modification [181, 182]. As illustrated in Figure 3-3, it is typically implemented in a dual-beam FIB–SEM system, where a focused beam of high-energy ions (typically Ga^{+}) is directed onto the sample surface to sputter material with nanometre-scale precision, while the electron beam provides simultaneous imaging for accurate positioning and monitoring of the milling process.

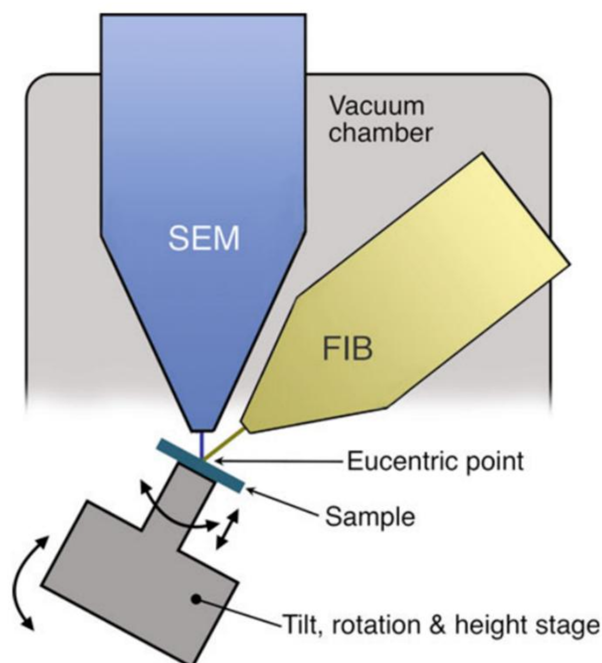

Figure 3-3 Schematic of a dual-beam FIB–SEM setup, illustrating a vertical SEM column and a tilted FIB column incident on the eucentric point of the sample stage. Adapted from [183].

Compared with conventional mechanical polishing or electropolishing, FIB enables precise targeting of specific microstructural features, which is essential for investigating localised nanoscale phenomena such as QWs and SFs in GaN-based materials. The site-specific lift-out capability allows selected regions of interest to be extracted and shaped into needle-like specimens suitable for APT or thin lamellae for TEM/STEM analysis.

In this study, FIB milling was primarily employed for the preparation of site-specific APT specimens and cross-sectional TEM samples from InGaN/GaN heterostructures. The use of FIB is crucial for precisely positioning the tip apex within the target QW layers or near SF, thereby ensuring that the nanoscale features of interest are preserved during sample fabrication. Detailed procedures and milling parameters are described in Section 3.3.3.

3.2.3. Transmission Electron Microscopy (TEM) & Scanning Transmission Electron Microscopy (STEM)

TEM and STEM are important techniques for nanoscale and atomic-scale characterisation. As illustrated in Figure 3-4(a), a conventional TEM operates by transmitting a broad, parallel beam of electrons through a thin specimen (<100 nm). The transmitted electrons are subsequently focused by a series of electromagnetic lenses to produce a two-dimensional projection image which reveals the internal structure of the sample. This technique reveals crystallographic features, defect distributions, and phase boundaries. An advancement of this technique, high-resolution (HR) TEM, extends these capabilities to atomic-level imaging. This is achieved

through phase contrast arising from the coherent scattering of electrons within the crystal, which enables the direct visualisation of atomic lattices and point defects.

Figure 3-4(b) demonstrates the STEM operational mode, where a finely focused electron beam scans the specimen in a raster pattern. This configuration employs specialised detectors to collect different scattering components: the high-angle annular dark field (HAADF) detector captures thermally diffuse scattering for atomic-number (Z)-contrast imaging, while the annular bright field (ABF) detector collects low-angle scattered electrons sensitive to light elements. This dual-detector approach provides comprehensive structural and compositional information, with HAADF-STEM particularly effective for locating heavy dopant atoms and ABF-STEM for imaging light elements like oxygen or nitrogen columns.

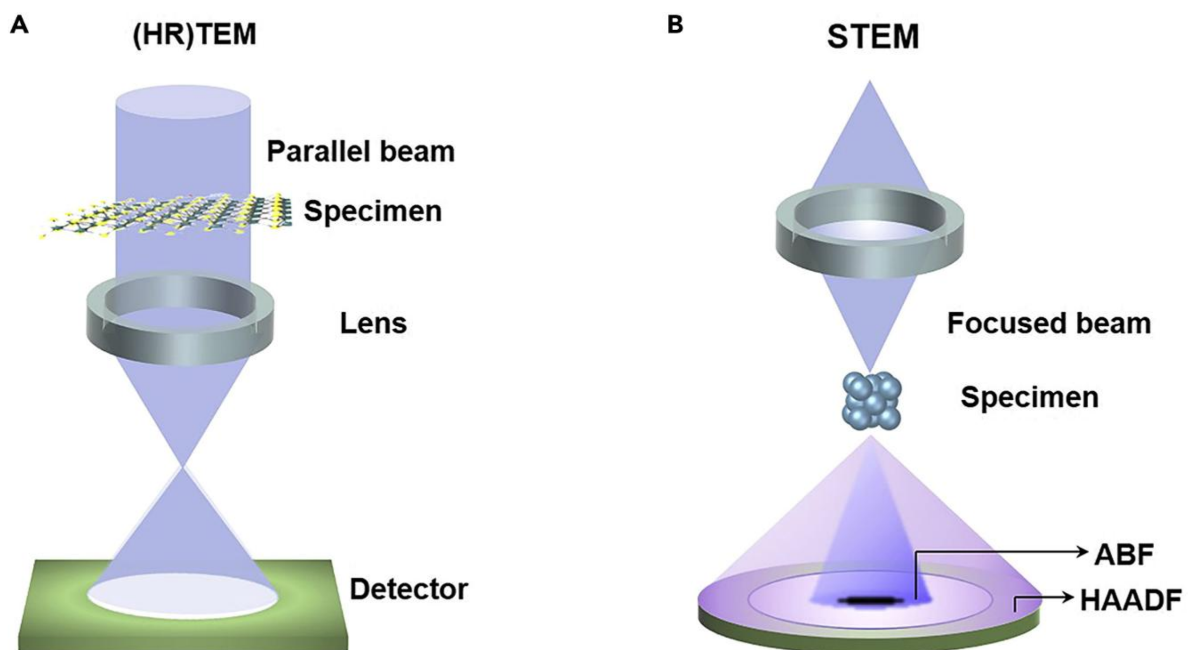

Figure 3-4 Illustration of Typical Imaging Modes: (A) (HR)TEM and (B) STEM [170]

In this work, cross-sectional specimens for STEM characterisation were prepared using an *in-situ* lift-out method in an *FEI Helios NanoLab™* FIB system. Initial STEM characterisation was performed using an FEI Tecnai Osiris microscope, followed by atomic-resolution imaging employing a probe-corrected *Thermo Fisher Scientific™* Titan Themis STEM. This instrument provided simultaneous acquisition of ABF and HAADF signals, enabling correlated structural and compositional analysis at atomic resolution. The FIB preparation and STEM imaging, including the cross-sectional TEM/STEM analysis, were carried out in collaboration with Dr. Abhiram Gundimeda, Dr. Boning Ding, and Dr. Martin Frentrup, at Cambridge Centre for Gallium Nitride, Cambridge University. For detailed protocols regarding sample preparation and imaging conditions, the reader is referred to reference [94].

3.3. Atom Probe Tomography (APT)

APT is a uniquely powerful nanoscale characterisation technique capable of providing 3D spatial reconstructions and quantitative chemical analysis with near-atomic resolution [184]. As illustrated in Figure 3-5, APT is particularly well-suited for resolving fine structural features such as solute atoms, dislocations, SFs, and boundaries (Figure 3-5a). With anisotropic but exceptional spatial resolution, approximately <0.1 nm in depth (z-direction) and <1 nm laterally in the case of pure metals [185], APT surpasses many conventional microscopy methods in both precision and compositional sensitivity. Compared to other analytical methods such as SEM/STEM or secondary ion mass spectrometry (SIMS), including NanoSIMS, APT occupies a distinctive position in terms of spatial resolution and chemical sensitivity (Figure 3-5b). It offers near-uniform detection efficiency across the entire periodic table, enabling

unbiased elemental quantification regardless of atomic mass. This makes APT especially valuable for studying nanoscale features with high chemical complexity or low concentration elements that are challenging to detect by conventional methods.

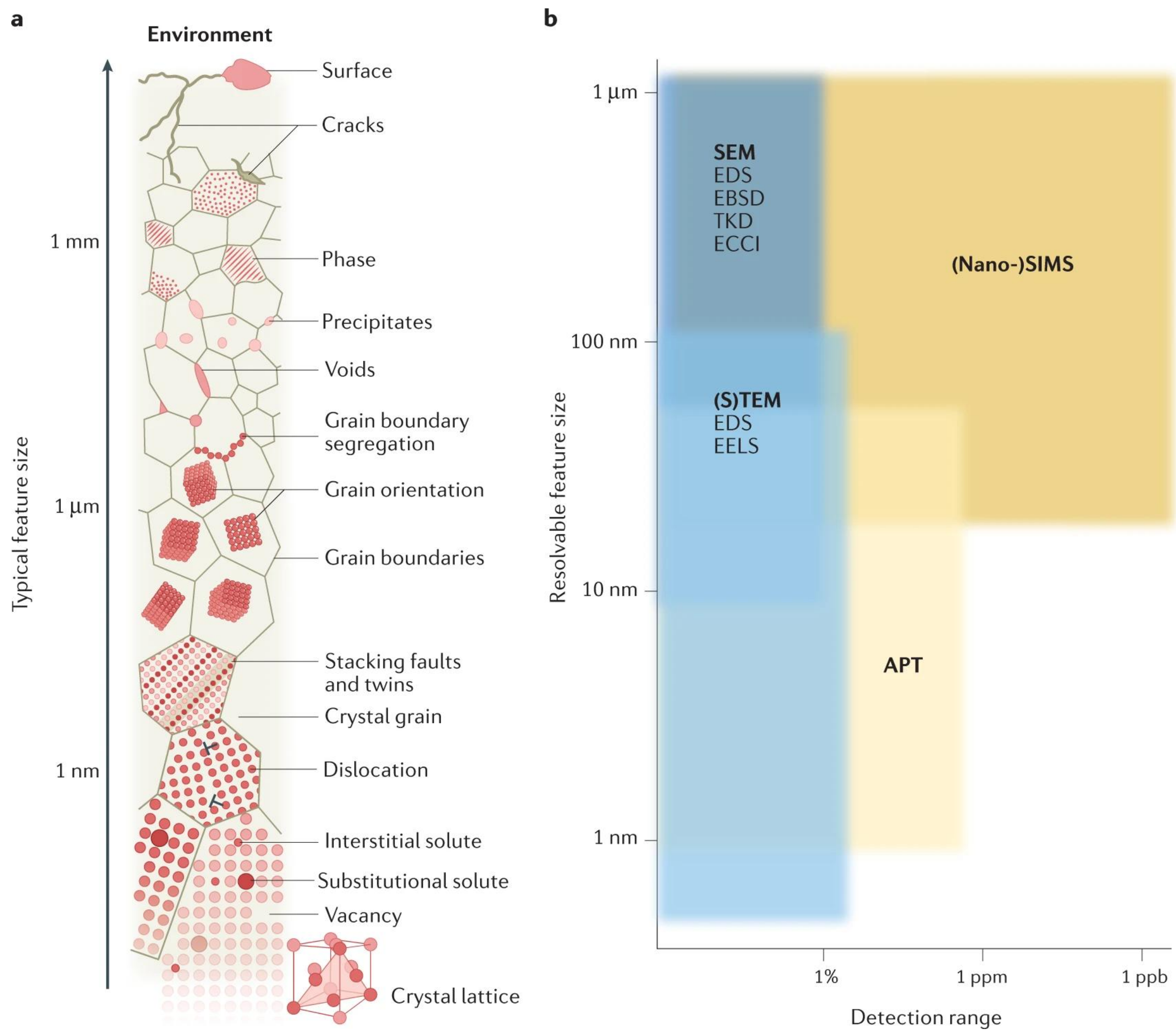

Figure 3-5 Microstructural features with their typical size and some analytical techniques used to analyse them. (a) Typical microstructural features of an engineering material. (b) Sensitivity and analysable feature size for some materials analysis techniques. Modified from J. Duarte, Max Planck Institute for Iron Research (MPIE), Ref. [137]

3.3.1. Basic Principles

As a microscopy technique producing 3D datasets, APT is based on the controlled field evaporation of ions under ultrahigh vacuum conditions (10^{-9}–10^{-8} Pa, [137, 184]) at cryogenic

temperature (20–80 K) [184]. The sample is prepared in the form of a sharp needle with a diameter of less than 200 nm [184], and is oriented toward a counter electrode in the analysis chamber. A high voltage is applied to the specimen, superimposed with either voltage or laser pulses, to induce the field evaporation of surface atoms. Once ionised, these atoms are accelerated toward a position-sensitive, time-resolving detector. A schematic illustration of the APT experiment is provided in Figure 3-6.

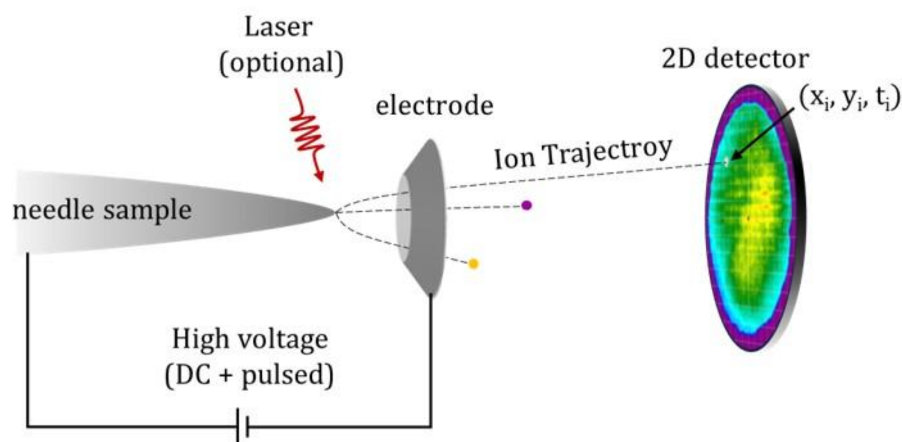

Figure 3-6 Schematic diagram of APT experiment. Dimensions of components are not to scale.

The physical mechanism involves applying voltage pulses to locally increase the electric field strength at the specimen surface, thereby inducing field evaporation [184]. Therefore, before laser pulsing techniques were introduced, conventional APT using high voltage pulsing was not suitable for low- or non-conductive specimens, such as semiconductors and geological samples, due to their inability to support the rapid charging and discharging cycles required for effective evaporation. In laser pulsing mode, it is generally accepted that this process is thermally activated by the laser pulse energy [184]. The laser pulse raises the temperature on the specimen surface temperature, thereby triggering field evaporation.

The local electric field F at the apex of the needle tip is decisive for ion evaporation and can be estimated as:

$$F = \frac{V}{k_f R} \qquad (3.1)$$

where V is the applied voltage, k_f is a geometric factor (typically ranging from 3 to 5 depending on tip geometry and material), and R is the tip radius of curvature.

The detector records the two-dimensional impact coordinates, (x, y), of each ion, while the z-coordinate is determined by the successive arrival of ions at the detector. During this process, each atom will be identified by measuring its flight times through time-of-flight mass spectrometry (ToF-MS) [186]. The TOF is related to the ion's mass-to-charge ratio by:

$$t = \frac{L}{\sqrt{2eV}} \cdot \sqrt{\frac{m}{n}} \text{ or } M = \frac{m}{n} = 2eV\left(\frac{t}{L}\right)^2 \qquad (3.2)$$

where L is the flight path length, e is the elementary charge of the electron, V is the total voltage, m is the ion mass, and n is its charge. Here, the ratio of mass to charge state ratio, $M=\frac{m}{n}$, is usually expressed in Daltons (Da) and presented in the form of a histogram, also known as mass spectrum [184].

With this data, a 3D atomic map of the specimen can be reconstructed based on the phenomenological point projection model and empirical reconstruction algorithms [187]. This approach approximates the atomic positions prior to evaporation and enables analysis of structural and chemical features at the atomic scale [184, 188]. The reconstruction is typically performed using IVAS 6.3 or AP Suite 6.1(Cameca, Madison, Wisconsin, USA).

3.3.2. Common Artefacts and Challenges

While APT is a powerful technology in characterisation, there are several limitations and challenges needed to be considered, especially for layered semiconductors investigated in this thesis.

3.3.2.1. Surface Diffusion

When a strong electric field or elevated temperature is applied before evaporation, atoms on the surface can migrate along the specimen, which may blur compositional boundaries and lead to artificial broadening of features [189, 190]. This effect is more pronounced in metallic materials when using laser mode, because of the increased surface mobility from thermal activation [184]. To minimise this, optimisation of APT experimental conditions is necessary.

3.3.2.2. Electrostatic Effects

High electric fields are essential for field evaporation in the APT, however, the variation in the fields can lead to phenomena like chromatic aberrations and local magnification effects which lead to inaccuracies in the reconstructions [184, 191]. These effects are particularly pronounced in those inhomogeneous samples containing multiple phases [192, 193].

In terms of chromatic aberrations, as shown in Figure 3-7, the difference in evaporation fields between species A and B causes B to evaporate later, which results in their misplacement in the reconstruction volume. In addition, the preferential evaporation of A atoms also results in the change of the tip geometry, namely the local curvature of the tip, which in turn affects the magnification. As a result, the projected position of the ions would be locally different for A and B, which leads to an apparent expansion or contraction of the features, especially near

interfaces. This chemically dependent behaviour introduces spatial distortions in the reconstruction and should be carefully considered when interpreting APT data.

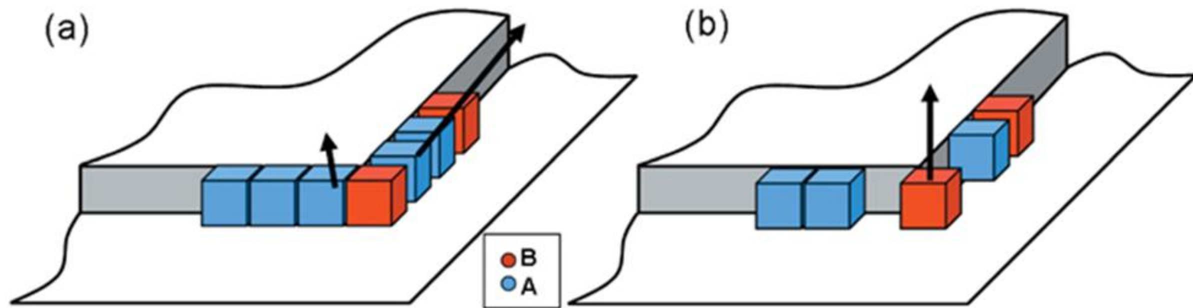

Figure 3-7 Schematic of evaporation near the edges of the terraces: blue atoms with lower evaporation field evaporate first, changing the local field and geometry, and the red atoms requiring a higher field remain longer on the surface and evaporate later with a different surrounding affecting its initial trajectory. [191]

3.3.2.3. Trajectory Distortion

Trajectory distortion refers to the deviation of ion paths from their ideal trajectories (as shown in Figure 3-6) during their flight from the specimen to the detector. This deviation is primarily caused by non-uniformities in the local electrostatic field, which are influenced by factors such as tip geometry, local curvature, crystallographic orientation, and chemical variations [184]. According to the expression for the local electric field F at the apex of the needle-shaped specimen (as mentioned earlier in 3.3.1), irregularities in the shape of the tip, or sudden changes in its curvature, can lead to the change of the local field strength [184]. In addition, as elements have different evaporation fields, chemical variation within the sample can also lead to field distortions near interfaces or precipitates. In semiconductor sample like $Al_xGa_{1-x}N$, for example, the Ga evaporation field is around 15 V/nm, while that of Al is at 19 V/nm. However, N evaporation is significantly more challenging due to its strong bonding and high ionisation energy. Similarly, this also occurs between difference phases. Therefore, it is important to

carefully control the tip shape during sample preparation while considering the effect of non-uniform field by comparing the measured densities of the different phases. Although new methods have been proposed to partially compensate for some surface-induced distortions [194-196], especially in heterogeneous materials, this phenomenon still cannot be fully corrected. As a result, spatial inaccuracies remain an inherent challenge in reconstructions involving multiphase systems or significant chemical inhomogeneity.

3.3.2.4. Multiple Events

Multiple events mean more than one ion is detected in the detection window of a single pulse. It occurs more frequently in low- or non-conductive materials compared to metals, due to slower charge redistribution, greater molecular ion formation, and increased sensitivity to laser-induced heating [184, 187]. These events are thought to originate primarily from two mechanisms. First, the rapid rearrangement of surface charges after initial evaporation can trigger further evaporation of neighbouring atoms, especially in materials with low electrical conductivity [137]. Secondly, a higher fraction of molecular ions in these materials increases the likelihood of dissociation during the flight, which contributes to multiple events [137]. As a result of ion dissociation and the generation of additional ionic species, the mass spectra may contain overlapping peaks that complicate compositional interpretation. Multiple-hit events can further increase this complexity by producing coincident signals, which may lead to peak misidentification or quantitative errors.

3.3.2.5. Background Noise

Background noise is also an important factor to be considered in APT analysis. It mainly originates from residual gas ions, delayed evaporation events, and random field ionisation

within the specimen chamber. High background levels can interfere with accurate elemental identification, and signals from minor species may be obscured or lost within the background noise. In particular, those materials with poor thermal or electrical conductivity tend to retain thermal energy between laser pulses, leading to delayed field evaporation which shows as thermal tails on mass peaks [187]. Such tails can overlap with adjacent peaks and raise the local spectral background, potentially obscuring minor elemental signals [187].

3.3.3. Atom Probe Sample Preparation

To ensure adequate field strength and achieve a sufficiently uniform electrical field, which are essential for obtaining high-quality atom probe datasets, the needle-shaped specimen must meet several key requirements. These include: a radius of curvature at the apex between approximately 50 nm and 150 nm, a smooth surface, a circular cross-section, the feature of interest located within about 100 nm of the apex, sufficient specimen length and tip cleanliness and an appropriate shank angle [184]. This can be achieved by two main methods: electropolishing or FIB milling from its bulk material. Electropolishing uses electrochemical reactions to gradually shape a conductive material in the form of a matchstick into a sharp tip, making it effective for preparing metallic specimens. However, it is not suitable for site-specific investigations as the location of the final tip is hard to control. On the other hand, FIB milling employs a focused beam of ions, typically Ga, to sputter material from the surface with nanometre-scale precision, which allows for controlled tip-shaping and site-specific extraction of the specimen. In addition, while electropolishing is suitable for metals, FIB is particularly necessary for layered semiconductor materials, such as those examined on this thesis. The

precision and site-specific capability of FIB allows accurate targeting and preservation of delicate interfaces and nanostructures within the layers.

In this study, all needle-shaped APT specimens were prepared using FIB to target the specific features of in the material, such as stacking faults (SFs) and QWs. A comprehensive overview of the standard procedure of FIB can be found in [181, 197], and following this, the key steps and parameters used to prepare specimens in this thesis are summarised in Figure 3-8 and described below. Apart from that, several modifications were introduced in this work to improve the quality and success rate of GaN tip fabrication, especially for accurately targeting specific layers or features, which will be described in detail in the Chapter 4. In terms of instruments, a dual-beam SEM/ FIB instruments of Zeiss Crossbeam 540 Analytical FIB-SEM (Zeiss GmbH, Oberkochen, Germany) was used for APT sample preparation in this study.

Prior to milling with the FIB, a protective layer of platinum was deposited on the area of interest ($2 \times 20\ \mu m^2$, 30 kV, 100 pA). The triangular cross-section wedge beneath the platinum rectangle was milled on three faces, employing a voltage of 30 kV and current ranging from 1.5 nA to 300 pA. For undercut milling, a current of 300 pA was used to mill underneath and along the edge of the protective layer. In the lift-out process, an *in-situ* micromanipulator was employed to approach one side of the wedge, maintaining a small gap with the sample. Subsequently, platinum was deposited to the junction of the wedge and the micromanipulator for soldering (30 kV, 50 pA) and then cut from the other side (30 kV, 300 pA). Subsequently, 1.5–2 μm wide segments were mounted sequentially onto standard Si column microarrays (Cameca

Instruments) and then separated from the wedge-shaped segments by milling (30 kV, 300 pA). Each segment was individually shaped into needles using a sequential annular milling pattern with decreasing inner diameters. Since the material is very sensitive to the ion beam [198], the sharpening process needs to be very careful. The process began at 30 kV and 300 pA, reducing the needle diameter to approximately 1 μm. Then the parameters were adjusted to 30 kV and 100 pA to further sharpen the needles to about 200–300 nm. A final refinement step was performed at 30 kV and 10 pA, reducing the diameter to less than 100 nm. To minimise milling damage, a treatment at 2 kV and 10 pA was applied during the last stage of sharpening. Careful polishing was then performed to remove the remaining platinum protective layer while retaining the near-surface layers of interest. After preparation, these specimens were transferred to the atom probe under non-vacuum ambient conditions at room temperature and atmospheric pressure.

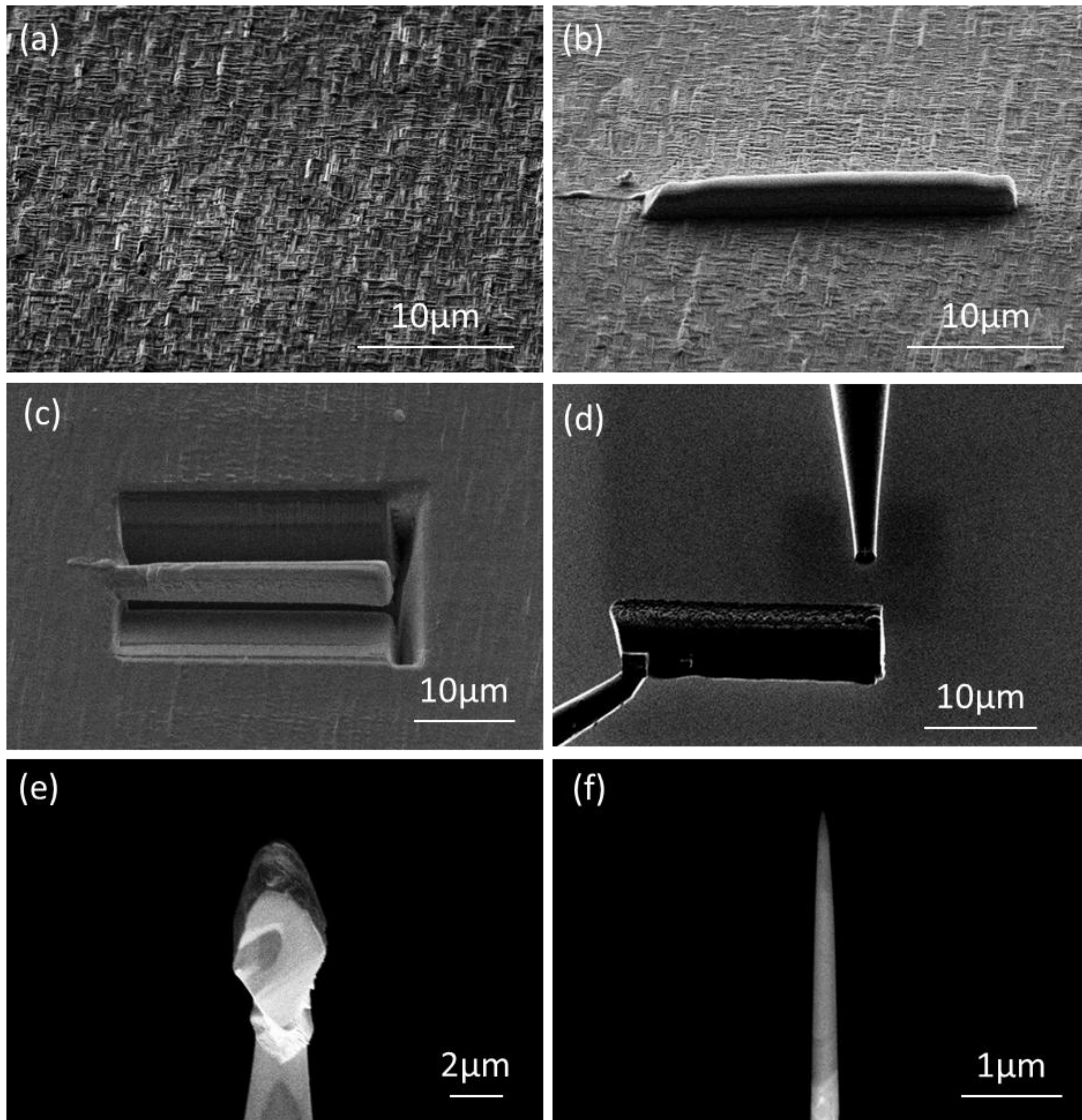

Figure 3-8 FIB-SEM lift-out and annular milling process. (a) Target area of interest (b) Deposition of platinum in the region of interest (c) Trenching and undercut milling (d) Lifting out by *in-situ* micromanipulator and in the position for mounting onto standard Si post (e) Segment mounted on a Si post for tip sharpening (f) Final sharpened tip for APT experiment

3.3.4. APT Data Collection and Reconstruction

3.3.4.1. Data Collection

Atom probe measurements were performed using a CAMECA LEAP 5000 XS operated in straight-flight-path configuration (~80% detection efficiency) under ultra-high vacuum (10^{-9}–10^{-8} Pa) and at a cryogenic temperature of about 50K [137, 184]. The straight-flight-path LEAP configuration was selected because it preserves the original ion trajectories and time-of-flight

relationships, unlike reflectron-type instruments which introduce additional ion path corrections. This characteristic is particularly advantageous for analysing molecular ion dissociation and correlated evaporation events, which are common in GaN-based materials. Therefore, the use of a straight-flight-path instrument allows for a more reliable interpretation of the dissociation trajectories and associated mass spectral features in this thesis.

As the materials in this study are semiconductors, which have low electrical conductivity compared to metals, all experiments were performed in laser pulsing mode, instead of voltage mode. To explain this in detail, there are several reasons for applying laser mode for semiconductors. Firstly, voltage pulsing relies on field evaporation driven by increased electric field. However, semiconductors have lower electrical conductivity than metals, where the electric field doesn’t propagate efficiently and thus making the voltage pulses less effective. In contrast, laser pulsing introduces localised thermal energy at the tip of the specimen which can help atoms overcome evaporation barrier and enabling more controlled and stable evaporation. Additionally, as the voltage pulse can cause sudden field surges and electrostatic charging, it increases the risk of tip damage. With laser pulsing, the mechanical stress and risk of sample fracture can be significantly reduced, enabling the collection of longer and more complete datasets.

During the experiment, there are several parameters that need to be carefully selected by the user to ensure efficient and accurate data collection, including base temperature, laser energy, pulse frequency, and detection rate.

The base temperature refers to the thermal environment of the specimen during analysis. In APT experiments, it typically ranges from 20–80 K, depending on the material. For thermally sensitive materials like GaN, lower temperatures are preferred, since they help reduce atomic migration, minimise thermal damage, and stabilise the specimen during field evaporation [184].

The base voltage represents the standing voltage required to generate the electric field for atom evaporation at the specimen tip. It is not a fixed parameter but dynamically adjusted during analysis, depending on the specimen geometry and evaporation conditions. In this study, the voltage typically started between 2 and 4 kV and gradually increased up to 8 kV as the tip radius expanded and the evaporation field changed, consistent with the relationship described in Equation (3.1) and illustrated in Figure 3-9. Field evaporation should only occur when additional voltage or laser pulses are applied to overcome the energy barrier, thus ensuring that ion emission is controlled [184].

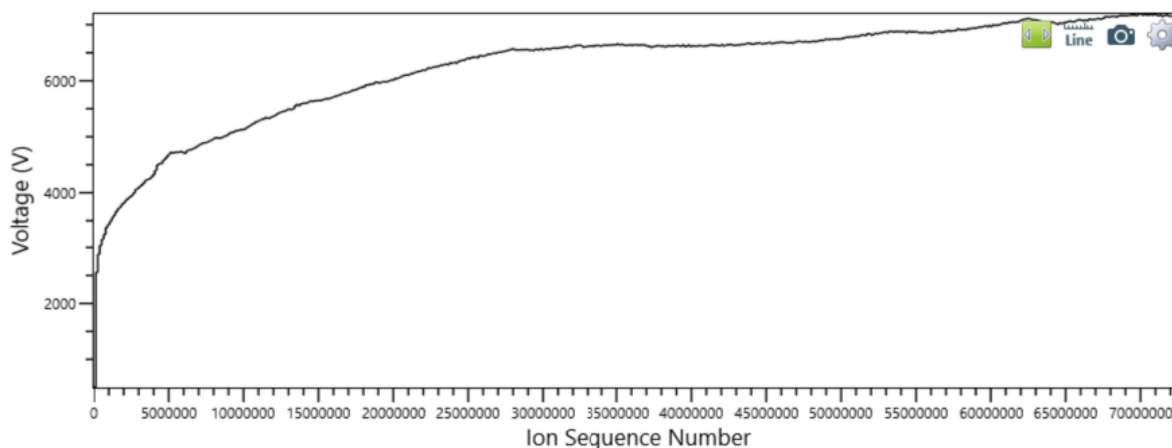

Figure 3-9 Voltage history plot showing the gradual increase in applied voltage as a function of ion sequence number during APT analysis. The voltage increases dynamically to maintain a stable evaporation rate as the tip radius changes over time.

Laser pulse energy is another critical parameter in laser mode APT experiments. It refers to the energy delivered by each laser pulse to thermally assist ion evaporation. In the case of GaN, excessive laser energy can lead to undesirable effects such as Ga migration, N loss, and thermal tails in the mass spectrum [184]. As GaN is highly sensitive to laser power, lower laser energies are preferred to minimise damage and preserve stoichiometry, if needed [137]. The specific laser energy settings used in this study are discussed in detail in Chapter 4.

Pulse frequency is another key parameter that influences evaporation behaviour. It defines how frequently laser pulses are applied, directly affecting both the data acquisition rate and the thermal load on the specimen. While higher pulse frequencies enable faster data collection, they require careful tuning of the laser energy to prevent excessive heating and potential damage to the sample [184].

The detection rate refers to the average number of atoms detected per single laser pulse [184]. Ideally, it is adjusted to detect only single atoms while minimising multiple detection events which would affect the accuracy of data. In this study, a detection rate of 0.5% was selected based on a series preparatory experiment, which will be discussed in detail in Chapter 4. The detection rate is closely related to the applied voltage, and experiments are usually performed with a fixed detection rate, while the voltage is varied dynamically to maintain consistent ion emission.

In this study, atom probe measurements were conducted at a cryogenic temperature of 50 K, using a pulsed laser (333–500 kHz, 0.03–10pJ per pulse). Multiple datasets were obtained from various APT tips at different laser energies within this range. Further details regarding the parameter selection are provided in Chapter 4.

3.3.4.2. Reconstruction Protocol

Data reconstruction is an important step in APT analysis where it transforms the raw detector data into a 3D atomic scale map of the specimen. In this thesis, the APT datasets were analysed using the commercial software packages IVAS 6.3 and AP Suite 6.1 (Cameca, Madison, Wisconsin, USA).

The reconstruction of the APT data involves several key steps. First, data selection is carried out based on the voltage history plot (z-direction) and the detector hit map (x/y-direction). Typically, ions collected during stable running are chosen for analysis. Next, time-of-flight

(TOF) calibration is automatically performed by the software to address the variations in the flight path that would slightly alter TOF measurements. Following this, the calibration of mass spectrum is conducted using several known feature peaks, which typically including one low-mass peak, a few mid-range peaks, and one high-mass peak. In this study, the calibration was based on 14.0 Da (N), 34.5 Da (Ga), 68.9 Da (Ga), and 114.9 Da (In), for example. After calibrations, the individual peaks in the mass spectrum are manually identified and ranged based on the atomic weights of the elements and the natural abundances for all relevant isotopes. To avoid artefact induced by subjectivity, and to improve the reproducibility, full width at nine-tenths maximum (FW9/10M) ranging is applied in this thesis [184]. In addition, the peak overlap issues were addressed using the MATLAB package AtomProbeLab v0.2.4 developed by London *et al.* [199, 200]. More details about ranging can be found later in 3.3.5.1 and 3.3.5.2.

An important step in APT reconstruction is to calibrate the parameters for an accurate and reliable 3D model. Typically, it is critical to adjust instrument parameters, including image compression factor (ICF) and k factor (k_f, a geometric factor), accordingly. The ICF indicates how ion trajectories are compressed during flight, which affects the lateral resolution of the reconstruction; while the k factor relates the applied voltage to the electric field at the tip surface, which affects the depth scaling of the reconstruction. Ideally, they can be finely tuned by using crystallographic features of the materials, such as interplanar spacing of atomic planes around poles shown in the detector hit maps. However, in the layered InGaN/GaN samples investigated in this work, no clear crystallographic poles were observed. This is most likely caused by the characteristic evaporation behaviour of semiconductors, as also no distinct poles

were detected in the cubic GaN matrix. Therefore, in this study, default instrument values for these two parameters were adopted (ICF=1.65, and k_f=3.3).

To improve the accuracy of the reconstructed model, the initial specimen geometry parameters (such as the tip radius and shank angle) were first estimated from SEM images prior to reconstruction. This provided reasonable input values for the 3D reconstruction algorithm, as illustrated in Figure 3-10. Subsequently, the reconstruction was further calibrated based on the measured quantum well (QW) thickness and spacing to ensure consistency with the actual multilayer structure observed in the sample. In this approach, a defined shank angle was applied; therefore, the reconstruction did not explicitly follow the voltage evolution during the analysis. Although the apex may appear slightly blurred due to charging effects typical of semiconductor materials, the overall reconstructed geometry remained suitable for APT analysis. Apart from that, the voltage history of the data was examined to monitor changes in the tip radius during acquisition. For example, to identify possible small fractures or tip instabilities. In addition, certain features within the reconstructed data can also help validate the accuracy of the reconstruction. For example, in studies of aged Al-Mg-Si(-Cu) alloys, clusters or GP-zones have been observed to form along distinct, often orthogonal crystallographic directions, particularly the <001> Al directions [201, 202]. These mutually perpendicular precipitate alignments reflect the cubic symmetry of the aluminium matrix and can serve as useful indicators for assessing the spatial accuracy of reconstructed APT datasets [201, 202]. Similarly, in this thesis, the angle between crossed SFs in the examined samples is used as a reference feature for validating the reconstruction accuracy. Further details are provided in Chapter 5.

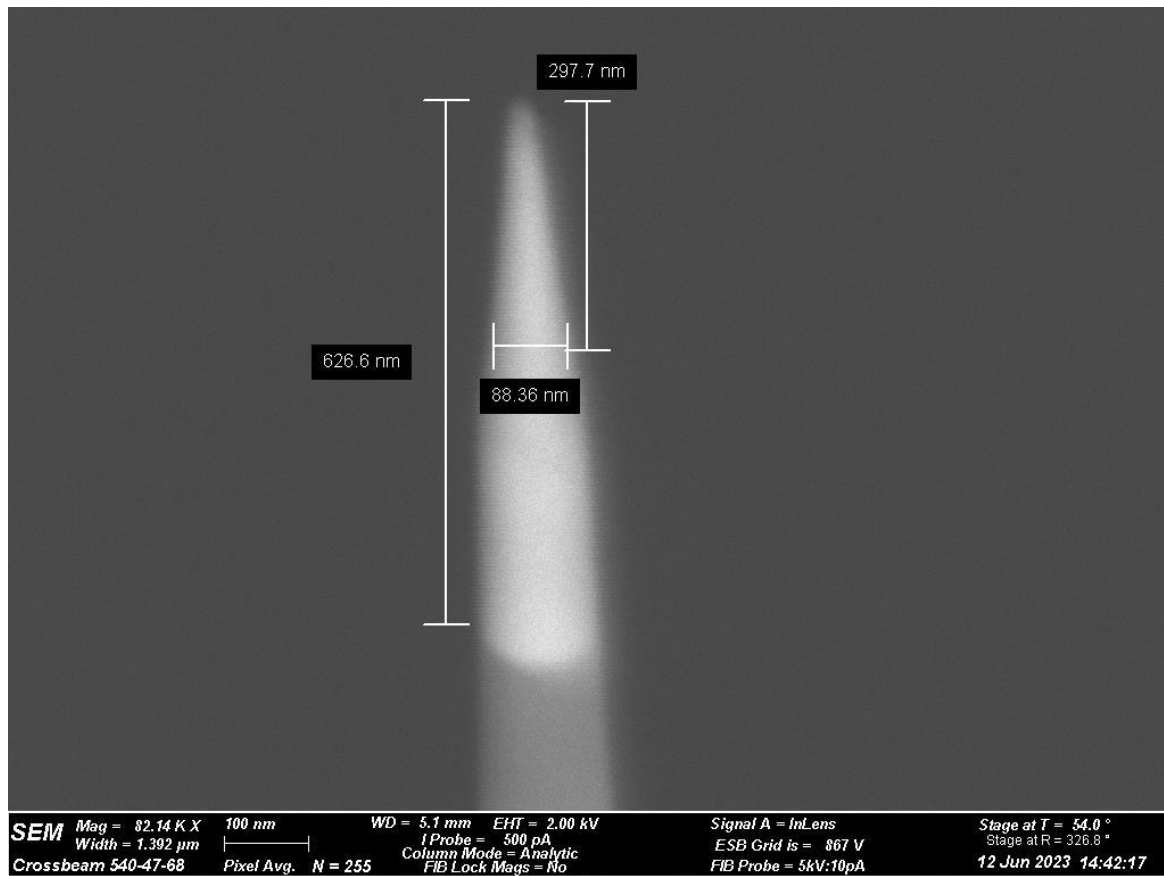

Figure 3-10 SEM image of a prepared APT tip from a MQW sample prior to analysis.

In summary, by combining geometrical estimates based on SEM, certain features within the material and default instrument parameters, a physically realistic and reproducible 3D reconstruction can still be achieved, even without crystallographic features like poles.

3.3.5. APT Data Analysis Tool and Techniques

3.3.5.1. Mass Spectrum Ranging

As discussed previously, the field evaporation of surface atoms generates a time-of-flight mass spectrum, which serves as the basis for compositional analysis in APT. A critical analytical step in interpreting this spectrum is the assignment of detected mass-to-charge state ratio peaks to specific atomic or molecular ions, which is also known as 'ranging'. Common mass spectrometry techniques are mostly designed for biomaterials and large organic molecules

relying on fragmentation patterns and fingerprint databases [203]. They are not applicable in APT analysis, which is concerned with the detection of individual atoms and small molecular clusters. Instead, the interpretation of APT mass spectra relies on manual or semi-automated strategies to identify peaks. In order to reduce subjectivity and improve consistency in APT peak identification, Haley *et al.* [204] developed an algorithm that systematically enumerates all plausible ion identities for a given peak and ranks them according to likelihood. However, the width around the peak maximum used to define counts under the peak is determined by the user during ranging. To make the results of this thesis as reliable and reproducible as possible, peak ranges were defined using the full width at nine-tenths maximum (FW9/10M), combined with local background subtraction (range-assisted correction), as this method has been demonstrated to provide the most accurate compositional results in APT analysis [184].

3.3.5.2. Peak Overlap

In complex mass spectra, multiple species produce ions with very close mass-to-charge ratios, which is known as peak overlap. These peaks may show direct overlap or tail overlap, which may potentially lead to inaccurate compositional analysis. These overlaps can often be treated as deconvolution problems, where the relative contributions of each ion are estimated by examining adjacent, non-overlapping isotopic peaks of the same species [184]. This allows the individual intensities to be calculated even when peaks partially overlap. This method is effective when at least one of the overlapping ions has an adjacent isotopic peak that does not overlap with another ion, however, there is no unique solution if the isotopic abundance matrix for a given overlap contains more unknown ions than measured peaks [184].

In the present study, most cases of peak overlaps correspond to the former case, where at least one overlapping ion has a unique, non-overlapping isotopic peak, and thus the method can be applied reliably. In this thesis, the peak overlap resolved compositions were determined using the MATLAB package AtomProbeLab v0.2.4. The methods used to resolve overlapping peaks and quantify the associated uncertainties follow the approach outlined by London *et al.* [199, 200]. In an example in this thesis, the peaks at 25.0 Da and 26.1 Da can be associated with either Cr^{2+} ions or Mg^{+} ions, as shown in Figure 3-11. According to the method mentioned above, Figure 3-12 shows an ion count histogram and the approximate contribution of each ion type to the different peaks, where the peak at 24 Da does not overlap and was used to calculate the deconvolution. The overlapping peak at 25 Da contains 55.6% Cr^{2+} and 44.4% Mg^{+}, and that at 26.1 Da contains 96.1% Cr^{2+} and 3.9% Mg^{+}.

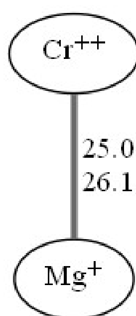

Figure 3-11 An example of ion overlap between Cr^{2+} and Mg^{+}. Ellipses represent ion species, and the connecting line indicates overlapping mass-to-charge positions at 25.0 Da and 26.1 Da. The line thickness reflects the product of isotopic abundances, representing the likelihood and complexity of peak overlap. The plot was drawn using AtomProbeLab-v0.2.4.

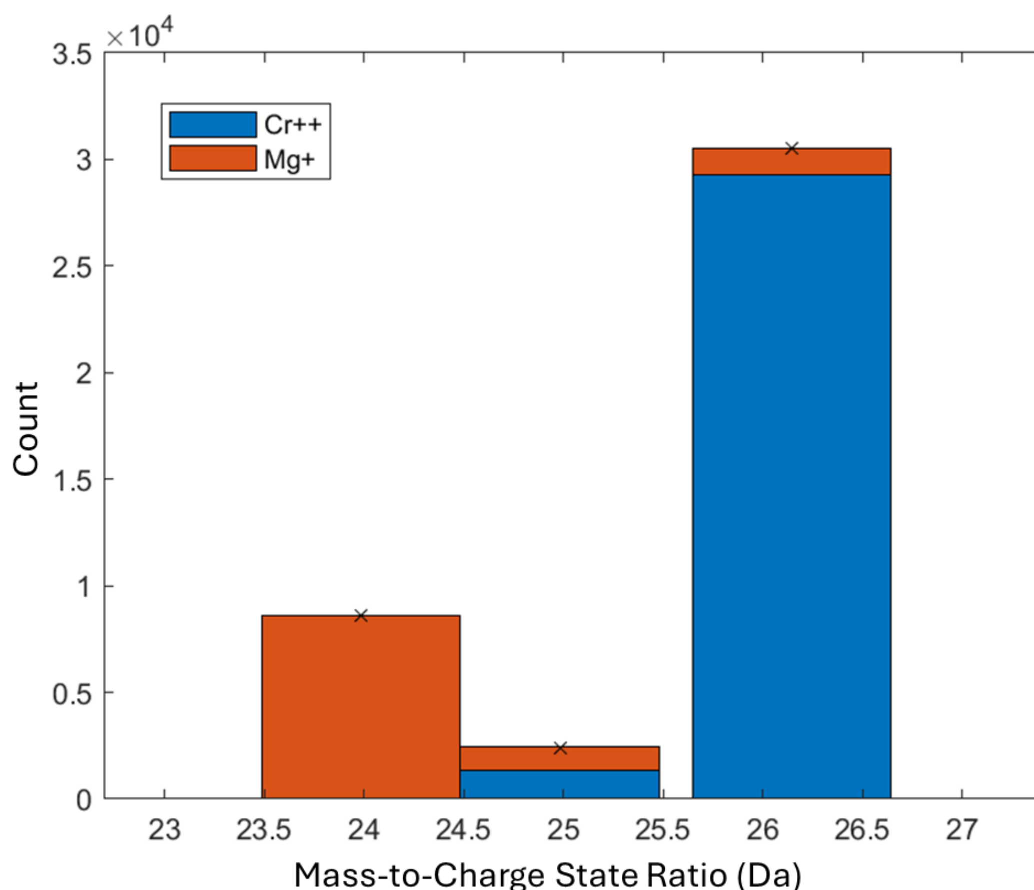

Figure 3-12 Ion count histogram showing the contribution of each ion type to the different mass-to-charge state ratio peaks. The plot was drawn using AtomProbeLab-v0.2.4.

3.3.5.3. Density Analysis

As mentioned earlier, artefacts such as trajectory distortion and local magnification effects may occur during evaporation processes. As this will result in density variations, the assessment of atomic density in APT analyses is necessary to assess the accuracy of 3D reconstructions. The distribution of atomic densities is obtained by dividing the dataset into a uniform 3D voxel grid and then calculating the number of atoms in each voxel divided by the voxel volume [184].

To improve accuracy, a delocalisation algorithm is applied [205]. This refers to the use of a Gaussian or other kernel function centred on the atom's position to spread the contribution of each atom over multiple nearby voxels, rather than assigning it to a single voxel [205]. It

improves spatial resolution without sacrificing statistical reliability [184]. In addition, a k-nearest-neighbour (kNN) approach can be used to detect fine-scale variations, helping to identify real structural features like precipitates, voids, or interfaces [184].

3.3.5.4. Volume Renderings

Volume rendering is a qualitative 3D visualisation technique on IVAS 6.3 or AP Suite 6.1 (Cameca, Madison, Wisconsin, USA) for displaying spatial variations in composition or density across a dataset. After delocalisation, each voxel or block within the specimen reconstruction is assigned a normalised colour value based on local concentration or density to form a 3D heat map [31]. The opacity can be adjusted for better visualisation. Notably, the software also allows creation of local volume renderings by defining iso-concentration or iso-density surfaces. This enables a focused visualisation within sub-regions of the reconstruction, which is particularly useful for isolating and analysing specific microstructural features.

3.3.5.5. Concentration Measurement and Mapping

Concentration measurement in APT is preformed using one-dimensional concentration profiles and two-dimensional compositional maps to evaluate the distribution of elements and solutes. One-dimensional concentration profiles can be generated by defining rectangular or cylindrical regions of interests (ROIs) aligned perpendicular to interfaces or across features. The concentrations are calculated as the atomic fractions within discrete sampling bins, while bin widths should be dynamically adjusted based on local atomic density to avoid the distortion in areas of density variation [184]. Similarly, two-dimensional maps are created by slicing the dataset or target ROIs into thin cross-sectional slabs, where the thickness of the slice also needs to be adjusted for better visualisation [184].

3.3.5.6. Proximity Histogram (Proxigram) Analysis

Proximity histogram (proxigram) analysis is used for characterising compositional gradients normal to more complex 3D features such as precipitates or interfaces [184, 206]. It is based on a specific iso-concentration or iso-density surface that isolates the feature of interest, and adjacent atoms are binned into shells based on their distance to the local normal from this surface. Atomic concentrations are then calculated in each shell, and thus generating a 3D composition profile independent of the interface geometry [207]. It should be noted that the accuracy of a proxigram strongly depends on the precise placement of the reference iso-surface, which should ideally align with the steepest composition gradient to minimise geometric artefacts [184, 207].

3.3.5.7. Saxey Diagram

During evaporation process, certain ions that are unstable under high-field conditions, such as Ga-containing molecular ions like GaN_3^{2+}, exhibit a strong tendency to be detected as part of multi-hit events [208]. This suggests they dissociate during their flight to the detector, leading to correlated fragment ions [152]. To investigate these dissociation events and better understand molecular ion behaviour and potential artefacts in the mass spectrum, Saxey diagrams were used in this thesis.

Saxey diagrams are also called correlation histograms [184]. They are a two-dimensional plot mapping the frequency distribution of each mass-to-charge ratio, together with all its co-evaporated ions [184], and the characteristic dissociation tracks appear as curved or diagonal features linking pairs of mass-to-charge state ratios [209]. As shown in Figure 3-13, the vertical

and horizontal lines indicate that one of the correlated species evaporates at the instant of the pulse, followed by a delayed evaporation of the second correlated species. The diagonal line from the lower left to the upper right corner (grey line in Figure 3-13) indicates the simultaneous delayed evaporation of both correlated species. The diagonal, vertical and horizontal lines indicate the presence of thermal tails in the mass spectra. Lastly, the pink curves indicate the dissociation of molecular ions as they reach the detector [209].

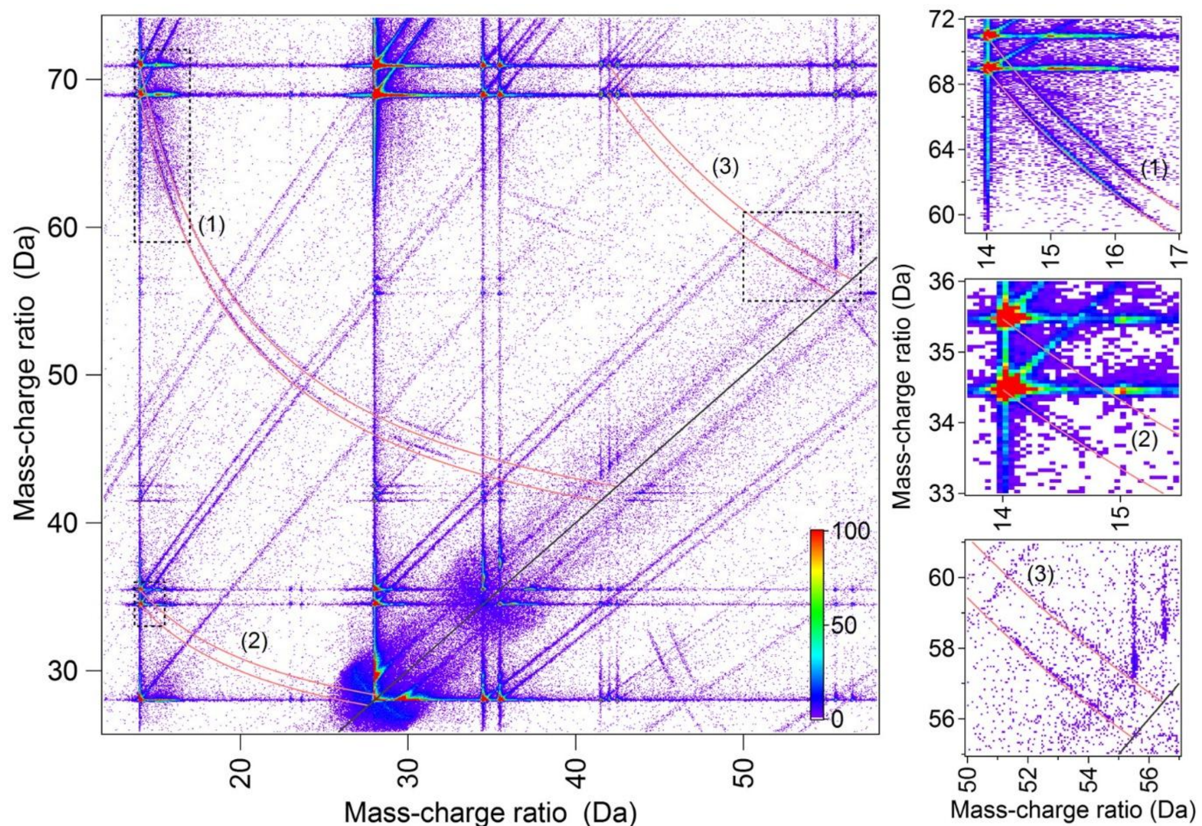

Figure 3-13 Left: Saxey diagram for a set of GaN data presented in Ref. [209]. The curves (pink) superimposed on the correlation histogram are generated based on the flight-path model. The grey diagonal line corresponds to the symmetry axis of the histogram, where the dissociation tracks terminate. Right: Close-up on the three subfigures showing details of each dissociation track: (1) $GaN^{2+} \rightarrow Ga^{+} + N^{+}$ (2) $GaN^{3+} \rightarrow Ga^{2+} + N^{+}$ (3) $GaN_3^{2+} \rightarrow Ga^{+} + N_3^{+}$ [209].

According to Saxey's work [209], assuming that molecular ion dissociation occurs close to the surface of the specimen, he demonstrated that the deviation from the mass-to-charge ratio value

and the shape of the curved dissociation trajectory can be plotted by the following relationship:

$$m_1' = m_1 \left[1 - \frac{V_d}{V_0}\left(1 - \frac{m_1}{m_p}\right)\right]^{-1}$$

where m_1' represents the shifted measured mass-to-charge ratio of one of the ions formed during dissociation, m_1 represents the mass-to-charge ratio of the same ion if it had not been formed from mid-flight dissociation, m_p represents the mass-to-charge ratio of the original molecular ion, V_0 represents the voltage at the moment of evaporation, and V_d represents the drop in potential when a molecular ion leaves the surface and dissociates.

It should be noted that Saxey diagrams are strictly applicable to straight-flight-path atom probe instruments, where ion trajectories can be approximated as linear during flight [209]. For reflectron-type instruments, the curved ion paths and additional time-of-flight corrections complicate the direct interpretation of dissociation tracks. In this thesis, all APT experiments were conducted on a straight-flight-path LEAP instrument, and therefore the interpretation of Saxey diagrams follows this assumption.

Based on this assumption, the dissociation of complex ions can result in systematic ion loss for two key reasons. Firstly, when dissociation occurs far from the specimen surface, the ions' time-of-flight changes, which makes it difficult to identify them and eventually they contribute to the background noise [209]. In addition, the dissociation of some molecular ions may produce neutral atoms or molecules, which are not affected by the electric field and are less likely to have enough kinetic energy to reach the detector [209].

In summary, the features of Saxey diagrams not only help to reconstruct the dissociation paths, but also provide insights into the spatial and energetic context of fragmentation, revealing the sources of systematic losses that lead to biases in component measurement [152, 209].

3.4. Summary

This chapter has outlined the materials, experimental techniques, and analytical procedures employed in this thesis to investigate SFs and QW structures in zincblende InGaN/GaN heterostructures. Electron microscopy techniques, including SEM, FIB, and TEM/STEM, were introduced to describe the workflow for site-specific specimen preparation and nanoscale structural characterisation.

An overview of APT principles, artefacts, and data analysis procedures tailored for III-nitride heterostructures was presented. Strategies for minimising these effects through careful optimisation of experimental parameters were discussed.

Detailed procedures for APT specimen preparation, data acquisition, reconstruction, and quantitative analysis were further described. These methodologies establish a robust framework for the high-resolution chemical and structural investigation of nanoscale defects and interfaces, forming the basis for the experimental results and discussions presented in the subsequent chapters.

Chapter IV Best Practices for APT of Layered GaN

This chapter outlines the experimental methodology developed to obtain reproducible and reliable atom probe tomography (APT) data from GaN, paving the way for all subsequent InGaN/GaN studies presented in this thesis. The first section briefly addresses the key challenges encountered during the analysis of GaN, including issues such as fracture, artefacts induced by focused ion beam (FIB) implantation and stoichiometric drift in data collection. Following this, the subsequent section presents protocols for preparing and analysing GaN-based specimens. FIB techniques were developed to control apex geometry and achieve precise positioning of layered structures, and a systematic study was conducted to assess the influence of acquisition parameters on GaN stoichiometry. An optimised parameter set was established at the end of this chapter, and a site-fraction calculation method is introduced to ensure reliable chemical interpretation.

In summary, the chapter consolidates the previous research and practical results into a best-practice protocol that enables the acquisition of reproducible, high-fidelity GaN datasets. This also serves as the experimental foundation for the multi-quantum well (MQW) and single quantum well (SQW) analyses discussed in Chapters 5 and 6.

4.1. Challenges of GaN in Practical APT

GaN is widely regarded as one of the most mechanically brittle and analytically demanding semiconductors for APT [210-212]. Due to its semiconducting nature, its APT sample needs to be prepared by FIB techniques. However, the high mechanical hardness of GaN would slow down material removal, making it challenging to precisely shape the specimen apex [213]. In addition, its considerable brittleness makes the fragile tip easy to fracture, especially during the final sharpening stage [212]. Therefore, FIB conditions play a vital role in the sample preparation process. Excessive ion currents or accelerating voltages can lead to rapid, uncontrolled material removal, or even localised 'melting', which results in damaging artefacts and risking missing or damaging the target layer of interest. FIB-induced phenomena such as Ga implantation can also reduce sample quality and measurement reliability [210].

Apart from careful sample preparation, APT acquisition parameters, such as laser pulse energy [210], detection rate [210], and base temperature [214], also need systematic testing and optimisation for GaN. These parameters can significantly influence field-evaporation behaviour, charge-state distributions and compositional accuracy.

Therefore, producing GaN APT samples with ideal tip geometry that both protects the target layer and survives the APT run is very challenging. Both specimen preparation conditions and APT experimental parameters must be carefully optimised to obtain high quality, reproducible datasets. The work covered in this chapter explores and discusses the best protocols for the different stages of GaN APT experiments.

4.2. FIB APT Specimen Preparation

4.2.1. Best-Practice Protocol for GaN

Preparing GaN APT specimens with FIB remains challenging due to the material's brittleness and high sensitivity to FIB parameters. The following section illustrates these issues and highlights best-practice considerations for GaN FIB preparation.

Figure 4-1(a) shows an SEM image of a final polished APT tip, which does not exhibit a smooth and sharp apex shape due to suboptimal conditions during the milling process. This kind of non-ideal tip geometry is frequently encountered during GaN sample preparation and is highly susceptible to fracture shortly after the start of APT experiments. The irregular shape is likely the result of high-current milling in the final sharpening step (30kV, 50pA in this case), where the intense ion beam can cause uneven material removal near the apex. The resulting relatively large final apex radius requires a higher standing voltage (around 5–7 kV) to initiate field evaporation at the start of the APT run. However, the applied voltage is usually adjusted during the analysis to maintain a nearly constant field, and may even be reduced as the field of view increases. The increased initial standing voltage can raise local electrostatic stress at the apex, thereby increasing the likelihood of tip fracture and reducing overall data quality. On the other hand, Figure 4-1(b) shows an ideal tip geometry with a smooth, steeply angled cone that balances mechanical strength with the small radius required for uniform field evaporation, maximising the chance of a successful, high-quality APT run.

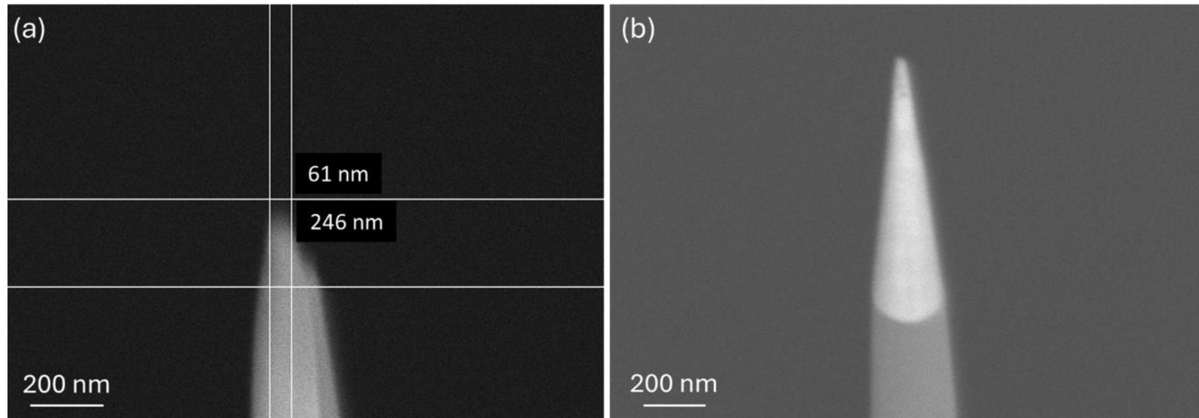

Figure 4-1 SEM images of final polished GaN APT specimens. (a) Sub-optimal specimen: prepared using a relatively high beam current in the final milling step (30 kV, 50 pA). The apex is blunt and asymmetric, very likely to have missed the target layer, increasing the risk of fracture during field evaporation. (b) Optimal specimen: produced using a lower current for the final polishing step (30 kV, 10 pA). The apex is sharp and symmetric with a smooth shank, suitable for stable APT analysis.

Previous studies on III-Nitride semiconductor have shown that the standard 30 kV Ga^+ beam produces an amorphous surface layer thicker than 10 nm, which embeds Ga and disrupts stoichiometry in the heterostructure of III-Nitrides, reducing the fidelity of the mass spectra [210, 215]. Figure 4-2(a) illustrates ion evaporation behaviour during APT within the crystalline tip and the surrounding amorphous layer. Normally, ion evaporation from the crystalline GaN core is relatively controlled, however, the presence of thick amorphous shell surrounding the tip can lead to increased absorption of laser energy and enhanced localised heating, resulting in less controlled evaporation and broader mass spectrum peaks [216]. Beam energy and dose studies on Ga^+, Xe^+ and He^+ ion sources have shown that reducing the accelerating voltage or switching to an inert gas plasma beam can suppress lattice disorder during this process [217-219].

Recent studies show that voltage reduction protocols, from 30 kV to 5 kV to 2 kV, can reduce Ga implantation in GaN/InAlN tips by an order of magnitude and significantly improve the quality of the dataset [210]. Figure 4-2(b) and (c) show high-resolution transmission electron microscopy (TEM) images of GaN APT tips after final FIB cleaning stage at different beam energies. In both cases, a distinct amorphous GaN (α-GaN) layer is observed surrounding the crystalline GaN (c-GaN) core. The tip cleaned at 8 kV (Figure 4-2(b)) shows a ~2.2 nm thick amorphous GaN (α-GaN) layer, while the 1 kV-cleaned tip (Figure 4-2(c)) exhibits a significantly thinner layer of ~1.2 nm. As higher beam energy penetrates deeper into the sample, it creates a thicker amorphous layer and increases subsurface damage. The results suggest that lowering the FIB voltage effectively minimises surface damage, which is critical for achieving controlled ion evaporation and higher mass resolution in APT [220]. Additionally, simulations performed using the Stopping and Range of Ions in Matter (SRIM) code supported the experimental observations reported by Uzuhashi and Ohkubo [221]. The SRIM calculations predict the depth distribution of implanted Ga ions and associated displacement damage, consistent with the experimentally observed amorphous surface layer and underlying crystal distortion region.

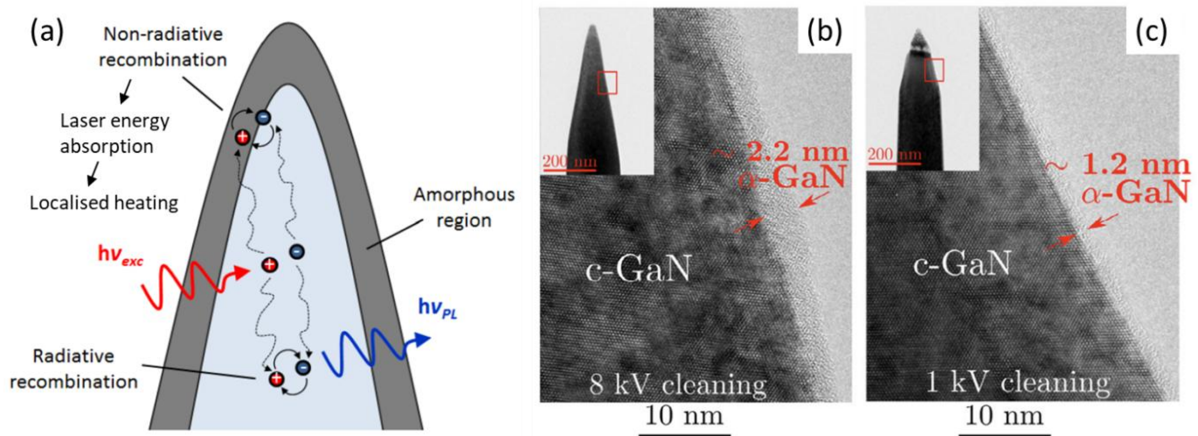

Figure 4-2 (a) Schematic of a GaN APT tip illustrating the impact of the amorphous surface layer on ion evaporation behaviour. The outer amorphous region absorbs more laser energy, enhancing non-radiative processes and leading to localised heating, which contributes to less controlled evaporation. Adapted from Ref. [216] (b) TEM image of a GaN APT tip after final FIB cleaning at 8 kV, showing an ~2.2 nm thick amorphous GaN (α-GaN) layer surrounding the crystalline GaN (c-GaN) core [220]. (c) Reduced amorphous layer thickness (~1.2 nm) observed after 1 kV cleaning, demonstrating the effectiveness of low-energy FIB in minimising surface damage and improving tip quality [220].

However, low beam energy can also lead to a further reduction in the milling rate, which is already low for GaN [219]. Therefore, the parameters and methods should be carefully optimised to achieve a good balance between good sample quality and practical productivity. Typically, annular circular patterns are applied during the initial sharpening steps to efficiently shape the APT tip, as shown in Figure 4-3(a), which require precise alignment between the ion beam and the tip apex. As the diameter of the tip decreases, it sometimes becomes increasingly challenging to maintain the alignment. Therefore, in this work, we introduce a modified solid circular milling pattern for the final cleaning stage (as shown in Figure 4-3(b)), which improves tip stability by reducing sensitivity to misalignment and minimising internal stress-induced fractures.

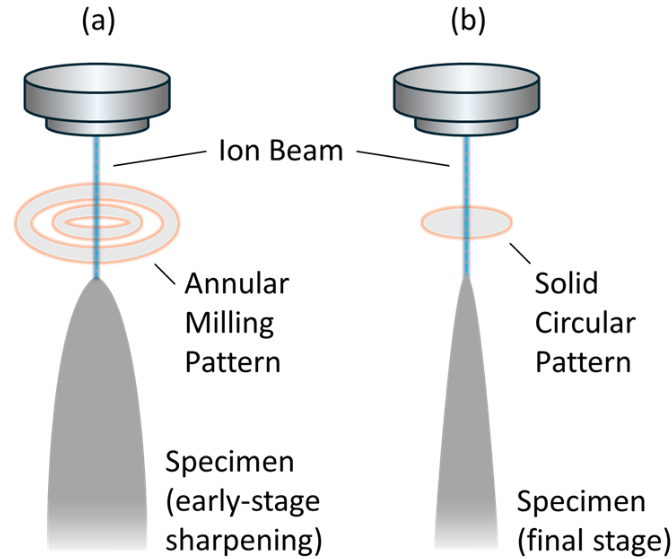

Figure 4-3 Schematic of ion beam pattern strategies during APT tip preparation. (a) Annular patterns are effective for early-stage sharpening but require precise alignment. (b) Solid circular pattern during the final cleaning step offers greater reliability by reducing alignment sensitivity and minimising stress-induced fractures.

After extensive trials and systematic evaluation of different preparation parameters, we established an optimised FIB workflow specifically tailored for GaN APT specimens, where the material's brittleness and hardness require non-standard milling conditions. The optimised procedure, performed using a Zeiss Crossbeam 540 Analytical FIB-SEM, consists of the following steps:

1. Deposition of the protective layer: A layer of Pt (approx. 2 μm × 20 μm) is deposited over the region of interest to shield the surface during milling, using 30 kV and 50 pA for 5 minutes, then switching to 30 kV and 100 pA.
2. Wedge trenching: A triangular cross-section wedge is milled around and beneath the Pt layer on three faces using a voltage of 30 kV and beam currents of 1.5 nA and 300 pA. The current of 300 pA was used specifically for undercutting near the protective layer.
3. Lift-out: The *in-situ* micromanipulator contacts one side of the wedge, maintaining a small

gap. Pt is deposited at the junction (30 kV, 50 pA) to secure the lift-out, which is then cut from the other side (30 kV, 300 pA).

4. Mounting: Segments approximately 1.5–2 μm wide is mounted onto standard Si microtip arrays (Cameca Instruments) and separate from the main wedge using 30 kV and 300 pA.
5. Initial needle shaping: Each segment is milled into a needle using a sequential annular pattern. Shaping began with 30 kV, 300 pA to reduce the tip diameter to ~1 μm.
6. Progressive sharpening: The beam parameters are then reduced to 30 kV, 100 pA to sharpen the tip diameter to 200-300 nm, and finally to 30 kV, 10 pA to create a sub-80 nm tip.
7. Low-energy clean-up: To minimise ion beam damage, a final treatment with a solid circular pattern at 2 kV and 10 pA was applied in the last stage of sharpening.

4.2.2. Layer-Targeted Positioning by Correlative SEM-EDX and FIB

For layered materials, such as the InGaN/GaN quantum well (QW) samples in this thesis, the preparation protocol should be carefully balanced to obtain a sufficiently sharp apex and to ensure that the target layer is included in the initial stages of the APT analysis. As mentioned earlier, over-milling increases the risk of target layer loss and tip failure. Conversely, insufficient sharpening can lead to suboptimal tip shape, which reduces data quality and experimental success rate.

To accurately target specific layers within a multilayered sample during APT specimen preparation, scanning electron microscopy–energy dispersive X-ray spectroscopy (SEM-EDX) was used to map the elemental distribution within the tip. Figure 4-4 shows an SEM image (a)

of a partially milled needle specimen and corresponding EDX elemental maps for Pt (b), Ga (c), and Si (d). The Pt cap is clearly visible at the top of the tip, deposited to protect the region of interest during the milling process. Beneath it, a Ga-rich layer is distinctly resolved in panel (c), allowing the target region to be visually and chemically tracked during annular milling. The Si signal (d) identifies the underlying support and substrate, providing a useful depth reference. Therefore, with the assistance of SEM-EDX, the height of the needle can be controlled during preparation. Milling can be stopped when the Pt signal remained approximately 100 nm below the tip surface, ensuring that the Ga-rich layer of interest would be captured within the initial reconstruction. A final low-energy polish at 2 kV, 10 pA removes the last 80-100 nm of material, simultaneously thinning the Pt cap and positioning the GaN layer within the optimal analysis zone.

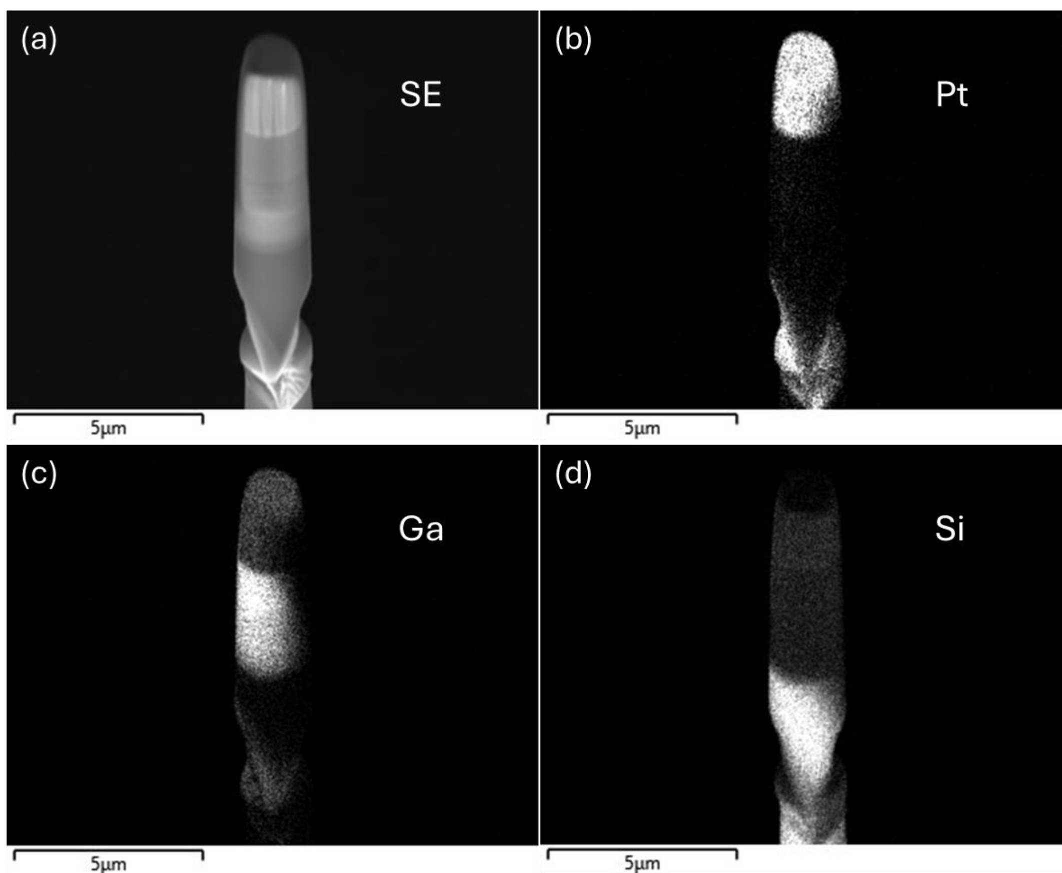

Figure 4-4 (a) Secondary-electron (SE) overview of a partially milled tip; (b) Pt $M\alpha_1$ map,

showing the ion-beam-deposited protective cap at the apex and the Pt weld at the base; (c) Ga $L\alpha_{1,2}$ map, highlighting the Ga-rich layer as a bright band beneath the Pt cap; (d) Si $K\alpha_1$ map, locating the Si micro-pillar support. Images were acquired on a Zeiss Crossbeam 540 dual-beam FIB-SEM equipped with the Oxford Instruments $XMax^N$ 150 EDX detector.

4.2.3. Accurate Height and Diameter Control

Distinguishing individual layers during the final milling stage can be challenging as the layers of interest in this thesis are typically very thin. For example, a SQW layer is only 2 nm thick. This can be challenging to track due to the limited sensitivity and spatial resolution of EDX on a fully milled tip. In order to address this issue, several methods were employed in this study.

Firstly, markers are used to ensure accurate targeting and controlled thinning of the region of interest. As illustrated in the Figure 4-5, the use of a height marker helps to track vertical position changes throughout the annular milling process, which can otherwise shift subtly as the tip becomes thinner. This is helpful when the sample contains nanometre-scale heterostructures, such as MQWs, and both height and diameter need to be precisely controlled during the sharpening process. Otherwise, there is a high risk of over-milling or misalignment, leading to the loss of target features. The final image (Figure 4-5(d)) confirms the successful inclusion of a GaN region longer than 570 nm (626.6 nm), ensuring MQWs are retained. Thus, the consistent use of height markers improves reproducibility, spatial precision, and the overall success rate of APT sample fabrication.

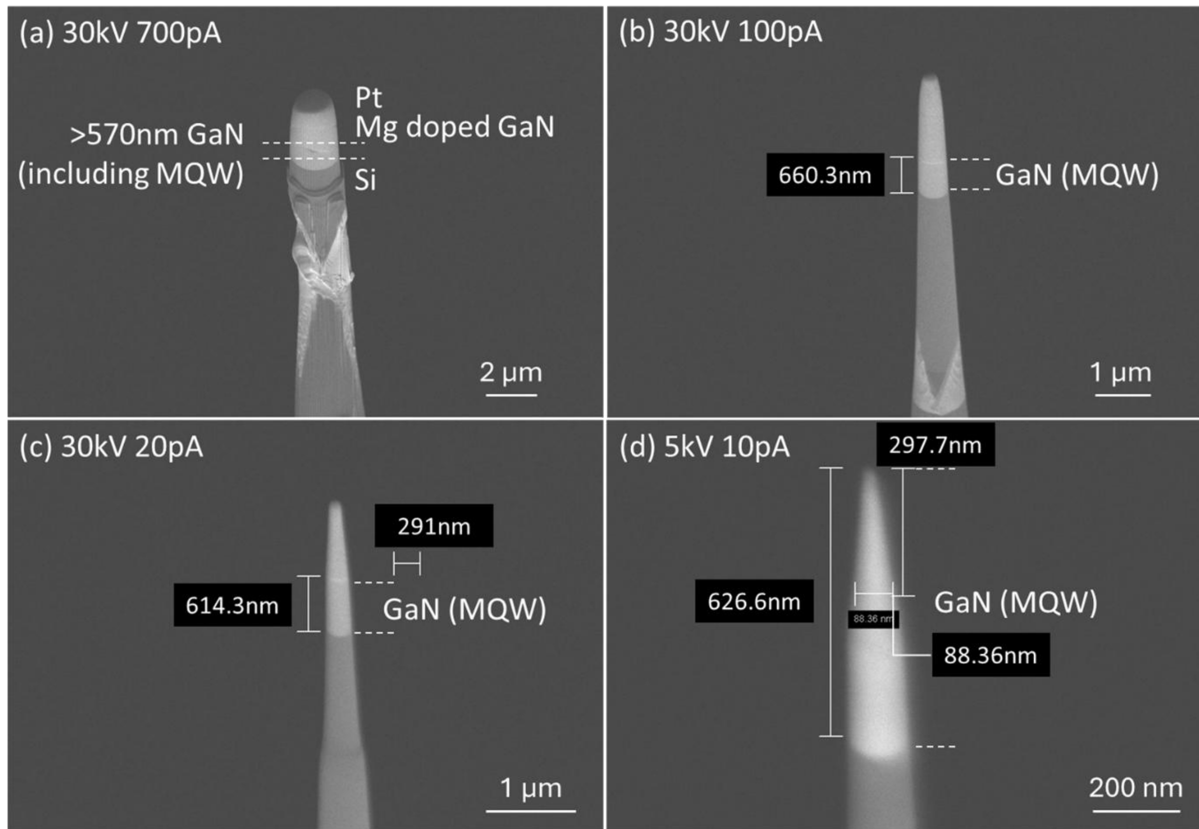

Figure 4-5 Progressive annular milling of a GaN-based APT tip targeting a MQW region using different FIB conditions. (a) Initial coarse shaping at 30 kV, 700 pA. A distinct line appears between the Si layer and the GaN layer (b) Intermediate refinement at 30 kV, 100 pA maintains the GaN segment with MQWs. (c) Further thinning at 30 kV, 20 pA reduces the apex diameter while preserving over 600 nm of GaN. (d) Final polishing at 5 kV, 10 pA.

Another way to precisely control the sharpening process and reach a thin target layer is to apply an additional layer, such as Cr, before the Pt protective layer is applied. As mentioned earlier, EDX spectra are usually obtained at an intermediate stage, when the tip was partially shaped but still sufficiently wide to establish a reliable compositional contrast, and the depth of the target layer can be labelled. However, since the measured relative height of the target layer may vary slightly as the diameter decreases, it is challenging to confidently produce APT samples that retain the layer of interest. In particular, it can be challenging to track it when the target layer is close to the surface and very thin, such as the 2 nm thick SQW GaN in this study, which

is sandwiched between different doped and undoped layers of GaN and is less than 10 nm from the sample surface.

To address this, a layer of Cr (about 20 nm) was applied to the sample surface prior to the Pt protective layer. This layer not only enhances visibility of the target layer in SEM, making it easier to monitor during sharpening, but also serves as a stabilising intermediary layer that reduces stress and enhances tip stability during an APT experiment. Furthermore, it also enables tracking of target layer during the running and data analysis. As shown in the SEM image in Figure 4-6(a), the position of SQW layer is clearly visible with the help of a Cr layer during the early stages of annular milling. The contrast lines can serve as consistent internal references during the process. The vertical distance between the SQW layer and the contrast line was measured (~693 nm in this case), which can be used as a reliable depth marker for later stages. During the final sharpening stage, as shown in Figure 4-6(b), the SQW layer becomes increasingly challenging to distinguish due to reduced image contrast at smaller tip diameters. However, the lower contrast line remains visible, allowing the previously measured spacing to guide the milling process. By aligning the height marker at the same relative depth as this contrast line, it is possible to ensure with confidence that the SQW layer remains positioned within the apex of the finished needle, and, consequently, will be incorporated into the APT analysis volume. It should be noted that, at this final annular milling stage (Figure 4-6(b)), the marker distance from the contrast line to needle apex is increased to ~766 nm, which is slightly greater than the previously measured value of 693 nm. This minimises the risk of inadvertently milling away the SQW layer in the final cleaning stage, offering a reliable

way of estimating its position even when minor dimensional changes occur during the process. Thus, this approach increases the confidence and reliability of capturing the target layer within the APT analysis volume.

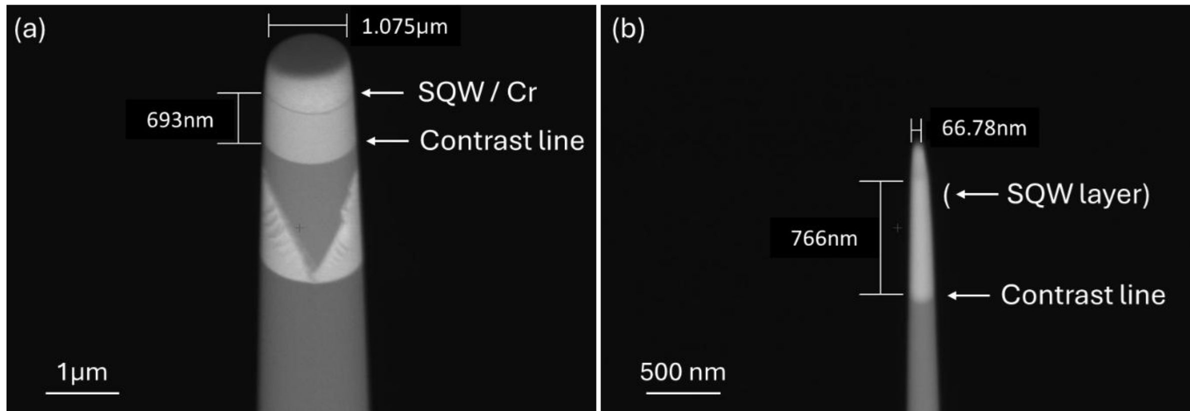

Figure 4-6 (a) SEM image for the SQW sample at the early annular milling stage, showing the target SQW layer (marked by Cr layer) located about 693 nm above the reference contrast line (b) SEM image for the SQW sample at final annular milling stage (prior to the final 2 kV polish), with the apex diameter reduced to around 66 nm. The remaining distance from the apex to the target layer ensures that the SQW is included within the first few million ions detected during the APT experiment.

4.3. Protocol for Reproducible GaN APT Acquisition

4.3.1. APT Parameter Effect on GaN

To establish a framework for optimising reproducible APT analysis of GaN, this section summarises key experimental parameters identified in previous studies that influence field-dependent evaporation behaviour. These insights provided the rationale for the experimental design adopted in this work.

GaN is highly sensitive to the experimental conditions used in APT, and accurate determination of its composition is a persistent challenge. Key parameters such as laser energy and laser frequency should be carefully identified and optimised for GaN, as they govern the balance

between ionic and neutral evaporation. Achieving stoichiometric evaporation (Ga/N ≈ 1) typically requires relatively high effective fields, whereas at lower fields, nitrogen ions tend to recombine on the tip surface to form neutral N_2 molecules, which cannot be detected [158, 211]. Even minor adjustments to the experimental settings can significantly change the apex field and shift the balance between ionic and neutral evaporation.

Several studies have systematically investigated this field dependence. Riley *et al.* demonstrated that lowering the specimen temperature to about 37 K and increasing the pulse frequency from 250 to 750 kHz, together with careful adjustment of DC voltage and laser pulse energy, significantly reduced uncorrelated N_2 evaporation, leading to improved stoichiometric accuracy [155]. Diercks *et al.* extended this study to c-axis GaN nanowires and found that tuning the 355 nm laser energy from 0.002 to 10 pJ lowered the effective field and shifted the apparent Ga/N ratio, confirming that apex field strength strongly influences compositional accuracy [156]. Similarly, Di Russo *et al.* reported that raising the UV-laser energy reduced the effective field and reversed the measured composition from a Ga deficiency at high field to an N deficiency at low field [158]. Morris *et al.* further observed that the nitrogen deficit is most pronounced at low fields, indicating that multi-hit events are not the primary cause of the field-dependent nitrogen underestimation in GaN [222].

Collectively, these studies demonstrate that accurate control of the apex field is essential for minimising apparent nitrogen loss during GaN APT analysis. Figure 4-7 (adapted from Mancini

et al. [151]) illustrates this field dependence, showing stoichiometric evaporation near a Ga^{2+}/Ga^{+} charge-state ratio of approximately 0.1 (corresponding to an effective field of ~24.3 V/nm). This reference framework was used to define suitable experimental field conditions for the optimisation experiments conducted in this study.

Based on these insights, in this work, we first performed systematic optimisation experiments to determine suitable APT acquisition conditions on a LEAP 5000 XS for GaN-based materials. Although the primary focus of this thesis is on zincblende structured GaN heterostructures, bulk wurtzite (pure-phase) GaN was selected for this initial calibration. While the crystal structures are different, the key evaporation behaviour as monitored via charge-state ratios (e.g., Ga^{2+}/Ga^{+}) is primarily governed by the local surface field and ionisation energy. Therefore, it is expected to follow the same Kingham post-ionisation trends regardless of crystal phase. The wurtzite samples were compositionally uniform and readily available, making them ideal for controlled parameter studies (further background on this material is provided in Appendix A).

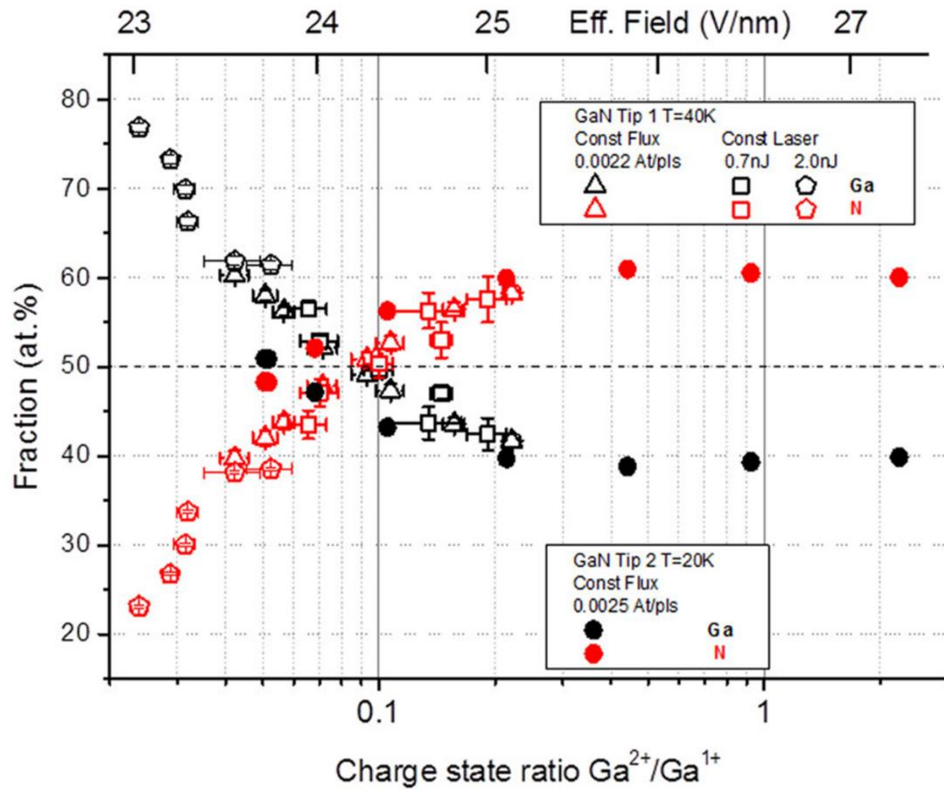

Figure 4-7 Atomic fractions of Ga (black) and N (red) in bulk GaN as a function of Ga^{2+}/Ga^{+} charge state ratio (CSR, an indicator of the surface electric field). Stoichiometric evaporation occurs near $Ga^{2+}/Ga^{+} \approx 0.1$ (~24.3 V/nm). Data from two tips under different conditions show consistent field dependence. Adapted from [151].

4.3.2. APT Results

In this section, we examine the effects of laser energy, detection rate and pulse frequency on the measured stoichiometry, with the dual aim of validating the trends reported in existing papers and tailoring them to the materials studied in this thesis. To minimise variability due to tip orientation and geometry [151, 158], all parameter sweeps were conducted on the same specimen wherever possible. The same experimental protocols were then repeated on several nominally identical GaN tips to verify reproducibility. These optimised conditions were then applied to the layered structures analysed in the subsequent chapters. The operating parameters for each acquisition are summarised in Table 4-1.

Table 4-1 Operating conditions for bulk GaN analyses

Analysis	**Stage Temperature (K)**	**Pulse Frequency (kHz)**	**Detection Rate (%)**	**Laser Energy (pJ)**
Temperature	40, 50, 60, 70	250	1	0.015, 0.05, 0.1, 0.12
Laser Energy	50	250	1	0.005 - 10
Pulse Frequency	50	200, 250, 500	1	0.015, 0.07, 0.15, 0.5, 1, 10
Detection Rate	50	250	1,2,3	0.1, 0.5, 1, 10

A representative acquisition history from the parameter-testing experiments is shown in Figure 4-8. In these tests, detection rate, laser pulse energy, and pulse frequency, were systematically varied to investigate their combined influence on the measured Ga/N ratio. A non-sequential order of energy settings (e.g., 20 fJ → 60 fJ → 40 fJ → 80 fJ) was deliberately employed to avoid potential systematic errors associated with time-dependent effects such as tip evolution or thermal drift. Details of the experimental conditions and original dataset corresponding to all figures presented in this section are provided in Appendix B.

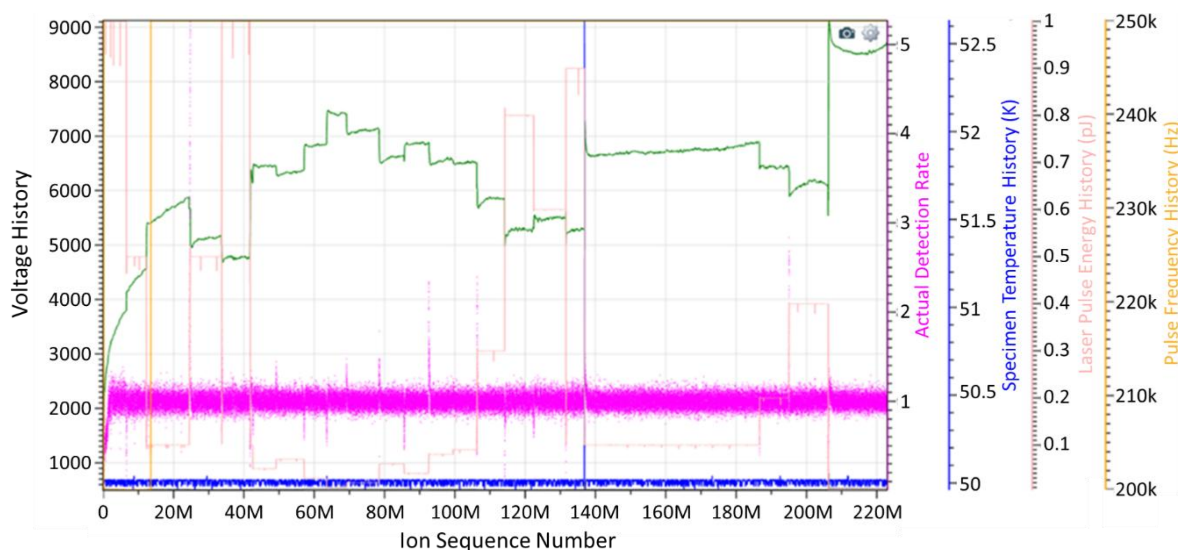

Figure 4-8 Acquisition history showing voltage (green), actual detection rate (bright pink), temperature (blue), laser energy (pale pink), and pulse frequency (orange) during parameter sweeps on a single GaN tip. Laser energy was varied in a non-sequential order to minimise systematic bias.

4.3.2.1. Base Temperature

The measured Ga/N atomic ratio as a function of laser energy at four different temperatures (40K, 50K, 60K, 70K) is shown in Figure 4-9. For all temperatures, the Ga/N ratio increases with laser energy, though the extent of the increase varies depending on the temperature. The most pronounced increase is observed at 40 K, where the Ga/N ratio reaches a maximum of approximately 5.0 at 100 fJ, before slightly decreasing at 120 fJ. A similar but slightly less steep trend is observed at 60 K and 70 K, with the slope of 70 K rising more gradually across the full energy range. In contrast, the 50 K dataset exhibits a relatively flat trend from 40 to 100 pJ, followed by a moderate increase at 120 pJ. The broader error bar at 100 pJ arises from the inclusion of multiple independent measurements performed under identical conditions, rather than from increased experimental uncertainty. This reproducibility test confirms that the small variation observed is within normal statistical limits. Overall, the results indicate a consistent positive correlation between laser energy and Ga/N ratio at all temperatures tested.

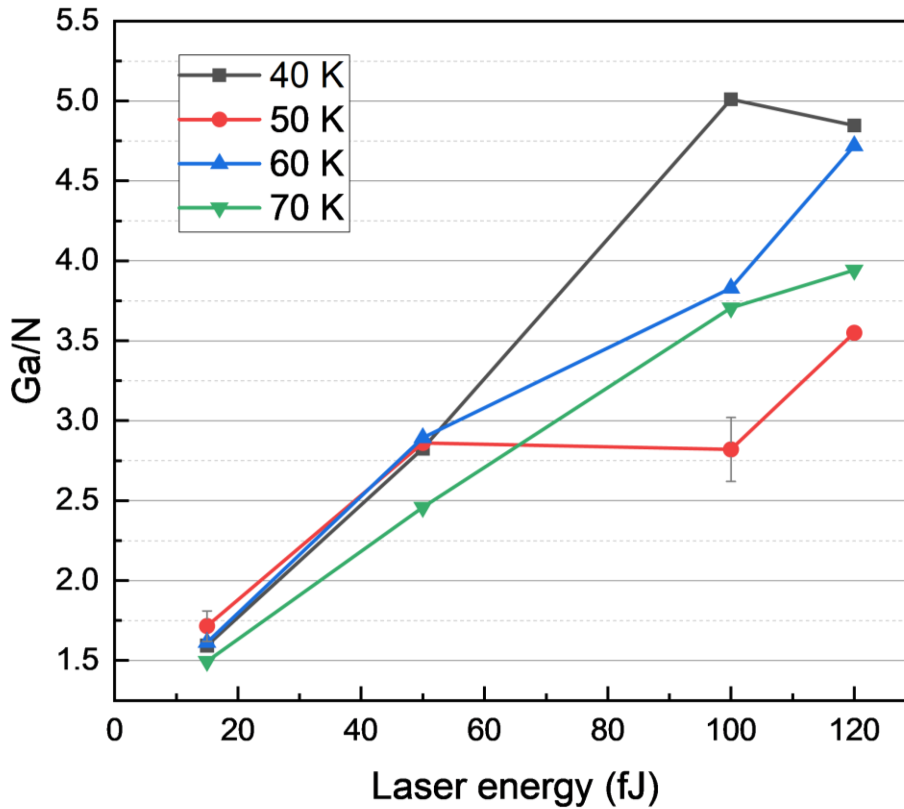

Figure 4-9 Measured Ga/N ratio as a function of laser pulse energy for four temperatures (40, 50, 60, and 70 K), with a pulse frequency of 250 kHz and detection rate at 1%. Multiple datasets were acquired at 50 K and 100 pJ to assess reproducibility, leading to the larger error bar shown.

4.3.2.2. Laser Energy

Figure 4-10 shows the measured concentrations of Ga and N as a function of laser pulse energy. As laser energy increases, the measured N concentration decreases while the Ga concentration increases correspondingly. At low laser energies (<30 fJ), the Ga and N concentrations are close to their nominal stoichiometric values (≈50 at.% each). As the laser energy increases, the N concentration steadily decreases from about 48 at.% to below 10 at.% at approximately 600 fJ, and approaches zero above 1 nJ, with a complementary increase in Ga concentration.

This trend indicates that excessive laser energy enhances thermal effects at the specimen apex, promoting neutralisation and loss of N_2 molecules, thereby causing apparent nitrogen depletion.

In this work, however, compositional fidelity was not the primary objective; instead, the emphasis was placed on achieving stable and reproducible data acquisition. A laser energy of 10 pJ was therefore selected as it provided reliable specimen stability with minimal tip fracture during APT runs.

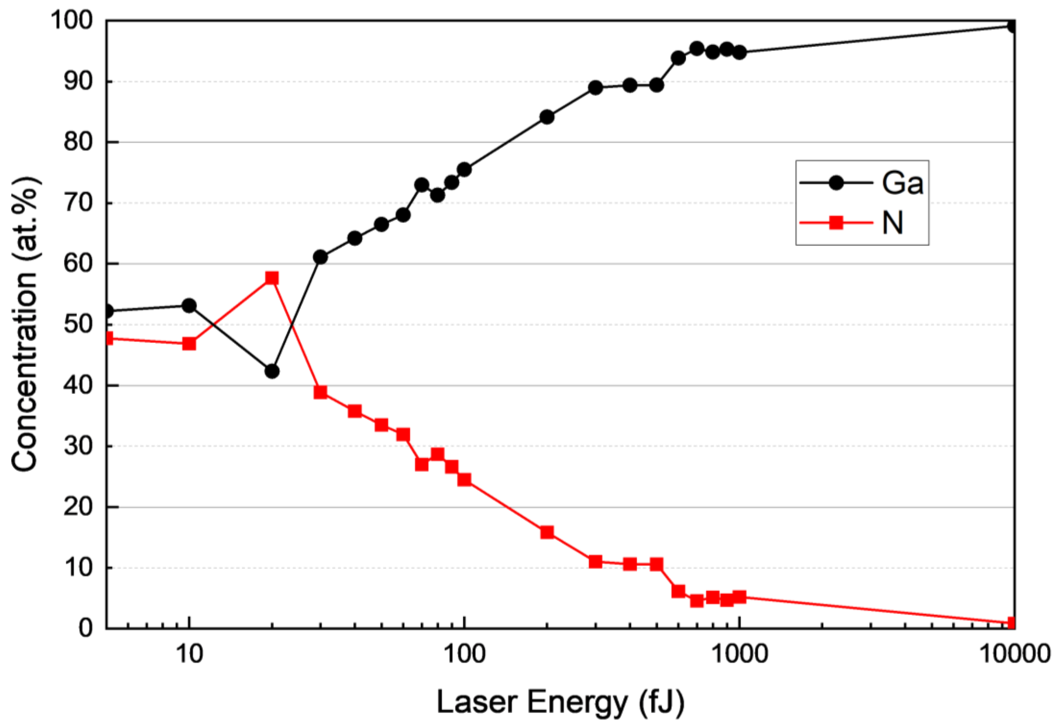

Figure 4-10 Measured concentrations of Ga and N as a function of laser pulse energy, with the base temperature at 50 K, pulse frequency at 250 kHz and detection rate at 1%.

4.3.2.3. Pulse Frequency

The effect of laser pulse frequency on the measured Ga/N ratio is shown in Figure 4-11. The left panel, Figure 4-11(a), is a zoomed-in view of the Ga/N ratio trend over a lower laser energy range (from 15 to 100 fJ). It can be seen that, at both 250 kHz and 500 kHz, the Ga/N ratio shows an upward trend as the laser pulse energy increases, although at 500 kHz it exhibits a slightly steeper rise. Figure 4-11(b) extends the energy range (from 15 fJ to 10 pJ) and includes the result of 200 kHz at 0.5 pJ and 1 pJ. Across the full range, the Ga/N ratio increases at all pulse frequencies with laser energy, but the extent of deviation from stoichiometry strongly

dependent on the frequency. The highest Ga/N ratios are observed at 250 kHz and 10 pJ, followed by 500 kHz and 10 pJ, and the 200 kHz condition shows the least deviation in the figure. In addition, the separation between different frequencies becomes increasingly pronounced at higher laser energies.

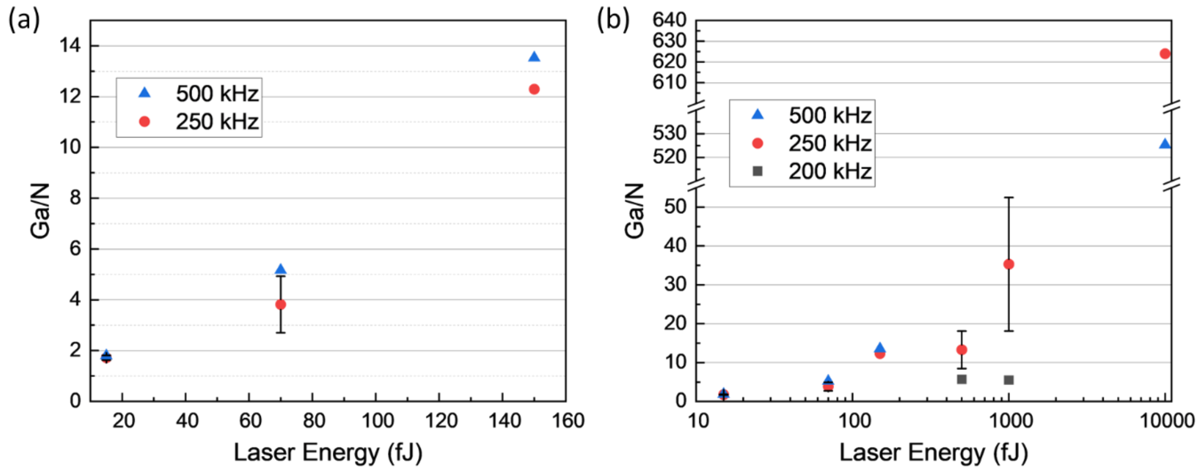

Figure 4-11 Effect of laser pulse frequency on measured composition ratio (Ga/N). (a) Ga/N ratio as a function of laser pulse energy at laser frequencies of 250 and 500 kHz, as a zoomed-in section of (b), highlighting the deviations from stoichiometry at low laser energies. (b) Ga/N ratio as a function of laser pulse energy at laser frequencies of 200, 250, and 500 kHz and over a wide range of laser energies (from 0.015 to 10 pJ).

Figure 4-12 shows the background noise as a function of laser pulse energy at 250 kHz and 500 kHz conditions. For both frequencies, the background noise levels decrease with increasing energy. Across the full measured range, the 500 kHz condition consistently shows higher noise than that of 250 kHz, and the gap becomes narrower at higher energies where both converge to about 10 units. Although higher frequencies are generally expected to reduce background noise due to improved signal statistics, the opposite trend observed here suggests additional physical effects are involved. At 500 kHz, the shorter pulse interval (about 2 μs) allows less time for the tip to cool between laser pulses, resulting in cumulative thermal loading and local temperature fluctuations. This can increase the probability of random field-evaporation events, thereby

increasing the background count rate. These combined effects could reasonably account for the elevated noise levels observed under the 500 kHz condition.

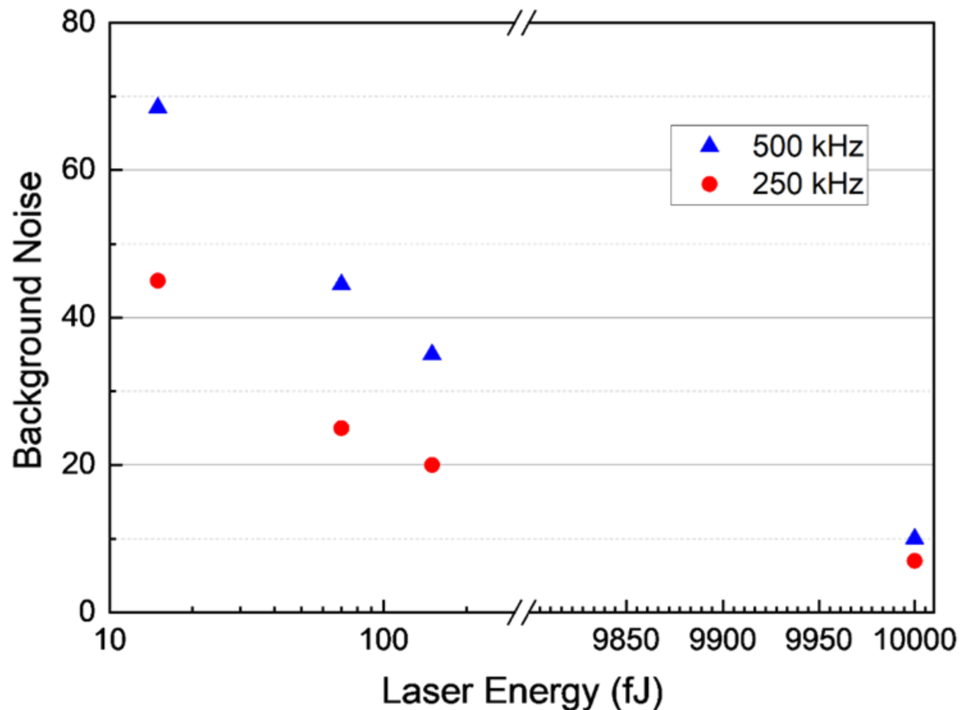

Figure 4-12 Background noise versus laser pulse energy at 250 kHz and 500 kHz.

4.3.2.4. Detection Rate

Figure 4-13 shows the measured Ga/N atomic ratio as a function of laser pulse energy at three detection rates (1%, 2%, and 3%). In all cases, the Ga/N ratio increases with increasing laser energy, consistent with the behaviour observed for other parameters. At the lowest energy (~100 fJ), all detection rates give similar Ga/N values, whereas at higher energies the 1% dataset shows the steepest increase.

The relatively large error bar at 1 pJ arises from multiple measurements performed on different specimens, rather than random noise. The apparent reversal in the order of the 1% and 3% datasets between 1 pJ and 10 pJ likely reflects the limited number of measurements at 3%

detection rate (only two runs), rather than a genuine trend. Overall, the results suggest that detection rate effects become more evident only when the laser energy is sufficiently high.

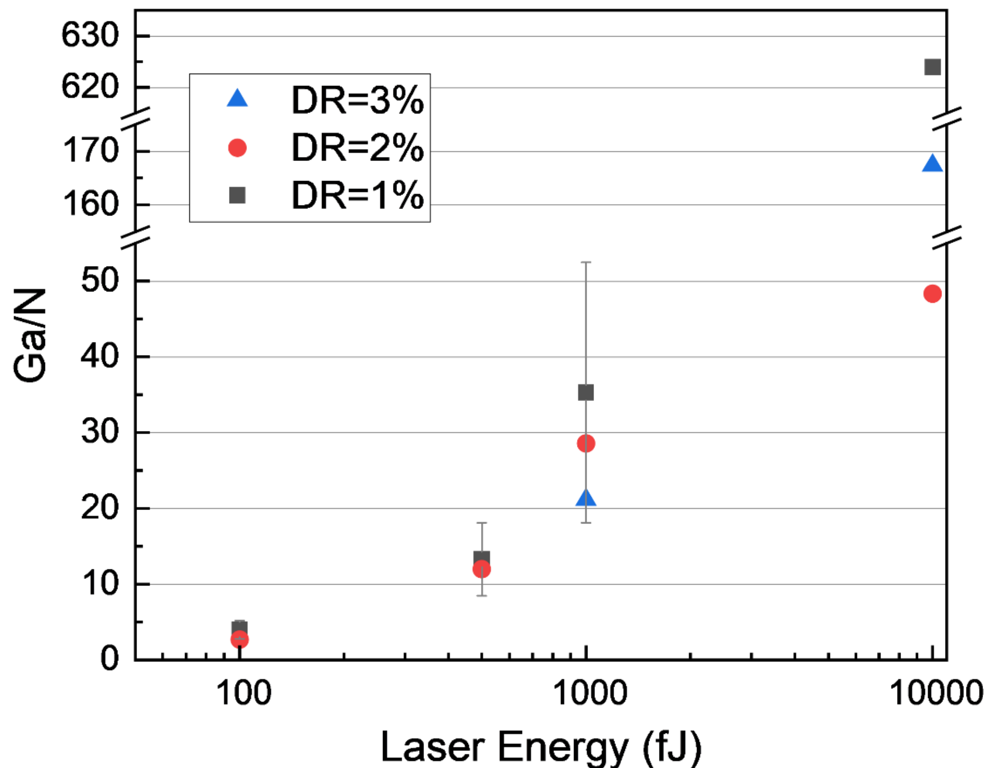

Figure 4-13 Measured Ga/N ratio as a function of laser pulse energy at three detection rates (1%, 2%, and 3%). The large error bar at 1 pJ corresponds to multiple measurements on different specimens, while the DR = 3% dataset includes only two runs.

4.3.3. Discussion

4.3.3.1. Base Temperature

In APT analysis, the base (stage) temperature can influence both specimen stability and the extent of laser-induced heating during field evaporation [184, 223]. As mentioned, Ga and N have different evaporation thresholds, therefore, changes in temperature can affect the effective evaporation field and thus also influence the relative evaporation behaviour of the two primary elements in GaN. Figure 4-9 assesses this influence with four base temperatures (40, 50, 60, and 70 K) over a range of laser pulse energies. In general, Ga/N increases with increasing pulse

energy at all base temperatures, while the ratios stay close for each different temperature, suggesting that laser energy, rather than base temperature, is the primary factor controlling the stoichiometry during analysis. The effect of temperature is most pronounced at 40 K, with the highest ratio observed at the lowest temperature (40 K, 100fJ); while the increase is much moderate at all higher temperatures examined.

This phenomenon can be explained by the combined thermal and electronic responses of the GaN tip under laser-mode APT. At lower base temperatures, the tip generally exhibits improved mechanical stability, as indicated by fewer premature fractures and more consistent data acquisition. Although lower temperatures can increase material brittleness, the suppression of thermal stress and slower tip evolution during APT runs appear to enhance overall stability. However, at very low temperatures (below ~115 K), longer carrier lifetimes may enhance nitrogen loss through hole-assisted desorption, as reported by Diercks *et al.* [224], leading to a further increase in the measured Ga/N ratio. Based on these observations, a base temperature of 50 K was selected for all subsequent experiments, as it provides a practical balance between stable acquisition and reliable field evaporation without compromising tip integrity. This choice is consistent with previous studies on GaN-based and related materials [211, 225], where similar temperatures have been found to support reproducible APT analysis.

4.3.3.2. Laser Energy

The results in Figure 4-10 show that as the laser pulse energy increases, the measured Ga atom concentration shows a continuous upward trend, while the N atom concentration shows an

opposite trend. The change in Ga and N fractions indicates that the enrichment in Ga is driven by progressive under-detection of nitrogen. At higher laser energies, the accumulated energy from repeated pulses leads to a local temperature rise at the specimen apex. This enhances evaporation and increases the tip's sensitivity to laser heating, which can gradually amplify nitrogen loss during field evaporation [226]. High laser energy lowers the effective field at the tip, promoting the recombination and neutral desorption of N_2, which has been widely reported in GaN APT studies in temperature sweep experiments [137, 155, 158, 227].

The experimental parameters of temperature and laser energy affect the applied apex electric field, promoting or suppressing the formation of undetected neutral N_2 molecules. To quantitatively estimate the field strength at the emitter during a run and thus more reliably interpret the results, the Kingham post-ionisation model can be applied to the analysis using the Ga^{2+}/Ga^{+} CSR [153, 228]. According to Kingham's post-ionisation theory, the CSR is strongly dependent on the applied local field strength and can be mapped to an absolute field value using empirically calibrated curves. Although Kingham's model can be inaccurate for certain oxides and highly covalent materials such as Fe_3O_4 or Si [229], it has been shown to work reliably for metallic and semiconductor systems, including GaN [152, 158].

Figure 4-14 shows the Ga^{2+}/Ga^{+} charge-state ratio and the corresponding apex electric field as a function of laser energy. The fields were calculated based on Kingham's post-ionisation theory [153] using a Matlab programme package, AtomProbeLab v0.2.2. As can be seen in Figure 4-14, with an increase of laser energy, the Ga^{2+}/Ga^{+} ratio drops sharply along with a

reduction in the corresponding field strength at the tip apex. When the laser energy exceeds 600 fJ, the ratio approaches zero (i.e. very few Ga^{2+} ions generated) and remains relatively stable, meanwhile, the corresponding electric field also stabilises around 19.3 V/nm. This corresponds to the increased nitrogen loss observed at higher laser energies in Figure 4-10, which helps to explain the earlier observed compositional trends.

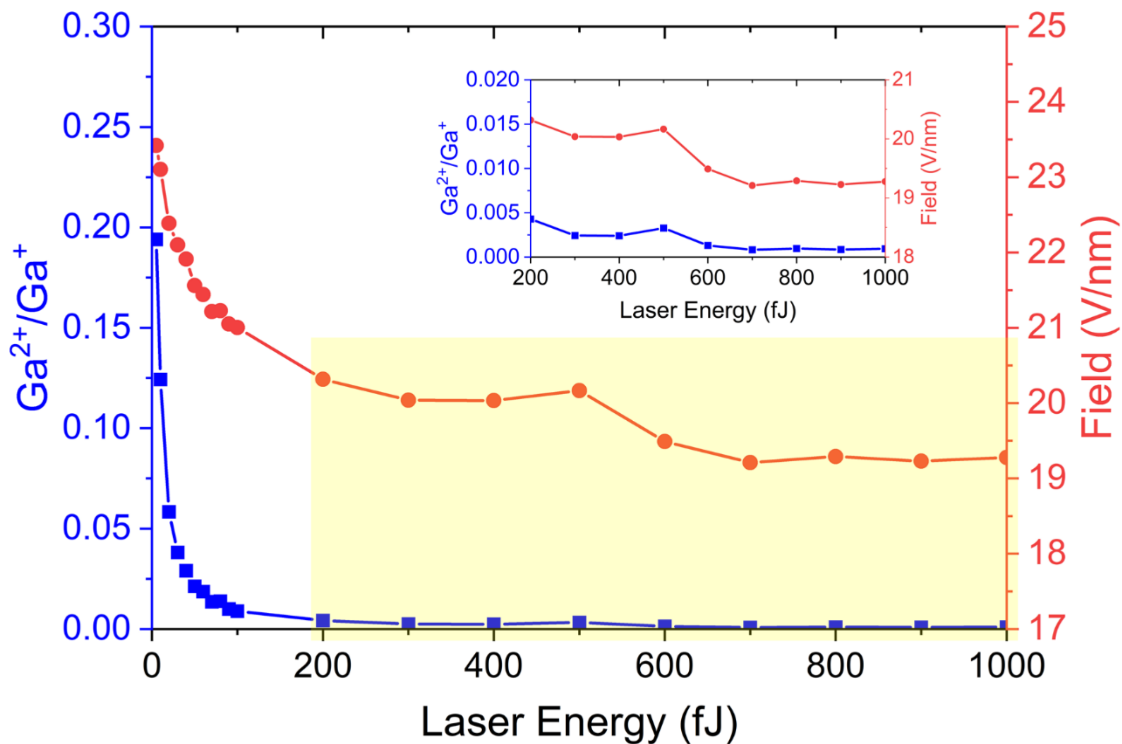

Figure 4-14 Ratio of Ga^{2+}/Ga^{+} (blue, left axis) and electric field (red, right axis) as a function of laser energy. The inset shows a zoomed-in view of the laser energy range from 200 to 1000 fJ (highlighted in the yellow shaded region).

Since some element behaviours and their corresponding concentrations are highly sensitive to changes in field, such as N, the use of Kingham Curves can be a more stable reference for comparing experiments conducted under different laser conditions. Therefore, in the following chapters of this thesis, this approach based on Kingham Curve is employed to evaluate evaporation conditions and interpret the data accurately and reliably.

4.3.3.3. Pulse Frequency

The compositional results also showed dependence on pulse frequency according to Figure 4-11 and Figure 4-12, where the results show the impact of laser pulse frequency on both the measured Ga/N atomic ratio and background noise levels across a range of laser energies.

In the lower energy regime (< 200 fJ), left panel of Figure 4-11, the Ga/N ratio increases more steeply at higher pulse frequency (500 kHz), indicating enhanced nitrogen loss which is attributed to cumulative thermal effects; higher repetition rates reduce the thermal recovery time between laser pulses, in turn resulting in lower effective fields at the specimen apex for the same (fixed) evaporation rate. When the specimen apex remains at an elevated temperature, the effective field required for ion evaporation is reduced, which promotes the formation of neutral N_2 molecules through recombination and thus enhances the apparent nitrogen loss. This cumulative thermal effect is more pronounced at higher pulse frequencies where the tip has insufficient time to cool between pulses. However, at higher laser energies, as shown in the right panel of Figure 4-11, this trend is partially reversed, where the 250 kHz curve surpasses 500 kHz at 10 pJ, indicating a higher Ga/N ratio at intermediate frequencies. This suggest that the interaction between laser energy and pulse frequency may be nonlinear. However, it is also important to note that the available dataset at high energies in this section is limited. Therefore, the apparent crossover in Ga/N ratio between 250 kHz and 500 kHz at high laser energies may be also influenced by statistical variability, specimen-to-specimen differences, or small variations in tip geometry. It should be noted that all specimens were prepared using identical FIB milling parameters, ensuring consistent processing conditions. However, due to the

nanometric scale of the tips, small variations in apex geometry are unavoidable. These minor differences, combined with the inherent statistical variability of APT data, may contribute to the observed scatter.

Nevertheless, the overall trend indicates that the Ga/N ratio variation mainly reflects the coupled influence of laser energy and pulse frequency rather than specimen-to-specimen differences. The same cumulative thermal effect is also reflected in the background noise behaviour shown in Figure 4-12, where higher pulse frequencies (500 kHz) lead to incomplete thermal recovery between successive laser pulses. This results in residual heat accumulation at the specimen apex, producing delayed evaporation events and a broader ion energy distribution, which appear as thermal tails and elevated background noise between mass peaks [184, 230]. At higher laser energies, this effect becomes less significant, and the background noise level decreases for both frequencies, indicating improved thermal stability of the tip.

Based on these observations, 500 kHz was chosen for subsequent experiments, as it provides a high data-acquisition rate without introducing significant thermal artefacts at the chosen laser energy of 10 pJ. Additionally, the successful dataset acquisition yield was observed to be higher at 500 kHz. Although this trend contrasts with the conventional expectation that higher pulse frequencies increase specimen stress and reduce yield, the relatively low laser energy used in this study likely mitigated excessive heating, enabling stable and continuous evaporation without tip fracture.

4.3.3.4. Detection Rate

The Ga/N ratio increased with laser pulse energy across all detection rates, with the deviation from stoichiometry becoming more evident at higher energies, as shown in Figure 4-13. At low laser energies (≤ 200 fJ), all detection rates yield Ga/N ratios close to stoichiometry, indicating that laser-induced effects are minimal and that evaporation is primarily field-driven. As the laser energy increases, however, differences between detection rates become more pronounced, with lower detection rates showing higher Ga/N ratios.

This behaviour can be explained by the balance between field- and laser-driven evaporation. For a fixed laser pulse energy, lowering the detection rate reduces the standing DC voltage required to sustain the target ion flux, thereby decreasing the effective field at the specimen apex. Under these conditions, evaporation becomes increasingly laser-assisted, and nitrogen is more likely to recombine and desorb as neutral N_2, leading to an apparent enrichment of Ga. It should be noted that Ga and N exhibit different evaporation field thresholds, with Ga requiring a comparatively lower field for field evaporation than N. Consequently, when the effective field decreases, nitrogen atoms are less likely to ionise and more likely to escape as neutral species, whereas Ga continues to evaporate, further amplifying the apparent compositional shift. In contrast, higher detection rates are maintained by stronger DC fields, promoting field-driven evaporation and yielding compositions closer to stoichiometry.

It should also be noted that the differences between detection rates are relatively small at laser energies below 1000 fJ, within the experimental scatter of the dataset. At higher energies, the

observed deviation likely reflects the combined influence of the laser–field interaction and the limited number of data points available under these conditions.

Based on these observations, a detection rate of 0.5% was selected for subsequent experiments. Although slightly lower than the tested values, this rate provided a balance between stable data acquisition, reduced thermal effects, and reduced risk of tip fracture in the layered samples, ensuring consistent and reliable measurements.

4.3.4. Optimised Parameters for Stable Running on layered InGaN/GaN

The pure GaN binary system in this chapter shows the influence of experimental conditions on the results. It is worth emphasising that the direct quantification of overall composition in Group III-V materials presents challenges, primarily stemming from potential biases related to variances in the evaporation fields of distinct elements. The inaccuracy in N concentration can lead to distorted measurements of the concentrations of the group III elements such as In. Previous studies have demonstrated that while there is a bias in the measurement of III:N ratios in this material using APT, there is no observable bias in the measurement of site fractions of the Group III elements, e.g. In/(In+Ga), in InGaN QWs with random alloy distributions [151, 231]. However, a more recent work by Di Russo *et al.* [232] has suggested that even the Group III site fraction in InGaN may exhibit a weak dependence on the surface electric field, which is likely due to preferential Ga evaporation under high-field conditions. In the context of our study, where all structures were analysed under consistent experimental parameters, the Group III site fraction remains a reliable measure for assessing local compositional variations. To enhance the precision of the analysis regarding the compositional variations in Group III

elements, the Group III site fraction is employed wherever possible to minimise the bias introduced by local changes in the electric field.

Based on the systematic parameter studies presented above and the successful rate of practical layered samples in this study, it was determined that a base temperature of 50 K, a laser pulse energy of 10 pJ, a pulse frequency of 500 kHz, and a detection rate of 0.5% are the optimal parameters. These conditions provided consistent results with minimal composition distortion and reliable data acquisition, particularly suited for the more fragile layered GaN-based structures examined in later chapters.

4.4. Conclusion

In this chapter, a complete experimental framework was established for reliable APT of GaN-based materials. Through optimised FIB specimen preparation and precise layer targeting, reproducible tips with controlled geometry were achieved. Systematic parameter studies revealed the combined influence of temperature, laser pulse energy, pulse frequency, and detection rate on evaporation behaviour and compositional accuracy. A base temperature of 50 K, laser pulse energy of 10 pJ, pulse frequency of 500 kHz, and detection rate of 0.5% were identified as the optimal conditions, balancing tip stability and reliable data acquisition. These optimised parameters enabled stable field evaporation with minimal compositional distortion and reduced fracture probability. Overall, the methodologies developed here form the experimental foundation for the detailed compositional and interfacial analyses of layered InGaN/GaN heterostructures presented in the following chapter.

Chapter V Multi-quantum well LED Analysis

This chapter mainly presents an atom probe tomography (APT) investigation of zincblende (zb) InGaN-based multi-quantum well (MQW) light-emitting diode (LED) structures with a specific focus on the influence of stacking faults (SFs) within the system, with the APT work complemented by also using scanning transmission electron microscopy (STEM).

It is demonstrated that the visualisation of SFs in atom probe reconstructions is possible due to sensitivities of measured composition in III-V materials to local variations in electric field during the experiment. This chapter quantifies the composition of In in the InGaN QWs and establishes that distinct elongated regions exist, parallel to ridges on the sample surface, in which the In content is locally higher. This observation is discussed in the context of STEM data which suggests that such In rich regions are associated with SFs. The experiments not only showcase the feasibility of SF characterisation in InGaN-based MQW LEDs through APT but also offer a practical pathway towards 3D imaging and compositional analysis of SFs at the atomic scale.

5.1.Experimental

5.1.1. Zincblende InGaN/GaN MQW Sample Growth

The zincblende InGaN/GaN MQW heterostructure investigated in this study was grown using metalorganic vapour phase epitaxy (MOVPE) inside a 6 × 2-inch close-coupled showerhead reactor from Thomas Swan. The sample was prepared using a 20 × 20 mm^2 section of a 150 mm diameter 3C-SiC/Si substrate (supplied by Anvil Semiconductors Ltd), where 3C refers to the cubic polytype of SiC. This substrate comprised a ~3 µm thick layer of 3C-SiC grown on a 1000 µm thick Si (001) substrate with a 4° miscut towards one of the ⟨110⟩ in-plane directions. The nitride epitaxial layers consist of a 460 nm Si-doped GaN layer, an active region consisting of five InGaN quantum well (QW) layers with a thickness of 3 nm each, alternating with 11 nm GaN barriers and 10 nm undoped GaN layers, then a 15 nm AlGaN electron-blocking layer doped with magnesium below a 180 nm p-cap layer doped with Mg. The schematic structure of the MQW sample is shown in Figure 5-1 on the left.

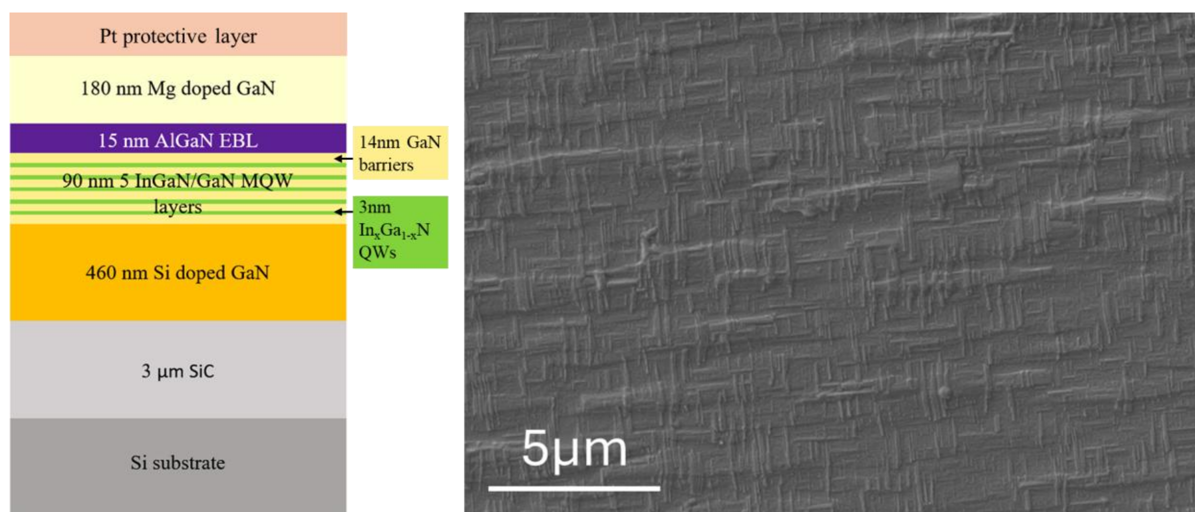

Figure 5-1 (Left) Schematic structure of the MQW sample. (Right) SEM image showing the surface morphology of the MQW sample.

The surface morphology of the sample was examined by SEM, as shown in Figure 5-1 on the right. No major surface pits or cracks were observed at this magnification, suggesting a relatively smooth MQW surface. However, it shows a uniformly distributed crosshatch-like pattern aligned along specific crystallographic directions. These features may be associated with extended defects such as misfit dislocations or SFs intersecting the surface. Given that SFs are the dominant extended defects in zb-GaN, and that they are known to intersect the surface along defined crystallographic directions [39], the observed crosshatch pattern in this SEM image is highly likely to be associated with a network of intersecting SFs propagating along {111} planes. While it may be misfit dislocations, the directional alignment of the pattern is more consistent with SF planes, particularly in light of the literature's emphasis on their prevalence in cubic GaN systems [39]. For APT analysis in this thesis, the lift-out bars were prepared approximately along the crosshatch morphology direction. However, due to the high density of SFs in zb-GaN, the analysed volumes inevitably intersect multiple SFs regardless of their exact orientation, so the precise site selection is not expected to have a significant impact on the results. To confirm the exact nature of these features, further characterisations (e.g., STEM) have been applied in the study, following the process described in Chapter 3.

5.1.2. Experimental methods

STEM was performed according to the procedures described in Chapter 4, with further details provided therein. The APT specimens were prepared following the protocol also described in Chapter 4 and subsequently transferred to a CAMECA LEAP 5000 XS with a direct flight path. Atom probe measurements were conducted at a cryogenic temperature of 50 K using a pulsed

laser operating at 500 kHz, with a detection rate of 0.5% and a pulse energy of either 10 pJ or 500 fJ. Multiple APT datasets were collected and analysed using the commercial software packages IVAS 6.3 and AP Suite 6.1 (Cameca, Madison, Wisconsin, USA).

5.2. Results

5.2.1. Visualisation of Atomic Structures with STEM

Figure 5-2 presents structural and atomic-scale characterisation of a zincblende GaN sample. In Figure 5-2(a), a low-magnification high-angle annular dark field (HAADF) STEM image provides an overview of the heterostructure, revealing distinct layers including the GaN:Mg, AlGaN electron-blocking-layer (EBL), InGaN QWs, and GaN:Si. Multiple SFs are observed, as indicated by the red dashed arrows. A blue box marks a region containing the five-layer InGaN QW structure. The presence of SFs traversing the QW region suggests potential implications for carrier recombination and transport. Figure 5-2(b) shows a high-resolution RGB composite image combining annular bright field (ABF) and HAADF STEM images, allowing clear identification of atomic columns. In this image, large green dots correspond to Ga atoms, while the smaller dark spots indicate N atoms. Two SFs (SF1 and SF2) are highlighted by white dashed lines intersecting at an angle of ~70°, confirming the presence and nature of stacking disorder within the zb-GaN matrix.

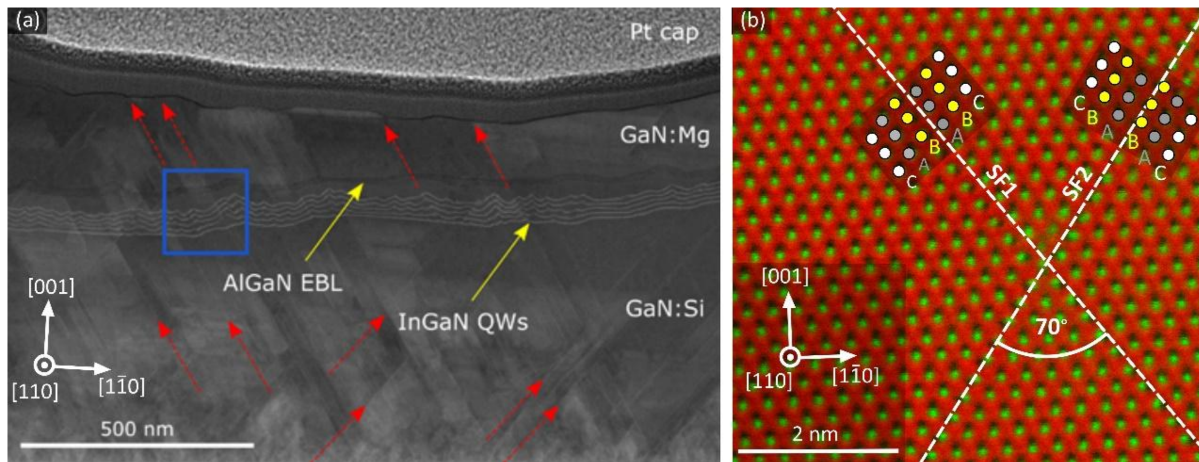

Figure 5-2 (a) HAADF STEM overview image of a zb-GaN sample. The red dashed arrows represent SFs. The blue box highlights a region of the five-layer QW structure.[25] (b) RG mixture of ABF and HAADF images. The large green dots represent Ga, and the small dark ones correspond to N. The white dashed lines illustrate two intrinsic SFs, with the grey, yellow, and white dots indicate the atomic columns with stacking type of -A-, -B-, and -C-, respectively.

5.2.2. APT Results

A high success rate in acquiring valid APT data was achieved across multiple samples, without any tip fractures observed during the experiments. Data volumes ranging from 35 million to 75 million ions on different samples were successfully collected. Representative mass spectra from the various different sample layers are provided in Figure 5-3.

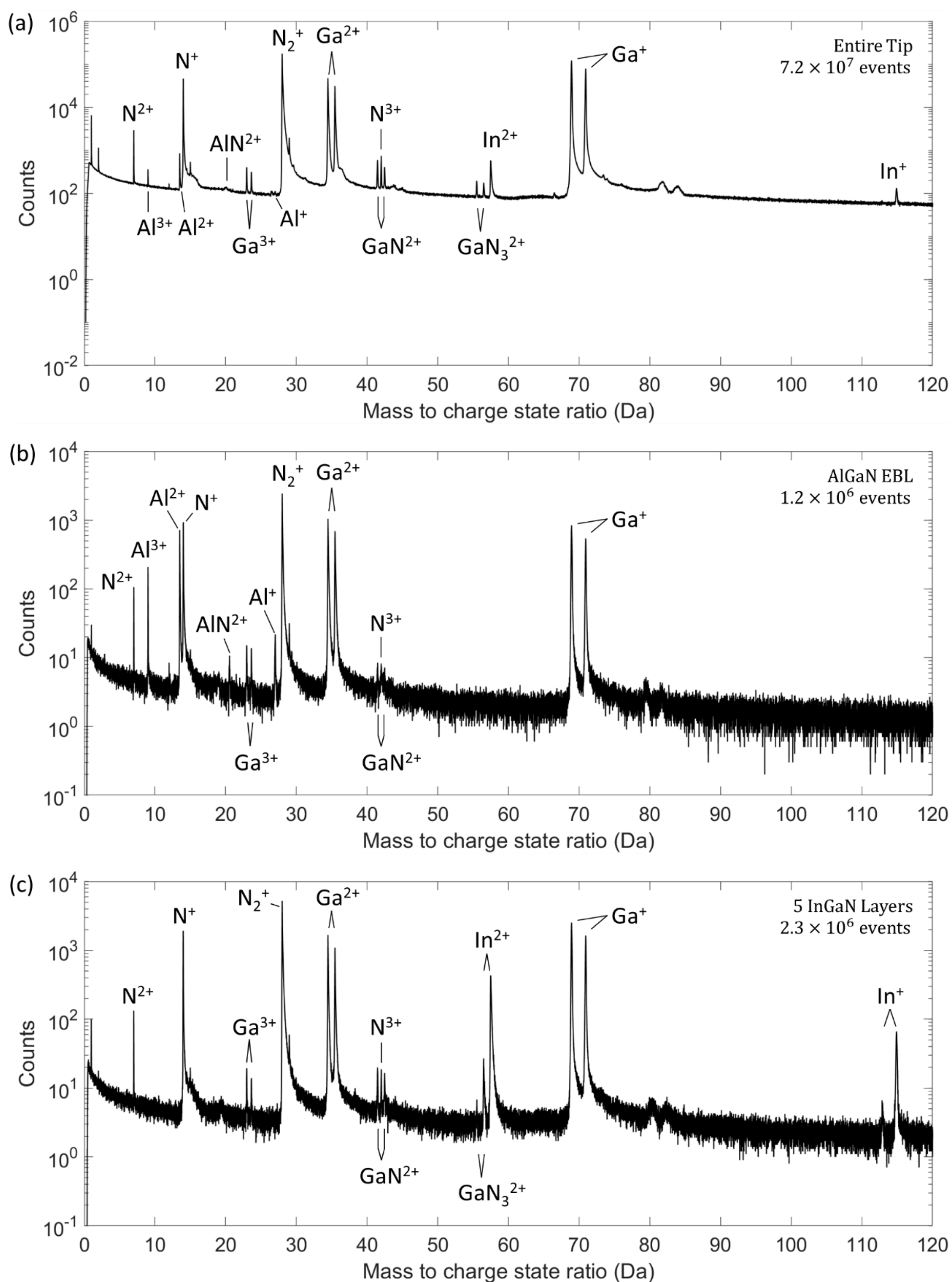

Figure 5-3 Atom probe mass spectra acquired from different regions of the sample: (a) entire analysed volume, (b) AlGaN EBL, and (c) five InGaN QW layers. Spectra were collected under identical APT conditions (laser pulse energy: 10 pJ, temperature: 50 K). Major peaks corresponding to Al, Ga, In, N, and other relevant species are labelled. These spectra serve as representative references for identifying species and charge states in III-nitride APT data.

An example of a zb-GaN reconstruction containing both the EBL and MQW layers is shown in Figure 5-4. This dataset contains 73 million ranged ions acquired using a pulse energy of 10 pJ. Characteristic elements such as Ga, N, In and Al were successfully identified. The atom maps in Figure 5-4 showcase a relatively uniform distribution of Ga and N. Additionally, the active layer region contains distinct layers of In-containing material, and these InGaN layers directly correspond to the expected positions of the QWs, although they are not strictly parallel to each other as designed. The AlGaN layer was also clearly imaged using APT. The reconstructions demonstrate the successful collection of the QWs and the AlGaN layer in the zb-GaN LED structure.

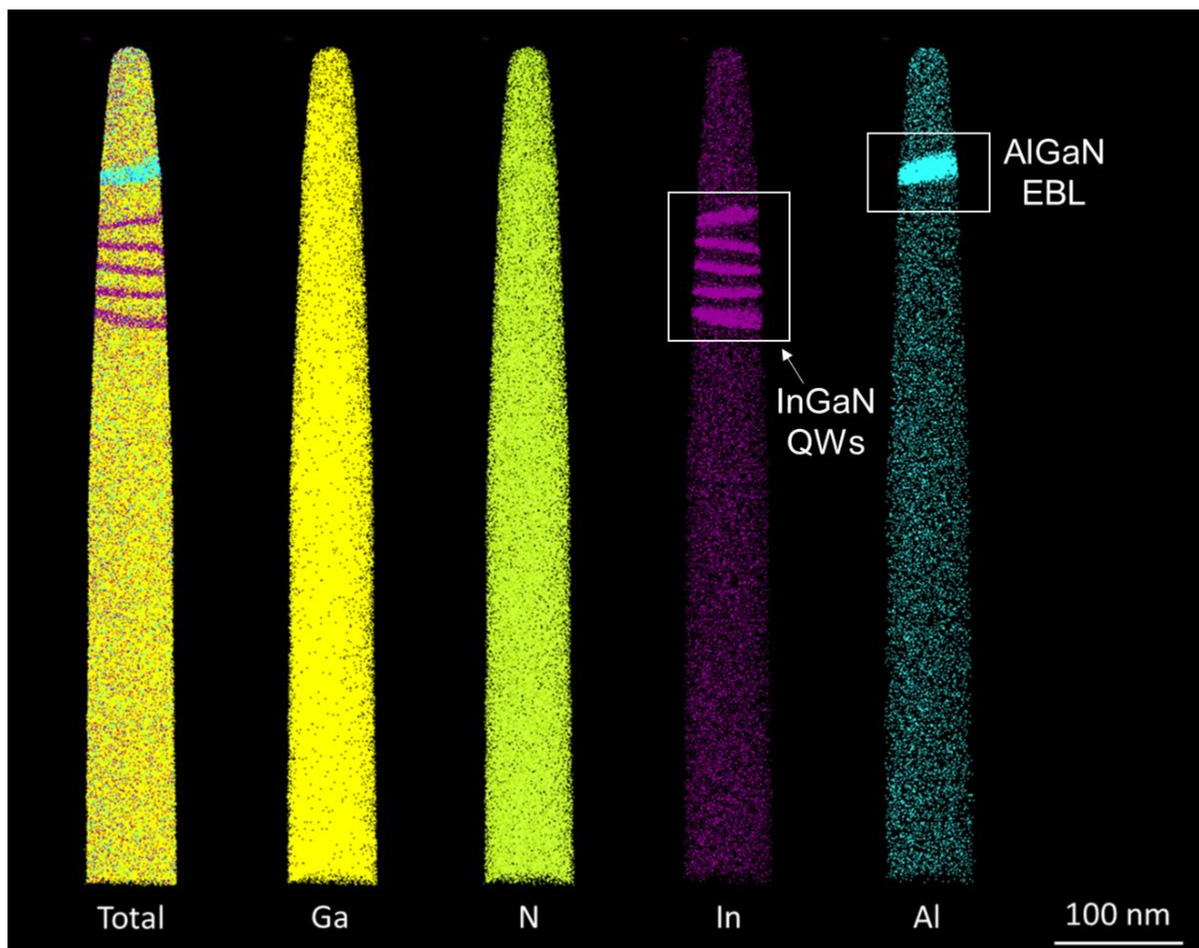

Figure 5-4 Atom maps for Ga, N, In and Al and illustrating the presence of 5 InGaN QWs and the AlGaN EBL.

5.2.3. Detection of SFs Using APT

Figure 5-5 presents the APT analysis of an InGaN/GaN MQW LED sample containing SFs. In Figure 5-5(a), the atom map shows the spatial distribution of Ga, In, and N atoms. The presence of SFs is evident in the right-hand region of the map, highlighted using the Ga iso-concentration surface. Figure 5-5 (b) shows the one-dimensional Ga concentration profile extracted along the direction of the red arrow in Figure 5-5(a), within a volume of 10 nm × 30 nm × 20 nm. A distinct drop in Ga concentration is observed within the yellow-shaded region, which corresponds to the SF. This localised depletion suggests a compositional or structural change is associated with the SF plane. Figure 5-5(c) illustrates the charge-state ratio of Ga^{2+}/Ga^{+} as a function of distance along this same analysis cylinder, alongside the corresponding calculated local electric field (right axis). Within the SF region (again highlighted in yellow), a notable increase in the Ga^{2+}/Ga^{+} ratio is detected, where a slight rise also occurs in the evaporation field at the same position.

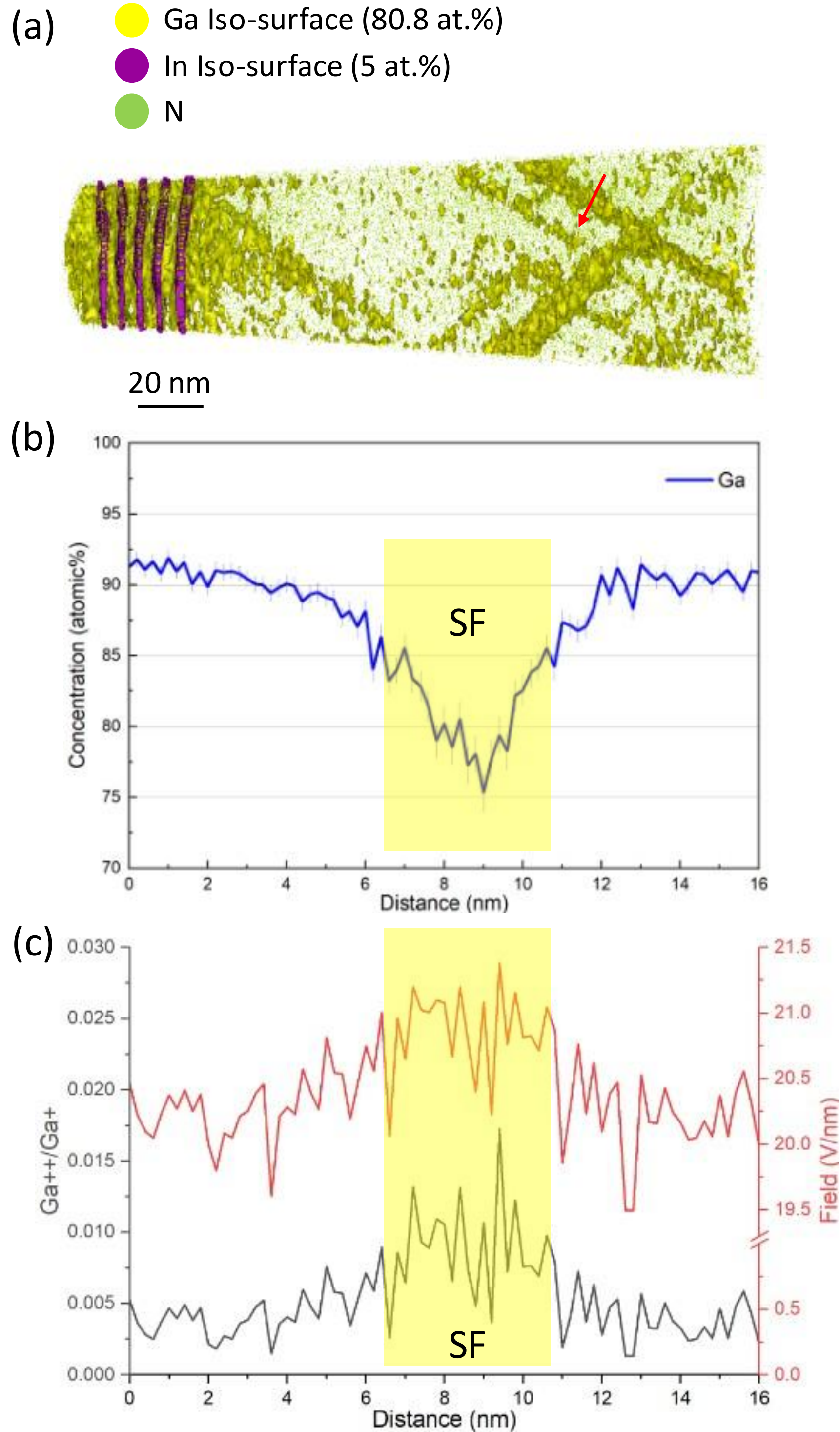

Figure 5-5 (a) Atom map of InGaN/GaN MQW LED containing SFs. The yellow Ga iso-concentration surfaces on the right indicate the SFs. The red arrow is aligned perpendicular to the SF plane. (b) One-dimensional concentration distribution of Ga in the volume (10nm × 30nm × 20nm) along the red arrow in (a), the yellow-coloured area corresponds to the SF region. (c) Charge-state ratio of Ga^{2+}/Ga^{+} as a function of distance along the direction of the red arrow in (a) (left axis) and the corresponding electric field (right axis). The yellow-coloured area again corresponds to the SF region.

5.2.4. Elemental Segregation at SFs

A typical APT analysis of MQW sample is shown in Figure 5-6, containing five InGaN/GaN QWs and a region below containing SFs. Ga and In atoms are shown in yellow and purple, respectively, in Figure 5-6(a). Figure 5-6(b) shows plan-view two-dimensional site fraction maps of In for each QW. These maps reveal inhomogeneous In distributions within each QW. Next to this, Figure 5-6(c) shows more details of the third QW from different views. In-rich regions are visualised using 22% In iso-surfaces, and both side and plan views confirm compositional rod-like fluctuations within the QW. The top panel of Figure 5-6(d) shows GaN with Ga iso-surfaces marking SFs, corresponding to the red dashed region containing SFs in the Figure 5-6(a). The bottom panel of Figure 5-6(d) shows the Ga concentration profile and corresponding electric field along the red arrow direction (20 nm × 20 nm × 40 nm volume), where local Ga depletion and field variations align with SF positions. These results indicate the impact of SFs on composition and field distribution within the QWs. Additionally, this figure also demonstrates the strength of APT in providing high-resolution, 3D insights into these complex nanoscale features.

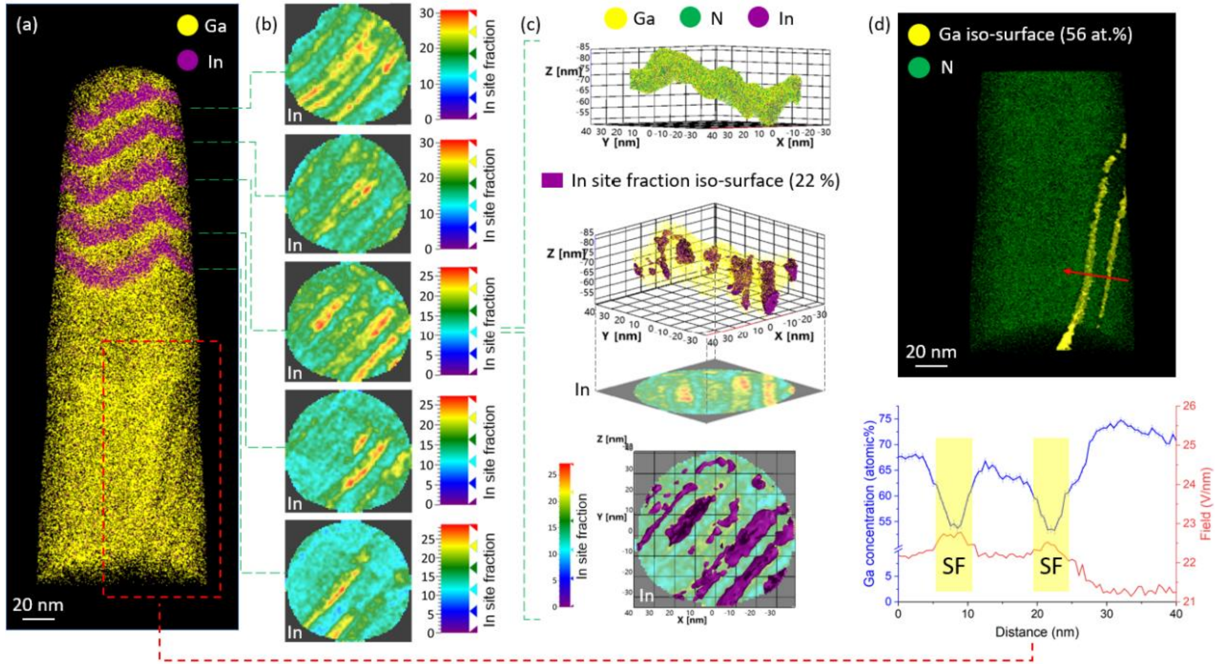

Figure 5-6 (a) APT reconstruction containing five QW layers (purple) and a region containing SFs (marked by red dashed box). (b) 2D site fraction map of In in each QW in plan view. (c) Top: Side view of the 3rd QW. Middle: In-rich regions in the 3rd QW indicated by purple iso-surfaces (≥22%). Bottom: Plan view of 2D site fraction map and In site fraction iso-surfaces in the 3rd QW. (d) Top: APT reconstruction showing the GaN region. The yellow concentration iso-surfaces show the SFs. Bottom: Concentration profile of Ga (left axis) and corresponding electric field (right axis) in the volume (20nm × 20nm × 40nm) represented by the red arrow through the SF region in the above figure

Figure 5-7 presents an APT reconstruction section containing the AlGaN layer with SFs going through. The Ga and Al iso-surfaces are shown in yellow and cyan, respectively (Figure 5-7(a)), with red dashed lines marking the SFs. Figure 5-7(b) shows the two-dimensional plan-view site fraction maps of Al and Ga, where black arrows suggest the direction of SFs. Figure 5-7(c) shows side views of Al and Ga atom maps, where white arrows, corresponding to the black ones above in (b), point to the SF directions. The red arrow, which is perpendicular to the SF direction, indicates the direction of the plotted composition profile in Figure 5-7(d). The corresponding site fraction profile shown in Figure 5-7(d) reveals the variations in Al and Ga content across the SFs, with the SF regions highlighted in yellow. The site fraction profiles of

Ga and Al across the AlGaN layer reveal clear compositional variations at the SF regions, highlighted in yellow. Within these SF zones, the Al site fraction shows an obvious increase, while the Ga site fraction shows a corresponding decrease. This anti-correlated behaviour suggests local redistribution of cations near SFs, potentially linked to strain relaxation or altered incorporation dynamics during growth.

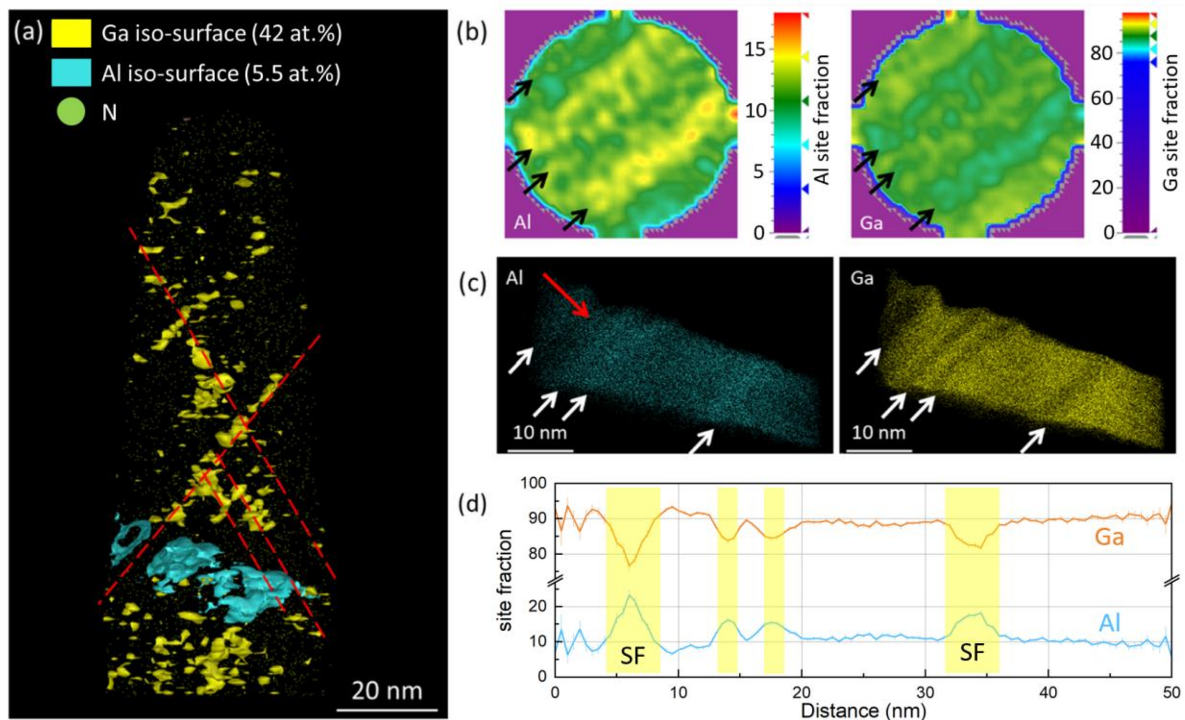

Figure 5-7 (a) Atom map showing sub-volume from same dataset in Figure 5-4 capturing the AlGaN layer. The red dashed lines indicate the regions affected by the SFs. (b) 2D site fraction maps of Al and Ga from top view of (a). The black arrows indicate the regions through which the SFs pass. (c) Side view of the atom maps of Al and Ga, respectively. The white arrows represent the direction of SFs. (d) Site fraction profile of Al and Ga through the AlGaN layer along the red arrow in (c), perpendicular to the SF plane with the SF plane as the datum. Yellow shaded area corresponds to the SF regions.

5.3.Discussion

5.3.1. STEM Structural Interpretation

As shown in Figure 5-2(a), SFs are observed to extend from the GaN/SiC interface through all

the layers in the sample. These SFs occur in two distinct orientations that incline toward each other, as indicated by the red arrows. As discussed elsewhere, for SFs viewed perpendicular to the sample miscut, one set of SFs is at a shallower angle (51°) and the other at a steeper angle (59°) with respect to the GaN/SiC interface [120]. Oppositely inclined SFs can meet and annihilate one another [120], but a substantial proportion of the SFs extends through the material, reaching the surface of the sample.

The detailed structure of SFs was previously examined in a zincblende GaN sample grown on 3C-SiC/Si (Ref. [94]), which is compositionally and structurally similar to the GaN buffer layer underlying the MQW region in this LED structure. In that study, the combined aberration-corrected HAADF and ABF STEM imaging technique was employed to directly reveal the bonding configuration and polarity at individual SFs, providing valuable insight into the defect structures that may also be present in the current sample. Following the approach used in that work, Figure 5-2(b) shows the result of merging an ABF and a HAADF image of the zb-GaN (zone axis = [110]), so that Ga atomic columns appear as green circles, whilst N atomic columns appear as smaller dark dots, against a red background. The region of zb-GaN examined here contains two intersecting SFs at an angle of ~70°, which can be initially identified by considering the stacking sequence on the Ga sub-lattice. The stacking sequence is labelled on the figure, and at the faults, there is a change from ABC-ABC stacking to ABC-AB-ABC, consistent with the expected structure of intrinsic-SFs (i-SFs). Notably, directly at the i-SF plane (depicted by the white dashed line), the coordination of the N atoms is rotated by 180° around the polar axis along [1-11], consistent with previous observations [94]. A key

point of note for comparison with APT data that will be presented later is that in this case the two SFs intersect one another but both propagate unimpeded through the crystal structure. This behaviour is consistent with non-cancelling Burgers vectors associated with the partial dislocations bounding the SFs, which makes their mutual annihilation energetically unfavourable [120].

5.3.2. Analysis of APT Results

Although the QWs and AlGaN layers are clearly visible in all the atom maps, they are not flat and oriented parallel to one another like the planar layers usually observed in APT analysis of LED structures grown from the more conventional wurtzite form of GaN [233, 234]. Some angular differences between the QW layers and between the QWs and the Al layers can be readily seen in the Figure 5-4. This is consistent with the STEM data in Figure 5-2(a) and in Ding *et al.* [25] which show changes in orientation of the QWs, some of which may be associated with SFs.

5.3.3. Analysis of SFs

Further investigation revealed that the observed Ga distribution is not always uniform. In the dataset collected at 500 fJ, as shown in Figure 5-5, an uneven distribution of Ga is clearly visible in the lower section of the atom map. In Figure 5-5(a), the Ga iso-concentration surfaces highlight an apparently inhomogeneous distribution of Ga and reveal the presence of straight, planar features. These planar Ga iso-concentration surfaces intersect at an approximate 70°

angle corresponding to the expected angle of two intersecting {111} planes and to the angles at which the two SFs intersect one another in the STEM image in Figure 5-2(b). As this is influenced by the APT reconstruction, it is worth noting that the initial reconstruction of the APT data was calibrated using known QW spacings, revealing an apparent angle of approximately 70°. After identifying the planar features as intersecting SFs, a further slight geometric adjustment was performed during reconstruction calibration to achieve an improved match between the angle observed in the dataset and the expected angle between them while maintaining the QW spacings as observed in the transmission electron microscopy (TEM) data [25]. Consequently, the reconstructed planar Ga iso-concentration surfaces in the dataset displayed in Figure 5-5 now intersect very close to 70°, underlining the benefits of combining TEM and APT approaches. The one-dimensional concentration profile running through (perpendicular) to the planar feature in Figure 5-5(b), reveals the Ga concentration shows a sharp decrease across the suspected SF region compared to the adjacent bulk. However, as a partially ionic crystal, GaN does not tolerate significant deviations from stoichiometry. Furthermore, the TEM data in Figure 5-2 show no deviation in the intensity of the atomic columns, which would indicate a change in Ga or N content, and instead reveal only a shift in their positions. Thus, despite the presence of the SF in the atom maps, it is expected that the actual Ga concentration here should be the same as in the other parts in the same layer.

Several APT studies on GaN-based semiconductors have shown that the observed stoichiometry is strongly affected by the analysis conditions [151, 158, 211, 235, 236], in particular the local electric field applied during the experiment. The instantaneous electric field

applied to a specific local area of the specimen surface during an experiment can be estimated by measuring the instantaneous charge state ratio (CSR) of an elemental ionic species [151] originating from a particular region of the specimen apex. Using this approach, it is possible to investigate whether variations in the local electric field in the vicinity of the SF are likely responsible for observed changes in the concentration.

Figure 4-10 presents the results from a series of APT calibration experiments with pure wurtzite GaN samples. Here, while maintaining a constant detection rate of 1%, different laser pulse energies were systematically applied, which in turn corresponds to the application of different electric fields. As expected, the measured composition exhibits significant variability as the laser energy changes. This experiment reaffirms the notion that a minor change in the applied electric field strength leads to a measurable change in the concentration measurement in GaN semiconductor materials. For this reason, the measured Ga content of approximately 92% away from the SF in Figure 5-5(b) is a consequence of this, and not the actual Ga concentration in the sample. The trend in Figure 4-10 shows that lower field strengths are associated with the measurement of an excess of the metallic element, Ga, while its concentration diminishes at higher fields. At such lower electric fields (corresponding to higher laser energies), this observation is most often attributed to the evaporation and subsequent decomposition of larger complex ions enroute to the detector. A potential product of this process is neutral N_2 molecules. These molecules will not be further accelerated towards the detector by the electric field and thus may lead to a systematic loss in the detection of nitrogen in the experiment. Although the impact of this phenomenon decreases under higher electric fields, compositional measurements

may still exhibit a bias towards the preferential evaporation of Ga. This bias persists irrespective of the applied laser pulse for energies higher than about 10fJ (as measured in Chapter 4), leading to the erroneous measurement of lower Ga concentrations [152]. This phenomenon has also been found to occur in the APT analysis of other III-V semiconductors and similar effects have also been observed in MgO [237].

Returning to our study of the zb-GaN samples, the change in the Ga^{2+}/Ga^{+} CSR across the width of the SF was evaluated. Figure 5-5(c) plots the measured CSR and the corresponding estimate of the electric field strength in the same volume and in the same direction as the one-dimensional concentration profile in Figure 5-5(b), respectively. The electric field strength was calculated from the CSR using the Kingham curves [153, 184]. In the region of the one-dimensional concentration profile where the Ga concentration decreases, there is a significant increase in the field strength. The increase is tentatively attributed to a local change in the apex shape of the specimen, potentially a consequence of the SF intersecting with the surface during the experiment. This supports our previous assumption that there are structural differences in this part of the sample. Thus, the apparent compositional inhomogeneity in the Ga distribution can be attributed to biased evaporation during the APT experiment.

However, the segregation of In and Al observed in Figure 5-6 and Figure 5-7 is real, reflecting genuine compositional variations associated with the SFs. This interpretation is further supported by the STEM-EDS results reported by Ding *et al.* [25], as shown in Figure 5-8, which clearly show enrichment of In and Al at SFs in zincblende GaN heterostructures. Therefore,

while the apparent Ga fluctuations arise from local field-evaporation artefacts, the In and Al enrichment represents a true segregation phenomenon consistently revealed by both APT and STEM analyses.

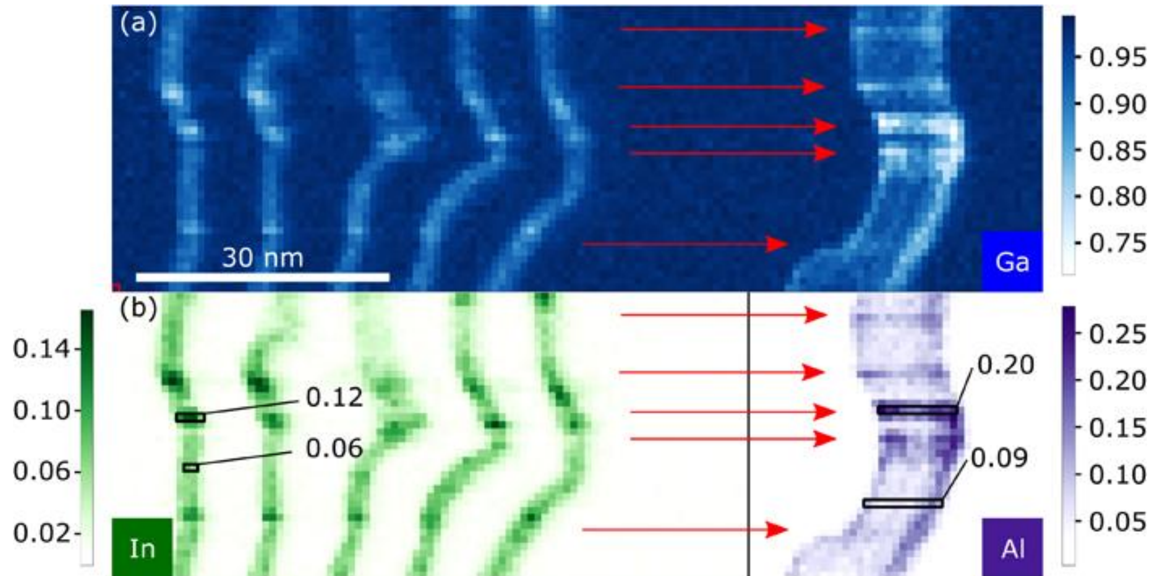

Figure 5-8 (a) Group III site fraction map of Ga and (b) Group III site fraction maps of In and Al in the region of MQW and AlGaN layer (same sample as in this Chapter), measured by STEM-EDS. The red arrows indicate the approximate positions of relevant SFs. The black boxes highlight the Group III site fractions of In and Al at SFs and at undefected areas, respectively. Reproduced from Ding *et al.* [25], "Alloy segregation at stacking faults in zincblende GaN heterostructures," Journal of Applied Physics 128, 155703 (2020), under the terms of the Creative Commons CC BY license.

In summary, although in reality the overall Ga concentration in the sample is constant, compositional fluctuations in the SF region are observed in APT due to local variations in field strength arising from crystallographic structural differences. In turn, this enables the indirect visualisation of SFs in the 3D reconstruction.

The apparent width of the SFs observed in the APT data is on the order of ~4 nm, based on variations in field strength and charge-state ratio within the reconstructed volume, as can be found in Figure 5-5. However, the STEM image in Figure 5-2(b) indicates that the actual

physical thickness of the SFs is limited to approximately one to two atomic planes and is much less than that. This discrepancy arises from trajectory aberration effects in APT, which locally distort ion trajectories and broaden sharp interfaces, thereby affecting the accuracy of defect width estimation. Nevertheless, the consistent alignment and relative angles of these regions across multiple QWs suggests that the observed features are not artefacts but reflect real structural variations.

5.3.4. Impact of SFs on Elemental Segregation

Having shown that the APT can reveal SFs in the lower section of the sample, the focus now shifts to determining their impact on the QW composition. Figure 5-6 tackles this in depth, examining in-depth features seen in the InGaN layers. In Figure 5-6(a), the 3D reconstruction reveals the spatial distribution of In across the QW layers. Note that although the QWs exhibit a layered configuration, they deviate from being perfectly parallel planar surfaces. Instead, they appear as a series of near-parallel surfaces undulating up and down, consistent with STEM observations as highlighted by the region in the blue box in Figure 5-2(a) [25].

As previously discussed, the direct quantification of overall composition in Group III-V materials presents challenges, primarily stemming from potential biases related to variances in the evaporation fields of the distinct elements. The inaccuracy in N concentration can lead to distorted measurements of the concentrations of the Group III elements such as In. Previous studies have demonstrated that while there is a bias in the measurement of III:N ratios in InGaN QWs using APT, there is however no observable bias in the measurement of site fractions of

the Group III elements, e.g. In/(In+Ga), with random alloy distributions [151, 231]. Nevertheless, more recent work by Di Russo *et al.* [232] has suggested that even the Group III site fraction in InGaN may exhibit a weak dependence on the surface electric field, which is likely due to preferential Ga evaporation under high-field conditions. In the context of our study, where all structures were analysed under consistent experimental parameters, the Group III site fraction remains a reliable measure for assessing local compositional variations. To enhance the precision of the analysis regarding the compositional variations in Group III elements, the Group III site fraction is employed wherever possible to minimise the bias introduced by local changes in the electric field.

The five images in Figure 5-6(b) offer a top-down perspective of the In/(Ga+In) site fraction for each QW, highlighting significant variations in the In content. It appears that each layer exhibits a non-uniform distribution of In, resulting in parallel stripes of high In content seen in plan view. The top section of Figure 5-6(c) provides a side view of the third QW depicted in Figure 5-6(b) that has been isolated and analysed further. In the middle section of Figure 5-6(c), In site fraction iso-concentration surfaces at 22% In are superposed on a 3D map of the In site. These iso-surfaces enclose the regions of In-rich material and hence illustrate their elongated shape. This is further emphasised in the bottom section of Figure 5-6(c), which shows the iso-surfaces in plan view. The use of iso-surfaces separates the impact of thickness variations and compositional variations in the QW, whereas thickness variations might influence the data visualisations in Figure 5-6(b). Hence, Figure 5-6(c) allows us to unambiguously identify elongated, wire-like regions of In enrichment in the QW. To quantitatively assess this In-

enrichment, the average In site fractions in both the In-enriched regions and the region between such features have been calculated. The average In site fraction in the high In content stripes is (24.87 ± 0.31) %, whereas in the region between the stripes it is (14.98 ± 0.10) %, yielding a ratio between 1.63 and 1.69. It is notable that the In-rich stripes run parallel to ridges in the overall QW morphology. Figure 5-6(d) presents the evidence of structural features in the lower half of the sample that are consistent with SFs. The yellow Ga iso-concentration surfaces highlight a set of parallel planes, separated by approximately 10 nm from one another. The corresponding Ga concentration profile and field strength plot reveal that Ga concentration decreases at positions where the local field increases, which mirrors the behaviour observed in Figure 5-5. This correlation between Ga charge-state ratio, field variation, and local composition again points to structural disruptions. Given the established relationship between these APT signatures and SFs, it is reasonable to interpret these features also as SFs.

It should be noted that the SFs identified in this dataset do not appear to intersect the QWs, so in this instance there is no direct insight into the compositional variations which SFs cause in InGaN QWs. However, the observation of In-rich stripes that are not clearly associated with SF features is somewhat unexpected. Previous analysis by Ding *et al.* suggested that In-rich QWires may form adjacent to SFs and may cause the light emission from the InGaN QW to exhibit a high degree of polarisation [105]. Here, the elongated In-rich QWires can be observed clearly, but they do not appear to be associated with SFs. There are two possible explanations. Firstly, In-rich QWires may form not only at SFs, but also at other locations. For example, the surfaces of the GaN surfaces on which the InGaN QWs are grown clearly exhibit elongated

striations [103], and the resulting changes of surface orientation may lead to changes in In incorporation. Hence, QWires may be more prevalent in the sample than expected. (This idea is also supported by the fact that the In-rich stripes run parallel to the ridges in the QW morphology, as noted above). Alternatively, there may be additional SFs in the sample which have not been picked up by our analysis of the apparent Ga-content variations. Since the zb-GaN here contains both bunches of SFs and isolated SFs [120], it is possible that collections of SFs lead to larger disturbances to the surface field and more pronounced variations in stoichiometry, whereas isolated SFs have lesser impact and are not necessarily detectable in APT. This point requires further investigation.

Meanwhile, our investigation of compositional changes along SFs also reveals their impact on elemental distribution within the Al layer. As highlighted by crossed red dashed lines in Figure 5-7(a), regions of reduced Ga content in the GaN cap above the AlGaN layer can be tentatively identified as SFs, some of which extend through the AlGaN layer. The iso-surface of Al in the AlGaN layer (drawn at 5.5 at.%) shows the variations in Al content associated with the SF locations. Examination of the site fraction distribution plots for Al and Ga from a top-down perspective in Figure 5-7(b) again demonstrates parallel stripes along which the composition changes, here with Al enrichment, mirroring the behaviour observed with In in the QW. The same trend can also be found in Figure 5-7(c), where the Al content shows an increase in the region with the suggested SFs while the Ga content drops. To illustrate the effect of SFs more clearly, Figure 5-7(d) shows the Al and Ga site fraction profiles measured along the direction of the red arrow in Figure 5-7 (c). The data were obtained from a volume of 40×40 nm^2 with

a bin size of 0.5 nm. A clear decrease in the Ga site fraction and a corresponding increase in Al are observed at the SFs.

The average Al site fractions (Al/Al+Ga) have been calculated to determine the Al site fractions at and away from the SFs. Making use of the one-dimensional site fraction profiles along the direction perpendicular to the SF plane in Figure 5-7(d), the near-SF site fraction was obtained by averaging the width within 3 nm of the SF centre, while the site fraction away from the SF was calculated by averaging the width within 5-8 nm from the SF centre. The near-SF Al site fraction was found to be (17.34 ± 0.66) %, and the Al site fraction away from the SF was (10.28 ± 0.27) %, resulting in a ratio of 1.58 to 1.80. It should be noted that changes in field strength may also affect the measured composition. A higher field at SF may lead to an artificially higher Al content [236], however, these results are consistent with earlier findings in STEM [25], suggesting that they are likely indicative of a real compositional variation rather than purely an artefact.

The results indicate that Al in the EBL is likely to enrich in the region of the SF compared to the SF-free region. The current resolution is insufficient to determine whether Al is segregating directly on the SF or in the region immediately adjacent to it, but previous STEM studies have suggested that Al segregates directly on the SF [25]. Meanwhile, it is worth noting that multiple neighbouring SFs can interfere with each other, affecting the extent of enrichment. Further studies are needed to assess the impact of these interactions on the measured concentrations.

Several potential mechanisms for alloy segregation, such as In and Al, in the SF region have been proposed, with further details provided in Ref [25]. Notably, the SF can be considered as an extremely narrow insertion of wurtzite (wz) material into the zb matrix. Bulk zb-GaN has a larger interplanar spacing between the close packed planes than bulk wurtzite GaN. (The relevant spacings are $d_{(111)}$ in zincblende, which is 2.602 Å, and $d_{(0001)}$ in wurtzite, which is 2.593 Å) [25]. Hence, at the SF, the local interplanar spacing may be slightly reduced. Given that Al is a smaller atom than Ga, the strain associated with the presence of Al in the lattice might be reduced if Al segregates to such regions of lower interplanar spacing, thereby lowing the total system energy. It should be noted that, for larger atoms like In, enrichment at SFs in the QW region likely arises from different mechanisms. As SFs are typically thin wurtzite inclusions within the zb matrix, which locally relax compressive strain, they reduce the energy cost of incorporating larger In atoms [25]. Additionally, these wurtzite segments may expose polar (0001) facets and semi-polar {10-11} facets during growth, where the altered surface polarity and incorporation kinetics can enhance In segregation [105].

5.4. Conclusion

This chapter presents the successful characterisation of the SF structure in GaN using STEM and APT to provide quantitative structural and compositional information, respectively. The results show that the presence of SF (or possibly SF bunches) can be observed in both STEM and the APT reconstructions. In terms of APT imaging, this is due to the structural changes at SF that cause variations in the local evaporation field, leading to inhomogeneity in the observed Ga concentrations. The presence of the SF leads to segregation of Al where the SF and the

AlGaN layer intersect. The In distribution in the QW layers exhibits similar features. However, since there is no direct evidence in the current dataset that this is caused by SFs, further study will be needed to determine the origin of these In-rich bands or to confirm whether all SFs within the sample have been identified by APT.

In this study, APT demonstrates promising capabilities for the 3D characterisation of SFs in zb-GaN, complementing STEM. However, investigating the structural effects of SFs on different regions of the material as well as compositional variations is still a complex task. The accuracy of the structural analysis is closely related to the way in which the 3D reconstructions are undertaken, while the precision of the compositional measurements is closely linked to the electric field. Future work will further explore the density and orientation of SFs and the enrichment of nearby Group III elements, as well as their relationship to the structures' optical properties.

Chapter VI Single quantum well LED Analysis

Single quantum well (SQW) structures provide a simplified model system in which the effects of stacking faults (SFs) can be examined directly without the additional structural complexity seen in multi-quantum wells (MQWs). By reducing the active region to a SQW, the effect of individual defects on composition and luminescence can be isolated, which offers a clearer insight into the fundamental mechanisms that also operate in MQW devices.

In this chapter, atom probe tomography (APT) is employed to investigate InGaN-based SQWs, with particular emphasis on elemental segregation at SFs. The results show that indium preferentially segregates along SF planes and at their intersections, forming inclined In-rich features that intersect the QWs. In Mg-doped SQW samples, APT revealed that magnesium also segregates to SFs and their intersections, indicating that these extended defects act as preferential sites for both indium and magnesium. The SQW specimen analysed in this chapter is intentionally Mg-doped. As a commonly used p-type dopant in GaN that forms charged substitutional acceptors, magnesium is sensitive to local strain and electrostatic potential variations. Therefore, this makes Mg-doped SQWs a suitable model system for probing the interaction between SFs and dopant segregation in a simplified QW structure.

APT results are also correlated with cathodoluminescence (CL) measurements carried out by collaborators. The CL data show that SF-rich regions are associated with variations in optical emission, including additional sub-bandgap peaks attributed to defect-related deep levels. These observations support the conclusion that compositional inhomogeneities at SFs degrade optical performance.

Overall, this chapter demonstrates the ability of APT to directly resolve compositional variations at SFs in a simplified SQW system. The results in this chapter also complement the MQW analysis presented in Chapter 5 and together establish a more comprehensive understanding of the link between SFs, elemental segregation, and luminescence behaviour in InGaN-based light-emitting diodes (LEDs). The majority of the results related to luminescence properties presented in this chapter have been published previously in collaboration with colleagues [238, 239], to which the author of this thesis contributed as a co-author.

6.1. Experimental

6.1.1. Zincblende InGaN/GaN SQW Sample Growth

The zincblende InGaN/GaN SQW heterostructure analysed in this study was grown by Dr. Menno Kappers. It was deposited on a 3C–SiC/Si (001) substrate with a 4° miscut using a 6 × 2' Aixtron close-coupled showerhead metalorganic vapour phase epitaxy (MOVPE) reactor. The substrate miscut was introduced to avoid the formation of antiphase domains [120]. The sample consists of an approximately 400 nm thick zincblende (zb) GaN epilayer followed by a 40 nm thick $In_xGa_{1-x}N$ underlayer ($x \approx 0.01$-0.02), a nominally 2 nm wide In0.1Ga0.9N SQW and capped by an 8 nm thick GaN layer, as shown in Figure 6-1.

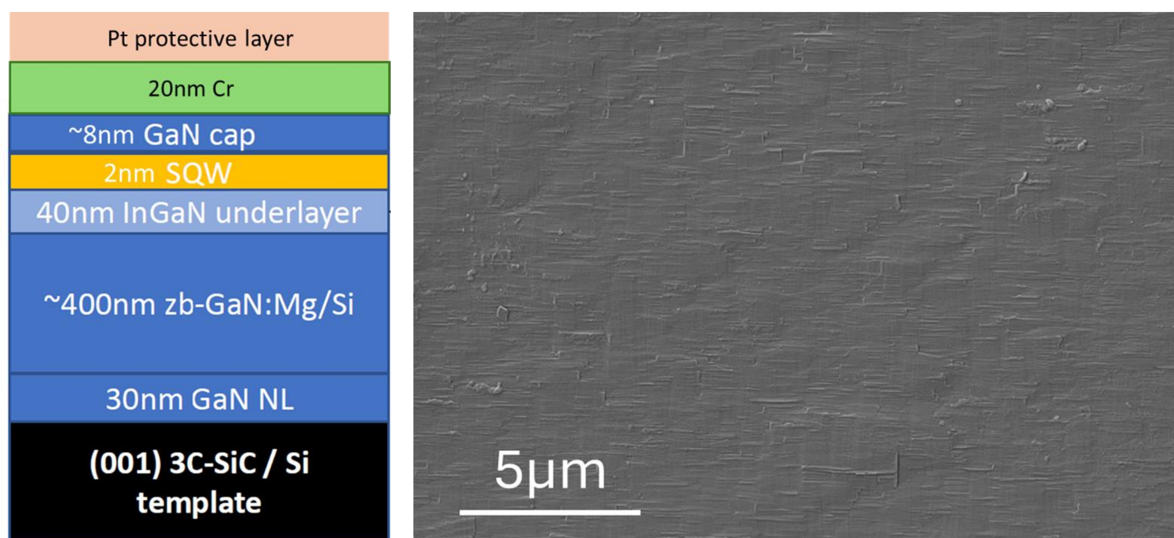

Figure 6-1 (Left) Schematic illustration of the SQW sample structure, including Cr and Pt layers that were added subsequently for surface protection during sample preparation. (Right) SEM image (secondary electron mode, SE) showing the surface morphology of the SQW sample.

Compared to the MQW structures shown previously, the SF-related crosshatch features appear less pronounced in this SQW sample, which is likely due to the presence of only a thin SQW and a thicker GaN cap layer that reduces the surface morphological modulation associated with

buried SFs, rather than indicating a significantly lower SF density. Additional protective layers were deposited to preserve the surface during sample preparation.

6.1.2. Experimental Methods

STEM was carried out according to the same procedures described in Chapter 4.

For the APT tip sample preparation, a 20 nm thick Cr layer was deposited on the sample surface with a Leica EM ACE600 sputter coater prior to the Pt protective layer. This Cr layer serves as an additional protective and marker layer for the very thin SQW region located near the surface, as explained in Chapter 4. Comparative experiments (Table 6-1) confirmed that the presence of the Cr layer can increase the success rate of SQW sample preparation, from approximately 22% to 50%, and improve the quality of the collected datasets. As shown in Table 1, samples incorporating the Cr layer generally exhibited a higher proportion of successful preparations and improved data quality; however, this observation may not necessarily indicate a direct causal relationship between the Cr layer and the observed improvement. The APT experiments were conducted under the same conditions and parameters as described in Chapter 4.

Additional datasets not included in the thesis were also analysed. SFs were observed across multiple datasets, including those where the SQW was not captured. The datasets presented in this thesis were selected as representative cases in which the SQW and different SF configurations (e.g., intersecting and parallel SFs intersecting the SQW) were simultaneously observed within the analysed volumes.

Table 6-1 Comparison of APT data quality for SQW samples prepared with and without a Cr protective layer.

	Sample No.	Dataset	Data quality
SQW sample without Cr	GaN_04_M-1	Failed	——
	GaN_04_M-3	R5111_25485	Good
	GaN_04_M-4	Failed	——
	GaN_04_M-5	R5111_25878	SQW missing
	GaN_04_M-6	R5111_26009	Good
	GaN_04_M-7	Failed	——
	GaN_04_M-8	R5111_25478	SQW missing
	GaN_04_M-9	R5111_25912	Contaminated
	GaN_04_M-10	R5111_25341	SQW missing
SQW sample with Cr	GaN_07_M-1	Failed	——
	GaN_07_M-3	R5111_26387	Good
	GaN_07_M-5	Failed	——
	GaN_07_M-6	R5111_26349	SQW missing
	GaN_07_M-7	R5111_26354	Good
	GaN_07_M-8	R5111_26344	Good
	GaN_07_M-9	R5111_26353	SQW missing
	GaN_07_M-10	R5111_26453	Good

6.2. Results

6.2.1. Visualisation with STEM

The cross-sectional scanning transmission electron microscopy (STEM) image in Figure 6-2 reveals the overall layer structure with clear interfaces. The SQW and the underlying (In)GaN layer exhibit uniform contrast, indicating a consistent composition and thickness across the region. In addition, SFs of different orientations can be seen extending through the zincblende GaN buffer and into the (In)GaN layers. These planar defects are characteristic of cubic GaN and are known to influence the structural and electronic properties of the heterostructure [39, 240]. They may also cause local compositional variations that impact its optical performance, which will be further investigated in the following sections.

To provide a clearer view of the SQW region, a higher-magnification high-angle annular dark-field (HAADF) STEM image together with the corresponding STEM-EDS elemental map of the same sample are shown in Figure 6-3. The SQW and the surrounding (In)GaN underlayer display uniform contrast, confirming their structural consistency. The EDS elemental map reveals localised indium enrichment around a bundle of SFs beneath the SQW, consistent with the compositional variations expected from SF-related segregation.

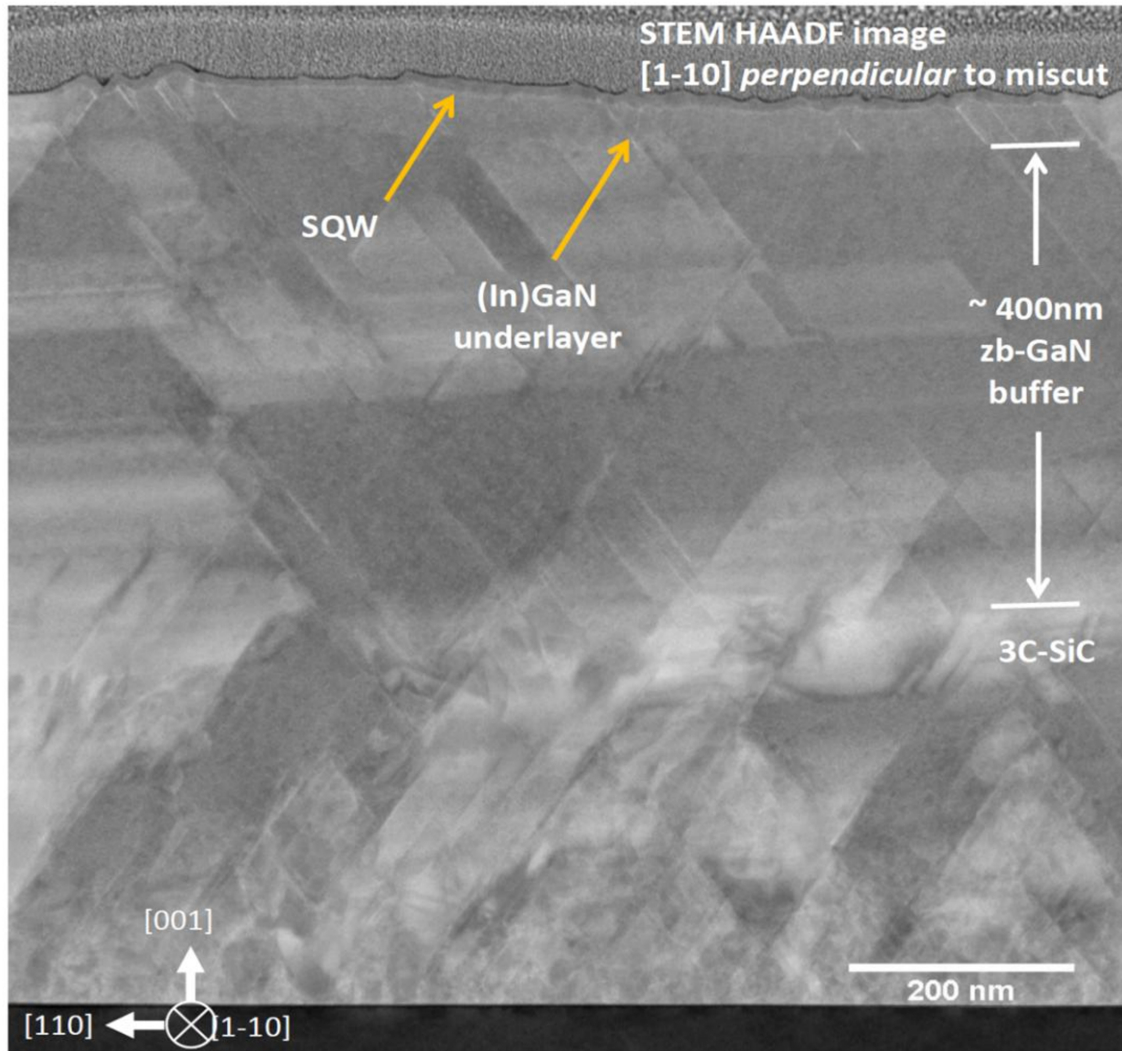

Figure 6-2 STEM HAADF image showing the cross-sectional structure of the sample viewed along the [1-10] direction, perpendicular to the substrate miscut. From bottom to top, the sample consists of the 3C-SiC substrate, an approximately 400 nm thick zincblende GaN buffer layer, an unintentionally doped (In)GaN underlayer with lower In content, and the SQW near the surface.

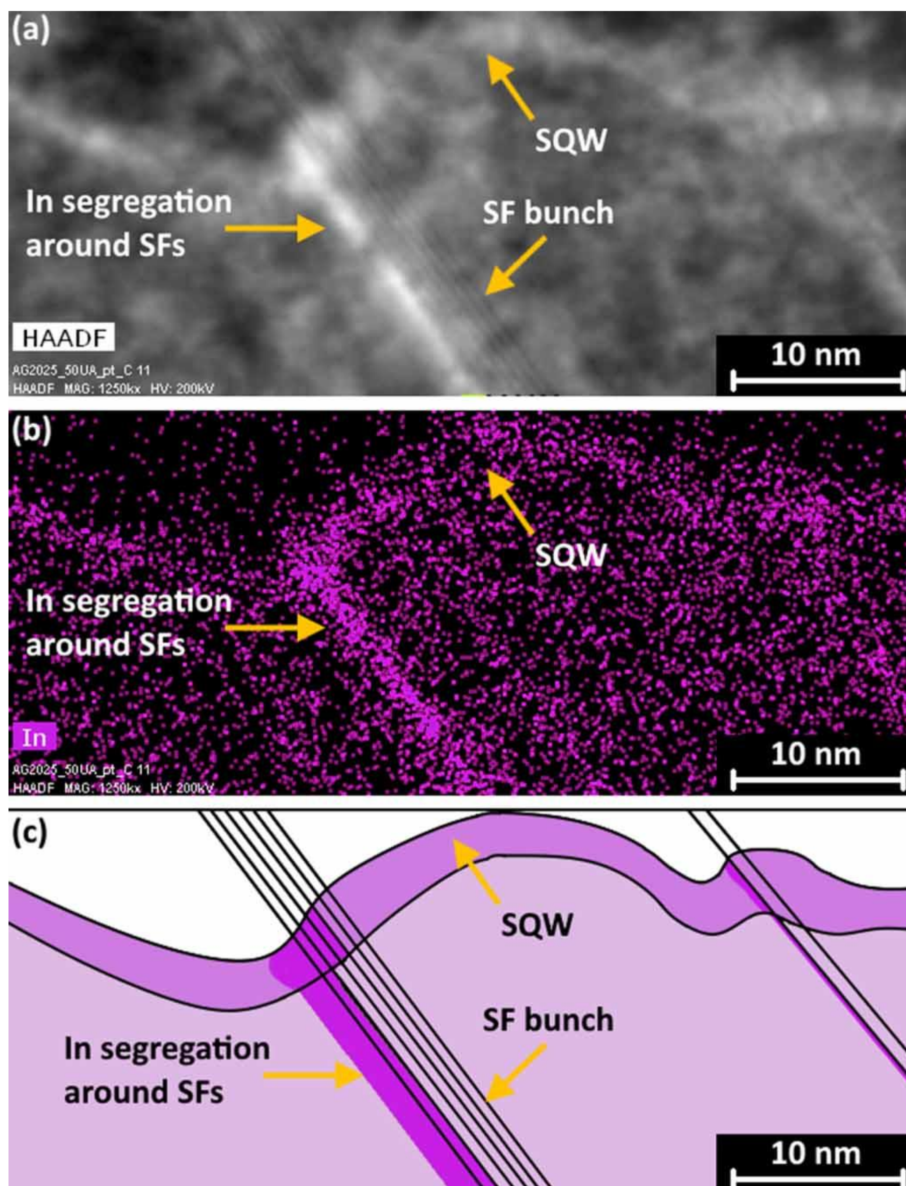

Figure 6-3 (a) High-magnification cross-sectional HAADF-STEM image of the zb-InGaN underlayer and zb-InGaN SQW from the same sample shown in Figure 6-4. The SQW and the surrounding (In)GaN layers display uniform contrast, confirming their consistent composition and thickness. (b) Corresponding STEM-EDS elemental map of In (purple), revealing In segregation around a bundle of SFs beneath the SQW. (c) Schematic illustration highlighting the position of the SQW and the In-rich regions associated with the SF bunch. Reproduced from Ref. [238] under the terms of the Creative Commons Attribution 4.0 license (CC BY 4.0).

6.2.2. APT Analysis of SF Configurations

The APT reconstructions reveal the elemental distribution within the SQW GaN samples, including compositional variations associated with SFs. The reconstruction of Dataset

R5111_26354 in Figure 6-4(a) captures both the Cr protective layer and the InGaN layers, as indicated by the presence of Cr and In, respectively. The planar Ga-depleted bands are clearly visible, which indicate that there are parallel SFs running through the analysed volume, as discussed in Chapter 5. Correspondingly, the distribution of Mg shows localised segregation along those features. A more complex SF arrangement is shown in Dataset R5111_26387 of Figure 6-4(b). Ga-depleted planes (correspond to SFs) intersect with each other and form a fishbone-like structure within the specimen. Mg segregation remains associated with these SFs, particularly enriched at their intersections.

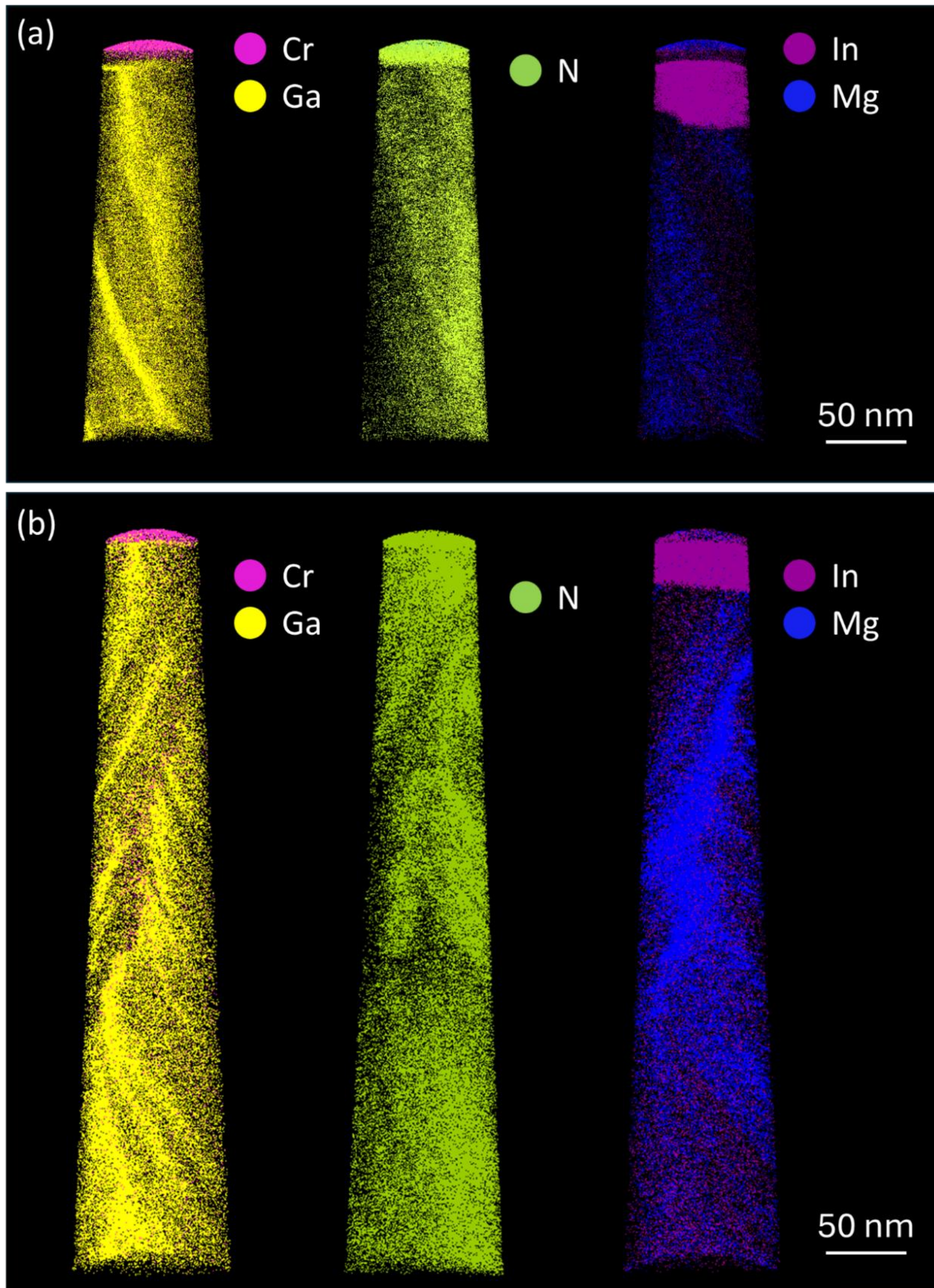

Figure 6-4 APT reconstructions illustrating two distinct SF arrangements in SQW GaN samples. Mg (blue) is enriched at SF regions and their intersections. Local variations in both Ga and N concentrations can also be observed along the SFs (a) Dataset R5111_26354: Parallel SFs extend through the APT needle, outlined by Ga (yellow) depletion. (b) Dataset R5111_26387: Several SFs intersect within the APT needle and form a fishbone-like mesh. Mg (blue) is enriched at their intersections. All maps share the same 50 nm scale bar.

6.2.3. Detection and Orientation-Dependent Indium Segregation at SFs

Figure 6-5 shows a closer look at the In distribution within the InGaN layers. The 3D reconstruction in Figure 6-5(a) left reveals a thin, In-rich layer located near the top of the analysed volume, with a thickness of about 2 nm, which can be assigned to the SQW. The lower region with less In atoms is assigned to the InGaN underlayer. Ga and In ions are shown in yellow and purple, respectively, and the red arrow indicates the analysis direction in the following discussion.

To assess the uniformity in both the growth direction and lateral direction, seven identical cylindrical regions of interests (ROIs) were placed uniformly into the tip cross-section, as shown in the Figure 6-5(a) right. One-dimensional In site-fraction profiles were extracted from each ROI along the analysis direction with a bin size of 0.2 nm. All profiles (Figure 6-5(b)-(h)) show the same trend: starting from the top of the ROI, a sharp In-enriched region corresponding to the SQW is observed, followed by a lower and nearly uniform In concentration in the underlying layer extending for 35–40 nm. Slight variations in peak position and In content within the two layers across all ROIs indicate that the SQW and the underlayer are not completely flat. While such non-uniformity could be consistent with the presence of SFs, it may also arise from general surface undulations or growth-related variations independent of SFs.

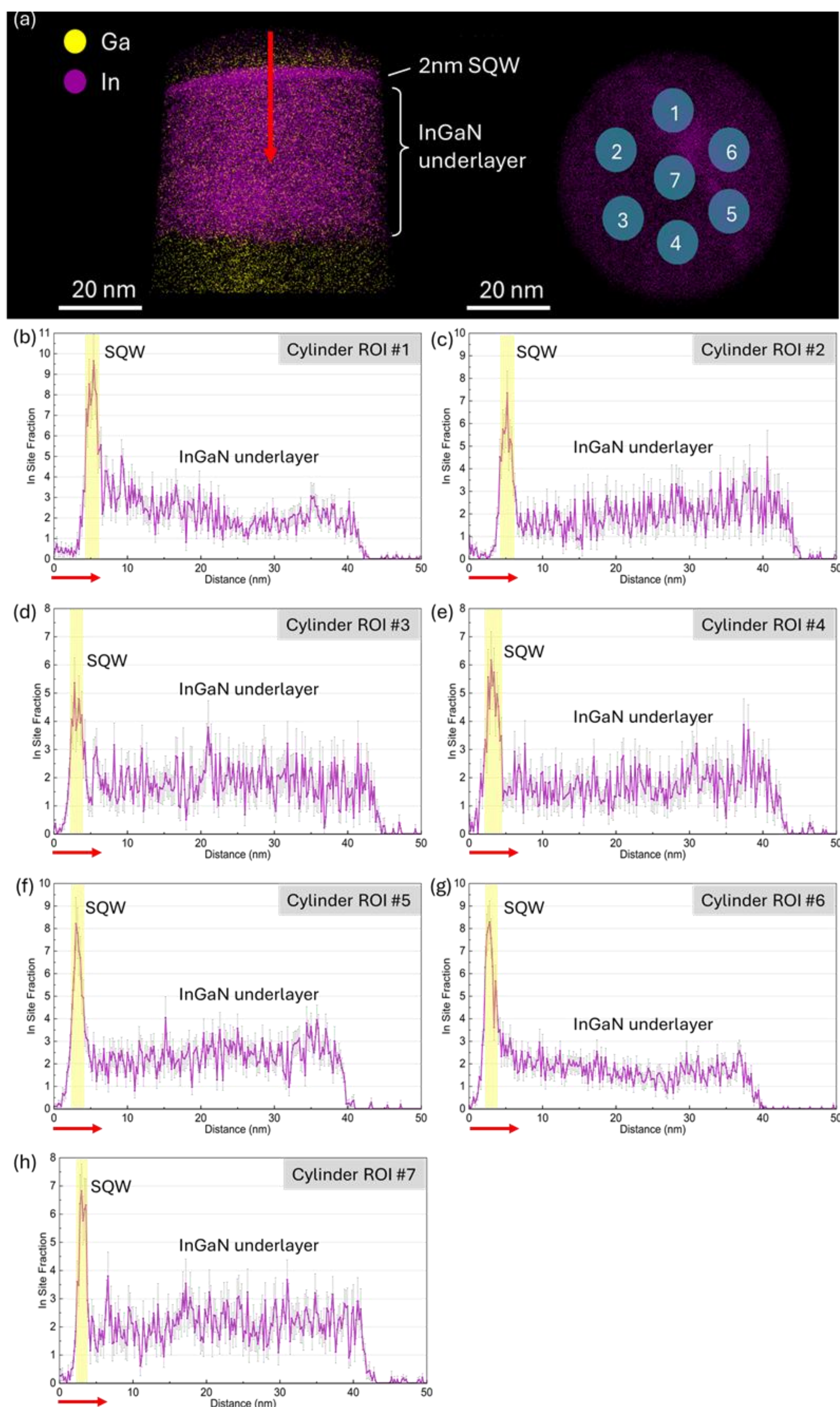

Figure 6-5 APT reconstruction of InGaN region within the analysed volume (R5111_26009). (a) Left: 3D reconstruction showing the distribution of Ga and In. Right: top view of the volume showing seven cylindrical regions of interest (ROIs 1–7) used for lateral sampling. (b–h) In site-fraction profiles versus distance extracted from ROIs 1–7 along the red direction in (a). Each profile shows a sharp In-rich peak at the SQW followed by a lower-In plateau from the InGaN underlayer, with slight variations between ROIs.

Figure 6-6 presents the compositional and field profiles extracted from two regions of the InGaN underlayer that contain SF-like features on different crystallographic orientations. Each profile was obtained from a $10 \times 50 \times 30$ nm^3 analysis volume oriented perpendicular to the SF-like plane, as indicated in the reconstruction. In both directions, a distinct In enrichment is observed at the location of the SF-like region, with Ga showing a complementary decrease. The segregation width and magnitude vary with orientation: the feature labelled A exhibits a wider and stronger In-enriched region, while that in orientation B shows a relatively weaker enrichment confined to a narrower zone. The corresponding field profiles are calculated by charge state ratio (CSR), Ga^{2+}/Ga^{+}. It should be noted that, in the region beyond ~18 nm of the bottom right panel, the Ga^{2+} counts are too low to produce a reliable ratio, which results in fewer valid data points in this portion of the profile, which results in fewer valid data points in this portion of the profile. The lines between neighbouring points are included only to guide the eye, and the field variations will be discussed in detail in the following discussion section.

The angle between SF-like features A and B further supports the presence of SFs. It should be noted that since the analysed volumes are located close to the specimen edge, part of the apparent field variation may arise from reconstruction geometry. In fact, the field profiles across the SF-like features do not exhibit any clear variation, which suggests that the local compositional change may be too small to induce a noticeable difference in the evaporation field. Moreover, the proximity to the tip edge and surface could further obscure any subtle field variation. Nevertheless, the repeated observation of indium enrichment at the same

crystallographic locations in multiple datasets indicates that this enrichment is genuine rather than an artefact of field effects or reconstruction geometry.

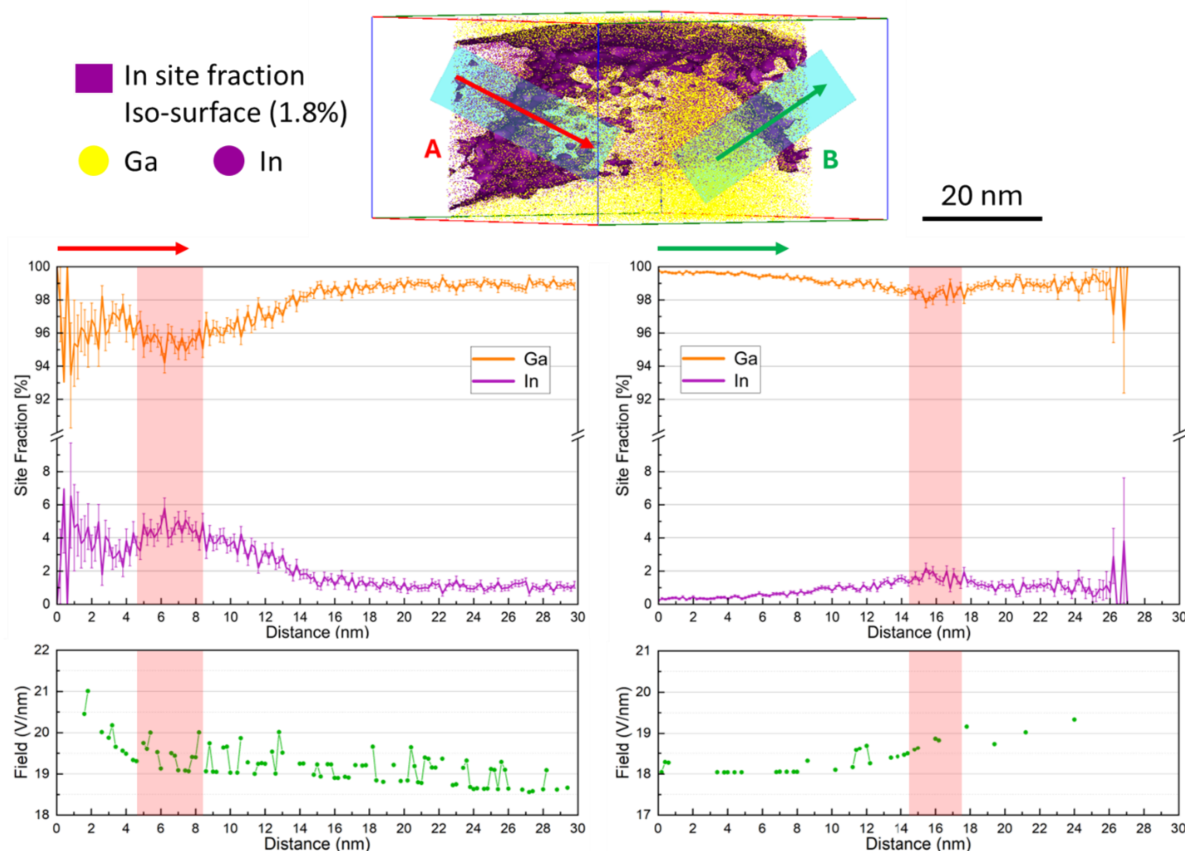

Figure 6-6 APT compositional and field profiles across two SFs of different orientations in the InGaN underlayer. The top panel shows the reconstruction (R5111_26387) with the regions of interest (SF-A and SF-B) indicated by arrows. The middle panels show the site-fraction profiles of Ga and In, demonstrating clear In enrichment at the SFs (red shaded regions), with complementary decreases in Ga. The bottom panels show the corresponding field profiles. The red-shaded regions are only used as visual markers to indicate the approximate locations of the SFs. The apparent width of these features depends strongly on APT reconstruction parameters and local field variations, therefore the physical spatial extent of SFs is not quantified or discussed here. The same convention is applied consistently in the following figures.

Figure 6-7 shows a closer look at the In distribution within the SQW of this dataset (same as in Figure 6-6). The 3D iso-surface map (In site fraction = 0.025) reveals a non-uniform In distribution, forming several extended In-enriched bands within the SQW. These bands appear at the intersection between the SQW and SFs and are roughly parallel to each other. The one-dimensional compositional profile in Figure 6-7(b) extracted along the indicated direction

(perpendicular to the bands) exhibits multiple peaks in the In site fraction at the SF and SQW intersections, accompanied by corresponding decreases in Ga. This confirms local In enrichment at these intersection regions. In addition, the extent of In enrichment clearly varies between the bands, with the In-enriched region on the left showing a higher In content of about 4–4.5% compared with approximately 2.8% on the right.

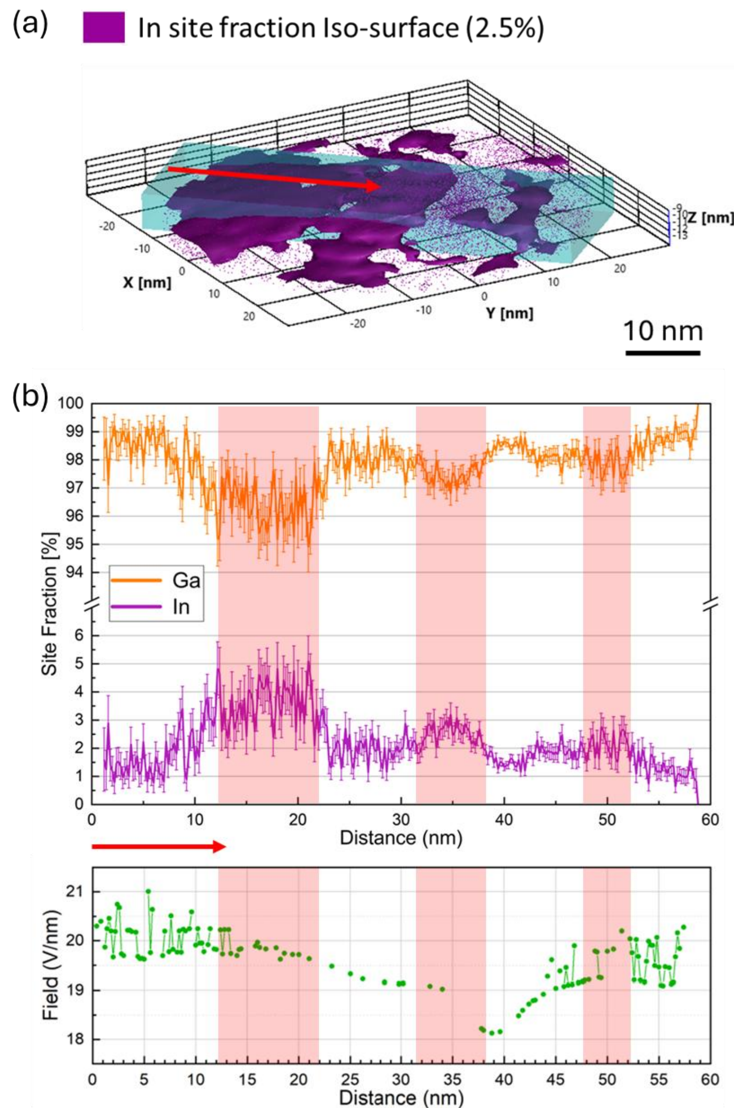

Figure 6-7 In distribution within the InGaN SQW (R5111_26387). (a) Iso-surface (In site fraction = 0.025) showing the In-enriched bands associated with SFs shown in Figure 6-6. The red arrow perpendicular to the In-enriched bands indicates the direction along which the site fraction profile and field profile in (b) were extracted. (b) (Top) Site-fraction profiles of Ga and In along the indicated direction, showing local In enrichment at the intersection of the SF and SQW (shaded area). (below) The corresponding field distribution. The SF regions are highlighted by red shaded boxes.

Figure 6-8 shows another reconstruction from the dataset R5111_26009 containing both SQW and the InGaN underlayer. A thin In-rich layer corresponding to the SQW is clearly visible in Figure 6-8(b), with an inclined In-enriched feature extending through the InGaN underlayer and intersecting the SQW. This feature is evident both in the atom map and in the corresponding In site-fraction iso-surfaces. In Figure 6-8(c), a top-down view of In site-fraction iso-surfaces further illustrates the In distribution. In addition to the indium enrichment on the inclined plane observed in Figure 6-8(b), as marked by the white dashed lines in the upper image of Figure 6-8(c), two additional In-enriched bands are visible in the upper image of Figure 6-8(c), as marked by the red dashed lines. These two bands are oriented nearly perpendicular to each other, with a measured angle of approximately 90°. This orthogonal arrangement supports the interpretation that SFs of different orientations intersect at the SQW, consistent with the expected geometry of {111}-type SF planes in cubic GaN. The corresponding two-dimensional indium site-fraction map below shows that the segregation of indium in these two additional bands is weaker than that in the primary In-rich band, while the indium enrichment tends to be higher at the junction of SFs, as indicated by the red high-intensity regions in Figure 6-8(c).

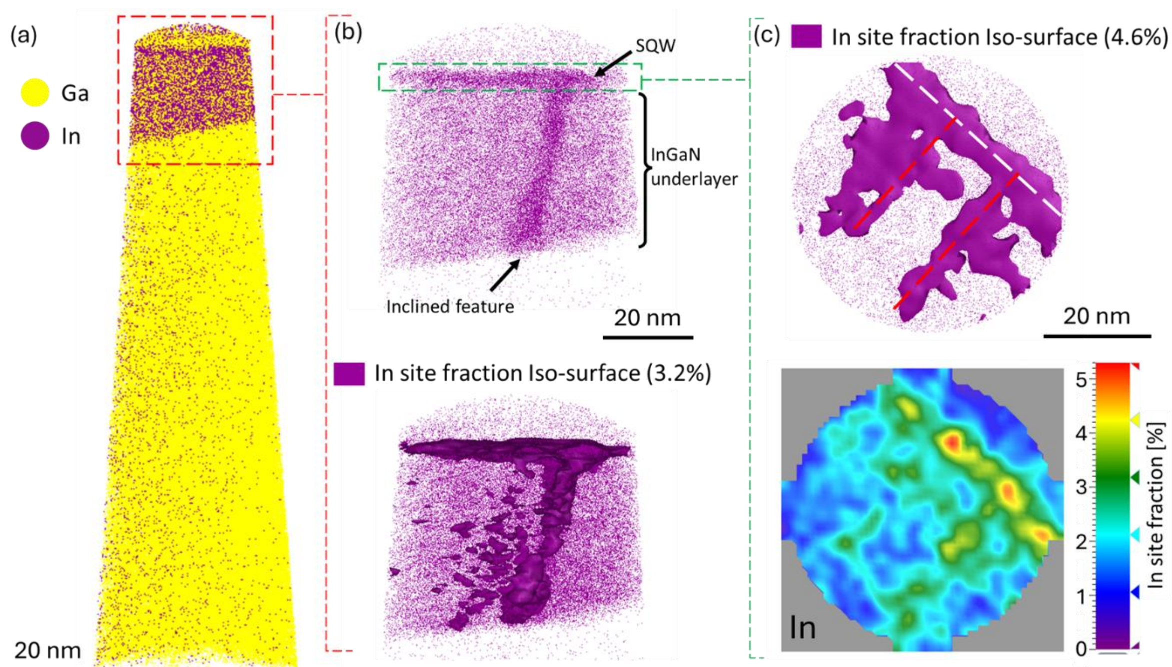

Figure 6-8 (a) APT reconstruction (R5111_26009) containing a SQW layer and the InGaN underlayer (region in red dashed box). (b) Above: A zoomed-in view of In distribution in the SQW and InGaN underlayer region. Below: The purple iso-surfaces show the In segregation. (c) Above: In segregation within the SQW from a top view, with SFs marked by the red dashed lines. Below: A 2D site fraction map of the distribution of In along the SQW from a top view. Data generated by the author and previously reported in *Journal of Physics D: Applied Physics* [238]. The figure has been modified by the author based on the published version and is reproduced under the terms of the Creative Commons Attribution 4.0 license (CC BY 4.0).

6.2.4. Mg Segregation and Local Field Variations at SFs

The Mg-doped GaN region also shows SF-related element segregation. As presented in Figure 6-9, the reconstructed volume reveals several planar features of same orientation across the analysed region. Three composition profiles were extracted from three ROIs perpendicular to the planar Mg-segregation features in the analysed region, as indicated by the blue boxes and red arrows in Figure 6-9(a). It should be noted that a carbon-rich surface layer appears in the reconstruction due to contamination during specimen preparation, transfer, and the APT experiment. Because carbon overlaps with Mg at 12 and 24 Da, it is rendered in the same colour. The Mg-segregation features appear in pairs, suggesting that segregation occurs on both sides

of the SF. These features are associated with SFs, which are discussed in detail in the following sections.

The fields were calculated based on the CSR across the same region of each profile. In the first profile (SF1) in Figure 6-9(b), a pronounced increase in Mg concentration is observed at the SF plane, with a corresponding decrease in Ga concentration and a distinct local reduction in the field. For SF2 and SF3, the Mg enrichment is still evident at each planar feature but much weaker. In Figure 6-9(d), the yellow shaded region corresponds to the extension of SF2, matching the second red-shaded region shown in Figure 6-9(c). The degree of Mg segregation in this region is noticeably lower than that in Figure 6-9(c). In terms of the field, SF3 shows apparent field increases in the vicinity of the Mg-enriched region, while SF2 shows intermediate behaviour with weaker field variations.

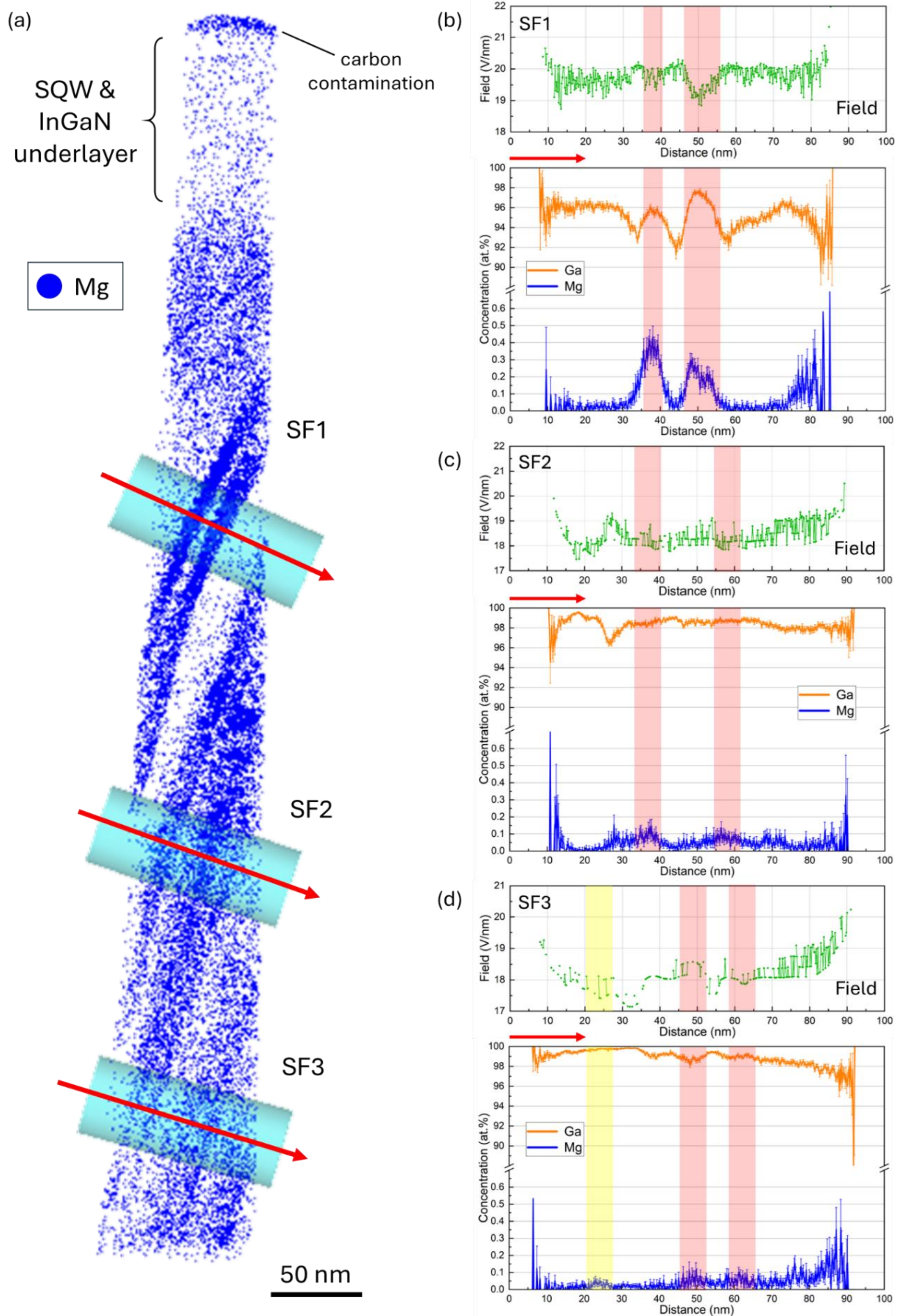

Figure 6-9 (a) APT reconstruction (R5111_26453) of the zb-GaN:Mg epilayer showing Mg segregation at individual SFs. Cylindrical ROIs are placed perpendicular to the planar features, and Mg atoms are rendered in blue. (b–d) Field and concentration profiles along ROIs (SF1–SF3), with SF-related regions highlighted by shaded boxes.

Rotating the same reconstructed volume in Figure 6-9 by approximately 90° about the axis of growth direction, another inclined Mg-enriched planar feature appears, as shown in the Figure 6-10(a). The SFs observed in Figure 6-9 and Figure 6-10 correspond to two intersecting {111} planes in cubic GaN, which appear perpendicular in the top-view projection, but the actual crystallographic angle between the two {111} planes is about 70.5°.

The compositional profile was extracted from the cylindrical ROI perpendicular to the SF-like region, as indicated by the blue box and red arrow in Figure 6-10(a). From this, Figure 6-10(b) shows the corresponding calculated field variations and concentration changes around the SF region. Different from the trend in Figure 6-9(a), although Mg is obviously increased at this region, the concentration of Ga decreases and the corresponding field strength increases locally.

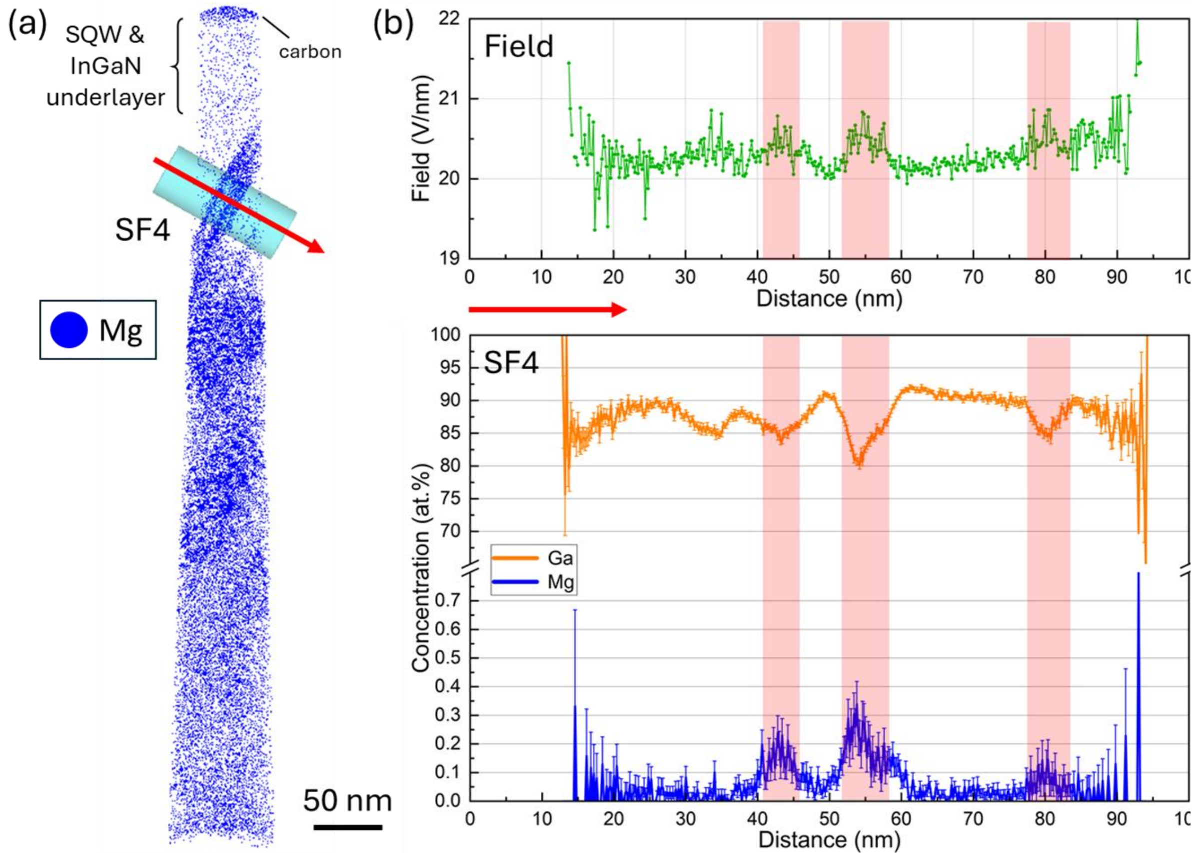

Figure 6-10 (a) APT reconstruction (R5111_26453, same tip as in Figure 6-9) highlighting a SF region in the zb-GaN:Mg epilayer, in another direction. Mg atoms are shown in blue. The top blue layer is carbon contamination accumulated during preparation, transfer, and the APT experiment. Due to peak overlap with Mg in the mass spectrum (e.g., at 12 and 24 Da), carbon is rendered in the same colour in the reconstruction. (b) 1D concentration profile taken along the direction indicated by the red arrow in (a). The blue box region measures $40 \times 40 \times 70 nm^3$. The regions corresponding to SFs are highlighted by red shaded boxes. All the data generated by the author and partly previously reported in *Journal of Applied Physics* [239]. The figure has been redrawn by the author based on the published data.

Another dataset captures the intersecting SFs, as shown in Figure 6-11. Figure 6-11(a) shows the segregation of Mg within the Mg-doped GaN region in the lower portion of the sample, highlighted by the blue Mg iso-concentration surfaces. The Mg-enriched planes on both sides of the specimen extend along two different directions and intersect in the blue band region, consistent with the structure and angles of {111} SFs. The reconstruction in Figure 6-11(b) shows a rectangular ROI made perpendicular to these SF planes to examine the Mg segregation

in more detail. The two-dimensional concentration map (right) further confirms the local Mg enrichment, with the concentration in the intersection region being several atomic percent higher than the surrounding area.

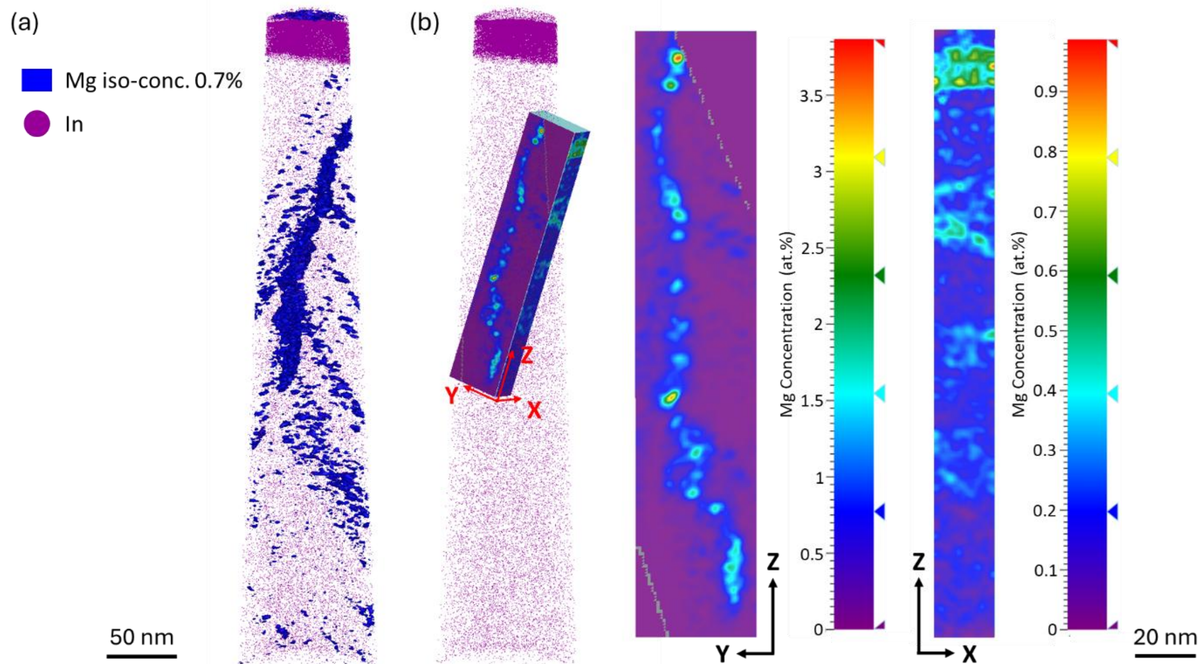

Figure 6-11 (a) APT reconstruction (R5111_26387) showing InGaN layers and Mg doped region. The intersecting SFs planes are highlighted by Mg iso-concentration surfaces (0.7%). The blue stripe-like region in the centre corresponds to the intersection of the SF planes. The viewing direction is approximately perpendicular to the SF planes, so they appear as stripe-like features in this projection. (b) A rectangular ROI was defined along this viewing direction, i.e., perpendicular to the SF planes, to include the intersection region. The two-dimensional Mg-concentration map derived from this ROI reveals local Mg enrichment along the SFs and at their intersection.

A cluster search analysis was additionally performed for Mg within the analysed volumes, and no statistically significant Mg clustering was detected. This indicates that the observed Mg enrichment is associated with planar SF features rather than 3D dopant clusters, in contrast to clustering behaviour often reported in wurtzite GaN [241, 242].

6.3. Discussion

6.3.1. Interaction between SFs

Figure 6-1 and Figure 6-2 correlate the structural and compositional features associated with SFs in the InGaN SQW, underlayer and the underlying GaN:Mg region via STEM and APT in this study. The STEM cross-sectional images in Figure 6-2 observed parallel and intersecting SFs propagating along the {111} planes and extending through all the layers. The APT reconstructions in Figure 6-4 show the elemental distribution in the corresponding layers, most notably the enrichment of indium within the SQW and of magnesium to planar features in the doped GaN. The close agreement between the location and orientations of the SFs identified in STEM and the planar enriched features in APT therefore provides clear evidence that these are indeed SFs.

In several APT datasets, such as R5111_26387 in Figure 6-11, the SFs are not isolated and parallel, but form intersecting networks, forming a characteristic 'fishbone-like' crossover when viewed in projection. The spacing between these SFs is typically in the range of tens of nanometres, and their intersections coincide with regions showing enhanced indium segregation within the SQW. For example, in Figure 6-8I, the indium site fraction reaches approximately 5% at the SF intersections, compared with about 3% along non-intersecting regions of SFs. This kind of crossover is consistent with the structural behaviour observed by Lee *et al.* [120], who reported in zincblende GaN, SFs propagating along different {111} directions were shown to interact with each other, with certain configurations leading to

annihilation whereas others remain stable. Their simulation (see Figure 6-12) demonstrates that such crossed configurations can naturally arise when SFs on multiple orientations propagate concurrently, regardless of the initial growth conditions. The similarity between the observed 'fishbone-like' structure in this APT study and their model suggests that mutual SF interactions play a key role in shaping the local SF morphology.

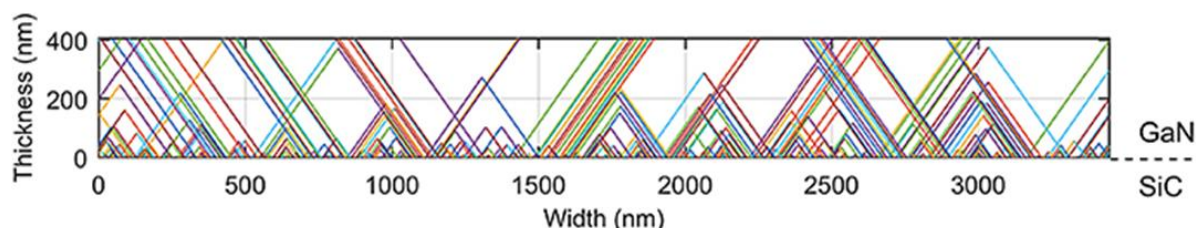

Figure 6-12 Simulation of SF annihilation in a zincblende epilayer reported by Lee *et al.* [120].

Therefore, the 'fishbone-like' structure observed in the APT reconstructions can be understood as a 3D manifestation of the interactions between intersecting SFs. This observation is consistent with previous reports [120], which showed that the local density and spatial distribution of SFs in InGaN are influenced not only by external growth parameters but also by mutual SF–SF interactions that affect their propagation and termination behaviour. In the regions of multiple SF intersections, enrichment of indium and magnesium is consistently observed. This implies that these intersections serve as preferential sites for solute accumulation, which is likely driven by increased local strain or variations in the local bonding environment associated with the combined SF structure.

Similarly, the weaker Mg segregation observed in the extended part of SF2 (yellow-shaded region in Figure 6-9(d)), with a peak concentration of about 0.05 at.%, is likely caused by the

higher SF density in the lower region of the sample. The presence of multiple SFs with different orientations may lead to a redistribution of Mg atoms among them, thereby reducing the degree of segregation compared with the region shown in Figure 6-9I, where the concentration reaches around 0.1 at.%.

6.3.2. Orientation-Dependent Segregation Behaviour

Multiple APT reconstructions in this chapter, such as in Figure 6-8 and Figure 6-9, reveal that both indium and magnesium segregate preferentially along planar features corresponding to SFs, which is also consistent with the In segregation trends discussed in Chapter 5. However, the SQW samples presented in this chapter suggest that the extent of segregation may vary between SFs of different orientations. In the SQW region, as shown in Figure 6-8I, indium enrichment appears more pronounced along the inclined plane marked by the white dashed line, while the perpendicular SFs highlighted by the red dashed lines show visibly weaker enrichment. Although no quantitative composition analysis was performed, the contrast between these regions is consistent across several reconstructions. The intersections of these SFs exhibit the highest indium site fraction, reaching approximately 5%. A similar trend is observed in the InGaN underlayer, as shown in Figure 6-6, where the indium site fraction along one orientation (~5%) is approximately 2.5 times higher than that along another direction (~2%). These results demonstrate that indium segregation occurs at SFs within the InGaN underlayer and that the extent of segregation may depend on the orientation of the SF plane. This difference can be attributed to variations in the local atomic configuration and strain state

between distinct {111} planes. Similar effects have been predicted by first-principles calculations, which show that different SF configurations produce distinct strain and potential distributions [100]. Local strain variations are also known to affect indium incorporation efficiency in InGaN [243]. In APT, these strain-induced differences in local bonding strength can also influence the field evaporation behaviour, as atoms in strained regions may require slightly higher or lower evaporation fields. Therefore, the changes in the apparent evaporation field observed here may reflect local modifications of the bonding environment [188]. Overall, these results indicate that the degree of indium segregation in the InGaN layers is not uniform. While a possible dependence on the crystallographic orientation of the SFs is suggested by the observed trends, further data would be required to confirm this relationship. It should be noted that APT cannot resolve the crystallographic orientation of individual SF, since no poles were observed within these datasets to extract crystallographic information. Therefore, the present discussion is limited to relative orientation effects, and possible correlations with polarity and SF type will be addressed in the following section.

In the Mg-doped region, a slight difference in the apparent extent of Mg segregation can also be observed between different SF orientations. As shown in Figure 6-9 and Figure 6-10, both views correspond to the same APT needle, with Figure 6-10 obtained by rotating the reconstruction in Figure 6-9 by 90° along the growth direction. The degree of Mg enrichment at SF1 appears slightly higher in the orientation shown in Figure 6-9 compared with the rotated view in Figure 6-10. However, the most pronounced variation in the Mg-doped layer is associated with the position of the SFs within the sample. In the Mg-doped region, a gradual

decrease in Mg segregation can be observed from the top towards the bottom of the APT specimen. As shown in Figure 6-9, Mg enrichment is strongest at SF1, located near the specimen surface, reaching approximately 0.4 at.%, whereas SF2 shows a weaker enrichment of about 0.1–0.15 at.%, and at SF3 the Mg concentration falls below 0.1 at.%. These values are directly obtained from the compositional profiles and illustrate a clear trend within this dataset. However, given the limited number of analysed SFs and the potential influence of local structural variations, this apparent difference should be interpreted cautiously. Combined with the SF annihilation simulation shown in Figure 6-12, which indicates the SF density in the lower part of the specimen is higher than near the surface, this may suggest that Mg segregation in the lower regions is likely affected by the presence of additional SFs nearby.

In addition to the individual SF, pronounced Mg enrichment can also be found at the intersections of SFs, as with the case of indium in SQW. As illustrated in Figure 6-11, the Mg concentration at these junctions of multiple $\{111\}$ SFs is noticeably higher than that of isolated SFs. It should be noted that the difference in apparent Mg concentration between the two projections in Figure 6-11(b) arises from volume dilution. In the projection perpendicular to the SF planes, the thin Mg-enriched layers are intersected directly, producing a stronger contrast. In contrast, the projection parallel to the SFs integrates the signal over a thicker volume, reducing the apparent enrichment. Six cylindrical ROIs ($4 \times 4 \times 50\ nm^3$) were placed at both SF intersections and along isolated SF, respectively. The average Mg concentration is 0.94 ± 0.18 at.% at the SF intersections and 0.15 ± 0.05 at.% along the isolated SFs, confirming that Mg segregation is significantly enhanced at the SF intersections.

The enhanced Mg segregation at SF intersections can be understood as a combined effect of local strain accumulation and potential variations associated with SFs, as discussed earlier for In segregation. When multiple {111} SFs intersect, the superposition of their strain field and electrostatic potential modifies the local atomic environment, potentially creating energetically favourable sites that facilitate Mg incorporation. Similar effects have been discussed in theoretical and experimental studies [100, 243], which demonstrated that individual SFs in GaN can induce local strain and potential perturbations that affect defect and impurity energetics. Recent investigations have also begun to explore the case of intersecting SFs [244, 245], revealing that the intersection of SFs with different orientations can cause local atomic rearrangements and strain redistribution. These findings provide useful context for interpreting the Mg enrichment observed at SF intersections in the present study. Atomistic simulations further revealed that when {111} SFs intersect, the local atomic arrangement becomes distorted and strain redistribution occurs, resulting in local lattice relaxation [120]. Therefore, such concentrated strain and lattice distortion at SF junctions may promote impurity incorporation in these regions.

6.3.3. Different Types of SFs and Their Field and Chemical Characteristics

Apart from elemental segregation, the SFs in the Mg-doped region show different behaviours in terms of their local evaporation field in APT. For example, in the SF1 shown in Figure 6-9(b), the local field decreases at the SF region, accompanied by an enrichment in Mg and an apparent

increase in Ga concentration compared to its immediate vicinity (designated here as Type-LF, according to the apparent lower evaporation field at the SF region). In contrast, the SF observed in Figure 6-10 shows a local field increase, with Mg enrichment still present but Ga concentration decreasing (designated as Type-HF). The apparent change in Ga concentration can be attributed to the dependence of the measured Ga and N concentrations on laser pulse energy, as shown in Figure 4-10. Higher laser energies correspond to lower fields, resulting in reduced N detection and consequently an apparent increase in Ga concentration. When quantified as Ga/(Ga+Mg) and Mg/(Ga+Mg); site fractions, as shown in Figure 6-13, Ga remains approximately constant or slightly decreases in both cases, indicating that the apparent Ga rise in Type-LF regions originates from nitrogen undercounting as a consequence of a reduced electric field rather than true enrichment.

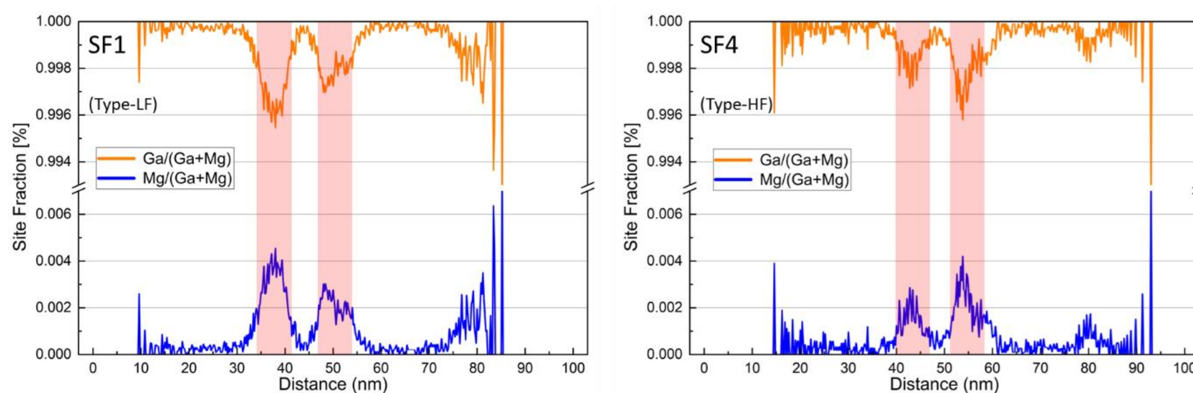

Figure 6-13 Comparison of Mg and Ga site fractions across two SFs, SF1 (Type-LF) and SF4 (Type-HF), within the Mg-doped GaN region. The SF related regions are highlighted by red shaded boxes.

These opposite field behaviours imply that the corresponding SFs may have different structural or electrostatic configurations. As mentioned in Chapter 2, each SF in zincblende GaN represents a local wurtzite-like bilayer insertion carrying a built-in polarisation along its local

c-axis. Structurally, SFs in zincblende GaN can be classified as intrinsic (i-SF) or extrinsic (e-SF), depending on whether one {111} plane in the normal ABC stacking sequence is missing or inserted. As shown in Figure 6-14, an i-SF occurs when a stacking plane is missing from the usual sequence, changing the pattern from -ABC-ABC-ABC- to -ABC-AC-ABC-, and introducing four monolayers of wurtzite stacking. On the contrary, an e-SF results from inserting an extra stacking plane, producing a sequence of -ABC-B-ABC-, corresponding to three monolayers of wurtzite stacking. It should be noted, however, that e-SFs are reported to be extremely rare in GaN and have only been observed occasionally even in high-resolution transmission electron microscopy (TEM) studies. Therefore, while both types are described here for completeness, the specific identification of an e-SF in the present APT data cannot be confirmed. In the meantime, these two types of SFs differ in their stacking sequence and formation energy [100, 243], but they do not necessarily correspond to opposite structural polarities. In other words, the polarity (Ga-polar or N-polar) refers to the orientation of the Ga–N bond along the c-axis, rather than to whether the SF is intrinsic or extrinsic. In the present APT analysis, polarity contrast can be inferred from the field–composition correlation (e.g., Ga depletion or enrichment), but the distinction between i-SF and e-SF cannot be determined from APT data alone.

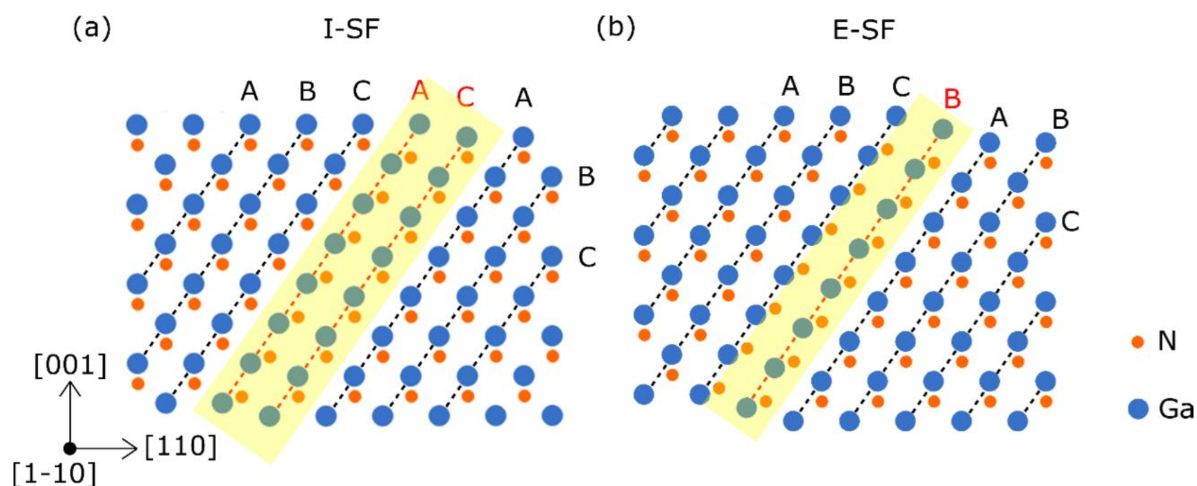

Figure 6-14 Schematics of (a) an i-SF with four monolayers and (b) an e-SF with three monolayers in a zincblende GaN lattice. The red dotted lines indicate the faulted regions that miss or have an extra (-1-11) lattice plane. The yellow shaded regions show the monolayers of wurtzite stacking. Adapted from [246].

Depending on the stacking sequence, their local polarisation may align parallel or antiparallel to the external electric field, leading to either field enhancement or reduction. First-principles and experimental studies have demonstrated the existence of such polarity-dependent charge accumulation at wurtzite–zincblende interfaces in GaN [243, 247]. More recently, Xiu *et al.* [94] confirmed that the {111}A (Ga-terminated) and {111}B (N-terminated) planes in cubic GaN possess opposite structural polarities, corresponding respectively to Ga-polar and N-polar orientations. Although the cubic GaN structure itself is centrosymmetric and non-polar, these planes are not the same in terms of crystallography. The {111}A planes are Ga-polar, with the polarity vector pointing along the [111] direction (from Ga to N), while the {111}B planes are N-polar, pointing along [–111]. It should be noted, however, that this polarity distinction does not directly correspond to the intrinsic or extrinsic nature of SFs. In practice, both types of SFs can occur on either polarity, but in GaN, most observed SFs are intrinsic. The SFs observed in

the present study are therefore most likely intrinsic SFs with opposite polarities, i.e., one Ga-polar and the other N-polar, which may account for their different field-chemical behaviours.

The I-SF is structurally equivalent to a wurtzite-like insertion with its c-axis oriented along [0001]. Depending on the local stacking sequence, the corresponding SF can occur on either the {111}A (Ga-polar) or {111}B (N-polar) plane. This polarity difference gives rise to opposite local fields and corresponding variations in elemental enrichment. This relationship between structure and polarity could explain the two opposite fields and corresponding composition signatures observed in the APT data. In the APT data, Type-LF SFs (local field decrease) and Type-HF SFs (local field increase) exhibit distinct field and compositional characteristics. These differences may reflect variations in the local polarity of the SFs, such as whether the internal polarisation opposes or aligns with the external field, rather than differences in their intrinsic or extrinsic nature. However, since the precise crystallographic orientations of the individual SFs cannot be confirmed from the present APT dataset, this interpretation should be considered a reasonable possibility rather than a firm conclusion. Although small variations in the apparent field may also be caused by tip geometry or reconstruction effects, the consistent correlation between the field behaviour and Mg segregation strongly supports an intrinsic polarity-related origin. The existence of opposite polarisation directions in different SF configurations has been experimentally verified by Lähnemann *et al.* [243] using time-resolved photoluminescence spectroscopy. They determined the spontaneous polarisation of GaN from the emission energies of excitons bound to SFs. Although their analysis included both intrinsic and extrinsic SFs, the key finding that

SFs can exhibit opposite polarisation directions between the wurtzite and zincblende segments is directly relevant here, supporting the polarity-dependent field variations observed in the present APT analysis. To the best of our knowledge, however, no APT studies have directly correlated solute segregation at SFs with their polarity. The present results therefore provide the first experimental indication that SF polarity may influence local Mg segregation behaviour.

The observation of Mg enrichment peaks on both sides of the SF indicates that the local polarisation field extends across the SF plane. The observed asymmetry in Mg segregation between SF1 and SF4 (with SF1 showing a higher Mg concentration in the first peak, while SF4 shows the opposite trend) may indicate that the two SFs possess opposite polarities, consistent with Ga- and N-terminated {111} planes. However, since multiple SFs may be present within the analysed region and cannot be completely resolved in the current APT reconstruction, this interpretation is tentatively proposed as a possible explanation for the observed asymmetry. Different from In, which generally segregates close to the SF plane due to strain-assisted incorporation in InGaN structures [248], the charged acceptor Mg is more sensitive to the local electrostatic potential and therefore accumulates on both sides of the polarised region. Considering the atomic configuration shown in Figure 6-14, Mg is most likely segregating to substitutional Ga sites (Mg_{Ga}) near the SF planes, rather than interstitial positions, since substitutional incorporation is energetically more favourable in GaN [249, 250]. The local polarity reversal across the SFs gives rise to internal electrostatic fields, which have been experimentally determined from excitonic emission of Intrinsic and extrinsic SFs [243]. Such fields can attract positively charged Mg_{Ga}^{+} towards the negatively polarised sides of the

SFs, providing a natural explanation for the double Mg-enrichment peaks observed in the present APT data [251]. This leads to the appearance of a double Mg-enrichment peak across the SF, whereas In has been reported to show a single maximum close to the SF plane due to its strain-driven incorporation [238], the limited spatial resolution of previous studies means that bilateral segregation cannot be completely excluded. For instance, Ding *et al.* [25] reported a double-peak In enrichment using high-resolution (HR) STEM and EDS under different growth conditions, suggesting that the local potential asymmetry and diffusion length may also affect the segregation behaviour. In addition, although the apparent double-peak feature in Mg may be partially amplified by local reconstruction effects or field gradients inherent to APT analysis, the consistent negative correlations between Mg and Ga and polarity-dependent asymmetries observed across multiple regions support that this phenomenon mainly reflects a genuine chemical redistribution driven by the internal polarisation field rather than an artefact of data reconstruction.

It is therefore necessary to determine whether the observed Mg segregation could be influenced by field-evaporation artefacts in APT. Several independent observations in the present work support the former interpretation. The spatial correspondence between the SF planes identified by STEM and the planar In-rich features observed in both STEM-EDS (Figure 6-3) and APT (Figure 6-8) indicates that these enriched features are spatially associated with the SFs. The co-localisation of Mg enrichment with the same planar features in APT further supports that Mg segregation is associated with the SFs rather than randomly distributed throughout the volume. In addition, the segregation behaviour is reproducibly observed across multiple independent

datasets (e.g. tips R5111_26387, R5111_26453, and R5111_26009), demonstrating that the effect is not specific to a single reconstruction or analysis condition. Furthermore, the magnitude of segregation exhibits a clear dependence on the crystallographic orientation of the SFs, with systematically different enrichment strengths and even opposite trends in inferred local field behaviour for different SF types. Such orientation-dependent behaviour is consistent with a physically driven segregation mechanism linked to local defect structure and polarity, rather than a uniform field-evaporation artefact. Moreover, the Mg concentration profiles reveal bilateral enrichment on both sides of the SF plane, as shown in Figure 6-13, which is physically consistent with electrostatic interactions with the internal polarisation fields associated with the SFs, whereas field artefacts more commonly produce asymmetric smearing along the analysis direction.

Taken together, the spatial correlation with SFs, reproducibility across independent datasets, crystallographic orientation dependence, and physically consistent bilateral enrichment profiles strongly support that the Mg segregation represents a genuine dopant redistribution at SFs rather than a field-evaporation artefact.

In summary, these relationships are shown in Table 6-2, which compares the observed field and chemical features with their likely structural polarity and SF type. For the InGaN regions near the specimen apex, the apparent field signal shows no clear variation across the SFs in any of the analysed datasets. Therefore, it is not currently possible to make a reliable assessment of

SF polarity. Nevertheless, the pronounced In enrichment observed along the SFs confirms their structural correlation, even though the relationship between field and polarity cannot yet be established.

Table 6-2 Field-chemical characteristics of SFs with different polarities in Mg-doped GaN

Type	Evaporation field behaviour	Mg	Ga (at.%)	Ga/(Mg+Ga)	Polarity	Interpretation
Type-LF	↓ (lower field)	↑	↑ (due to N loss)	↓	{111}A (Ga-polar)	Polarisation opposes external field; reduced field causes apparent Ga rise; corresponds to Ga-polar SF
Type-HF	↑ (higher field)	↑	↓	↓	{111}B (N-polar)	Polarisation aligned with external field; higher local field, Ga depletion; corresponds to N-polar SF

6.3.4. Implications for Other Dopant Species

The segregation behaviour observed for Mg at SFs raises the question of whether similar redistribution would occur for other dopant species, such as in more conventional Si-doped GaN structures. Mg is known to incorporate as a substitutional acceptor (Mg_{Ga}^{+}), whereas Si typically acts as a shallow donor in GaN (Si_{Ga}^{0} or Si_{Ga}^{-}depending on the Fermi level position) [249, 250]. As a result, the driving forces for dopant redistribution at SFs are expected to be different.

The present results suggest that Mg segregation is strongly influenced by the internal polarisation fields associated with the SFs, consistent with previous reports [243, 247]. The observation of bilateral Mg enrichment on both sides of the SF plane is consistent with a

possible electrostatic attraction towards regions of opposite local polarity. In contrast, Si donors are therefore expected to be less sensitive to local electrostatic potential variations than charged acceptor species such as Mg, and more likely to follow strain- or bonding-energy-driven segregation mechanisms, similar to those reported for indium in InGaN alloys [25, 248].

Therefore, while some degree of dopant accumulation at SFs may still occur in Si-doped structures due to local strain and bonding variations, the pronounced polarity-dependent and double-peak segregation behaviour observed for Mg would not necessarily be expected. Instead, Si segregation, if present, would likely resemble the more symmetric and strain-assisted enrichment behaviour observed for indium rather than the polarity-driven asymmetric redistribution characteristic of Mg [25, 248].

It should also be noted that a direct experimental comparison with Si-doped structures is further complicated by mass-spectrum peak overlap in APT analysis, where Si-related peaks (e.g. 14 Da and 28 Da) coincide with those of nitrogen species. This overlap makes it challenging to quantify the Si segregation in GaN, and therefore such behaviour was not explicitly analysed in the MQW datasets presented in this thesis.

6.3.5. Related Optical Properties

The polarity-dependent variations in local field and chemical segregation described in the previous section are also expected to directly influence the optical response of the InGaN/GaN structures. The modulation of the internal electrostatic potential at SFs can locally alter carrier confinement, recombination rates, and transition energies within the QW. In particular, intersecting or high-density SF regions may act as sites for potential fluctuations or non-radiative centres, thus affecting both the emission intensity and spectral characteristics. To explore these effects, the present observations are compared with CL measurements reported for zincblende InGaN/GaN SQW sample.

In this APT study, the results reveal that In enrichment consistently occurs along SFs intersecting the SQW and the InGaN underlayer, with the strongest segregation found at the intersection of multiple SFs. The corresponding CL results from Gundimeda *et al.* demonstrate that the presence of SFs within the zincblende InGaN/GaN SQW strongly influences the local luminescence intensity and emission energy [238]. As shown in Figure 6-15, the regions without SFs (S1) exhibit strong quantum-well emission near 3.0 eV, while the regions containing a high density of SFs (S2) show a pronounced reduction and red-shift of the emission, which indicates that there are carrier localisation and non-radiative recombination associated with the extended defects. Intermediate emission behaviour is observed near the edges of individual SFs (S3), where strain relaxation and compositional modulation may partially compensate the internal potential fluctuations. These results directly support the

correlation between the SF distribution and local optical response. Together with the APT observations in this study, it can be concluded that the SF-related changes in local strain, composition, and polarisation would jointly modulate the SQW properties. Therefore, the regions containing dense or intersecting SFs tend to exhibit weaker and red-shifted luminescence, consistent with enhanced carrier capture and a possible increase in non-radiative recombination at these SF sites, which could lead to reduced radiative efficiency.

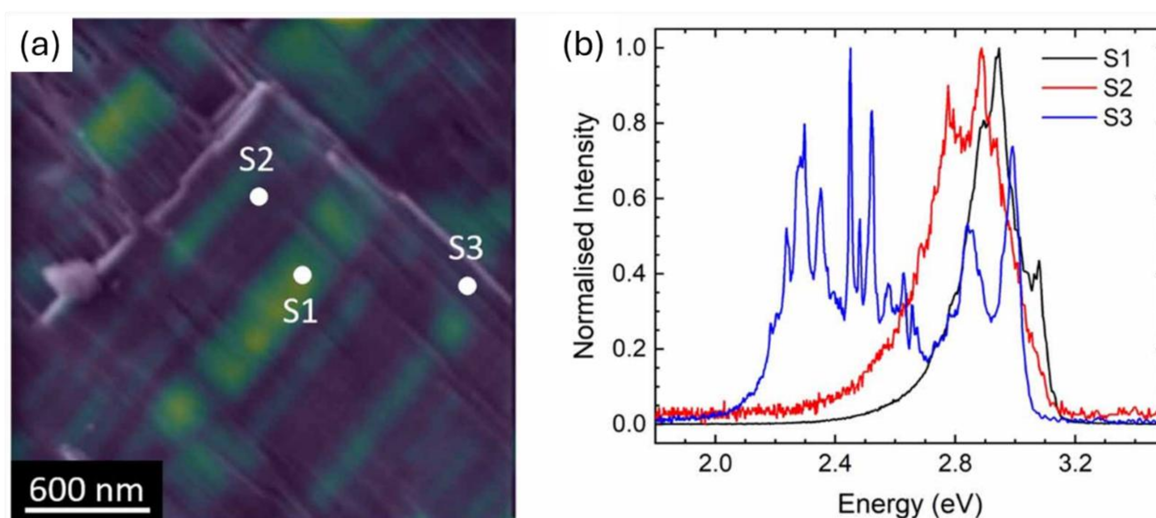

Figure 6-15 (a) An overlay of the SE and the panchromatic CL intensity map of the zincblende InGaN/GaN SQW sample (the same sample) showing variations in emission intensity associated with SFs. (b) Corresponding CL spectra recorded from the three representative positions indicated in (a). S1: undisturbed region free of SFs, showing strong SQW emission near 3.0 eV, S2: region rich in SFs, exhibiting quenched and red-shifted emission, S3: at the edge of a SF or SF bunch, showing suppressed SQW emission together with multiple sharp low-energy localised peaks. Adapted from [238].

In the Mg-doped zincblende GaN layer, the CL mapping and point spectra presented by Xu *et al.* [239] provide direct evidence of the impact of SFs on the optical behaviour. As shown in Figure 6-16, regions free of SFs (A, B) exhibit a dominant near-band-edge (NBE) emission at ~3.23 eV with minimal contributions from Mg-related transitions. In contrast, positions located on or near SFs (C, D) show a pronounced suppression of the NBE peak and an enhancement

of deeper Mg-related emission bands (peaks 2–4), indicating increased non-radiative recombination and altered local electronic potential near the SFs.

These observations are consistent with the APT results in this study, where Mg segregation was found to occur preferentially along SFs and particularly at SF intersections. The accumulation of Mg at these defects likely introduces local potential fluctuations and defect states, promoting radiative transitions from Mg-related levels, while the associated defect states could also act as non-radiative centres that reduce the relative intensity of band-edge emission. The combination of compositional modulation and internal polarisation fields at the SFs thus leads to spatial variations in luminescence intensity and spectral shape across the Mg-doped region.

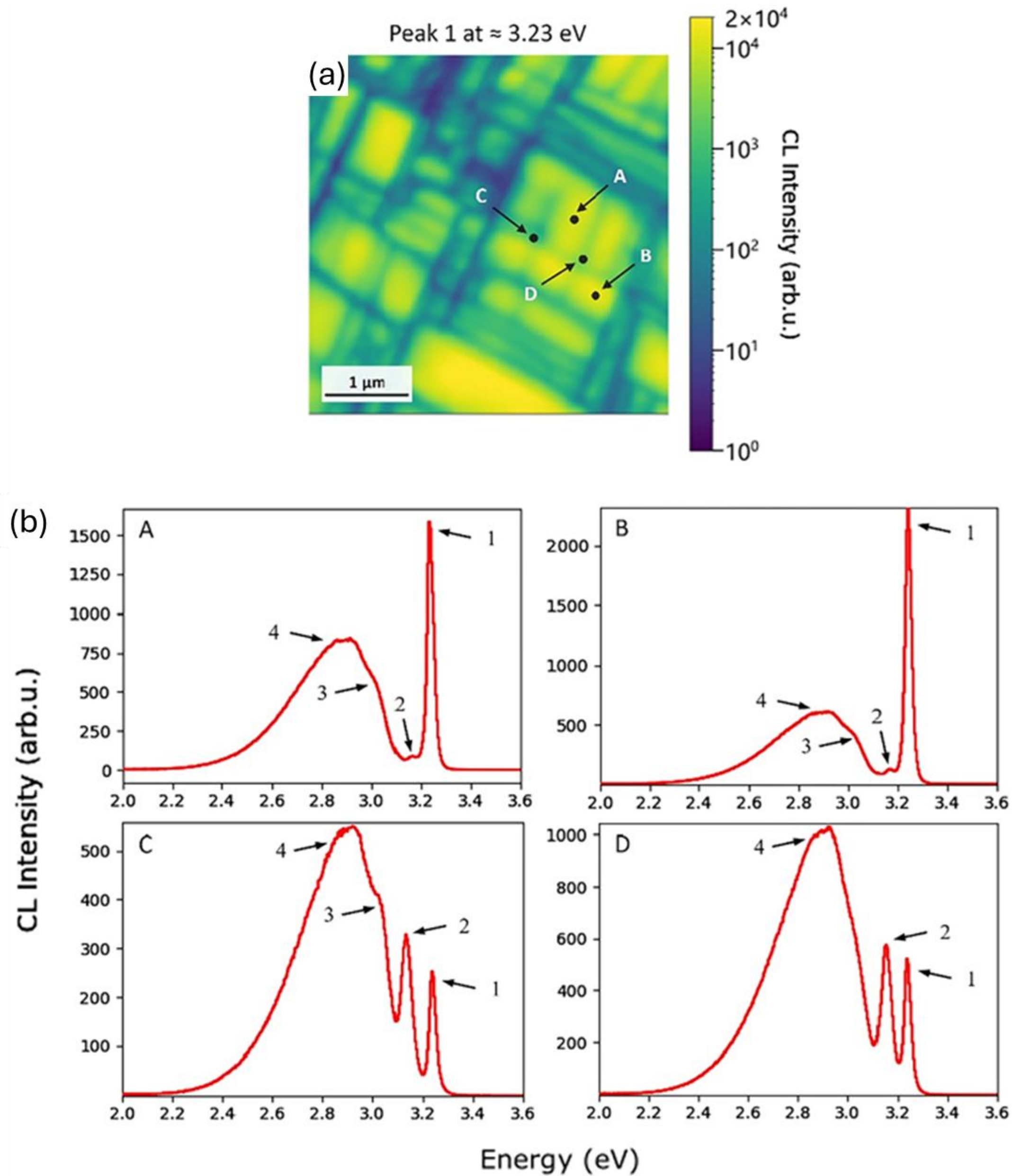

Figure 6-16 CL point spectra recorded at and away from SF locations in zincblende GaN:Mg. (a) CL intensity map showing the measurement positions. Points A and B correspond to regions free of SFs, C and D are located on SF-rich areas. (b) CL spectra from these positions showing the main band-edge emission at ~3.23 eV (peak 1) and additional peaks (2–4) associated with Mg-related states. The spectra from SF regions (C, D) exhibit reduced intensity of the band-edge emission and enhanced Mg-related features, indicating a strong influence of SFs on the local optical response. Adapted from [239].

Overall, the CL observations from both InGaN and Mg-doped GaN confirm that SFs significantly affect the local optical properties. In the InGaN SQW, SF-rich regions exhibit reduced and red-shifted emission due to carrier localisation and strain-induced potential

variations, while in GaN:Mg, SFs suppress near-band-edge emission and enhance Mg-related bands, consistent with Mg segregation revealed by APT.

6.4. Conclusion

In this chapter, combined STEM and APT analysis revealed that both In and Mg preferentially segregate along SFs in zincblende GaN-based structures. The extent of segregation varies with SF orientation and polarity, leading to two characteristic types (Type-LF and Type-HF) associated with Ga- and N-polar configurations. Intersecting SFs would also promote impurity accumulation due to the combined effects of local strain and internal electrostatic fields. These structural and chemical variations were correlated with optical observations, where SF-rich regions exhibited reduced near-band-edge emission and enhanced defect-related luminescence. Overall, SFs in the SQW sample are shown to actively influence both the electrical and optical behaviour of cubic GaN through their coupled structural, electrostatic, and chemical effects.

Chapter VII Conclusions and Future Work

7.1. Conclusion

This thesis develops a comprehensive experimental and analytical framework for understanding the structural, chemical and optical behaviour of GaN-based materials through the correlative use of atom probe tomography (APT), scanning transmission electron microscopy (STEM) and cathodoluminescence (CL).

Previous optical and structural studies on GaN and InGaN structures have mainly used PL, CL and (S)TEM to correlate stacking faults (SFs) with luminescence features, identifying SFs either as non-radiative centres or as locations of characteristic defect-related emission peaks, but without direct 3D chemical information [43, 92, 108]. Similarly, alloy segregation at SFs in zincblende GaN heterostructures has been reported using high-resolution STEM-EDS [25], showing enhanced In and Al concentrations in the vicinity of SFs. However, these studies are limited to two-dimensional cross-sections and do not directly link the segregation to local luminescence. Building upon these advances, this thesis developed and validated a methodology for the reliable APT analysis of GaN and InGaN/GaN heterostructures.

Chapter 4 optimised specimen preparation and acquisition protocols to deal with issues such as APT sample fracture, Ga implantation, and stoichiometric drift, enabling reproducible

datasets to be obtained with accurate quantification. This methodological framework provided the foundation for the defect analyses in later chapters and future studies.

Chapter 5 demonstrated that SFs in zincblende GaN can be visualised and quantitatively characterised using APT, owing to the local variations in the evaporation field associated with the SF regions. Quantitative APT-STEM correlation revealed that the apparent variations in Ga concentration arise from local evaporation-field changes at the SFs, whereas the observed Al enrichment at the intersections between SFs and AlGaN layers represents genuine compositional segregation rather than a field-evaporation artefact. With the site-fraction quantification method, reliable chemical accuracy can be achieved in the analysis of extended defects in GaN.

Chapter 6 further integrated CL spectroscopy with correlative STEM and APT to connect defect structure, chemistry, and optical response. Both In and Mg were found to segregate preferentially along SFs, with the degree of segregation dependent on local SF polarity. CL revealed that SF-rich regions exhibit quenched near-band-edge emission and enhanced defect-related luminescence. These results demonstrate that local strain and electrostatic fields associated with SFs govern impurity incorporation and radiative recombination in cubic GaN.

Collectively, this work advances the understanding of how extended defects and SFs influence both the electronic and optical properties of cubic GaN-based heterostructures. The combined use of APT, STEM, and CL provides a powerful multiscale approach for correlating nanoscale

chemistry with functional behaviour, bridging atomic-level analysis and device-relevant performance.

7.2. Outlook

Building upon the findings in this work, future studies could further extend this methodology to control defect formation and tune luminescence in polar and non-polar GaN systems for next-generation III-nitride devices.

7.2.1. Growth-Condition Dependence

This work has shown that APT can directly visualise SFs and associated chemical environments in zincblende InGaN/GaN quantum well (QW) structures. To further understand the origin of the observed segregation behaviour, it would be valuable to study samples grown under a wider range of temperature conditions. Comparative analyses of such samples could help distinguish between polarity-driven and growth-induced segregation effects. Correlative APT, STEM and optical mapping studies across the samples grown under different conditions would provide a systematic view of how growth dynamics influence defect formation, local chemistry, and the resulting optical and electronic responses. Such investigations would also clarify whether the observed segregation is intrinsic to the SF polarity or is affected by external growth parameters.

7.2.2. Crystallographic Orientation and Polarity Correlation

Another important direction for future work is to establish a direct link between segregation asymmetry and the polarity of SFs. This could be achieved by preparing focused ion beam (FIB)

lift-outs along controlled orientations and tracking the laser direction relative to the known crystallographic axes during APT analysis. Verification of the specimen orientation and SF polarity using TEM would provide a geometrical and polar reference for each dataset. Such APT experiments could enable direct atomic-scale validation of polarity-dependent segregation, providing deeper insight into how polarity influences the performance of GaN-based devices.

7.2.3. Atomistic Modelling of Bonding and Segregation Energetics

To complement the experimental observations, first-principles calculations could be employed to investigate the local bonding environment and segregation energetics of dopant atoms (e.g., In, Mg) near SFs with opposite polarities. By quantifying site-specific formation energies and bonding characteristics, such simulations would provide atomistic insight into how local chemistry and polarisation fields jointly drive asymmetric segregation. By comparing calculated energies with experimentally observed segregation distributions, a comprehensive atomistic-experimental model could be formed, which may provide valuable new insights into the relationship between local bonding chemistry and macroscopic behaviour of extended defects.

References

[1] U. K. Mishra, L. Shen, T. E. Kazior, and Y.-F. Wu, "GaN-based RF power devices and amplifiers," *Proceedings of the IEEE,* vol. 96, no. 2, pp. 287-305, 2008.

[2] H. Haas, L. Yin, Y. Wang, and C. Chen, "What is lifi?," *Journal of lightwave technology,* vol. 34, no. 6, pp. 1533-1544, 2015.

[3] M. H. Crawford, "LEDs for solid-state lighting: performance challenges and recent advances," *IEEE Journal of Selected Topics in Quantum Electronics,* vol. 15, no. 4, pp. 1028-1040, 2009.

[4] J. J. Wierer Jr, and N. Tansu, "III-Nitride micro-LEDs for efficient emissive displays," *Laser & Photonics Reviews,* vol. 13, no. 9, pp. 1900141, 2019.

[5] Z. Mi, and C. Jagadish, *III-Nitride Semiconductor Optoelectronics*: Academic Press, 2017.

[6] C. Zhou, A. Ghods, V. G. Saravade, P. V. Patel, K. L. Yunghans, C. Ferguson, Y. Feng, B. Kucukgok, N. Lu, and I. T. Ferguson, "The current and emerging applications of the III-nitrides," *ECS Journal of Solid State Science and Technology,* vol. 6, no. 12, pp. Q149, 2017.

[7] S. P. DenBaars, D. Feezell, K. Kelchner, S. Pimputkar, C.-C. Pan, C.-C. Yen, S. Tanaka, Y. Zhao, N. Pfaff, and R. Farrell, "Development of gallium-nitride-based light-emitting diodes (LEDs) and laser diodes for energy-efficient lighting and displays," *Acta Materialia,* vol. 61, no. 3, pp. 945-951, 2013.

[8] J. Piprek, and S. Nakamura, "Physics of high-power InGaN/GaN lasers," *IEE Proceedings-Optoelectronics,* vol. 149, no. 4, pp. 145-151, 2002.

[9] M. Meneghini, C. De Santi, I. Abid, M. Buffolo, M. Cioni, R. A. Khadar, L. Nela, N. Zagni, A. Chini, F. Medjdoub, G. Meneghesso, G. Verzellesi, E. Zanoni, and E. Matioli, "GaN-based power devices: Physics, reliability, and perspectives," *Journal of Applied Physics,* vol. 130, no. 18, 2021.

[10] Y. Zhang, S. Lu, Y. Qiu, J. Wu, M. Zhang, and D. Luo, "Experimental and modeling investigations of miniaturization in InGaN/GaN light-emitting diodes and performance enhancement by micro-wall architecture," *Frontiers in Chemistry,* vol. 8, pp. 630050, 2021.

[11] S. Nakamura, T. Mukai, and M. Senoh, "Candela-class high-brightness InGaN/AlGaN double-heterostructure blue-light-emitting diodes," *Applied Physics Letters,* vol. 64, no. 13, pp. 1687-1689, 1994.

[12] E. F. Schubert, and J. K. Kim, "Solid-state light sources getting smart," *Science,* vol. 308, no. 5726, pp. 1274-1278, 2005.

[13] M. R. Krames, O. B. Shchekin, R. Mueller-Mach, G. O. Mueller, L. Zhou, G. Harbers, and M. G. Craford, "Status and future of high-power light-emitting diodes for solid-state lighting," *Journal of display technology,* vol. 3, no. 2, pp. 160-175, 2007.

[14] P. Pust, P. J. Schmidt, and W. Schnick, "A revolution in lighting," *Nature materials,* vol. 14, no. 5, pp. 454-458, 2015.

[15] T. Mukai, M. Yamada, and S. Nakamura, "Characteristics of InGaN-based UV/blue/green/amber/red light-emitting diodes," *Japanese Journal of Applied Physics,* vol. 38, no. 7R, pp. 3976, 1999.

[16] Y. Zhao, S. H. Oh, F. Wu, Y. Kawaguchi, S. Tanaka, K. Fujito, J. S. Speck, S. P. DenBaars, and S. Nakamura, "Green semipolar (2021) InGaN light-emitting diodes with small wavelength shift and narrow spectral linewidth," *Applied Physics Express,* vol. 6, no. 6, pp. 062102, 2013.

[17] Y. Jiang, Y. Li, Y. Li, Z. Deng, T. Lu, Z. Ma, P. Zuo, L. Dai, L. Wang, and H. Jia, "Realization of high-luminous-efficiency InGaN light-emitting diodes in the "green gap" range," *Scientific reports,* vol. 5, no. 1, pp. 1-7, 2015.

[18] C. Humphreys, J. Griffiths, F. Tang, F. Oehler, S. Findlay, C. Zheng, J. Etheridge, T. Martin, P. Bagot, and M. Moody, "The atomic structure of polar and non-polar InGaN quantum wells and the green gap problem," *Ultramicroscopy,* vol. 176, pp. 93-98, 2017.

[19] H. Hu, S. Zhou, H. Wan, X. Liu, N. Li, and H. Xu, "Effect of strain relaxation on performance of InGaN/GaN green LEDs grown on 4-inch sapphire substrate with sputtered AlN nucleation layer," *Scientific Reports,* vol. 9, no. 1, pp. 3447, 2019.

[20] C. Zhang, Y. Wu, B. Xia, P. Su, and J. Ma, "Improvement in quantum efficiency of green GaN-based micro-LED by trapezoidal quantum well," *Journal of Luminescence,* vol. 263, pp. 120027, 2023/11/01/, 2023.

[21] Y. Huang, E.-L. Hsiang, M.-Y. Deng, and S.-T. Wu, "Mini-LED, Micro-LED and OLED displays: present status and future perspectives," *Light: Science & Applications,* vol. 9, no. 1, pp. 105, 2020.

[22] A. R. Anwar, M. T. Sajjad, M. A. Johar, C. A. Hernández-Gutiérrez, M. Usman, and S. Łepkowski, "Recent progress in micro-LED-based display technologies," *Laser & Photonics Reviews,* vol. 16, no. 6, pp. 2100427, 2022.

[23] R. Kemper, M. Weinl, C. Mietze, M. Häberlen, T. Schupp, E. Tschumak, J. Lindner, K. Lischka, and D. As, "Growth of cubic GaN on nano-patterned 3C-SiC/Si (0 0 1) substrates," *Journal of crystal growth,* vol. 323, no. 1, pp. 84-87, 2011.

[24] S. Church, S. Hammersley, P. Mitchell, M. Kappers, S. Sahonta, M. Frentrup, D. Nilsson, P. Ward, L. Shaw, and D. J. Wallis, "Photoluminescence studies of cubic GaN epilayers," *physica status solidi (b),* vol. 254, no. 8, pp. 1600733, 2017.

[25] B. Ding, M. Frentrup, S. Fairclough, M. Kappers, M. Jain, A. Kovács, D. Wallis, and R. Oliver, "Alloy segregation at stacking faults in zincblende GaN heterostructures," *Journal of Applied Physics,* vol. 128, no. 14, 2020.

[26] D. D. Zhu, *Lighting/appliances*, 2012.

[27] R. Baleja, J. Šumpich, P. Bos, B. Helštýnová, K. Sokanský, and T. Novšk, "Comparison of LED properties, compact fluorescent bulbs and bulbs in residential areas." pp. 566-571.

[28] J. Cho, J. H. Park, J. K. Kim, and E. F. Schubert, "White light-emitting diodes: history, progress, and future," *Laser & photonics reviews,* vol. 11, no. 2, pp. 1600147, 2017.

[29] R. Haitz, and J. Y. Tsao, "Solid-state lighting:'The case'10 years after and future prospects," *physica status solidi (a),* vol. 208, no. 1, pp. 17-29, 2011.

[30] C. Elliott, M. Yamada, J. Penning, S. Schober, and K. Lee, *Energy Savings Forecast of Solid-State Lighting in General Illumination Applications*, United States, 2019.

[31] N. U. Islam, M. Usman, S. Rasheed, and T. Jamil, "Review—White Light-Emitting Diodes: Past, Present, and Future," *ECS Journal of Solid State Science and Technology*, 2021.

[32] M.-L. Lee, S.-S. Wang, Y.-H. Yeh, P.-H. Liao, and J.-K. Sheu, "Light-emitting diodes with surface gallium nitride p–n homojunction structure formed by selective area regrowth," *Scientific reports,* vol. 9, no. 1, pp. 1-7, 2019.

[33] T. D. Moustakas, and R. Paiella, "Optoelectronic device physics and technology of nitride semiconductors from the UV to the terahertz," *Reports on Progress in Physics,* vol. 80, no. 10, pp. 106501, 2017.

[34] J. J. Wierer Jr, J. Y. Tsao, and D. S. Sizov, "Comparison between blue lasers and light-emitting diodes for future solid-state lighting," *Laser & Photonics Reviews,* vol. 7, no. 6, pp. 963-993, 2013.

[35] Y. Narukawa, M. Ichikawa, D. Sanga, M. Sano, and T. Mukai, "White light emitting diodes with super-high luminous efficacy," *Journal of physics D: Applied physics,* vol. 43, no. 35, pp. 354002, 2010.

[36] M. Sheen, Y. Ko, D.-u. Kim, J. Kim, J.-h. Byun, Y. Choi, J. Ha, K. Y. Yeon, D. Kim, and J. Jung, "Highly efficient blue InGaN nanoscale light-emitting diodes," *Nature,* vol. 608, no. 7921, pp. 56-61, 2022.

[37] J. Lee, K. Min, Y. Park, K. S. Cho, and H. Jeon, "Photonic crystal phosphors integrated on a blue LED chip for efficient white light generation," *Advanced Materials,* vol. 30, no. 3, pp. 1703506, 2018.

[38] F. Rahman, "The shrinking green gap: trends in solid-state green emitters," *Photonic Spectra,* vol. 53, pp. 52-59, 2019.

[39] D. J. Binks, P. Dawson, R. A. Oliver, and D. J. Wallis, "Cubic GaN and InGaN/GaN quantum wells," *Applied Physics Reviews,* vol. 9, no. 4, 2022.

[40] D. R. Elsaesser, M. T. Durniak, A. S. Bross, and C. Wetzel, "Optimizing GaInN/GaN light-emitting diode structures under piezoelectric polarization," *Journal of Applied Physics,* vol. 122, no. 11, 2017.

[41] S.-H. Park, and S.-L. Chuang, "Comparison of zinc-blende and wurtzite GaN semiconductors with spontaneous polarization and piezoelectric field effects," *Journal of Applied Physics,* vol. 87, no. 1, pp. 353-364, 2000.

[42] D. J. As, and C. Mietze, "MBE growth and applications of cubic AlN/GaN quantum wells," *physica status solidi (a),* vol. 210, no. 3, pp. 474-479, 2013.

[43] D. Dyer, S. A. Church, R. Ahumada-Lazo, M. J. Kappers, M. P. Halsall, P. Parkinson, D. J. Wallis, R. A. Oliver, and D. J. Binks, "Efficiency droop in zincblende InGaN/GaN quantum wells," *Nanoscale,* vol. 16, no. 29, pp. 13953-13961, 2024.

[44] Y. Du, B. Chang, X. Fu, X. Wang, and M. Wang, "Electronic structure and optical properties of zinc-blende GaN," *Optik,* vol. 123, no. 24, pp. 2208-2212, 2012/12/01/, 2012.

[45] D. K. Gaskill, C. D. Brandt, and R. J. Nemanich, "III-Nitride, SiC, and Diamond Materials for Electronic Devices: symposium held April, 1996, San Francisco, California, USA," *(No Title)*, 1996.

[46] T. Lei, M. Fanciulli, R. Molnar, T. Moustakas, R. Graham, and J. Scanlon, "Epitaxial growth of zinc blende and wurtzitic gallium nitride thin films on (001) silicon," *Applied physics letters,* vol. 59, no. 8, pp. 944-946, 1991.

[47] I. Vurgaftman, and J. n. Meyer, "Band parameters for nitrogen-containing semiconductors," *Journal of applied physics,* vol. 94, no. 6, pp. 3675-3696, 2003.

[48] B. Heying, I. Smorchkova, C. Poblenz, C. Elsass, P. Fini, S. Den Baars, U. Mishra, and J. Speck, "Optimization of the surface morphologies and electron mobilities in GaN grown by plasma-assisted molecular beam epitaxy," *Applied Physics Letters,* vol. 77, no. 18, pp. 2885-2887, 2000.

[49] D. C. Look, C. Stutz, R. J. Molnar, K. Saarinen, and Z. Liliental-Weber, "Dislocation-independent mobility in lattice-mismatched epitaxy: application to GaN," *Solid state communications,* vol. 117, no. 10, pp. 571-575, 2001.

[50] S. Nakamura, and S. F. Chichibu, *Introduction to nitride semiconductor blue lasers and light emitting diodes*: CRC Press, 2000.

[51] J. Kim, A. Frenkel, H. Liu, and R. Park, "Growth by molecular beam epitaxy and electrical characterization of Si-doped zinc blende GaN films deposited on β-SiC coated (001) Si substrates," *Applied physics letters,* vol. 65, no. 1, pp. 91-93, 1994.

[52] D. Gaskill, L. Rowland, K. Doverspike, and J. H. Edgar, "Properties of Group III Nitrides," *London: INSPEC, IEE*, pp. 101-16, 1994.

[53] D. As, D. Schikora, A. Greiner, M. Lübbers, J. Mimkes, and K. Lischka, "p-and n-type cubic GaN epilayers on GaAs," *Physical Review B,* vol. 54, no. 16, pp. R11118, 1996.

[54] D. Florescu, V. Asnin, F. H. Pollak, R. Molnar, and C. Wood, "High spatial resolution thermal conductivity and Raman spectroscopy investigation of hydride vapor phase epitaxy grown n-GaN/sapphire (0001): Doping dependence," *Journal of Applied Physics,* vol. 88, no. 6, pp. 3295-3300, 2000.

[55] M. E. Levinshtein, S. L. Rumyantsev, and M. S. Shur, *Properties of Advanced Semiconductor Materials: GaN, AIN, InN, BN, SiC, SiGe*: John Wiley & Sons, 2001.

[56] M. Leszczynski, H. Teisseyre, T. Suski, I. Grzegory, M. Bockowski, J. Jun, S. Porowski, K. Pakula, J. Baranowski, and C. Foxon, “Lattice parameters of gallium nitride,” *Applied Physics Letters,* vol. 69, no. 1, pp. 73-75, 1996.

[57] Y. Dai, J. Liu, X. Sun, X. Zhan, Y. Luo, S. Zhang, Q. Sun, L. Wang, Y. Ji, M. Ikeda, and H. Yang, “Boosting the efficiency of InGaN-based green LEDs grown on Si through buffer strain engineering,” *Applied Physics Letters,* vol. 125, no. 2, 2024.

[58] A. Dussaigne, C. Paillet, N. Rochat, D. Cooper, A. Grenier, S. Vézian, B. Damilano, A. Michon, and B. Hyot, “Regular red-green-blue InGaN quantum wells with In content up to 40% grown on InGaN nanopyramids,” *Communications Materials,* vol. 5, no. 1, pp. 280, 2024/12/27, 2024.

[59] I. H. Brown, I. Pope, P. M. Smowton, P. Blood, J. D. Thomson, W. Chow, D. Bour, and M. Kneissl, “Determination of the piezoelectric field in InGaN quantum wells,” *Applied Physics Letters,* vol. 86, no. 13, 2005.

[60] K. Pieniak, M. Chlipala, H. Turski, W. Trzeciakowski, G. Muziol, G. Staszczak, A. Kafar, I. Makarowa, E. Grzanka, and S. Grzanka, “Quantum-confined Stark effect and mechanisms of its screening in InGaN/GaN light-emitting diodes with a tunnel junction,” *Optics Express,* vol. 29, no. 2, pp. 1824-1837, 2021.

[61] M. Usman, M. Munsif, U. Mushtaq, A.-R. Anwar, and N. Muhammad, “Green gap in GaN-based light-emitting diodes: in perspective,” *Critical Reviews in Solid State and Materials Sciences,* vol. 46, no. 5, pp. 450-467, 2021.

[62] J.-J. Huang, H.-C. Kuo, and S.-C. Shen, *Nitride semiconductor light-emitting diodes (LEDs): materials, technologies, and applications*: Woodhead Publishing, 2017.

[63] A. Daami, F. Olivier, L. Dupré, C. Licitra, F. Henry, F. Templier, and S. Le Calvez, "Green InGaN/GaN based LEDs: high luminance and blue shift." pp. 20-25.

[64] C. P. Singh, and K. Ghosh, “Lower current density driven InGaN/GaN micro-LED with improved quantum efficiency,” *Optik,* vol. 300, pp. 171664, 2024/04/01/, 2024.

[65] A. Bojarska-Cieślińska, Ł. Marona, S. Grzanka, E. Grzanka, and P. Perlin, “InGaN multiquantum wells—problem of carrier injection,” *Scientific Reports,* vol. 15, no. 1, pp. 2902, 2025/01/23, 2025.

[66] S. M. Sze, Y. Li, and K. K. Ng, *Physics of semiconductor devices*: John wiley & sons, 2021.

[67] T. Bhattarai, A. Ebong, and M. Y. A. Raja, “A Review of Light-Emitting Diodes and Ultraviolet Light-Emitting Diodes and Their Applications,” *Photonics,* vol. 11, no. 6, pp. 491, 2024.

[68] E. F. Schubert, *Light-emitting diodes*: Cambridge university press, 2006.

[69] A. I. Alhassan, N. G. Young, R. M. Farrell, C. Pynn, F. Wu, A. Y. Alyamani, S. Nakamura, S. P. DenBaars, and J. S. Speck, “Development of high performance green

c-plane III-nitride light-emitting diodes," *Optics express,* vol. 26, no. 5, pp. 5591-5601, 2018.

[70] S. Lu, J. Li, K. Huang, G. Liu, Y. Zhou, D. Cai, R. Zhang, and J. Kang, "Designs of InGaN micro-LED structure for improving quantum efficiency at low current density," *Nanoscale research letters,* vol. 16, no. 1, pp. 99, 2021.

[71] H. Round, "Electrical World (New York)," 1907.

[72] O. Losev, "Telegrafiya i Telefoniya bez Provodov," *vol,* vol. 44, pp. 485-494, 1927.

[73] O. Losev, "Telegrafi ya i Telefoniya bez Provodov 44, 485 (1927)," *Phil. Mag,* vol. 6, pp. 1024, 1928.

[74] O. Losev, "Uber die Anwendung der Quantentheorie zur Leuchtenerscheinungen am Karborundumdetektor," *Physikalische Zeitschrift,* vol. 30, pp. 920-923, 1929.

[75] O. Losev, "Luminosity of silicon carbide detectors; electrical conductivity of silicon carbide," *Phys. Zs,* vol. 32, pp. 692, 1931.

[76] O. Losev, "Uber den lichtelektrischen Effektin besonderer aktiven Schicht der Karborundumkrystalle," *Physikalische Zeitschrift,* vol. 34, pp. 397-403, 1933.

[77] N. Holonyak, and S. F. Bevacqua, "Coherent (visible) light emission from Ga (As1−xPx) junctions," *Applied Physics Letters,* vol. 1, no. 4, pp. 82-83, 1962.

[78] S. Nakamura, and M. R. Krames, "History of gallium–nitride-based light-emitting diodes for illumination," *Proceedings of the IEEE,* vol. 101, no. 10, pp. 2211-2220, 2013.

[79] H. Amano, M. Kito, K. Hiramatsu, and I. Akasaki, "P-type conduction in Mg-doped GaN treated with low-energy electron beam irradiation (LEEBI)," *Japanese journal of applied physics,* vol. 28, no. 12A, pp. L2112, 1989.

[80] S. Nakamura, T. Mukai, M. S. M. Senoh, and N. I. N. Iwasa, "Thermal annealing effects on p-type Mg-doped GaN films," *Japanese Journal of Applied Physics,* vol. 31, no. 2B, pp. L139, 1992.

[81] S. Nakamura, M. S. M. Senoh, and T. M. T. Mukai, "P-GaN/N-InGaN/N-GaN double-heterostructure blue-light-emitting diodes," *Japanese Journal of Applied Physics,* vol. 32, no. 1A, pp. L8, 1993.

[82] I. Akasaki, H. Amano, and S. Nakamura, "Blue LEDs–Filling the world with new light," *Nobel Prize*, 2014.

[83] M. Kneissl, T.-Y. Seong, J. Han, and H. Amano, "The emergence and prospects of deep-ultraviolet light-emitting diode technologies," *nature photonics,* vol. 13, no. 4, pp. 233-244, 2019.

[84] M. Monavarian, A. Rashidi, and D. Feezell, "A Decade of Nonpolar and Semipolar III-Nitrides: A Review of Successes and Challenges," *physica status solidi (a),* vol. 216, no. 1, pp. 1800628, 2019.

[85] S. Tan, J. Zhang, T. Egawa, and G. Chen, "Influence of quantum-well number and an AlN electron blocking layer on the electroluminescence properties of AlGaN deep ultraviolet light-emitting diodes," *Applied Sciences,* vol. 8, no. 12, pp. 2402, 2018.

[86] C. Li, Z. Ji, J. Li, M. Xu, H. Xiao, and X. Xu, "Electroluminescence properties of InGaN/GaN multiple quantum well-based LEDs with different indium contents and different well widths," *Scientific Reports,* vol. 7, no. 1, pp. 15301, 2017/11/10, 2017.

[87] X. Li, N. Pant, S. I. Rahman, R. Armitage, S. Rajan, E. Kioupakis, and D. Feezell, "Impact of quantum well thickness on efficiency loss in InGaN/GaN LEDs: Challenges for thin-well designs," *Applied Physics Letters,* vol. 126, no. 13, 2025.

[88] M. Z. Baten, S. Alam, B. Sikder, and A. Aziz, "III-Nitride Light-Emitting Devices," *Photonics,* vol. 8, no. 10, pp. 430, 2021.

[89] E. O. Odoh, and A. S. Njapba, "A review of semiconductor quantum well devices," *Advances in Physics Theories and Applications,* vol. 46, pp. 26-32, 2015.

[90] R. En-nadir, H. El-ghazi, L. Leontie, M. Tihtih, S. E. Zaki, W. Belaid, A. Carlescu, and I. Zorkani, "Tailoring optoelectronic properties of InGaN-based quantum wells through electric field, indium content, and confinement shape: A theoretical investigation," *Physica B: Condensed Matter,* vol. 663, pp. 414976, 2023/08/15/, 2023.

[91] F. Zhang, M. Ikeda, S.-M. Zhang, J.-P. Liu, A.-Q. Tian, P.-Y. Wen, Y. Cheng, and H. Yang, "Reduction of Polarization Field Strength in Fully Strained c-Plane InGaN/(In)GaN Multiple Quantum Wells Grown by MOCVD," *Nanoscale Research Letters,* vol. 11, no. 1, pp. 519, 2016/11/25, 2016.

[92] S. A. Church, M. Quinn, K. Cooley-Greene, B. Ding, A. Gundimeda, M. J. Kappers, M. Frentrup, D. J. Wallis, R. A. Oliver, and D. J. Binks, "Photoluminescence efficiency of zincblende InGaN/GaN quantum wells," *Journal of Applied Physics,* vol. 129, pp. 175702, 2021.

[93] P. Vacek, M. Frentrup, L. Y. Lee, F. C.-P. Massabuau, M. J. Kappers, D. J. Wallis, R. Gröger, and R. A. Oliver, "Defect structures in (001) zincblende GaN/3C-SiC nucleation layers," *Journal of Applied Physics,* vol. 129, no. 15, 2021.

[94] H. Xiu, S. M. Fairclough, A. Gundimeda, M. J. Kappers, D. J. Wallis, R. A. Oliver, and M. Frentrup, "Polarity determination of crystal defects in zincblende GaN by aberration-corrected electron microscopy," *Journal of Applied Physics,* vol. 133, no. 10, 2023.

[95] E. L. Luna, and M. Á. Vidal, "Review of the Properties of GaN, InN, and Their Alloys Obtained in Cubic Phase on MgO Substrates by Plasma-Enhanced Molecular Beam Epitaxy," *Crystals,* vol. 14, no. 9, pp. 801, 2024.

[96] Y. J. Sun, O. Brandt, U. Jahn, T. Y. Liu, A. Trampert, S. Cronenberg, S. Dhar, and K. H. Ploog, "Impact of nucleation conditions on the structural and optical properties of M-plane GaN (1 $\bar{1}$00) grown on γ-LiAlO 2," *Journal of Applied Physics,* vol. 92, no. 10, pp. 5714-5719, 2002.

[97] G. Jacopin, L. Rigutti, L. Largeau, F. Fortuna, F. Furtmayr, F. Julien, M. Eickhoff, and M. Tchernycheva, "Optical properties of wurtzite/zinc-blende heterostructures in GaN nanowires," *Journal of Applied Physics,* vol. 110, no. 6, 2011.

[98] P. Corfdir, and P. Lefebvre, "Importance of excitonic effects and the question of internal electric fields in stacking faults and crystal phase quantum discs: The model-case of GaN," *Journal of Applied Physics,* vol. 112, no. 5, 2012.

[99] C. A. Hernández-Gutiérrez, Y. L. Casallas-Moreno, V.-T. Rangel-Kuoppa, D. Cardona, Y. Hu, Y. Kudriatsev, M. A. Zambrano-Serrano, S. Gallardo-Hernandez, and M. Lopez-Lopez, "Study of the heavily p-type doping of cubic GaN with Mg," *Scientific Reports,* vol. 10, no. 1, pp. 16858, 2020/10/08, 2020.

[100] C. Stampfl, and C. G. Van de Walle, "Energetics and electronic structure of stacking faults in AlN, GaN, and InN," *Physical Review B,* vol. 57, no. 24, pp. R15052, 1998.

[101] A. Benbedra, S. Meskine, A. Boukortt, R. Hayn, M. Texier, O. Thomas, and T. W. Cornelius, "Energetics, electronic structure and electric polarization of basal stacking faults in wurtzite GaN and ZnO," *Computational Condensed Matter,* vol. 43, pp. e01033, 2025.

[102] J. Moneta, M. Kryśko, J. Domagala, E. Grzanka, G. Muziol, M. Siekacz, M. Leszczyński, and J. Smalc-Koziorowska, "Influence of GaN substrate miscut on the XRD quantification of plastic relaxation in InGaN," *Acta Materialia,* vol. 276, pp. 120082, 2024.

[103] L. Y. Lee, M. Frentrup, M. J. Kappers, R. A. Oliver, C. J. Humphreys, and D. J. Wallis, "Effect of growth temperature and V/III-ratio on the surface morphology of MOVPE-grown cubic zincblende GaN," *Journal of Applied Physics,* vol. 124, no. 10, 2018.

[104] J. Pernot, E. Bustarret, M. Rudziński, P. R. Hageman, and P. K. Larsen, "Strain relaxation in GaN grown on vicinal 4H-SiC (0001) substrates," *Journal of applied physics,* vol. 101, no. 3, 2007.

[105] B. Ding, M. Frentrup, S. M. Fairclough, G. Kusch, M. J. Kappers, D. J. Wallis, and R. A. Oliver, "Multimicroscopy of cross-section zincblende GaN LED heterostructure," *Journal of Applied Physics,* vol. 130, no. 11, 2021.

[106] J. Lähnemann, U. Jahn, O. Brandt, T. Flissikowski, P. Dogan, and H. T. Grahn, "Luminescence associated with stacking faults in GaN," *Journal of Physics D: Applied Physics,* vol. 47, no. 42, pp. 423001, 2014.

[107] P. Corfdir, C. Hauswald, J. Zettler, T. Flissikowski, J. Lähnemann, S. Fernández-Garrido, L. Geelhaar, H. Grahn, and O. Brandt, "Stacking faults as quantum wells in nanowires: Density of states, oscillator strength, and radiative efficiency," *Physical Review B,* vol. 90, no. 19, pp. 195309, 2014.

[108] S. A. Church, B. Ding, P. W. Mitchell, M. J. Kappers, M. Frentrup, G. Kusch, S. M. Fairclough, D. J. Wallis, R. A. Oliver, and D. J. Binks, "Stacking fault-associated

polarized surface-emitted photoluminescence from zincblende InGaN/GaN quantum wells," *Applied Physics Letters,* vol. 117, no. 3, 2020.

[109] F. Wu, Y.-D. Lin, A. Chakraborty, H. Ohta, S. P. DenBaars, S. Nakamura, and J. S. Speck, "Stacking fault formation in the long wavelength InGaN/GaN multiple quantum wells grown on m-plane GaN," *Applied Physics Letters,* vol. 96, no. 23, 2010.

[110] F. C. Massabuau, L. Trinh-Xuan, D. Lodié, S. Sahonta, S. Rhode, E. Thrush, F. Oehler, M. Kappers, C. Humphreys, and R. Oliver, "Towards a better understanding of trench defects in InGaN/GaN quantum wells." p. 012042.

[111] A. Gundimeda, G. Kusch, M. Frentrup, M. J. Kappers, D. J. Wallis, and R. A. Oliver, "Cathodoluminescence studies of the optical properties of a zincblende InGaN/GaN single quantum well," *Nanotechnology,* vol. 35, no. 39, Jul 11, 2024.

[112] B. Mounika, J. Ajayan, S. Bhattacharya, and D. Nirmal, "Recent developments in materials, architectures and processing of AlGaN/GaN HEMTs for future RF and power electronic applications: A critical review," *Micro and Nanostructures,* vol. 168, pp. 207317, 2022.

[113] E. Di Russo, T. Verstijnen, P. Koenraad, K. Pantzas, G. Patriarche, and L. Rigutti, "Order and disorder at the atomic scale: Microscopy applied to semiconductors," *Reviews of Modern Physics,* vol. 97, no. 2, pp. 025006, 2025.

[114] B.Gil, *III-Nitride Semiconductors and their Modern Devices*: Oxford University Press, 2013.

[115] K. Prabakaran, M. Jayasakthi, S. Surender, S. Pradeep, S. Sanjay, R. Ramesh, M. Balaji, N. Gautier, and K. Baskar, "Structural, morphological, optical and electrical characterization of InGaN/GaN MQW structures for optoelectronic applications," *Applied Surface Science,* vol. 476, pp. 993-999, 2019.

[116] Z. Benzarti, T. Sekrafi, A. Khalfallah, Z. Bougrioua, D. Vignaud, M. Evaristo, and A. Cavaleiro, "Growth temperature effect on physical and mechanical properties of nitrogen rich InN epilayers," *Journal of Alloys and Compounds,* vol. 885, pp. 160951, 2021.

[117] C. M. Furqan, J. Y. L. Ho, and H. S. Kwok, "GaN thin film: Growth and Characterizations by Magnetron Sputtering," *Surfaces and Interfaces,* vol. 26, pp. 101364, 2021/10/01/, 2021.

[118] L. A. Martínez-Ara, J. R. Aguilar-Hernández, J. Sastré-Hernández, L. A. Hernández-Hernández, M. d. l. Á. Hernández-Pérez, P. Maldonado-Altamirano, R. Mendoza-Pérez, and G. Contreras-Puente, "Structural and Optical Properties of GaN Thin Films Grown on Si (111) by Pulsed Laser Deposition," *Materials Research,* vol. 22, 2019.

[119] A. K. Dhasiyan, F. W. Amalraj, S. Jayaprasad, N. Shimizu, O. Oda, K. Ishikawa, and M. Hori, "Epitaxial growth of high-quality GaN with a high growth rate at low temperatures by radical-enhanced metalorganic chemical vapor deposition," *Scientific Reports,* vol. 14, no. 1, pp. 10861, 2024/05/13, 2024.

[120] L. Y. Lee, M. Frentrup, P. Vacek, M. J. Kappers, D. J. Wallis, and R. A. Oliver, "Investigation of stacking faults in MOVPE-grown zincblende GaN by XRD and TEM," *Journal of Applied Physics,* vol. 125, no. 10, 2019.

[121] X. J. Chen, J. S. Hwang, G. Perillat-Merceroz, S. Landis, B. Martin, D. Le Si Dang, J. Eymery, and C. Durand, "Wafer-scale selective area growth of GaN hexagonal prismatic nanostructures on c-sapphire substrate," *Journal of Crystal Growth,* vol. 322, no. 1, pp. 15-22, 2011/05/01/, 2011.

[122] T. Schulz, A. Duff, T. Remmele, M. Korytov, T. Markurt, M. Albrecht, L. Lymperakis, J. Neugebauer, C. Chèze, and C. Skierbiszewsk, "Separating strain from composition in unit cell parameter maps obtained from aberration corrected high resolution transmission electron microscopy imaging," *Journal of Applied Physics,* vol. 115, no. 3, 2014.

[123] L. Rigutti, I. Blum, D. Shinde, D. Hernández-Maldonado, W. Lefebvre, J. Houard, F. Vurpillot, A. Vella, M. Tchernycheva, C. Durand, J. Eymery, and B. Deconihout, "Correlation of Microphotoluminescence Spectroscopy, Scanning Transmission Electron Microscopy, and Atom Probe Tomography on a Single Nano-object Containing an InGaN/GaN Multiquantum Well System," *Nano Letters,* vol. 14, no. 1, pp. 107-114, 2014/01/08, 2014.

[124] L. Chen, X. Shen, J. Wei, Z. Wang, F. Hu, L. Bian, and Q. Ouyang, "Temperature-dependent photoluminescence characterization and electrochemical applications of highly stable CsPb(Cl/Br)3-CNTs heterojunctions," *Optical Materials,* vol. 153, pp. 115636, 2024/07/01/, 2024.

[125] N. Dalla, P. Kulboka, M. Kobecki, J. Misiak, P. Prystawko, H. Turski, P. Kossacki, and T. Jakubczyk, "Off-resonant photoluminescence spectroscopy of high-optical quality single photon emitters in GaN," *Solid State Communications,* vol. 397, pp. 115845, 2025/03/01/, 2025.

[126] J. Lähnemann, V. M. Kaganer, K. K. Sabelfeld, A. E. Kireeva, U. Jahn, C. Chèze, R. Calarco, and O. Brandt, "Carrier Diffusion in Ga N: A Cathodoluminescence Study. III. Nature of Nonradiative Recombination at Threading Dislocations," *Physical Review Applied,* vol. 17, no. 2, pp. 024019, 2022.

[127] E. Smith, and G. Dent, *Modern Raman spectroscopy: a practical approach*: John Wiley & Sons, 2019.

[128] T. Kirchartz, J. A. Márquez, M. Stolterfoht, and T. Unold, "Photoluminescence-based characterization of halide perovskites for photovoltaics," *Advanced energy materials,* vol. 10, no. 26, pp. 1904134, 2020.

[129] R. R. Jones, D. C. Hooper, L. Zhang, D. Wolverson, and V. K. Valev, "Raman techniques: fundamentals and frontiers," *Nanoscale research letters,* vol. 14, pp. 1-34, 2019.

[130] M.-H. Sheen, S.-D. Kim, J.-H. Lee, J.-I. Shim, and Y.-W. Kim, "V-pits as barriers to diffusion of carriers in InGaN/GaN quantum wells," *Journal of Electronic Materials,* vol. 44, pp. 4134-4138, 2015.

[131] I. A. Ajia, P. R. Edwards, Y. Pak, E. Belekov, M. A. Roldan, N. Wei, Z. Liu, R. W. Martin, and I. S. Roqan, "Generated Carrier Dynamics in V-Pit-Enhanced InGaN/GaN Light-Emitting Diode," *ACS Photonics,* vol. 5, no. 3, pp. 820-826, 2018/03/21, 2018.

[132] P. Agüi-Gonzalez, S. Jähne, and N. T. Phan, "SIMS imaging in neurobiology and cell biology," *Journal of Analytical Atomic Spectrometry,* vol. 34, no. 7, pp. 1355-1368, 2019.

[133] H. Gnaser, "Greatly enhanced detection sensitivity for carbon, nitrogen, and oxygen in silicon by secondary-ion-mass spectrometry," *Applied Physics Letters,* vol. 79, no. 4, pp. 497-499, 2001.

[134] H. Jiang, E. Favaro, C. N. Goulbourne, P. D. Rakowska, G. M. Hughes, M. G. Ryadnov, L. G. Fong, S. G. Young, D. J. P. Ferguson, A. L. Harris, and C. R. M. Grovenor, "Stable isotope imaging of biological samples with high resolution secondary ion mass spectrometry and complementary techniques," *Methods,* vol. 68, no. 2, pp. 317-324, 2014/07/01/, 2014.

[135] H. Tian, A. Wucher, and N. Winograd, "Reducing the Matrix Effect in Organic Cluster SIMS Using Dynamic Reactive Ionization," *Journal of The American Society for Mass Spectrometry,* vol. 27, no. 12, pp. 2014-2024, 2016/12/01, 2016.

[136] A. Hospodková, F. Hájek, J. Pangrác, M. Slavická Zíková, T. Hubáček, K. Kuldová, J. Oswald, T. Vaněk, A. Vetushka, J. Čížek, M. O. Liedke, M. Butterling, and A. Wagner, "A secret luminescence killer in deepest QWs of InGaN/GaN multiple quantum well structures," *Journal of Crystal Growth,* vol. 536, pp. 125579, 2020/04/15/, 2020.

[137] B. Gault, A. Chiaramonti, O. Cojocaru-Mirédin, P. Stender, R. Dubosq, C. Freysoldt, S. K. Makineni, T. Li, M. Moody, and J. M. Cairney, "Atom probe tomography," *Nature Reviews Methods Primers,* vol. 1, no. 1, pp. 51, 2021.

[138] M. J. Galtrey, R. A. Oliver, M. J. Kappers, C. J. Humphreys, D. J. Stokes, P. H. Clifton, and A. Cerezo, "Three-dimensional atom probe studies of an InxGa1− xN⁄ GaN multiple quantum well structure: Assessment of possible indium clustering," *Applied physics letters,* vol. 90, no. 6, 2007.

[139] M. J. Galtrey, R. A. Oliver, M. J. Kappers, C. McAleese, D. Zhu, C. J. Humphreys, P. H. Clifton, D. Larson, and A. Cerezo, "Compositional inhomogeneity of a high-efficiency InxGa1−xN based multiple quantum well ultraviolet emitter studied by three dimensional atom probe," *Applied Physics Letters,* vol. 92, no. 4, 2008.

[140] M. Galtrey, R. Oliver, M. Kappers, C. Humphreys, P. Clifton, D. Larson, D. Saxey, and A. Cerezo, "Three-dimensional atom probe analysis of green-and blue-emitting InxGa1− xN⁄ GaN multiple quantum well structures," *Journal of Applied Physics,* vol. 104, no. 1, 2008.

[141] S. E. Bennett, D. W. Saxey, M. J. Kappers, J. S. Barnard, C. J. Humphreys, G. D. Smith, and R. A. Oliver, "Atom probe tomography assessment of the impact of electron beam exposure on InxGa1−xN/GaN quantum wells," *Applied Physics Letters,* vol. 99, no. 2, 2011.

[142] M. Müller, G. D. W. Smith, B. Gault, and C. R. M. Grovenor, "Phase separation in thick InGaN layers – A quantitative, nanoscale study by pulsed laser atom probe tomography," *Acta Materialia,* vol. 60, no. 10, pp. 4277-4285, 2012/06/01/, 2012.

[143] L. Rigutti, L. Mancini, W. Lefebvre, J. Houard, D. Hernàndez-Maldonado, E. Di Russo, E. Giraud, R. Butté, J. F. Carlin, N. Grandjean, D. Blavette, and F. Vurpillot, "Statistical nanoscale study of localised radiative transitions in GaN/AlGaN quantum wells and AlGaN epitaxial layers," *Semiconductor Science and Technology,* vol. 31, no. 9, pp. 095009, 2016/08/25, 2016.

[144] S. Choi, F. Wu, R. Shivaraman, E. C. Young, and J. S. Speck, "Observation of columnar microstructure in lattice-matched InAlN/GaN grown by plasma assisted molecular beam epitaxy," *Applied Physics Letters,* vol. 100, no. 23, 2012.

[145] Y. Yamaguchi, Y. Kanitani, Y. Kudo, J. Uzuhashi, T. Ohkubo, K. Hono, and S. Tomiya, "Atomic Diffusion of Indium through Threading Dislocations in InGaN Quantum Wells," *Nano Letters,* vol. 22, no. 17, pp. 6930-6935, 2022/09/14, 2022.

[146] E. Di Russo, P. Dalapati, J. Houard, L. Venturi, I. Blum, S. Moldovan, N. Le Biavan, D. Lefebvre, M. Hugues, J. M. Chauveau, D. C. Blavette, B. Deconihout, A. Vella, F. Vurpillot, and L. Rigutti, "Super-resolution Optical Spectroscopy of Nanoscale Emitters within a Photonic Atom Probe," *Nano Letters,* vol. 20, no. 12, pp. 8733-8738, 2020/12/09, 2020.

[147] J. Houard, A. Normand, E. Di Russo, C. Bacchi, P. Dalapati, G. Beainy, S. Moldovan, G. Da Costa, F. Delaroche, C. Vaudolon, J. M. Chauveau, M. Hugues, D. Blavette, B. Deconihout, A. Vella, F. Vurpillot, and L. Rigutti, "A photonic atom probe coupling 3D atomic scale analysis with in situ photoluminescence spectroscopy," *Review of Scientific Instruments,* vol. 91, no. 8, 2020.

[148] E. Weikum, A. Diaz-Damian, J. Houard, G. Da Costa, F. Delaroche, A. Vella, G. Muzioł, H. Turski, and L. Rigutti, "Microscopic correlation of doping distribution and luminescence in a nitride laser junction by Photonic Atom Probe," *Physical Review Materials,* vol. 8, no. 7, pp. 074603, 07/18/, 2024.

[149] S. K. Gautam, S. Ndiaye, J. Houard, D. Lefebvre, J.-M. Chauveau, M. Hugues, A. Vella, and L. Rigutti, "A Photonic Atom Probe Study of Thermal Effects at the Nanosecond and Nanometer scale," *Nano Letters*, 2025.

[150] L. Mancini, "Atom Probe-Based Correlative Multi-Microscopy for the Study of Low-Dimensional Semiconductors," Rouen, 2016.

[151] L. Mancini, N. Amirifar, D. Shinde, I. Blum, M. Gilbert, A. Vella, F. Vurpillot, W. Lefebvre, R. Lardé, and E. Talbot, "Composition of wide bandgap semiconductor

materials and nanostructures measured by atom probe tomography and its dependence on the surface electric field," *The Journal of Physical Chemistry C,* vol. 118, no. 41, pp. 24136-24151, 2014.

[152] B. Gault, D. W. Saxey, M. W. Ashton, S. B. Sinnott, A. N. Chiaramonti, M. P. Moody, and D. K. Schreiber, "Behavior of molecules and molecular ions near a field emitter," *New Journal of Physics,* vol. 18, no. 3, pp. 033031, 2016.

[153] D. R. Kingham, "The post-ionization of field evaporated ions: A theoretical explanation of multiple charge states," *Surface Science,* vol. 116, no. 2, pp. 273-301, 1982.

[154] R. Haydock, and D. R. Kingham, "Post-ionization of field-evaporated ions," *Physical Review Letters,* vol. 44, no. 23, pp. 1520, 1980.

[155] J. R. Riley, R. A. Bernal, Q. Li, H. D. Espinosa, G. T. Wang, and L. J. Lauhon, "Atom probe tomography of a-axis GaN nanowires: analysis of nonstoichiometric evaporation behavior," *ACS nano,* vol. 6, no. 5, pp. 3898-3906, 2012.

[156] D. R. Diercks, B. P. Gorman, R. Kirchhofer, N. Sanford, K. Bertness, and M. Brubaker, "Atom probe tomography evaporation behavior of C-axis GaN nanowires: Crystallographic, stoichiometric, and detection efficiency aspects," *Journal of Applied Physics,* vol. 114, no. 18, 2013.

[157] M. A. Khan, S. P. Ringer, and R. Zheng, "Atom probe tomography on semiconductor devices," *Advanced Materials Interfaces,* vol. 3, no. 12, pp. 1500713, 2016.

[158] E. Di Russo, I. Blum, J. Houard, M. Gilbert, G. Da Costa, D. Blavette, and L. Rigutti, "Compositional accuracy of atom probe tomography measurements in GaN: Impact of experimental parameters and multiple evaporation events," *Ultramicroscopy,* vol. 187, pp. 126-134, 2018.

[159] A. Diagne, L. G. Garcia, S. Ndiaye, N. Gogneau, M. Vrellou, J. Houard, and L. Rigutti, "Field-dependent abundances of hydride molecular ions in atom probe tomography of III-N semiconductors," *Journal of Microscopy,* vol. 293, no. 3, pp. 153-159, 2024.

[160] Y. Li, Y. Wei, Z. Wang, X. Liu, T. Colnaghi, L. Han, Z. Rao, X. Zhou, L. Huber, and R. Dsouza, "Quantitative three-dimensional imaging of chemical short-range order via machine learning enhanced atom probe tomography," *Nature Communications,* vol. 14, no. 1, pp. 7410, 2023.

[161] C. F. Holder, and R. E. Schaak, "Tutorial on Powder X-ray Diffraction for Characterizing Nanoscale Materials," *ACS Nano,* vol. 13, no. 7, pp. 7359-7365, 2019/07/23, 2019.

[162] P. R. Edwards, and R. W. Martin, "Cathodoluminescence nano-characterization of semiconductors," *Semiconductor Science and Technology,* vol. 26, no. 6, pp. 064005, 2011.

[163] G. Pozina, R. Ciechonski, Z. Bi, L. Samuelson, and B. Monemar, "Dislocation related droop in InGaN/GaN light emitting diodes investigated via cathodoluminescence," *Applied Physics Letters,* vol. 107, no. 25, 2015.

[164] J. T. Griffiths, S. Zhang, B. Rouet-Leduc, W. Y. Fu, A. Bao, D. Zhu, D. J. Wallis, A. Howkins, I. Boyd, and D. Stowe, “Nanocathodoluminescence reveals mitigation of the stark shift in InGaN quantum wells by Si doping,” *Nano letters,* vol. 15, no. 11, pp. 7639-7643, 2015.

[165] P. Makuła, M. Pacia, and W. Macyk, "How to correctly determine the band gap energy of modified semiconductor photocatalysts based on UV–Vis spectra," 23, ACS Publications, 2018, pp. 6814-6817.

[166] W. Zhou, R. Apkarian, Z. L. Wang, and D. Joy, “Fundamentals of scanning electron microscopy (SEM),” *Scanning microscopy for nanotechnology: techniques and applications*, pp. 1-40, 2007.

[167] R. Egerton, P. Li, and M. Malac, “Radiation damage in the TEM and SEM,” *Micron,* vol. 35, no. 6, pp. 399-409, 2004.

[168] C. Kübel, A. Voigt, R. Schoenmakers, M. Otten, D. Su, T.-C. Lee, A. Carlsson, and J. Bradley, “Recent advances in electron tomography: TEM and HAADF-STEM tomography for materials science and semiconductor applications,” *Microscopy and Microanalysis,* vol. 11, no. 5, pp. 378-400, 2005.

[169] P.-C. Shen, C. Su, Y. Lin, A.-S. Chou, C.-C. Cheng, J.-H. Park, M.-H. Chiu, A.-Y. Lu, H.-L. Tang, and M. M. Tavakoli, “Ultralow contact resistance between semimetal and monolayer semiconductors,” *Nature,* vol. 593, no. 7858, pp. 211-217, 2021.

[170] Y. Lin, M. Zhou, X. Tai, H. Li, X. Han, and J. Yu, “Analytical transmission electron microscopy for emerging advanced materials,” *Matter,* vol. 4, no. 7, pp. 2309-2339, 2021.

[171] D. K. Schroder, *Semiconductor material and device characterization*: John Wiley & Sons, 2015.

[172] K. Li, J. Liu, C. R. Grovenor, and K. L. Moore, “NanoSIMS imaging and analysis in materials science,” *Annual Review of Analytical Chemistry,* vol. 13, no. 1, pp. 273-292, 2020.

[173] S. N. Magonov, and D. H. Reneker, “Characterization of polymer surfaces with atomic force microscopy,” *Annual Review of Materials Science,* vol. 27, no. 1, pp. 175-222, 1997.

[174] ionTOF. "The ultimate M6 TOF Analyser," https://www.iontof.com/m6-tof-sims-technical-details.html.

[175] U. o. Cambridge. "Image resolution," https://www.doitpoms.ac.uk/tlplib/tem/resolution.php.

[176] J.-F. JEOL. "JEM-F200 Multi-purpose Electron Microscope," https://www.jeol.com/products/scientific/tem/JEM-F200.php.

[177] P. E. Batson, N. Dellby, and O. L. Krivanek, “Sub-ångstrom resolution using aberration corrected electron optics,” *Nature,* vol. 418, no. 6898, pp. 617-620, 2002/08/01, 2002.

[178] G. E. Lloyd, “Atomic number and crystallographic contrast images with the SEM: a review of backscattered electron techniques,” *Mineralogical Magazine,* vol. 51, no. 359, pp. 3-19, 1987.

[179] P. J. Goodhew, and J. Humphreys, *Electron microscopy and analysis*: CRC press, 2000.

[180] B. J. Inkson, "2 - Scanning electron microscopy (SEM) and transmission electron microscopy (TEM) for materials characterization," *Materials Characterization Using Nondestructive Evaluation (NDE) Methods*, G. Hübschen, I. Altpeter, R. Tschuncky and H.-G. Herrmann, eds., pp. 17-43: Woodhead Publishing, 2016.

[181] K. Thompson, D. Lawrence, D. Larson, J. Olson, T. Kelly, and B. Gorman, “In situ site-specific specimen preparation for atom probe tomography,” *Ultramicroscopy,* vol. 107, no. 2-3, pp. 131-139, 2007.

[182] D. J. Larson, T. J. Prosa, D. E. Perea, K. Inoue, and D. Mangelinck, “Atom probe tomography of nanoscale electronic materials,” *Mrs Bulletin,* vol. 41, pp. 30-34, 2016.

[183] D. Brüggemann, B. Wolfrum, and J. P. de Silva, "Fabrication, Properties and Applications of Gold Nanopillars," *Handbook of Nanomaterials Properties*, B. Bhushan, D. Luo, S. R. Schricker, W. Sigmund and S. Zauscher, eds., pp. 317-354, Berlin, Heidelberg: Springer Berlin Heidelberg, 2014.

[184] B. Gault, M. P. Moody, J. M. Cairney, and S. P. Ringer, *Atom probe microscopy*: Springer Science & Business Media, 2012.

[185] B. Gault, M. P. Moody, F. De Geuser, A. La Fontaine, L. T. Stephenson, D. Haley, and S. P. Ringer, “Spatial Resolution in Atom Probe Tomography,” *Microscopy and Microanalysis,* vol. 16, no. 1, pp. 99-110, 2010.

[186] M. K. Miller, *Atom probe tomography: analysis at the atomic level*: Springer Science & Business Media, 2012.

[187] M. K. Miller, and R. G. Forbes, “Atom-probe tomography: the local electrode atom probe,” 2014.

[188] T. F. Kelly, and M. K. Miller, “Atom probe tomography,” *Review of scientific instruments,* vol. 78, no. 3, 2007.

[189] G. Ehrlich, and K. Stolt, “Surface diffusion,” *Annual Review of Physical Chemistry,* vol. 31, no. 1, pp. 603-637, 1980.

[190] G. Antczak, and G. Ehrlich, *Surface diffusion: metals, metal atoms, and clusters*: Cambridge University Press, 2010.

[191] E. A. Marquis, and F. Vurpillot, “Chromatic Aberrations in the Field Evaporation Behavior of Small Precipitates,” *Microscopy and Microanalysis,* vol. 14, no. 6, pp. 561-570, 2008.

[192] F. Vurpillot, A. Bostel, A. Menand, and D. Blavette, “Trajectories of field emitted ions in 3D atom-probe,” *The European Physical Journal Applied Physics,* vol. 6, no. 2, pp. 217-221, 1999.

[193] F. Vurpillot, A. Bostel, and D. Blavette, "Trajectory overlaps and local magnification in three-dimensional atom probe," *Applied Physics Letters,* vol. 76, no. 21, pp. 3127-3129, 2000.

[194] F. De Geuser, W. Lefebvre, F. Danoix, F. Vurpillot, B. Forbord, and D. Blavette, "An improved reconstruction procedure for the correction of local magnification effects in three-dimensional atom-probe," *Surface and Interface Analysis: An International Journal devoted to the development and application of techniques for the analysis of surfaces, interfaces and thin films,* vol. 39, no. 2-3, pp. 268-272, 2007.

[195] D. J. Larson, B. Gault, B. P. Geiser, F. De Geuser, and F. Vurpillot, "Atom probe tomography spatial reconstruction: Status and directions," *Current Opinion in Solid State and Materials Science,* vol. 17, no. 5, pp. 236-247, 2013.

[196] D. Beinke, C. Oberdorfer, and G. Schmitz, "Towards an accurate volume reconstruction in atom probe tomography," *Ultramicroscopy,* vol. 165, pp. 34-41, 2016/06/01/, 2016.

[197] T. J. Prosa, and D. J. Larson, "Modern focused-ion-beam-based site-specific specimen preparation for atom probe tomography," *Microscopy and Microanalysis,* vol. 23, no. 2, pp. 194-209, 2017.

[198] R. Barabash, Y. Gao, G. E. Ice, O. M. Barabash, J.-S. Chung, W. Liu, R. Kröger, H. Lohmeyer, K. Sebald, and J. Gutowski, "Mapping strain gradients in the FIB-structured InGaN/GaN multilayered films with 3D X-ray microbeam," *Materials Science and Engineering: A,* vol. 528, no. 1, pp. 52-57, 2010.

[199] A. J. London, D. Haley, and M. P. Moody, "Single-ion deconvolution of mass peak overlaps for atom probe microscopy," *Microscopy and Microanalysis,* vol. 23, no. 2, pp. 300-306, 2017.

[200] A. J. London, "Quantifying uncertainty from mass-peak overlaps in atom probe microscopy," *Microscopy and Microanalysis,* vol. 25, no. 2, pp. 378-388, 2019.

[201] S. Jin, H. Su, F. Qian, Y. Li, and G. Sha, "Effects of atom probe analysis parameters on composition measurement of precipitates in an Al-Mg-Si-Cu alloy," *Ultramicroscopy,* vol. 235, pp. 113495, 2022/05/01/, 2022.

[202] K. Buchanan, K. Colas, J. Ribis, A. Lopez, and J. Garnier, "Analysis of the metastable precipitates in peak-hardness aged Al-Mg-Si(-Cu) alloys with differing Si contents," *Acta Materialia,* vol. 132, pp. 209-221, 2017/06/15/, 2017.

[203] A. M. Belu, D. J. Graham, and D. G. Castner, "Time-of-flight secondary ion mass spectrometry: techniques and applications for the characterization of biomaterial surfaces," *Biomaterials,* vol. 24, no. 21, pp. 3635-3653, 2003.

[204] D. Haley, P. Choi, and D. Raabe, "Guided mass spectrum labelling in atom probe tomography," *Ultramicroscopy,* vol. 159, pp. 338-345, 2015/12/01/, 2015.

[205] O. C. Hellman, J. B. Du Rivage, and D. N. Seidman, "Efficient sampling for three-dimensional atom probe microscopy data," *Ultramicroscopy,* vol. 95, pp. 199-205, 2003.

[206] O. C. Hellman, J. A. Vandenbroucke, J. Rüsing, D. Isheim, and D. N. Seidman, "Analysis of three-dimensional atom-probe data by the proximity histogram," *Microscopy and Microanalysis,* vol. 6, no. 5, pp. 437-444, 2000.

[207] O. C. Hellman, and D. N. Seidman, "Measurement of the Gibbsian interfacial excess of solute at an interface of arbitrary geometry using three-dimensional atom probe microscopy," *Materials Science and Engineering: A,* vol. 327, no. 1, pp. 24-28, 2002.

[208] M. Müller, D. W. Saxey, G. D. Smith, and B. Gault, "Some aspects of the field evaporation behaviour of GaSb," *Ultramicroscopy,* vol. 111, no. 6, pp. 487-492, 2011.

[209] D. Saxey, "Correlated ion analysis and the interpretation of atom probe mass spectra," *Ultramicroscopy,* vol. 111, no. 6, pp. 473-479, 2011.

[210] F. Tang, M. P. Moody, T. L. Martin, P. A. Bagot, M. J. Kappers, and R. A. Oliver, "Practical issues for atom probe tomography analysis of III-nitride semiconductor materials," *Microscopy and Microanalysis,* vol. 21, no. 3, pp. 544-556, 2015.

[211] R. Morris, R. Cuduvally, D. Melkonyan, C. Fleischmann, M. Zhao, L. Arnoldi, P. van der Heide, and W. Vandervorst, "Toward accurate composition analysis of GaN and AlGaN using atom probe tomography," *Journal of Vacuum Science & Technology B,* vol. 36, no. 3, 2018.

[212] C. Dreyer, A. Janotti, and C. Van de Walle, "Brittle fracture toughnesses of GaN and AlN from first-principles surface-energy calculations," *Applied Physics Letters,* vol. 106, no. 21, 2015.

[213] I. Yonenaga, "Hardness of bulk single-crystal GaN and AlN," *MRS Internet Journal of Nitride Semiconductor Research,* vol. 7, no. 1, pp. 6, 2020/09/27, 2020.

[214] E. A. Marquis, and B. Gault, "Determination of the tip temperature in laser assisted atom-probe tomography using charge state distributions," *Journal of Applied Physics,* vol. 104, no. 8, 2008.

[215] D. A. Cullen, and D. J. Smith, "Assessment of surface damage and sidewall implantation in AlGaN-based high electron mobility transistor devices caused during focused-ion-beam milling," *Journal of Applied Physics,* vol. 104, no. 9, 2008.

[216] E. Di Russo, "Study of the physical mechanisms leading to compositional biases in atom probe tomography of semiconductors," Normandie Université, 2018.

[217] N. I. Kato, "Reducing focused ion beam damage to transmission electron microscopy samples," *Journal of electron microscopy,* vol. 53, no. 5, pp. 451-458, 2004.

[218] S. Norris, "A Comparison of Beam Induced Damage from Xenon and Gallium Focused Ion Beams," 2019.

[219] K. Loeto, S. Fairclough, I. Griffiths, G. Kusch, S. Ghosh, M. Kappers, N. Young, and R. Oliver, "Influence of Xe+ and Ga+ milling species on the cathodoluminescence of wurtzite and zincblende GaN," *Journal of Applied Physics,* vol. 136, no. 4, 2024.

[220] J. Bogdanowicz, A. Kumar, C. Fleischmann, M. Gilbert, J. Houard, A. Vella, and W. Vandervorst, "Laser-assisted atom probe tomography of semiconductors: The impact

of the focused-ion beam specimen preparation," *Ultramicroscopy,* vol. 188, pp. 19-23, 2018.

[221] J. Uzuhashi, and T. Ohkubo, "Systematic study of FIB-induced damage for the high-quality TEM sample preparation," *Ultramicroscopy,* vol. 262, pp. 113980, 2024.

[222] R. J. Morris, R. Cuduvally, J.-R. Lin, M. Zhao, W. Vandervorst, M. Thuvander, and C. Fleischmann, "Field dependent study on the impact of co-evaporated multihits and ion pile-up for the apparent stoichiometric quantification of GaN and AlN," *Ultramicroscopy,* vol. 241, pp. 113592, 2022.

[223] B. Gault, M. P. Moody, F. De Geuser, G. Tsafnat, A. La Fontaine, L. T. Stephenson, D. Haley, and S. P. Ringer, "Advances in the calibration of atom probe tomographic reconstruction," *Journal of Applied Physics,* vol. 105, no. 3, 2009.

[224] D. R. Diercks, and B. P. Gorman, "Nanoscale Measurement of Laser-Induced Temperature Rise and Field Evaporation Effects in CdTe and GaN," *The Journal of Physical Chemistry C,* vol. 119, no. 35, pp. 20623-20631, 2015/09/03, 2015.

[225] N. A. Sanford, P. T. Blanchard, M. D. Brubaker, A. K. Rishinaramangalam, Q. Zhang, A. Roshko, D. F. Feezell, B. D. Klein, and A. V. Davydov, "Laser-assisted atom probe tomography of c-plane and m-plane InGaN test structures," *arXiv preprint arXiv:2102.06340*, 2021.

[226] F. Vurpillot, J. Houard, A. Vella, and B. Deconihout, "Thermal response of a field emitter subjected to ultra-fast laser illumination," *Journal of Physics D: Applied Physics,* vol. 42, no. 12, pp. 125502, 2009.

[227] N. A. Sanford, P. T. Blanchard, M. Brubaker, K. A. Bertness, A. Roshko, J. B. Schlager, R. Kirchhofer, D. R. Diercks, and B. Gorman, "Laser-assisted atom probe tomography of MBE grown GaN nanowire heterostructures," *physica status solidi c,* vol. 11, no. 3-4, pp. 608-612, 2014.

[228] C. M. De Castilho, and D. R. Kingham, "Calculations of field ionization in the field ion microscope," *Surface science,* vol. 173, no. 1, pp. 75-96, 1986.

[229] D. K. Schreiber, A. N. Chiaramonti, L. M. Gordon, and K. Kruska, "Applicability of post-ionization theory to laser-assisted field evaporation of magnetite," *Applied Physics Letters,* vol. 105, no. 24, 2014.

[230] G. Kellogg, and T. Tsong, "Pulsed-laser atom-probe field-ion microscopy," *Journal of Applied physics,* vol. 51, no. 2, pp. 1184-1193, 1980.

[231] J. R. Riley, T. Detchprohm, C. Wetzel, and L. J. Lauhon, "On the reliable analysis of indium mole fraction within InxGa1− xN quantum wells using atom probe tomography," *Applied Physics Letters,* vol. 104, no. 15, 2014.

[232] E. Di Russo, N. Cherkashin, M. Korytov, A. Nikolaev, A. Sakharov, A. Tsatsulnikov, B. Bonef, I. Blum, J. Houard, and G. Da Costa, "Compositional accuracy in atom probe tomography analyses performed on III-N light emitting diodes," *Journal of Applied Physics,* vol. 126, no. 12, 2019.

[233] F. Liu, L. Huang, R. F. Davis, L. M. Porter, D. K. Schreiber, S. V. Kuchibatla, V. Shutthanandan, S. Thevuthasan, E. A. Preble, and T. Paskova, "Composition and interface analysis of InGaN/GaN multiquantum-wells on GaN substrates using atom probe tomography," *Journal of Vacuum Science & Technology B,* vol. 32, no. 5, 2014.

[234] L. Rigutti, B. Bonef, J. Speck, F. Tang, and R. Oliver, "Atom probe tomography of nitride semiconductors," *Scripta Materialia,* vol. 148, pp. 75-81, 2018.

[235] R. Agrawal, R. A. Bernal, D. Isheim, and H. D. Espinosa, "Characterizing atomic composition and dopant distribution in wide band gap semiconductor nanowires using laser-assisted atom probe tomography," *The Journal of Physical Chemistry C,* vol. 115, no. 36, pp. 17688-17694, 2011.

[236] L. Rigutti, L. Mancini, D. Hernández-Maldonado, W. Lefebvre, E. Giraud, R. Butté, J. Carlin, N. Grandjean, D. Blavette, and F. Vurpillot, "Statistical correction of atom probe tomography data of semiconductor alloys combined with optical spectroscopy: The case of Al0. 25Ga0. 75N," *Journal of Applied Physics,* vol. 119, no. 10, 2016.

[237] A. Devaraj, R. Colby, W. P. Hess, D. E. Perea, and S. Thevuthasan, "Role of photoexcitation and field ionization in the measurement of accurate oxide stoichiometry by laser-assisted atom probe tomography," *The journal of physical chemistry letters,* vol. 4, no. 6, pp. 993-998, 2013.

[238] A. Gundimeda, G. Kusch, M. Frentrup, H. Xiu, R. Shu, C. Hofer, P. A. J. Bagot, M. P. Moody, M. J. Kappers, D. J. Wallis, and R. A. Oliver, "Impact of stacking faults on the luminescence of a zincblende InGaN/GaN single quantum well," *Journal of Physics D: Applied Physics,* vol. 58, no. 2, pp. 025112, 2024/10/24, 2025.

[239] X. Xu, M. Frentrup, G. Kusch, R. Shu, C. Hofer, P. A. J. Bagot, M. P. Moody, M. J. Kappers, D. J. Wallis, and R. A. Oliver, "Point defect luminescence associated with stacking faults in magnesium doped zincblende GaN," *Journal of Applied Physics,* vol. 137, no. 23, 2025.

[240] S. Church, S. Hammersley, P. Mitchell, M. Kappers, L. Lee, F. Massabuau, S. Sahonta, M. Frentrup, L. Shaw, and D. Wallis, "Effect of stacking faults on the photoluminescence spectrum of zincblende GaN," *Journal of Applied Physics,* vol. 123, no. 18, 2018.

[241] O. G. Licata, S. Broderick, E. Rocco, F. Shahedipour-Sandvik, and B. Mazumder, "Dopant-defect interactions in Mg-doped GaN via atom probe tomography," *Applied Physics Letters,* vol. 119, no. 3, 2021.

[242] Z. Xie, J. Buckeridge, C. R. A. Catlow, A. Zhang, T. W. Keal, P. Sherwood, Y. Lu, S. M. Woodley, and A. A. Sokol, "Overcoming the compensation of acceptors in GaN: Mg by defect complex formation," *APL Materials,* vol. 11, no. 8, 2023.

[243] J. Lähnemann, O. Brandt, U. Jahn, C. Pfüller, C. Roder, P. Dogan, F. Grosse, A. Belabbes, F. Bechstedt, and A. Trampert, "Direct experimental determination of the

spontaneous polarization of GaN," *Physical Review B—Condensed Matter and Materials Physics,* vol. 86, no. 8, pp. 081302, 2012.

[244] Z. Antoš, P. Vacek, and R. Gröger, "Intersections of two stacking faults in zincblende GaN," *Computational Materials Science,* vol. 180, pp. 109620, 2020/07/01/, 2020.

[245] L. Barbisan, E. Scalise, and A. Marzegalli, "Evolution and Intersection of Extended Defects and Stacking Faults in 3C-SiC Layers on Si (001) Substrates by Molecular Dynamics Simulations: The Forest Dislocation Case," *physica status solidi (b),* vol. 259, no. 9, pp. 2100584, 2022.

[246] B. Ding, "Study of wurtzite and zincblende GaN based green LED heterostructure," University of Cambridge, 2021.

[247] J. A. Majewski, and P. Vogl, "Polarization and band offsets of stacking faults in AlN and GaN," *MRS Internet Journal of Nitride Semiconductor Research,* vol. 3, no. 1, pp. 21, 1998.

[248] B. Bonef, M. Catalano, C. Lund, S. P. Denbaars, S. Nakamura, U. K. Mishra, M. J. Kim, and S. Keller, "Indium segregation in N-polar InGaN quantum wells evidenced by energy dispersive X-ray spectroscopy and atom probe tomography," *Applied Physics Letters,* vol. 110, no. 14, 2017.

[249] J. Neugebauer, and C. G. Van de Walle, "Atomic geometry and electronic structure of native defects in GaN," *Physical Review B,* vol. 50, no. 11, pp. 8067, 1994.

[250] S. Lany, and A. Zunger, "Dual nature of acceptors in GaN and ZnO: The curious case of the shallow MgGa deep state," *Applied Physics Letters,* vol. 96, no. 14, 2010.

[251] A. Kakanakova-Georgieva, A. Papamichail, V. Stanishev, and V. Darakchieva, "Incorporation of magnesium into GaN regulated by intentionally large amounts of hydrogen during growth by MOCVD," *physica status solidi (b),* vol. 259, no. 10, pp. 2200137, 2022.

Appendix A: Preliminary APT Study on Carbon-Doped Wurtzite GaN

This appendix presents the original motivation for studying carbon-doped wurtzite GaN and SIMS profiles which were obtained during initial examination. The overall goal of this aspect was to detect and spatially correlate low-concentration carbon dopants around extended defects such as threading dislocations (TDs) using APT.

The SIMS analysis on the wafer confirmed the presence of carbon (as shown in the Figure A1-1 below). However, this analysis is limited since it can only report the average concentration across the entire sample volume, and with limited spatial resolution. On the other hand, APT is only capable of analysing a few tens to hundreds of cubic nanometres. This makes it particularly challenging to detect low concentrations of carbon that are not uniformly distributed in the material, especially when these atoms segregate to specific microstructural features such as dislocations.

In the case of this study, carbon was not detected in the APT datasets, potentially due to the following factors:

1. Non-uniform carbon distribution: Carbon is expected to segregate preferentially around TDs or other extended defects. If such features are absent from the analysed volume, the local concentration may fall below the detection threshold of APT, despite the overall SIMS average being above it.
2. Absence of pre-characterisation: No TEM was performed prior to APT to locate TDs within the tip region. As carbon segregation is expected to occur preferentially near TDs, the lack of site-specific preparation meant the analysed volume may not have contained relevant features. This however provides a direction for future work.
3. Layer-dependent doping: According to SIMS data, only the surface region had a significant carbon content. However, since the samples were prepared externally by a collaborator, we did not have direct control over which layer was therefore analysed in the APT specimens. Therefore, it is possible that the region containing the highest carbon concentration was missed altogether.

Although these APT experiments did not show direct information on carbon segregation, the data collected from the GaN matrix was later repurposed to optimise APT acquisition parameters for GaN-based material. As the material is compositionally homogeneous and free

from internal interfaces, it can be used as a suitable test system for demonstrating the effect of operating parameters on stoichiometric Ga:N evaporation.

It is worth noting that the main material studied in the thesis is zincblende GaN. The use of wurtzite GaN in this preliminary study is a consequence of the original design of a doping study and sample availability at the time. Despite the different crystal structure, the field evaporation behaviour (as assessed via charge-state ratios) and overall optimisation strategy remain comparable and transferable. This work thus provided a solid foundation for the parameter choices applied in the main analysis presented in subsequent chapters.

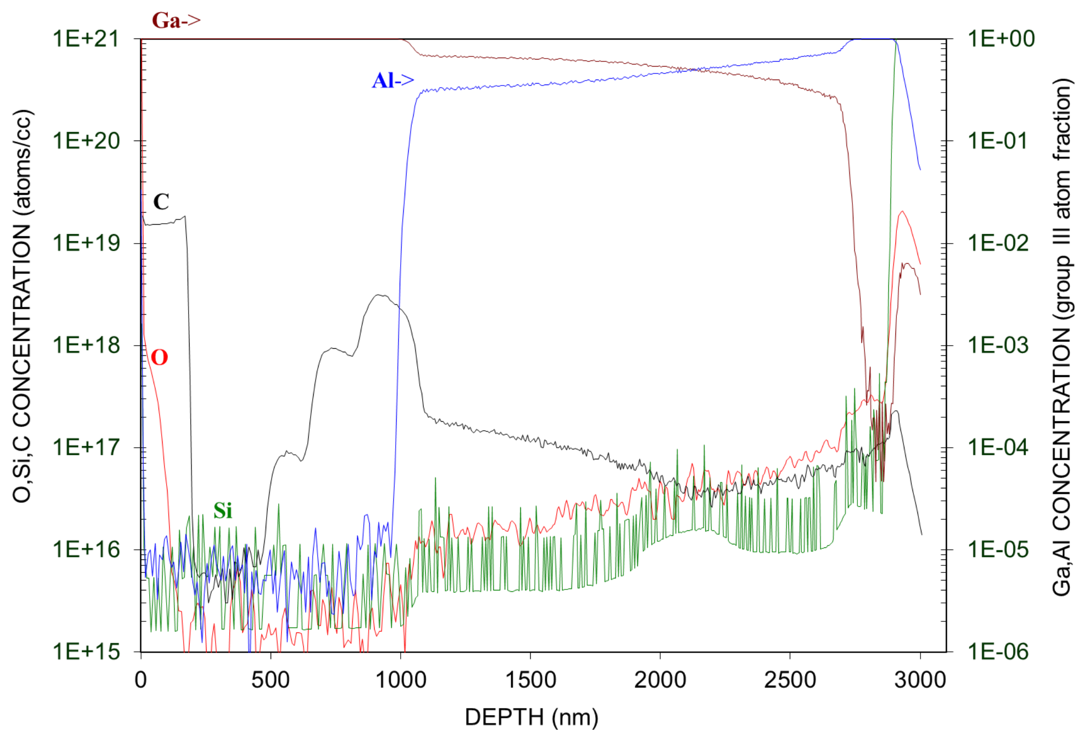

Figure A1-1 SIMS depth profile of the carbon-doped GaN sample, performed by EAG Laboratories, provided by University of Cambridge. The carbon concentration is significantly elevated in the surface region, then drops by several orders of magnitude after the first ≈200 nm, indicating strong layer dependence of the doping.

Appendix B: Operating Conditions for GaN Analysis

Table B2-1 APT acquisition parameters and measured compositions for bulk wurtzite GaN during parameter optimisation.

Section No.	Laser energy (fJ)	Temperature (K)	Detection Rate (%)	Pulse Frequency (kHz)	Voltage Range (V)		Ion Range (M)		N (%)	Ga (%)	Ion
					start	end	start	end			
GaN-M2-1	100	50	1	250	4000	5760	2.70	16.20	25.244	74.755	13.50
GaN-M2-2	120	50	1	250	5700	5900	16.90	22.00	21.981	78.018	5.10
GaN-M2-3	50	70	1	250	6022	6100	24.00	30.00	28.920	71.080	6.00
GaN-M2-4	15	70	1	250	6590	6670	30.50	38.20	40.095	59.905	7.70
GaN-M2-5	120	70	1	250	5720	5850	40.00	46.00	20.235	79.755	6.00
GaN-M2-6	100	70	1	250	5888	6018	47.00	59.50	21.252	78.747	12.50
GaN-M2-7	100	60	1	250	6130	6190	61.00	66.50	20.710	79.290	5.50
GaN-M2-8	120	60	1	250	6030	6125	67.00	73.50	17.485	82.513	6.50
GaN-M2-9	50	60	1	250	6517	6600	74.50	81.00	25.685	74.312	6.50
GaN-M2-10	15	60	1	250	7125	7220	82.00	90.00	38.290	61.710	8.00
GaN-M2-11	15	50	1	250	7340	7440	92.00	101.50	38.206	61.801	9.50
GaN-M2-12	50	50	1	250	6740	6946	102.50	113.00	25.905	74.093	10.50
GaN-M2-13	50	40	1	250	6950	7070	114.50	121.00	26.142	73.858	6.50
GaN-M2-14	15	40	1	250	7655	7743	122.00	128.00	38.575	61.423	6.00

Section No.	Laser energy (fJ)	Temperature (K)	Detection Rate (%)	Pulse Frequency (kHz)	Voltage Range (V)		Ion Range (M)		N (%)	Ga (%)	Ion
					start	end	start	end			
GaN-M2-15	100	40	1	250	6500	6815	129.50	169.00	16.637	83.364	39.50
GaN-M2-16	120	40	1	250	6876	6958	169.50	177.00	17.105	82.895	7.50
GaN-M3-1	1000	50	1	200	3000	3800	1.5	6.5	15.439	84.561	5.0
GaN-M3-2	500	50	1	200	4147	4570	7.0	12.0	14.949	85.051	5.0
GaN-M3-3	100	50	1	250	5419	5877	14.0	24.0	29.229	70.771	10.0
GaN-M3-4	500	50	1	250	4947	5192	25.0	33.5	10.578	89.422	8.5
GaN-M3-5	1000	50	1	250	4663	4824	34.0	41.5	5.235	94.765	7.5
GaN-M3-6	50	50	1	250	6390	6484	43.0	49.0	33.516	66.484	6.0
GaN-M3-7	70	50	1	250	6260	6380	49.5	57.0	27.022	72.978	7.5
GaN-M3-8	30	50	1	250	6789	6870	57.5	63.5	38.881	61.119	6.0
GaN-M3-9	10	50	1	250	7368	7488	64.0	69.0	46.861	53.139	5.0
GaN-M3-10	20	50	1	250	7015	7160	69.5	78.3	57.671	42.329	8.8
GaN-M3-11	60	50	1	250	6491	6659	78.8	85.5	31.952	68.048	6.7
GaN-M3-12	40	50	1	250	6826	6900	86.0	92.5	35.790	64.210	6.5
GaN-M3-13	80	50	1	250	6456	6623	93.0	99.5	28.706	71.294	6.5
GaN-M3-14	90	50	1	250	6462	6601	99.6	106.1	26.621	73.379	6.5
GaN-M3-15	300	50	1	250	5669	5900	106.5	114.0	11.025	88.975	7.5

Appendix B: Operating Conditions for GaN Analysis

Section No.	Laser energy (fJ)	Temperature (K)	Detection Rate (%)	Pulse Frequency (kHz)	Voltage Range (V)		Ion Range (M)		N (%)	Ga (%)	Ion
					start	end	start	end			
GaN-M3-16	800	50	1	250	5162	5352	115.0	122.0	5.179	94.821	7.0
GaN-M3-17	600	50	1	250	5405	5530	123.0	131.5	6.145	93.855	8.5
GaN-M3-18	900	50	1	250	5200	5334	131.8	136.8	4.706	95.294	5.0
GaN-M3-19	100	50	1	250	6588	6924	137.5	186.5	24.506	75.494	49.0
GaN-M3-20	200	50	1	250	6384	6481	187.0	194.5	15.853	84.147	7.5
GaN-M3-21	400	50	1	250	5928	6216	195.5	206.0	10.633	89.367	10.5
GaN-M3-22	5	50	1	250	8489	9117	207.0	222.8	47.753	52.247	15.8
GaN-M5-1	10,000	50	2	250	2688	3045	1.5	8.0	2.027	97.973	6.5
GaN-M5-2	10,000	50	3	250	3090	3276	9.0	14.0	0.594	99.406	5.0
GaN-M5-3	1,000	50	3	250	4682	5083	15.0	22.3	4.522	95.478	7.3
GaN-M5-4	1,000	50	2	250	4905	5120	23.0	29.5	3.383	96.617	6.5
GaN-M5-5	500	50	2	250	5663	5790	30.0	36.0	7.712	92.288	6.0
GaN-M5-6	700	50	1	250	5233	5330	37.0	44.0	4.588	95.412	7.0
GaN-M5-7	100	50	2	250	6853	7121	45.0	52.0	27.313	72.687	7.0
GaN-M9-1	10000	50	1	250	2000	2550	1.00	12.00	0.160	99.840	11
GaN-M9-2	10000	50	1	500	2550	2750	12.30	15.10	0.190	99.810	2.8
GaN-M9-3	20000	50	1	250	2450	2500	15.40	17.80	0.150	99.850	2.4

Section No.	Laser energy (fJ)	Temperature (K)	Detection Rate (%)	Pulse Frequency (kHz)	Voltage Range (V)		Ion Range (M)		N (%)	Ga (%)	Ion
					start	end	start	end			
GaN-M9-4	5000	50	1	250	3100	3500	18.00	24.20	0.460	99.540	6.2
GaN-M9-5	1000	50	1	250	4700	4450	24.50	35.50	1.870	98.130	11
GaN-M9-6	500	50	1	250	5000	4700	35.90	41.4	5.238	94.762	5.5
GaN-M9-7	300	50	1	250	5100	5000	41.70	48.1	4.468	95.532	6.4
GaN-M9-8	100	50	1	250	5900	6000	48.40	61.3	11.69	88.31	12.9
GaN-M9-9	50	50	1	250	6500	6650	61.50	79.6	21	79	18.1
GaN-M9-10	70	50	1	250	6450	6550	80.20	98.2	16.871	83.129	18
GaN-M9-11	70	50	1	500	6550	6650	98.40	118.6	16.22	83.78	20.2
GaN-M9-12	30	50	1	250	7200	7300	118.80	128.2	27.824	72.176	9.4
GaN-M9-13	150	50	1	250	6000	6200	128.50	138.1	7.522	92.478	9.6
GaN-M9-14	150	50	1	500	6200	6200	138.30	141.7	6.884	93.116	3.4
GaN-M9-15	15	50	1	500	8000	7800	142.50	148.3	35.793	64.207	5.8
GaN-M9-16	15	50	1	250	7800	7850	148.50	158.7	35.545	64.455	10.2
GaN-M9-17	200	50	1	250	5700	6100	159.40	165	5.163	94.837	5.6
GaN-M9-18	30000	50	1	250	3000	3000	166.60	170.3	3.503	96.497	3.7